

# Continuum Systems in the No-Core Shell Model

Alexa, Stefan Vasco

(2020)

DOI (TUprints): <https://doi.org/10.25534/tuprints-00013435>

Lizenz:



CC-BY-NC-ND 4.0 International - Creative Commons, Attribution Non-commercial, No-derivatives

Publikationstyp: Ph.D. Thesis

Fachbereich: 05 Department of Physics

Quelle des Originals: <https://tuprints.ulb.tu-darmstadt.de/13435>

---



TECHNISCHE  
UNIVERSITÄT  
DARMSTADT

---

# Continuum Systems in the No-Core Shell Model

---

**Dem Fachbereich Physik  
der Technischen Universität Darmstadt**

**zur Erlangung des Grades  
eines Doktors der Naturwissenschaften  
(Dr. rer. nat.)**

Genehmigte Dissertation von  
Stefan Vasco Alexa, M.Sc.  
geboren in Luxemburg, Luxemburg

Darmstadt 2020  
D17

Continuum Systems in the No-Core Shell Model  
Kontinuumssysteme im No-Core Shell Model

Referent: Prof. Dr. Robert Roth  
Korreferent: Prof. Dr. Jens Braun

Tag der Einreichung: 16.06.2020

Alexa, Stefan Vasco: Continuum Systems in the No-Core Shell Model

Darmstadt, Technische Universität Darmstadt

Jahr der Veröffentlichung: 2020

URN: urn:nbn:de:tuda-tuprints-134358

Tag der mündlichen Prüfung: 13.07.2020



Veröffentlicht unter CC BY-NC-ND 4.0

<https://creativecommons.org/licenses/by-nc-nd/4.0/>

# Abstract

The progress of *ab initio* nuclear structure in the past two decades revealed the need to incorporate continuum degrees of freedom. They are indispensable in the treatment of nuclear structure and for connecting theory to experiments performed at the extremes of low-energy many-body scattering. Many-body continuum calculation are a challenging task. It makes sense to build on the proven *ab initio* bound-state methods, if possible. In this work, we present combinations of the *ab initio* nuclear structure method of the No-Core Shell Model (NCSM) with two approaches that give access to observables in the nuclear continuum. These methods are the Harmonic Oscillator Representation of Scattering Equations (HORSE) and the Analytic Continuation in the Coupling Constant (ACCC). The focus is on the determination of resonance parameters, which is motivated by the possible existence of a resonating four-neutron  $J^\pi = 0^+$  state, the tetra-neutron, proposed by a recently conducted experiment. We employ various state-of-the-art Chiral Effective Field Theory ( $\chi$ EFT) interactions.

We first introduce the HORSE method and its simplification, the Single-State HORSE, which belong to the so-called  $J$ -matrix methods. The  $J$ -matrix approach uses the tridiagonality of the kinetic energy in a specific basis representation to connect an interior, interacting region, to an exterior, free region. With the Single-State HORSE method, we calculate tetra-neutron phase shifts derived in a hyperspherical framework. We use various Similarity Renormalization Group evolved  $\chi$ EFT interactions and two phenomenological potentials, studying their effects on phase shifts. The calculations are performed in large NCSM model spaces. The phase shifts are in line with the existence of a resonance, showing characteristic features of such states. We further show a way of obtaining a hyperspherical basis within the framework of the Jacobi-NCSM. This paves the way for future studies involving full HORSE Green's function.

The second method used to investigate resonances, with an application to the dineutron and tetra-neutron, is the ACCC. The method provides access to resonances on the complex  $k$ -plane by using the analytic properties of the Jost function as a function of a coupling constant. It relies solely on bound-state calculations by artificially binding the system to obtain energies at different coupling strengths, which are fitted by Padé approximants and extrapolated to the initial interaction strength. We show two different binding procedures, an additional four-body potential constructed on matrix element level from the smallest NCSM model spaces, dubbed eigenvector binding. This is motivated by the desire to avoid bound substructures. The second procedure is a straightforward multiplication of the interaction matrix elements by a factor. The dineutron results show that the binding methods do not falsely produce resonances. The tetra-neutron results support a resonance in the case of eigenvector binding, but not so for the direct matrix element modification.



# Zusammenfassung

Der Fortschritt der ab-initio Kernstrukturtheorie innerhalb der letzten zwei Jahrzehnte hat gezeigt, dass Kontinuumsfreiheitsgrade berücksichtigt werden müssen. Diese sind unverzichtbar bei der Beschreibung der Kernstruktur und der Verbindung von Theorie und Experiment. Die Berechnung von Observablen des Vielkörperkontinuums ist eine anspruchsvolle Aufgabe. Es ist daher wünschenswert, auf die bewährten ab-initio Methoden für gebundene Zustände zurückzugreifen, wenn dies möglich ist.

Thema dieser Arbeit ist die Kombination des “No-Core Shell Model” (NCSM), einer ab-initio Kernstrukturmethode, mit zwei Ansätzen, die Zugang zu Observablen des nuklearen Kontinuums ermöglichen. Diese Methoden sind die “Harmonic Oscillator Representation of Scattering Equations” (HORSE) und die “Analytic Continuation in the Coupling Constant” (ACCC). Der Schwerpunkt liegt auf der Bestimmung von Resonanzparametern, motiviert durch ein kürzlich durchgeführtes Experiment, welches die mögliche Existenz eines  $J^\pi = 0^+$  Resonanzzustandes vierer Neutronen, des so genannten Tetraneutrons, postuliert. Wir setzen verschiedene moderne Wechselwirkungen der “Chiral Effective Field Theory” ( $\chi$ EFT) ein.

Wir stellen zunächst die HORSE-Methode und ihre Vereinfachung, die “Single-State HORSE”-Methode vor, die zu den sogenannten  $J$ -matrix-Methoden gehören.

Der  $J$ -matrix-Ansatz nutzt die Tridiagonalität der kinetischen Energie in einer speziellen Basisdarstellung aus, um eine Verbindung zwischen einer wechselwirkenden inneren Region und einer äußeren, freien Region herzustellen. Mit der Single-State HORSE-Methode berechnen wir Tetraneutron-Phasenverschiebungen. Wir verwenden dazu verschiedene in der “Similarity Renormalization Group” (SRG) evolvierte  $\chi$ EFT-Wechselwirkungen und zwei durch das inverse Streuproblem erzeugte Potentiale und untersuchen deren Auswirkungen auf die Phasenverschiebungen. Die Berechnungen werden in großen NCSM-Modellräumen durchgeführt. Die bestimmten Phasenverschiebungen zeigen charakteristische Merkmale einer Resonanz. Wir zeigen ferner einen Weg auf, wie man eine hypersphärische Basis im Rahmen des Jacobi-NCSM konstruiert. Dies ebnet den Weg für zukünftige Studien, die die volle Green’s-Funktion der HORSE-Methode einbeziehen.

Die zweite Methode zur Untersuchung von Resonanzen ist die ACCC, welche wir auf das Dineutron und Tetraneutron anwenden. Die Methode macht Resonanzen auf der komplexen  $k$ -Ebene durch Verwendung der analytischen Eigenschaften der Jost-Funktion als Funktion einer Kopplungskonstante zugänglich. Die Methode basiert ausschließlich auf Berechnungen gebundener Zustände, indem das System künstlich gebunden wird, um Energien bei verschiedenen Kopplungsstärken zu erhalten, die an Padé-Approximanten angepasst und dann zurück auf die ursprüngliche Bindungsstärke extrapoliert werden. Wir zeigen zwei unterschiedliche Ansätze zur Erzeugung der Bindung. Zunächst ein zusätzliches Vier-Körper-Potential, das auf Matrixelementebene aus den kleinsten Modellräumen konstruiert wird, welche wir Eigenvektorbindung nennen. Dies ist durch den Wunsch motiviert, gebundene Substrukturen zu vermeiden. Die zweite Methode ist eine einfache Multiplikation der Wechselwirkungsmatrixelemente mit einem Faktor. Die Dineutron-Ergebnisse zeigen, dass die Bindungsmethoden nicht fälschlicherweise Resonanzen erzeugen. Die Tetraneutron-Ergebnisse unterstützen eine Resonanz im Falle der Eigenvektorbindung, jedoch nicht für die direkte Matrixelementmodifikation.



# Contents

<b>1. Introduction</b>	<b>13</b>
<b>2. Chiral Effective Field Theory and Similarity Renormalization Group</b>	<b>17</b>
2.1. Chiral Effective Field Theory . . . . .	17
2.2. Similarity Renormalization Group . . . . .	18
2.3. Chiral Effective Field Theory Interactions Used in This Work . . . . .	19
<b>3. Scattering Theory – Two-Body Scattering</b>	<b>21</b>
3.1. Introduction . . . . .	21
3.2. Coordinate-Independent Scattering Theory . . . . .	21
3.3. Elastic and Single-Channel Scattering . . . . .	25
3.3.1. Coordinate Representation and Centre-of-Mass Coordinates . . . . .	26
3.3.2. Radial Schrödinger Equation and Partial Wave Expansion . . . . .	28
3.3.3. Coulomb Scattering . . . . .	31
3.4. Analyticity and Symmetries of the Solution of the Radial Schrödinger Equation	32
3.4.1. The Regular and Irregular Solutions . . . . .	32
3.4.2. The Jost Functions . . . . .	34
3.5. Resonances . . . . .	36
3.6. Spin, Inelastic and Multi-Channel Scattering . . . . .	39
3.6.1. Spin Degrees of Freedom . . . . .	39
3.6.2. Coupled-Channels . . . . .	41
3.6.3. Resonances in Multi-Channel Scattering . . . . .	41
<b>4. Scattering Theory – Many-Body Scattering</b>	<b>43</b>
4.1. Limits of Two-Body Scattering and the Three-Body Problem . . . . .	43
4.2. Many-Body Methods in the Continuum . . . . .	46
<b>5. No-Core Shell Model</b>	<b>47</b>
5.1. Single-Particle $m$ -Scheme NCSM . . . . .	48
5.2. Jacobi-NCSM . . . . .	49
<b>6. J-Matrix and Harmonic Oscillator Representation of Scattering Equations</b>	<b>53</b>
6.1. Harmonic Oscillator Representation of Scattering Equations . . . . .	55
6.1.1. Connection to the No-Core Shell Model . . . . .	60
6.2. Single-State Harmonic Oscillator Representation of Scattering Equations . . . . .	60
6.3. True Many-Particle Scattering in the Oscillator Representation . . . . .	61
6.4. Construction of Hyperspherical States from Jacobi-NCSM Eigenstates . . . . .	64
<b>7. Tetraneutron in the Single-State HORSE</b>	<b>67</b>
7.1. Identifying Resonances . . . . .	68
7.2. Data Generation . . . . .	69
7.3. Main Findings . . . . .	69
7.3.1. NCSM Model Space Dependence . . . . .	70
7.3.2. Similarity Renormalization Group Dependence . . . . .	73

7.3.3. Two- and Three-body Interaction Effects . . . . .	74
7.3.4. Chiral Order Dependence . . . . .	74
7.4. Conclusion . . . . .	78
<b>8. Analytic Continuation in the Coupling Constant</b>	<b>79</b>
8.1. Proof of Analyticity . . . . .	80
8.2. Using Padé Approximants . . . . .	84
8.2.1. Inverse ACCC . . . . .	86
8.3. Using the ACCC with the Jacobi-NCSM . . . . .	86
8.3.1. Modification of Matrix Elements . . . . .	87
8.3.2. Eigenvector Binding . . . . .	88
8.4. Obtaining the Fit and Parameters . . . . .	88
8.4.1. Parameters . . . . .	88
8.4.2. Fit Protocol and Data Collection . . . . .	90
8.5. Example Discussion With Phenomenological Gaussian Potential . . . . .	91
8.5.1. Inverse ACCC – $\lambda_0$ and Resonance . . . . .	93
8.5.2. ACCC . . . . .	95
8.5.3. Conclusion . . . . .	96
<b>9. Results Analytic Continuation in the Coupling Constant</b>	<b>99</b>
9.1. Dineutron . . . . .	100
9.2. Tetraneutron: Eigenvector Binding . . . . .	104
9.2.1. Input Data . . . . .	104
9.2.2. ACCC and IACCC Analysis, Algorithm-, Start Value- and Data Point Dependence . . . . .	108
9.2.3. Harmonic Oscillator Length Dependence . . . . .	119
9.2.4. $N_{\max}$ Behaviour . . . . .	122
9.2.5. Dependence on $N_{\max}^{\text{bin}}$ and $n_{\text{ev}}$ . . . . .	123
9.2.6. Main Findings and Comparison to Other Works . . . . .	126
9.3. Tetraneutron: Modification of $\chi$ EFT Matrix Elements . . . . .	128
9.3.1. $2N + 3N$ Modification . . . . .	129
9.3.2. $2N + 3N$ Excluding $^1S_0$ Partial Wave . . . . .	134
9.4. Tetraneutron Conclusion . . . . .	135
<b>10. Summary and Outlook</b>	<b>137</b>
<b>Appendix</b>	<b>141</b>
<b>A. Properties of Padé approximants</b>	<b>141</b>
<b>B. Special Functions</b>	<b>142</b>
<b>C. Phase Shift <math>N_{\max}</math> Sequences of Interactions Used in the Single-State HORSE Analysis</b>	<b>144</b>
<b>D. Alternative Derivation of Low-Energy Behaviour of <math>k(\lambda)</math></b>	<b>148</b>
<b>E. ACCC Fits to Fixed Data Sets</b>	<b>150</b>
<b>Bibliography</b>	<b>155</b>

<b>Danksagung</b>	<b>167</b>
<b>Akademischer Werdegang</b>	<b>168</b>



# List of Figures

1.1.	The double charge exchange reaction of ${}^4\text{He}({}^8\text{He}, {}^8\text{Be}){}^4\text{n}$ with an energy of 186 MeV/u, performed at the RIKEN facility by Kisamori et al. [KSM <sup>+</sup> 16], which led to numerous theoretical investigations into the matter. A radioactive ${}^8\text{He}$ isotope impinges on a liquid ${}^4\text{He}$ target, forming ${}^8\text{Be}$ and four neutrons, possibly resonant, as reaction products. . . . .	15
3.1.	Scattered wave function (blue) compared to the unperturbed wave (black). The scattering potential is overlaid in grey. The free solutions are Coulomb functions, as the potential is a phenomenological parametrization for a ${}^{12}\text{C} + p$ scattering process. The wave function is obtained within an $\mathcal{R}$ -matrix framework. . . . .	31
3.2.	The position of the zeros of the Jost function in the complex $k$ -plane. Bound and virtual states lie on the positive and negative imaginary axis, respectively. Resonances lie symmetric to the left and right of the imaginary axis. . . . .	35
3.3.	Sketch of an effective potential with angular momentum barrier, $V(r) + \frac{\ell(\ell+1)}{2r^2}$ . For $\ell = 0$ , the potential has to provide some form of barrier. . . . .	36
3.4.	Sketch of phase shifts. The dashed phase shift is a zero energy bound-state phase shift, according to Levinson's theorem. In blue is a resonant phase shift corresponding to a narrow resonance, a "quasi-bound state". . . . .	39
5.1.	Truncation scheme of the NCSM in the case of ${}^{10}\text{B}$ . The left plot shows one possible configuration of lowest energy. On the right, one possible configuration with excitation energy of $6\hbar\Omega$ . Neutrons and protons depicted as red and blue dots, respectively, unoccupied states depicted as open circles. . . . .	49
6.1.	Truncation scheme cartoon. The inner region consists of the truncated kinetic term plus the potential term. . . . .	54
7.1.	Tetraneutron Single-State HORSE phase shifts, comparison of various interactions. All data shown are $N_{\text{max}} = 26$ , as well as all blue lines SRG flow parameter $\alpha = 0.08 \text{ fm}^4$ . See table 7.1 as well as the text for details on the used interactions. The plot markers represent calculated data points, the lines connecting the markers are linear interpolations and only serve to guide the eye. . . . .	70
7.2.	Tetraneutron NCSM eigenenergies as function of the HO frequency $\hbar\Omega$ . Interaction $\text{N}^3\text{LO}_{\text{EM}} + \text{N}^2\text{LO}_{500,\text{L}}$ SRG evolved with $\alpha = 0.08 \text{ fm}^4$ . . . . .	71
7.3.	Tetraneutron Single-State HORSE phase shifts as function of the HO frequency $\hbar\Omega$ . Interaction $\text{N}^3\text{LO}_{\text{EM}} + \text{N}^2\text{LO}_{500,\text{L}}$ SRG evolved with $\alpha = 0.08 \text{ fm}^4$ . . . . .	72
7.4.	Tetraneutron phase shift as function of the energy. Interaction $\text{N}^3\text{LO}_{\text{EM}} + \text{N}^2\text{LO}_{500,\text{L}}$ SRG evolved with $\alpha = 0.08 \text{ fm}^4$ . . . . .	73
7.5.	Resonance position $E_R$ and width $\Gamma$ for the largest six $N_{\text{max}}$ , labelled accordingly. The position and width were determined via equations (7.2) and (7.3), respectively. The error bars give the difference to the previous value. . . . .	74
7.6.	Tetraneutron phase shift of the NN bare (non-SRG evolved) $\text{N}^3\text{LO}_{\text{EM}}$ interaction. The $N_{\text{max}}$ sequence is not converged, even with a large model space of $N_{\text{max}} = 30$ . . . . .	75

7.7.	Tetraneutron phase shift comparison of bare interaction with SRG evolved interactions at $N_{\max} = 26$ . Further comparison of two different SRG flow parameters $\alpha$ , as well as two values of $\chi$ EFT three-body cut-off parameter $\Lambda$ . Note that the bare interaction is far from convergence. . . . .	76
7.8.	Tetraneutron phase shift comparison of the effect of NN vs. NN+3N induced vs. initial 3N interaction. Shown interactions are $N^3\text{LO}_{\text{EM}}$ and $N^2\text{LO}_{500,\text{L}}$ . SRG parameter $\alpha = 0.08 \text{ fm}^4$ , $N_{\max} = 26$ . . . . .	77
7.9.	Tetraneutron phase shift dependence of the phase shift on the chiral order. The interaction is $N^x\text{LO}_{\text{EMN}}$ including SRG induced three-body forces. All at $N_{\max} = 26$ . . . . .	77
8.1.	Gaussian $\alpha + \alpha$ potential for $\ell = 4$ in units of the reduced mass $\mu = 2m_N$ . The unmodified potential is blue. The external potential in orange at a value $\lambda = 0.712$ , the prefactor modification in green with $\lambda = 0.445$ . These $\lambda$ are the approximate threshold values to achieve binding. . . . .	92
8.2.	Gaussian $\alpha + \alpha$ : Binding energies which are used to perform the Padé fits, 151 points each. In red, data obtained from binding with the external potential in equation (8.60) and (8.61). In blue the modification as in equation (8.62). The dashed lines are linear fits, the dotted lines quadratic fits to the energy. . . . .	93
8.3.	Gaussian $\alpha + \alpha$ scattering potential: Threshold value $\lambda_0$ , obtained by fitting to 38 points, up to tenth Padé order. Four different fitting algorithms with $\sigma_{\text{rel}}^{\text{fit}} = 6$ . The erratic behaviour of Levenberg-Marquardt method might indicate the overshooting of the optimal Padé order. . . . .	94
8.4.	Example of how the $S$ -matrix pole moves through the complex plane with specific values of the coupling constant. The black dots are the data obtained from a Jacobi-NCSM calculation and are fitted to. The grey dashed line indicates where $\text{Re}(k) = \text{Im}(k)$ . Order (5,5) of $V^{\text{ext}}$ with BFGS algorithm, shown in figure 8.5a. . . . .	96
8.5.	Gaussian $\alpha + \alpha$ scattering potential: ACCC for fixed $\lambda_0$ for the two different binding approaches, full data set of 150 points. $\lambda_0$ determined by linear interpolation. BFGS in solid lines, dashed lines Levenberg-Marquardt and $\sigma_{\text{rel}}^{\text{fit}} = 6$ . Parametrization as in equation (8.45b). Experimental reference is the grey box, the width uncertainty is set to arbitrary 5%. . . . .	97
8.6.	Gaussian $\alpha + \alpha$ scattering potential: Statistical ACCC for the two different binding approaches. 200 sets each. Parametrization as in equation (8.45b). The large dots with a line to the axis are the mean values of all points, the boxes give the standard deviation from the mean. Experimental reference is the grey box, the width uncertainty is set to arbitrary 5% for better visibility. Levenberg-Marquardt algorithm. . . . .	98
8.7.	Gaussian $\alpha + \alpha$ scattering potential: Statistical ACCC for the two different binding approaches. 1000 sets each. Parametrization as in equation (8.45b). The large dots with a line to the axis are the mean values of all points, the boxes give the standard deviation from the mean. Experimental reference is the grey box, the width uncertainty is set to arbitrary 5% for better visibility. BFGS algorithm. . . . .	98
9.1.	Dineutron bound state produced with two different harmonic oscillator lengths $a_{\text{HO}} = 2.5$ and $a_{\text{HO}} = 3.5 \text{ fm}$ . Note the difference in binding energies. Dashed lines are linear fits, dotted lines quadratic fits to the full data set of 402 points. . . . .	101
9.2.	Statistical ACCC for two binding methods. Performed with Levenberg-Marquardt with $\sigma_{\text{rel}}^{\text{fit}} = 8$ , $a_{\text{HO}} = 3.5 \text{ fm}$ , 500 subsets of 30 points, unitary weights. . . . .	102

9.3. Statistical ACCC for two binding methods. Performed with BFGS with $\sigma_{\text{rel}}^{\text{fit}} = 8$ , $a_{\text{HO}} = 3.5$ fm, 500 subsets of 30 points, unitary weights. . . . .	103
9.4. Statistical ACCC for two binding methods. Performed with Newton with $\sigma_{\text{rel}}^{\text{fit}} = 8$ , $a_{\text{HO}} = 3.5$ fm, 500 subsets of 30 points, unitary weights. . . . .	103
9.5. $N_{\text{max}}$ sequence for the interaction $\text{N}^3\text{LO}_{\text{EM}} + \text{N}^2\text{LO}_{500,\text{L}}$ at different oscillator lengths in the pure, unmodified pseudo continuum. . . . .	105
9.6. $N_{\text{max}}$ sequence for the interaction $\text{N}^3\text{LO}_{\text{EMN}} + \text{N}^3\text{LO}_{500,\text{NL}}$ for three different oscillator lengths in the pure, unmodified pseudo continuum. . . . .	106
9.7. First four energy levels with $J^\pi = 0^+$ as a function of the coupling constant. Interaction $\text{N}^3\text{LO}_{\text{EMN}} + \text{N}^3\text{LO}_{500,\text{NL}}$ Eigenvector binding with $N_{\text{max}}^{\text{bin}} = 2$ and $n_{\text{ev}} = 9$ . The data used for extrapolation is denoted with $E[0]$ . Note the different scales used on the plots. . . . .	106
9.8. $N_{\text{max}}$ sequence for $\text{N}^3\text{LO}_{\text{EM}} + \text{N}^2\text{LO}_{500,\text{L}}$ and $\text{N}^3\text{LO}_{\text{EMN}} + \text{N}^3\text{LO}_{500,\text{NL}}$ at $a_{\text{HO}} = 3.5$ . . . . .	107
9.9. The three data sets to compare the algorithm dependence from interaction $\text{N}^3\text{LO}_{\text{EMN}} + \text{N}^3\text{LO}_{500,\text{NL}}$ , $a_{\text{HO}}=2.5$ fm. Each set consists of 30 points. The threshold value is determined via linear interpolation $\lambda_0 \approx 6.702$ . . . . .	109
9.10. Tetraneutron $S$ -matrix pole trajectories. Data set B, $\lambda_0$ determination and fit performed with Quasi-Newton BFGS. $N_{\text{max}} = 28$ , $a_{\text{HO}} = 2.5$ fm. . . . .	113
9.11. Tetraneutron $S$ -matrix pole trajectories. Data set B, $\lambda_0$ determination and fit performed with Levenberg-Marquardt. $N_{\text{max}} = 28$ , $a_{\text{HO}} = 2.5$ fm. . . . .	114
9.12. SACCC, 100 sets of 30 points, Newton algorithm, $\text{N}^3\text{LO}_{\text{EMN}} + \text{N}^3\text{LO}_{500,\text{NL}}$ , $a_{\text{HO}} = 2.5$ fm. . . . .	115
9.13. Statistical ACCC, 100 sets of 30 points, Quasi-Newton BFGS with $\sigma_{\text{rel}}^{\text{fit}} = 8$ , $\text{N}^3\text{LO}_{\text{EMN}} + \text{N}^3\text{LO}_{500,\text{NL}}$ , $a_{\text{HO}} = 2.5$ fm. Comparison of different weightings. The grey box gives the experimental range [KSM <sup>+</sup> 16]. . . . .	116
9.14. Statistical ACCC, 100 sets of 30 points, Levenberg-Marquardt with $\sigma_{\text{rel}}^{\text{fit}} = 8$ , $\text{N}^3\text{LO}_{\text{EMN}} + \text{N}^3\text{LO}_{500,\text{NL}}$ , $a_{\text{HO}} = 2.5$ fm. Comparison of different weightings. The grey box gives the experimental range [KSM <sup>+</sup> 16]. . . . .	116
9.15. Tetraneutron binding energies close-up for different oscillator lengths near the threshold. Interaction $\text{N}^3\text{LO}_{\text{EM}} + \text{N}^2\text{LO}_{500,\text{L}}$ , $N_{\text{max}}^{\text{bin}} = 2$ , $n_{\text{ev}} = 1$ . . . . .	119
9.16. Tetraneutron binding energies close-up for three oscillator lengths near the threshold, combined with different $N_{\text{max}}^{\text{bin}}$ and $n_{\text{ev}}$ values, see also section 9.2.5. Interaction $\text{N}^3\text{LO}_{\text{EMN}} + \text{N}^3\text{LO}_{500,\text{NL}}$ . . . . .	120
9.17. Tetraneutron statistical ACCC extrapolation results for the data sets from figure 9.15, $\text{N}^3\text{LO}_{\text{EM}} + \text{N}^2\text{LO}_{500,\text{L}}$ interaction. 1000 subsets of 30 points, Levenberg-Marquardt with $\sigma_{\text{rel}}^{\text{fit}} = 8$ , mean and standard deviation not weighted. $N_{\text{max}} = 28$ , $N_{\text{max}}^{\text{bin}} = 2$ , $n_{\text{ev}} = 1$ . Parametrization as in equation (8.45b). Experimental candidate indicated by grey box. The labels denote the first two and the last corresponding $a_{\text{HO}}$ in fm. . . . .	121
9.18. The resonance and width as a function of $a_{\text{HO}}$ for the (4,4) Padé order, corresponding to results shown in figure 9.17. Interaction $\text{N}^3\text{LO}_{\text{EM}} + \text{N}^2\text{LO}_{500,\text{L}}$ , $N_{\text{max}}=28$ . The exponential fits are purely heuristic and are no prediction. One fit is performed with given errors as weights. . . . .	122
9.19. $N_{\text{max}}$ sequence of the mean values of statistical ACCC. 1000 subsets out of at least 221 total data points at $N_{\text{max}} = 10$ . $N_{\text{max}}^{\text{bin}} = 0$ , $n_{\text{ev}} = 2$ , for the interaction $\text{N}^3\text{LO}_{\text{EMN}} + \text{N}^3\text{LO}_{500,\text{NL}}$ at $a_{\text{HO}} = 3.5$ fm. The lowest three $N_{\text{max}}$ values are labelled for identification. The dashed lines connect points of the same order to guide the eye. Mean and standard deviation weighted with estimated fit error variance. The grey box gives the experimental range from [KSM <sup>+</sup> 16]. . . . .	123

9.20. The energy as a function of the binding parameter $\lambda$ for binding model spaces $N_{\max}^{\text{bin}} = 0, 2, 4, 6$ and $n_{\text{ev}}$ values of only one eigenvector and all eigenvectors contained in the corresponding $N_{\max}^{\text{bin}}$ . The grey line is a shift by a constant as it would be the case for $N_{\max}^{\text{bin}} = N_{\max}$ . The HO length is $a_{\text{HO}} = 3.5$ fm, interaction $\text{N}^3\text{LO}_{\text{EMN}} + \text{N}^3\text{LO}_{500,\text{NL}}$ , $N_{\max} = 28$ . . . . .	124
9.21. Statistical ACCC of the four-neutron system, for the $(N_{\max}^{\text{bin}}, n_{\text{ev}})$ pairs (0,1), (0,2), (2,1), (2,9), (4,1), (4,29), (6,1) and (6,79), indicated by the corresponding labels. Only the weighted mean values are shown. $N_{\max}=28$ , 1000 sets, 30 data points per set. Levenberg-Marquardt, $\sigma_{\text{rel}}^{\text{fit}}=8$ , with weighted mean and standard deviation. Excluding $c_0$ , equation (8.45b). Interaction $\text{N}^3\text{LO}_{\text{EM}} + \text{N}^2\text{LO}_{500,\text{L}}$ , $a_{\text{HO}} = 3.5$ fm. The grey lines connect each $(N_{\max}^{\text{bin}}, n_{\text{ev}})$ pair to guide the eye. . . . .	126
9.22. Tetraneutron SACCC extrapolation results for the data sets from figure 9.16. HO lengths of 2.5, 3.5, and 4.5 fm, $N_{\max} = 28$ , $N_{\max}^{\text{bin}} = 0$ , $n_{\text{ev}} = 2$ . Interaction $\text{N}^3\text{LO}_{\text{EMN}} + \text{N}^3\text{LO}_{500,\text{NL}}$ , 1000 subsets of 30 points, Levenberg-Marquardt algorithm with $\sigma_{\text{rel}}^{\text{fit}} = 8$ , points weighted equally for mean and standard deviation. Parametrization as in equation (8.45b). The experimental result [KSM <sup>+</sup> 16] is given as grey boxes, corresponding to uncertainty regions (stat.), (syst.) and (stat. + syst.). . . . .	128
9.23. Comparison of four different HO lengths $a_{\text{HO}}$ of the total binding energy as a function of the coupling constant. Interaction $\text{N}^3\text{LO}_{\text{EM}} + \text{N}^2\text{LO}_{500,\text{L}}$ . . . . .	130
9.24. Tetraneutron $N_{\max}$ sequence for three different points, corresponding to $x \approx 0.25, 1.5, 3$ at $N_{\max} = 28$ . On the left the absolute values, on the right the difference at each $N_{\max}$ to $N_{\max}=28$ . Interaction $\text{N}^3\text{LO}_{\text{EM}} + \text{N}^2\text{LO}_{500,\text{L}}$ , $\alpha = 0.08 \text{ fm}^4$ and $a_{\text{HO}} = 3.0$ fm. . . . .	131
9.25. Tetraneutron statistical ACCC for the matrix element manipulation. Parametrized as in equation (8.45a). $N_{\max} = 28$ , 1000 sets, 30 data points, Levenberg-Marquardt method with $\sigma_{\text{rel}}^{\text{fit}} = 8$ . In grey the experimental range from [KSM <sup>+</sup> 16].	132
9.26. Tetraneutron statistical ACCC for the matrix element modification. Parametrization as in equation (8.45b). 1000 subsets of 30 points. Newton method with $\sigma_{\text{rel}}^{\text{fit}} = 8$ . . . . .	133
9.27. Statistical ACCC of the four-neutron system, with increased matrix element strength, excluding the $^1S_0$ partial wave, which remains unmodified. $N_{\max}=28$ , 1000 sets, 30 data points per set. BFGS with weighted mean and standard deviation on the left, unweighted Levenberg-Marquardt on the right. . . . .	134
C.1. Tetraneutron phase shift as function of the energy. Interaction $\text{N}^3\text{LO}_{\text{EM}} + \text{N}^2\text{LO}_{400,\text{L}}$ SRG evolved with $\alpha = 0.08 \text{ fm}^4$ . . . . .	144
C.2. Tetraneutron phase shift. Interaction $\text{N}^2\text{LO}_{\text{EMN}}$ SRG evolved with $\alpha = 0.08 \text{ fm}^4$ . . . . .	145
C.3. Tetraneutron phase shift. Interaction $\text{N}^3\text{LO}_{\text{EMN}}$ SRG evolved with $\alpha = 0.08 \text{ fm}^4$ . . . . .	145
C.4. Tetraneutron phase shift. Interaction $\text{N}^4\text{LO}_{\text{EMN}}$ SRG evolved with $\alpha = 0.08 \text{ fm}^4$ . . . . .	146
C.5. Tetraneutron phase shift. Interaction $\text{N}^3\text{LO}_{\text{EM}} +$ induced 3N SRG evolved with $\alpha = 0.08 \text{ fm}^4$ . . . . .	146
C.6. Tetraneutron phase shift. Interaction $\text{N}^2\text{LO}_{\text{SAT}}$ SRG evolved with $\alpha = 0.08 \text{ fm}^4$ . . . . .	147
C.7. Tetraneutron phase shift. Interaction DAEJEON16. . . . .	147
E.1. Tetraneutron $S$ -matrix pole trajectories. Data set A, $\lambda_0$ determination and fit performed with Quasi-Newton BFGS. $N_{\max} = 28$ , $a_{\text{HO}} = 2.5$ fm. The grey dashed line is the angle bisector. . . . .	151
E.2. Tetraneutron $S$ -matrix pole trajectories. Data set A, $\lambda_0$ determination and fit performed with Levenberg-Marquardt. $N_{\max} = 28$ , $a_{\text{HO}} = 2.5$ fm. . . . .	152

E.3. Tetraneutron $S$ -matrix pole trajectories. Data set C, $\lambda_0$ determination and fit performed with Quasi-Newton BFGS. $N_{\max} = 28$ , $a_{\text{HO}} = 2.5$ fm. . . . .	153
E.4. Tetraneutron $S$ -matrix pole trajectories. Data set C, $\lambda_0$ from result with Quasi-Newton BFGS and fit performed with Levenberg-Marquardt. $N_{\max} = 28$ , $a_{\text{HO}} = 2.5$ fm. . . . .	154



# List of Tables

2.1. Interactions used in this work. Interaction constructed from inverse scattering potentials are denoted ISP. . . . .	20
7.1. Interactions used in this work. Interaction constructed from inverse scattering potentials are denoted ISP. . . . .	68
7.2. Resonances and widths as function of $N_{\max}$ , as shown in figure 7.5. Interaction $N^3\text{LO}_{\text{EM}} + N^2\text{LO}_{500,\text{L}}$ . Uncertainties give difference to previous smaller $N_{\max}$ . . . . .	72
7.3. $\chi^2/\text{datum}$ for $pp$ - plus $np$ -scattering for the 2016 NN data base of the interaction $N^x\text{LO}_{\text{EMN}}$ . Values taken from [EMN17]. . . . .	75
8.1. List of parameters considered in this work. . . . .	89
8.2. Resonance position by extrapolation from linear and quadratic fits to the energy as a function of the binding parameter. . . . .	93
8.3. Gaussian $\alpha + \alpha$ scattering potential: Resonance position and width for $V^{\text{ext}}$ obtained from solving for the roots of the numerator of the inverse ACCC. Selection of which root of the polynomial is the correct one has to be performed “by hand”. . . . .	95
9.1. Chiral interactions used in this study. . . . .	99
9.2. Threshold positions for the different binding methods. . . . .	101
9.3. Fits to the energy as function of $\lambda$ . Direct matrix element modification on top, eigenvector on the bottom. The two fits serve to better highlight the differences in behaviour with increasing $\lambda$ . The fits also serve as counter examples to the direct extrapolation without analytic continuation. . . . .	102
9.4. Threshold values $\lambda_0$ obtained via IACCC for three different sets consisting of 30 points, see text for details. Interaction $N^3\text{LO}_{\text{EMN}} + N^3\text{LO}_{500,\text{NL}}$ with $a_{\text{HO}}=2.5$ fm. Start values at all orders set to 0, except for $\lambda_0 = 6.70216$ . Note that the first IACCC Padé order starts at (2,2). NE = Newton, QN = Quasi-Newton (BFGS), LM = Levenberg-Marquardt, GR = gradient. . . . .	110
9.5. Threshold values $\lambda_0$ obtained via IACCC for three different sets consisting of 30 points, $a_{\text{HO}}= 2.5$ fm. Start values at all orders set to 1, except for $\lambda_0 = 6.70216$ . See also table 9.4. . . . .	112
9.6. Threshold values $\lambda_0$ obtained via IACCC for three different sets consisting of 30 points, $a_{\text{HO}}= 2.5$ fm. Start values are taken from the previous order. For details, see text as well as table 9.4. . . . .	112
9.7. Tetraneutron resonance energy position $E_R$ and width $\Gamma$ in MeV, rounded to two significant for values $> 1$ , three significant digits otherwise. Interaction $N^3\text{LO}_{\text{EMN}} + N^3\text{LO}_{500,\text{NL}}$ , at $a_{\text{HO}} = 2.5$ fm, $N_{\max}^{\text{bin}} = 0$ , $n_{\text{ev}} = 2$ . Levenberg-Marquardt results correspond to those depicted in figure 9.22. . . . .	117
9.8. See description of table 9.7. Levenberg-Marquardt results correspond to those depicted in figure 9.22. . . . .	117
9.9. See description of table 9.7. Levenberg-Marquardt results correspond to those depicted in figure 9.22. . . . .	118
9.10. See description of table 9.7. Levenberg-Marquardt results correspond to those depicted in figure 9.22. . . . .	118

*List of Tables*

9.11. Extrapolation result for a linear and quadratic fit to zero binding strength of the data set shown in figure 9.20. Units in MeV, around 100 points in each set. . .	125
9.12. Resonance parameters at each Padé order, from SACCC with standard deviation, corresponding to data shown in figure 9.22. Results are rounded to two decimals.	127
9.13. Comparison of resonance parameters from other references with our work. The presented values are approximated to be reasonably comparable. They are intended to reflect the main findings of the respective references, without claiming to be complete. See the original works for precise values. . . . .	127

# 1. Introduction

The picture of atomic nuclei, as we understand it today, was formed by the discovery of their existence by Rutherford in 1911 [Rut11] and his discovery of the proton in 1919 [Rut19]. The missing constituent in nuclei, the neutron, was confirmed to exist in 1932 by Chadwick [Cha32]. It was realized that a strong interaction of limited range must hold the nucleus together, in order to overcome the repulsion of the protons, due to the Coulomb force. The carrier of this force was proposed to be a meson, predicted by Yukawa in 1935 [Yuk35], and experimentally discovered in 1947 by Lattes, Muirhead, Occhialini, and Powell [LMOP47]. This meson is nowadays called the pion. This initiated the development of interaction models of increasing complexity to better understand nuclei. However, the growing evidence that nucleons are not elementary particles, but rather consist of quarks and gluons, marks the advent of quantum-chromodynamics (QCD), and ideally should be used for the description of nuclei. The efforts to apply QCD directly to atomic nuclei were, and are, met with substantial difficulties. The non-perturbative nature of QCD, due to the so-called confinement, prohibits a straightforward extension to the low-energy regime, which is relevant for the description of nuclei and corresponds to protons, neutron, and pions. For a true understanding of the nuclear interaction, a connection to QCD is required. One such connection was made by constructing an effective field theory, based on the work of Weinberg [Wei90], resulting in the development of Chiral Effective Field Theory ( $\chi$ EFT) interactions [EHM09].

Simultaneously to the progress on the nature of the interaction, different models to explain nuclear structure were developed, most notably the nuclear shell model by Göppert-Mayer [May49] and Haxel, Jensen, and Suess in 1949 [HJS49], which successfully explained the so-called magic numbers. The nuclear shell model has since been further improved and is still used today. The methods developed in the field of shell model approaches have been utilized to construct the No-Core Shell Model [ZBJ<sup>+</sup>93], which allows to solve the many-body Schrödinger equation exactly or with systematic improvability, and allows the use of realistic nuclear potentials.

The combination of this systematic improvability, together with the link to QCD, defines the realm of *ab initio* nuclear structure. Beside the NCSM, notable many-body methods are based on Monte Carlo calculations, like the Green's Function Monte Carlo method [Car88]. The reach in mass was extended via controlled approximations, resulting in methods like the Importance-Truncated NCSM [RN07], the Coupled Cluster technique [HPD<sup>+</sup>07], and the In-Medium Similarity Renormalization Group [TBS11].

We have reached the era of high-precision nuclear structure, having linked the inter-nucleon interaction to QCD, while the advances in solving the quantum many-body problem from first principles accelerated dramatically with the increase in available computational power. The reach of *ab initio* nuclear structure calculations has been extended up to  $^{100}\text{Sn}$  [MSS<sup>+</sup>18] and even  $^{132}\text{Sn}$  [BLCR14], while routinely being performed for *p*-shell and *sd*-shell nuclei. The point has been reached where the many-body method is no longer the dominant source of uncertainties, and systemic differences of the calculations to the experimental data can be traced back to the interaction, which can then be further improved, and fed back again into the many-body machinery. This feedback loop is, however, not yet possible for bound states close to the continuum threshold, or even above it. Basis expansion methods like the NCSM do not incorporate the correct single-particle asymptotics for these shallow bound or unbound cases, nor do they account for the coupling to the continuum. Even though the progress in predicting ground state

## 1. Introduction

properties has been tremendous, the inclusion of continuum degrees of freedom to treat shallow bound states, the calculation of reactions, resonances, and radio-active decay is a challenging endeavour. Maybe even more so, if the proven methods of *ab initio* nuclear structure are to be used. Significant progress has been made in enabling the continued use of some these methods while working close to or in the continuum. Directly based on the NCSM are approaches such as the NCSM with Resonating Group Method (NCSM/RGM) [QN08], NCSM with Continuum (NCSMC)[BNQ13b], and the No-Core Gamow Shell Model (NCGSM) [PRM<sup>+</sup>13]. Methods related to the expansion of scattering equations in a bound-state basis are the so-called *J*-matrix approaches. Formulated in a HO basis, they become the Harmonic Oscillator Representation of Scattering Equations (HORSE) [SMVM12], which can be combined in a straightforward manner with the NCSM. These already computationally expensive methods become even more so through the inclusion of the continuum, reducing the range of their applicability. The otherwise successful methods in extending the reach to medium and heavy-mass nuclei are only taking the first steps in the direction of treating the continuum. In the meantime, other alternatives are probed as an intermediate step towards unified approaches, which are computationally feasible and controllable in their approximations [JLA<sup>+</sup>19]. One such example is the extrapolation of *S*-matrix poles from bound-state calculations to the continuum through Analytic Continuation in the Coupling Constant (ACCC), put forward by Kukulín and Krasnopol'sky in 1977 [KK77], which is used in this work.

As a testing ground for our understanding of the nuclear interaction, neutron-rich system across the nuclear chart are of interest. Both the accurate theoretical description as well as the experimental accessibility of the neutron drip line pose a formidable challenge. The increase of number of particles not subject to the Coulomb force allows for a focused view on the nuclear interaction. Pushing it to the extreme, no system is more neutron rich than pure neutron systems. One system that is a contender to actually exist is the four-neutron system, the tetra-neutron.

First experiments to search for the tetra-neutron were performed by Schiffer and Vandenbosch in 1963 [SV63], but its existences as a bound system was ruled unlikely. In 2002, an experiment by Marqués et al. [MLO<sup>+</sup>02] reported on having measured a signal compatible with a bound tetra-neutron, but did not consider the possibility of a resonance. Reconsideration of a resonance signal for the same experiment lead to a possible resonance below 2 MeV [MOF<sup>+</sup>05]. The theoretical studies by Bertulani and Zelevinsky [BZ03] and Pieper [Pie03] following this event could not substantiate the existence of a bound state, and also a resonance was disfavoured by Lazauskas [LC05]. Solely the work of Meng [MLP14] supported a bound tetra-neutron.

A recent experiment performed at the RIKEN facility by Kisamori et al. [KSM<sup>+</sup>16] sparked renewed interest in a possible tetra-neutron resonance in the  $J^\pi = 0^+$  channel. The missing-mass analysis suggested a candidate resonant state with an energy position at  $0.83 \pm 0.65(\text{stat}) \pm 1.25(\text{syst})$  MeV and giving an upper limit for the width of 2.6 MeV, with a significance level of  $4.9\sigma$ . The experimental double charge exchange reaction of  ${}^4\text{He}({}^8\text{He} \text{ }^8\text{Be}){}^4\text{n}$  is sketched in figure 1.1. The numerous theoretical studies that followed disagree whether a resonance exists, let alone what its parameters are. While some come to the conclusion that it exists, with varying results regarding position and width [SPM<sup>+</sup>16, FRMP17, GHK<sup>+</sup>17, LMH<sup>+</sup>19], others find no evidence to support a resonance [HLCK16, LCH17, CLHK17, Del18, DL19b, HGKV20]. The origin of the disagreements is an interesting question, that will hopefully be answered in the near future.

Besides a better understanding of the nuclear force, the existence of a resonance would have implications for nucleosynthesis in supernova matter [PY19]. Further experiments have been performed and are still ongoing in their analysis.

This work aims to contribute to the ongoing discussion whether a tetra-neutron exists, and

if so, what its resonance parameters are. To that end, we combine the relative coordinate implementation of the NCSM, the Jacobi-NCSM, with the Single-State HORSE method and the ACCC and apply them to the tetra-neutron.

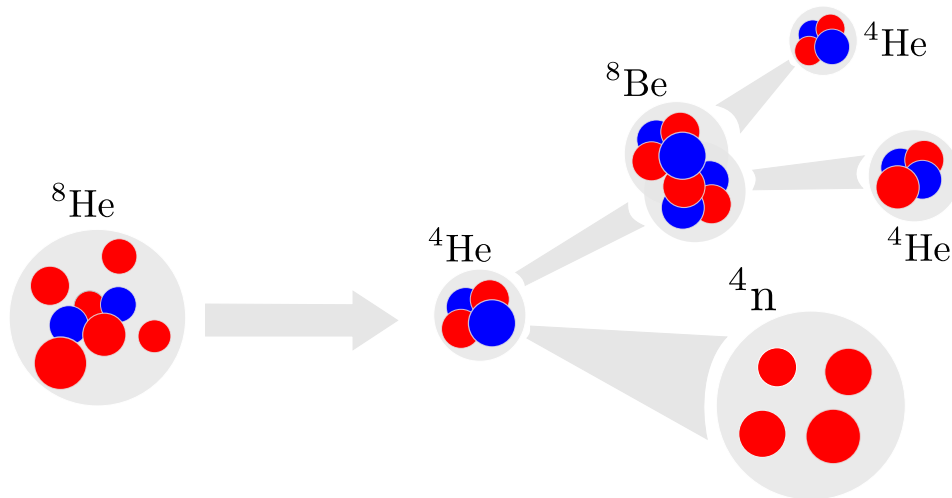


Figure 1.1.: The double charge exchange reaction of  ${}^4\text{He}({}^8\text{He}, {}^8\text{Be}){}^4\text{n}$  with an energy of 186 MeV/u, performed at the RIKEN facility by Kisamori et al. [KSM<sup>+</sup>16], which led to numerous theoretical investigations into the matter. A radioactive  ${}^8\text{He}$  isotope impinges on a liquid  ${}^4\text{He}$  target, forming  ${}^8\text{Be}$  and four neutrons, possibly resonant, as reaction products.

This thesis is structured as follows: We introduce the basic concept of  $\chi\text{EFT}$  and of the Similarity Renormalization Group, which is needed to improve numerical convergence, and the interactions used in this work in chapter 2. It follows a treatment of the concepts of scattering, in detail for the two-body case in chapter 3, which introduces all concepts needed to understand the presented results. Next, in chapter 4 few- and many-body scattering is discussed, however, only in so far as to understand the limitations of the two-body scattering formalism. We introduce the NCSM and the Jacobi-NCSM to solve the nuclear many-body problem in chapter 5. The first method employed to study continuum observables, the HORSE method, which belongs to the class of  $J$ -matrix methods, is discussed chapter 6. A variation of it, called Single-State HORSE, is introduced, and in the following chapter 7 applied to the tetra-neutron. There, we investigate different state-of-the-art  $\chi\text{EFT}$  interactions and their effect on phase shifts in the so-called democratic decay approximation. The last part is comprised of an introduction to the ACCC in chapter 8. It uses bound-state calculations by artificially binding the system to obtain energies at different coupling strengths, which are fitted to Padé approximants, allowing the analytic continuation to the complex plane and extracting resonance parameters. The method is applied to the dineutron, a non-resonant system, and to the tetra-neutron, in an exhaustive parameter study in chapter 9. Finally, we give a summary and outlook in chapter 10.



## 2. Chiral Effective Field Theory and Similarity Renormalization Group

The goal of *ab initio* theories is to base the description of a physical system on fundamental principles and use methods which are systematically improvable. Through this approach, the obtained results have quantifiable uncertainties. All necessary truncations due to, e.g., computational limitations, have a quantifiable impact. However, to actually be able to determine these uncertainties is a difficult task.

This is fundamentally different from a phenomenological approach. Here, fundamental connections to other areas of physics are traded off for high precision in reproducing experimental data and computational feasibility. In the field of nuclear structure, the phenomenological interactions of note are the Argonne  $v_{14}$  and  $v_{18}$  [WSS95] or the CD-Bonn [Mac01].

Within the context of *ab initio* nuclear structure, we want to connect the inter-nucleon interaction to the underlying theory of the strong interaction, which is quantum-chromodynamics (QCD). The direct calculation of nuclear properties from QCD is hindered by its non-perturbative nature. For a true understanding of the nuclear interaction, a connection to QCD is required. To obtain such a connection between the constituents of nuclei and their force carriers, nucleons and pions, respectively, with quarks and gluons, an alternative theory is required.

### 2.1. Chiral Effective Field Theory

One successful approach to connect QCD and the description of nuclei is the construction of an effective field theory based upon the general symmetries of QCD, introduced by Weinberg [Wei79, Wei90, Wei91]. The idea is that the most general Lagrangian, with the relevant degrees of freedom at the nuclear scale, nucleons and pions, is written down, respecting all relevant QCD symmetries. Of note is especially the chiral symmetry. At low energies, the QCD ground state is governed by confinement and the spontaneous breakdown of the aforementioned chiral symmetry, giving rise to the emergence of hadrons. As the latter is a continuous symmetry, the Goldstone theorem [GSW62] states that, in this case, massless bosons, the so-called Goldstone bosons, must exist. These are the pions, kaons, and eta-mesons in case of QCD. In addition to the spontaneous breakdown of the chiral symmetry, the current masses of the quarks generated by electroweak interactions lead to an explicit breaking of the chiral symmetry. The lightest three quarks are the up-quark, with  $m_u \approx 2.2$  MeV, the down-quark, with  $m_d \approx 4.7$  MeV, and the strange-quark, with  $m_s \approx 95$  MeV [THH<sup>+</sup>18]. Apparently, the masses of the up- and down-quarks are very small relative to the hadronic mass scale, which is of the order of 1 GeV. Still, the presence of these current masses and the associated breaking of the flavour symmetry is of great phenomenological relevance, as it renders the Goldstone bosons massive, with the pions being the lightest states in the QCD mass spectrum. Indeed, these states are significantly lighter than all the other mesonic and baryonic states, in particular, they are much lighter than the nucleons [THH<sup>+</sup>18].

The Chiral Effective Field Theory ( $\chi$ EFT) exploits the fact that there exists a separation of scales between the masses of the lightest mesons. The mass difference gives rise to a systematic expansion in a small parameter  $Q/\Lambda$ , such that the interaction terms obtained from the

## 2. Chiral Effective Field Theory and Similarity Renormalization Group

Lagrangian read [LTGL19]

$$V = \sum_{\nu} V^{\nu}(C_i^{\nu}) \left(\frac{Q}{\Lambda}\right)^{\nu}, \quad (2.1)$$

where  $V^{\nu}(C_i^{\nu})$  is the interaction term at given order  $\nu$ , the  $C_i^{\nu}$  are the so-called low energy constants (LEC), and  $Q$  is some low momentum compared to the break-down scale  $\Lambda \simeq 500 \text{ MeV} < m_{\rho}$ . The order  $\nu$  determines the power counting scheme and reads [Epe10]

$$\nu = 2(N + L - 2) + \sum_i \Delta_i, \quad (2.2)$$

where  $N$  is the number of nucleons, corresponding to lines in a diagrammatic approach,  $L$  are the number of loops in these diagrams, and  $\Delta_i = d_i + \frac{n_i}{2} - 2$ , with  $d_i$  being the number of derivatives and  $n_i$  the number of nucleon lines at vertex  $i$ . This expansion allows the systematic improvability of the derived nuclear interaction, letting higher-body forces appear at higher orders [Epe10]

$$\begin{aligned} V_{2N} &= V_{2N}^{(0)} + V_{2N}^{(2)} + V_{2N}^{(3)} + V_{2N}^{(4)} + \dots \\ V_{3N} &= V_{3N}^{(3)} + V_{3N}^{(4)} + \dots \\ V_{4N} &= V_{4N}^{(4)} + \dots \\ &\vdots \end{aligned} \quad (2.3)$$

It can be seen in the two-body forces,  $V_{2N}$ , that after the leading order (LO), directly the next-to-next-to-leading order ( $N^2$ LO) follows. The next-to-leading order is not parity conserving, hence it does not appear. Within this work, we denote the chiral orders with the notation  $N^{\nu}$ LO.

The LECs are undetermined and need to be fitted to experimental data. Strictly speaking, this is not in the essence of *ab initio* as introduced in the beginning. However, nuclear interactions based on  $\chi$ EFT represent the closest method to this ideal currently available, apart from direct nuclear QCD calculations. They are not arbitrary in their construction, meaning that even though there still is need for experimental input, the parameters that need to be fitted are not the result of a model, but instead are directly connected to physical observables. The  $\chi$ EFT expansion is systematically improvable by going to higher orders. The propagation of uncertainties from  $\chi$ EFT to nuclear observables is a current and ongoing research topic.

### 2.2. Similarity Renormalization Group

Nuclear interactions incorporate strong short-range correlations, caused by inter-nucleonic repulsion at short distances, resulting in significant coupling of different momenta. This effect is present in both phenomenological and chiral interactions and makes numerical calculations difficult to converge. Various methods have been developed to remedy this problem, e.g., the Ôkubo-Lee-Suzuki transformation [Ôku54, LS80], the Unitary Correlation Operator Method [FNRS98], the  $V_{\text{low}k}$  [BKS03], or the Similarity Renormalization Group (SRG) [GW93, Weg94, BFP07]. We use the SRG to soften the interaction, which is achieved via a pre-diagonalization, decoupling low and high momenta.

The SRG uses a unitary transformation of the Hamiltonian, depending on the continuous variable  $\alpha$

$$H(\alpha) = U^{\dagger}(\alpha)H(0)U(\alpha), \quad (2.4)$$

where  $U(\alpha)$  is a unitary operator,  $U^\dagger(\alpha)U(\alpha) = U(\alpha)U^\dagger(\alpha) = \mathbf{1}$ , thus leaving the eigenvalues of the initial Hamiltonian  $H(0)$  unchanged. Taking the derivative of the Hamiltonian with respect to the flow parameter  $\alpha$ , gives the SRG flow equation

$$\begin{aligned} \frac{dH(\alpha)}{d\alpha} &= \frac{dU^\dagger(\alpha)}{d(\alpha)}H(0)U(\alpha) + U^\dagger(\alpha)H(0)\frac{dU(\alpha)}{d(\alpha)} \\ &= [\eta(\alpha), H(\alpha)]. \end{aligned} \quad (2.5)$$

Here, the anti-hermitian generator is introduced

$$\eta(\alpha) = \frac{dU^\dagger(\alpha)}{d(\alpha)}U(\alpha) = -U^\dagger\frac{dU(\alpha)}{d(\alpha)}, \quad (2.6)$$

which can be chosen freely, as long as the anti-hermiticity is respected. The established choices for the generator, when written in a commutator relation

$$\eta(\alpha) = [X, H(\alpha)], \quad (2.7)$$

are the diagonal matrix elements of  $H(\alpha)$ ,  $X = H_d(\alpha)$  by Wegner [Weg94], or block-diagonal matrix elements by White [Whi02]. Alternatively, choosing the intrinsic kinetic energy  $X = m_N^2 T_{\text{int}}$  is also possible [BFP07].

Performing the SRG induces contributions of higher, irreducible, particle rank in an operator of fixed rank [RNF10]

$$H(\alpha) = H^{[1]}(\alpha) + H^{[2]}(\alpha) + H^{[3]}(\alpha) + \dots, \quad (2.8)$$

which is the price to pay to obtain a softer potential, as the computation of higher-body operators is increasingly difficult. In practice, the higher-order contributions are cut off, usually taking up to three-body operators into account.

## 2.3. Chiral Effective Field Theory Interactions Used in This Work

Within this work, we use various  $\chi$ EFT interactions, which we introduce in this section. For a better overview, they are listed in table 2.1. They are applied in the studies found in chapters 7 and 9.

Important work in the field of  $\chi$ EFT has been accomplished by Entem and Machleidt [EM03], whose chiral NN interaction defines the standard within the field. We refer to it by  $N^3\text{LO}_{\text{EM}}$ . The NN interaction by Ekström et al. [EJW<sup>+</sup>15] is additionally to the NN-scattering data and few-nucleon binding energies and radii, also adapted to carbon and oxygen isotopes. It is build to be consistent with the empirical saturation point of symmetric nuclear matter. We refer to it as  $N^2\text{LO}_{\text{SAT}}$ .

The most recent two-nucleon interaction in use by was developed by Entem, Machleidt, and Nosyk. This interaction is constructed up to  $N^4\text{LO}$ , with consistent power counting and cut-off treatment at all orders. The globally available NN-scattering data is reproduced to a high precision with a  $\chi^2/\text{datum}$  of 1.15. We denote the interaction by  $N^\nu\text{LO}_{\text{EMN}}$ .

The first three-nucleon force use in this work is by Navrátil [Nav07]. It is a local interaction, available at  $N^2\text{LO}$  with different cut-off parameters  $\Lambda$ . We use it in combination with the NN-interaction by Entem and Machleidt  $N^3\text{LO}_{\text{EM}}$ . However, the chiral orders are not consistent. It is referred to by us as  $N^2\text{LO}_{\Lambda, L}$ .

The second three-nucleon force we employ is that by Hüther, Vobig, Hebeler et al. [HVH<sup>+</sup>19]. It based on the NN-interaction  $N^\nu\text{LO}_{\text{EMN}}$ , and treats all two- and three-body contributions

## 2. Chiral Effective Field Theory and Similarity Renormalization Group

consistently up to  $N^3\text{LO}$ . It uses a non-local regulator. It represents one of the most recent developments in the field of  $\chi\text{EFT}$ . We refer to it as  $N^3\text{LO}_{500,\text{NL}}$ .

We use two additional phenomenological interaction, which do not belong to the chiral family. The so-called JISP16 interaction by Shirokov, Vary, Mazur, and Weber [SVMW07], is constructed from No-Core Shell Model (NCSM) calculations, from which an inverse scattering potential (ISP) is obtained. The inverse scattering is based on the  $J$ -matrix method, discussed in chapter 6.

Similarly, the DAEJEON16 interaction by Shirokov, Shin, Kim et al. [SSK<sup>+</sup>16] builds upon the same ISP approach. As initial interaction in the NCSM calculation serves the so-called Idaho  $N^3\text{LO}$  interaction by Entem and Machleidt [EM02], which has further been SRG evolved.

Name	Type	Year	Reference	SRG $\alpha$ [fm <sup>4</sup> ]
$N^3\text{LO}_{\text{EM}}$	$\chi\text{EFT}$ NN	2003	[EM03]	bare, 0.04, 0.08
$N^2\text{LO}_{\text{SAT}}$	$\chi\text{EFT}$ NN	2015	[EJW <sup>+</sup> 15]	0.04, 0.08
$N^x\text{LO}_{\text{EMN}}$	$\chi\text{EFT}$ NN	2017	[EMN17]	0.04, 0.08
$N^3\text{LO}_{\text{EM}} + N^2\text{LO}_{\Lambda,\text{L}}$	$\chi\text{EFT}$ NN + 3N	2007	[Nav07]	0.04, 0.08, 0.12
$N^3\text{LO}_{\text{EMN}} + N^3\text{LO}_{500,\text{NL}}$	$\chi\text{EFT}$ NN + 3N	2019	[EMN17, HVH <sup>+</sup> 19]	0.08
JISP16	ISP NN	2007	[SVMW07]	-
DAEJEON16	ISP NN	2016	[SSK <sup>+</sup> 16]	-

Table 2.1.: Interactions used in this work. Interaction constructed from inverse scattering potentials are denoted ISP.

# 3. Scattering Theory – Two-Body Scattering

## 3.1. Introduction

The theory of scattering encompasses a vast range of applications and specialized tools and methods to deal with a multitude of phenomena, with different notation, developed in different areas of physics over the years. Many relevant mathematical findings on differential equations and functional analysis stem from the late 19th and early 20th century. Owing to the nature of the scattering problem, combined with the pioneering work of mathematicians and their very own notation and nomenclature, the treatment of scattering is sometimes cumbersome and difficult to read. The efforts in the second half of the 20th century to arrive at a common language resulted in a number of text books, e.g., references [New82, Joa76, SN17], which, together with references [Fri13, Moo08], build the basis for this chapter.

The term “scattering” implies quite a few different topics. Classical collisions, the treatment of electro-magnetic waves, just as well as reaction theory in atomic, nuclear or high-energy physics. The large number of different topics and details inherent in a general treatment of scattering physics will naturally not be part of this chapter. The intent is to provide the framework necessary to understanding the results presented in this work. In the context of this work, the field of *ab initio* nuclear structure, the term scattering physics is often understood more in the sense of being juxtaposed to bound-state physics, with its finite number of square-integrable energy states. For the latter, powerful methods have been developed, but which are not well or not at all suited to deal with continuum states, in their original formulation. Current efforts [QN08, BNQ13a, SMVM12, SMMV16, PRM<sup>+</sup>13], see also [JLA<sup>+</sup>19] and references therein, attempt to bring the bound-state tools of *ab initio* nuclear structure into a shape, where the continuum effects that naturally are also a part of nuclear structure physics, can be handled as well.

We introduce the basics of quantum scattering theory in this chapter. Concentrating first on the two-body problem, we discuss the coordinate-independent formulation, in which most of the relevant quantities can be derived or motivated. Employing a concrete basis representation, we highlight the analytical properties of the wave-function solutions.

## 3.2. Coordinate-Independent Scattering Theory

In quantum mechanics, we search for solutions to the Schrödinger equation under different boundary conditions. It is further distinguished between the case of a time-dependent or a time-independent problem. Coming from the picture of two particles approaching each other, interacting with each other, and then drifting apart, the time dependent description is a natural choice. In this case, one would aim at solving the time-dependent Schrödinger equation (with  $\hbar = 1$ )

$$\begin{aligned} i \frac{d}{dt} |\psi, t\rangle &= H |\psi, t\rangle \\ i \frac{d}{dt} |\psi, t\rangle &= (H_0 + V) |\psi, t\rangle, \end{aligned} \tag{3.1}$$

### 3. Scattering Theory – Two-Body Scattering

where the state  $|\psi, t\rangle$  of a system at the time  $t$ , described by the Hamiltonian  $H$ , is the sought solution. The Hamiltonian is comprised of some unperturbed Hamiltonian  $H_0$ , which can be understood as the kinetic energy, or alternatively, as a Hamiltonian with known solution, with a perturbation potential  $V$ . In the following, we treat  $H_0$  as the kinetic energy. As solution, one obtains then the state  $|\psi, t\rangle$  and with it the energy  $E$  or observable of interest at a certain point in time.

In the following, the state

$$|\psi, t, \nu\rangle \rightarrow |\psi, t\rangle, \quad (3.2)$$

should be understood to carry all relevant quantum numbers of the system in the collective index  $\nu$ , which we have dropped for brevity.

The time-dependent description has some advantageous features regarding the formal treatment of scattering theory. For actual calculations or incorporating scattering theory with the proven methods of bound-state many-body physics, it is convenient to deal with the time-independent problem:

$$\begin{aligned} H|\psi\rangle &= E|\psi\rangle \\ (H_0 + V)|\psi\rangle &= E|\psi\rangle. \end{aligned} \quad (3.3)$$

#### Time-dependent Scattering

The formalism of scattering is best introduced in an explicitly time-dependent framework. In the later parts of this work, we will only work with the time-independent (stationary) formulation. It is nonetheless helpful to start with a few general aspects, which originated from the time-dependent problem. This is, for example, incoming and outgoing waves, a concept that only makes sense in a stationary context when keeping the time-dependence in mind, as one goes from time to energy as a variable via Fourier transform. This also explains the sign convention for incoming waves having the form  $e^{-ikr}$ , whereas outgoing waves are written as  $e^{ikr}$ , because their time dependence was per historic convention written with a negative exponent as  $e^{-i\omega t}$ . Another example for terms, which appear in the stationary formulation, but which were introduced in the time-dependent context, is the use of the complex valued  $i\epsilon$  in equation (3.12) and equation (3.13). In the time-dependent formulation, it ensures convergence of the integral, but in the stationary formulation, it ensures causality.

We treat the formal solution of the time-dependent Schrödinger equation (3.1) on operator level with the help of the Green's functions  $G^\pm(t)$  the differential equations

$$\begin{aligned} \left(i\frac{d}{dt} - H_0\right) G_0^\pm(t) &= \delta(t) \\ \left(i\frac{d}{dt} - H\right) G^\pm(t) &= \delta(t), \end{aligned} \quad (3.4)$$

where  $\delta(t)$  is the  $\delta$ -distribution. The Green's functions fulfil the initial conditions

$$\begin{aligned} G_0^+(t) = G^+(t) &= 0 \quad \text{for } t < 0 \\ G_0^-(t) = G^-(t) &= 0 \quad \text{for } t > 0. \end{aligned} \quad (3.5)$$

The subscript in  $H_0$  and  $G_0$  corresponds to the “free” Schrödinger equation. The two solutions of equations (3.4) and (3.5) can be written as

$$\begin{aligned} G^+(t) &= \begin{cases} -i e^{-iHt} & \text{for } t > 0 \\ 0 & \text{else} \end{cases} \\ G^-(t) &= \begin{cases} i e^{-iHt} & \text{for } t < 0 \\ 0 & \text{else,} \end{cases} \end{aligned} \quad (3.6)$$

and analogously for  $G_0^\pm$ . The plus and minus sign indicate to what part of the scattering event the respective Green's functions belong: The minus sign to the evolution before and the plus to the evolution after the event. This precludes the effect  $G^\pm$  has when applied to a state  $|\psi\rangle$ . Looking at  $G_0^+$ , we obtain

$$|\psi_0, t'\rangle = i G_0^+(t' - t) |\psi_0, t\rangle, \quad (3.7)$$

satisfying equation (3.4) for  $t' > t$ , which can be verified by inserting the analogue of equation (3.6) for  $G_0^+$  into equation (3.7). This means that the free state  $|\psi_0, t\rangle$  is propagated to a later time  $t'$ . Accordingly,  $G_0^\pm$  and  $G^\pm$  are also called propagators. This allows us now to define the incoming and outgoing states

$$|\psi_{\text{in}}, t'\rangle = \lim_{t \rightarrow -\infty} i G_0^+(t' - t) |\psi, t\rangle \quad (3.8)$$

and

$$|\psi_{\text{out}}, t'\rangle = \lim_{t \rightarrow \infty} i G_0^-(t' - t) |\psi, t\rangle. \quad (3.9)$$

The definitions can be understood follows: In the distant past, the known state is  $|\psi, t\rangle$ , whose time propagation is determined by the Green's function of the non-interacting system. This is the incoming state, with the analogue for the outgoing wave when ending with a known state  $|\psi, t\rangle$  in the distant future. A useful representation of the states is the integral form, which we obtain with the help of the Green's function. To that end, we apply the time derivative to  $G^+$ , which yields

$$\begin{aligned} i\partial_t G^+(t' - t) |\psi, t\rangle &= -i (\partial_t G^+(t' - t)) |\psi, t\rangle + G^+(t' - t) \partial_t |\psi, t\rangle \\ &= \delta(t' - t) |\psi, t\rangle + G^+(t' - t) V |\psi, t\rangle. \end{aligned} \quad (3.10)$$

Renaming  $t' \rightarrow t$  and vice versa, integrating over  $t'$  gives

$$|\psi, t\rangle = |\psi_{\text{in}}, t\rangle + \int_{-\infty}^{\infty} dt' G_0^+(t - t') V |\psi, t'\rangle. \quad (3.11)$$

The switch from formulating the scattering problem as a differential to an integral equation is a common technique. As integral equation, the boundary conditions imposed on the differential are incorporated by the Green's function and the integration limits, and solving techniques for integrals can be used. The integrals occurring in the scattering formalism further belong to the class of Fredholm and Volterra type integrals [AW13, LP12], which has important implications for three-body scattering, discussed in chapter 4, and is also used in the proof of analytic relations important for the method employed in chapter 8.

### Time-independent Scattering

The time-independent scattering formulation is obtained by taking the Fourier transform of the time-dependent Green's functions. As a consequence from going to the time-independent Schrödinger equation, we switch over from solving for the state of the system at a given time to obtaining the state of the system at a specific energy, or in the case of bound-state physics, what energies are allowed by the system. The integrals of the Fourier transform are only defined in time intervals of  $[0, \pm\infty]$ , the integrals are ill-defined, and a convergence factor  $e^{\mp\epsilon t}$  is inserted

$$\begin{aligned} G_0^\pm(E) &= \int_{-\infty}^{\infty} dt e^{iEt \mp \epsilon t} G_0^\pm(t) \\ G^\pm(E) &= \int_{-\infty}^{\infty} dt e^{iEt \mp \epsilon t} G^\pm(t). \end{aligned} \quad (3.12)$$

### 3. Scattering Theory – Two-Body Scattering

The factor  $\epsilon$  is a small, positive number, which can be treated to approach the limit  $\epsilon \rightarrow 0$ . Using the representation of equation (3.6) and inserting this into equation (3.12), one obtains

$$\begin{aligned} G_0^\pm(E) &= (E - H_0 \pm i\epsilon)^{-1}, \\ G^\pm(E) &= (E - H \pm i\epsilon)^{-1}. \end{aligned} \quad (3.13)$$

This can be understood as rotating the time-independent Green's functions into the complex plane. When taking the limit of  $\epsilon \rightarrow 0$ , writing the Green's function in the form

$$G(E) = (E - H)^{-1} \quad (3.14)$$

means that one approaches the real energy axis either from above or from below for  $G^+$  and  $G^-$ , respectively. This addition of  $i\epsilon$  ensures causality in the time-independent context. Any occurrence of  $G(E)$  as in equation (3.14) can be read with having an implicit  $i\epsilon$ . We obtain the time-independent states just as with the Green's function, by Fourier analysis of the time-dependent states from equation (3.11)

$$\int_{-\infty}^{\infty} dt e^{iEt} |\psi, t\rangle = \int_{-\infty}^{\infty} dt e^{iEt} |\psi_{\text{in}}, t\rangle + \int_{-\infty}^{\infty} \int_{-\infty}^{\infty} dt dt' e^{iEt} G_0^+(t - t') V |\psi, t'\rangle. \quad (3.15)$$

For the time-independent states, we use the shorter notation  $|\psi\rangle \equiv |\psi, E\rangle$ , equation (3.15) becomes

$$|\psi\rangle = |\psi_{\text{in}}\rangle + G_0^+ V |\psi\rangle. \quad (3.16)$$

Equation (3.16) is the so-called Lippmann-Schwinger equation [LS50]. The similar expression for the Green's function,

$$G = G_0 + G_0 V G, \quad (3.17)$$

is also referred to as Lippmann-Schwinger equation. We can replace the label  $|\psi_{\text{in}}\rangle$  with  $|\psi_0\rangle$  to specify the incoming wave to be that of the free problem, meaning that  $|\psi_0\rangle$  fulfils the relation

$$(H_0 - E) |\psi_0\rangle = 0. \quad (3.18)$$

With the choice of  $|\psi_{\text{in}}\rangle \rightarrow |\psi_0\rangle$  we make the choice to restrict ourselves to  $G_0^+$ . One could also use  $|\psi_{\text{out}}\rangle \rightarrow |\psi_0\rangle$  together with  $G_0^-$ . In most cases, it is easier to assume a known incoming state than the other way around, hence the choice for  $G_0^+$ . These results give the common interpretation of having the full state as a superposition of an incoming free state and an outgoing scattered state, corresponding to the experimental reality of an incident beam with known properties, which scatters on a target and is measured in a detector far away relative to the target size. We write

$$|\psi\rangle = |\psi_0\rangle + |\psi_s\rangle, \quad (3.19)$$

with the scattered state  $|\psi_s\rangle$ . Furthermore, the Lippmann-Schwinger equation (3.16) is the integral equation of the Schrödinger equation, albeit here in abstract notation. The rewriting as an integral opens up the pathway to different solving methods, e.g. by iteration due to its nature of being of the Volterra type [LP12, AW13], which can be written as

$$|\psi\rangle = (1 + G_0 V + G_0 V G_0 V + \dots) |\psi_0\rangle, \quad (3.20)$$

or alternatively for the scattering state

$$\begin{aligned} |\psi_s\rangle &= G_0 (V + V G_0 V + V G_0 V G_0 V + \dots) |\psi_0\rangle \\ &=: G_0 \mathcal{T} |\psi_0\rangle. \end{aligned} \quad (3.21)$$

We introduce the operator  $\mathcal{T}$  as an abbreviation for the iterative terms. In a basis representation, it is referred to as  $\mathcal{T}$ -matrix, and when expressed in momentum space, it is related to the scattering amplitude, see equation (3.35).

Under the assumption that the free states form a complete set, we can directly expand the free Green's function in terms of the free states

$$G_0(E) = \int_0^\infty dE' \frac{\sum_\nu |\psi_0, E', \nu\rangle \langle \psi_0, E', \nu|}{E - E'}. \quad (3.22)$$

Here, we have reintroduced the previously dropped collective index for all relevant quantum numbers. The same can be done for the full Green's functions if we assume a completeness relation of the form

$$\mathbb{1} = \sum_n |\psi_n\rangle \langle \psi_n| + \int dE' \sum_\nu |\psi, E', \nu\rangle \langle \psi, E', \nu|, \quad (3.23)$$

where  $|\psi_n\rangle$  are the bound states, if present. We obtain

$$G^\pm(E) = \sum_n \frac{|\psi_n\rangle \langle \psi_n|}{E - E_n} + \int_0^\infty dE' \frac{\sum_\nu |\psi^\pm, E', \nu\rangle \langle \psi^\pm, E', \nu|}{E - E'}. \quad (3.24)$$

These are the spectral decompositions of the Green's functions, whose construction is the goal of many solving methods.

From the interpretation of the scattering event as incoming particle with state  $|\psi_{in}\rangle = |\psi_0\rangle$ , we can introduce the scattering operator which relates the incoming and outgoing state directly

$$|\psi_{out}\rangle = S |\psi_{in}\rangle. \quad (3.25)$$

This is the scattering operator  $S$ ; it is time independent and when the in and out states form complete sets, it is unitary

$$S^\dagger S = S S^\dagger = 1. \quad (3.26)$$

### 3.3. Elastic and Single-Channel Scattering

We go over from the scattering formalism in abstract notation to the representation in three-dimensional coordinates. The choices are either a momentum or a position representation. To this end, we will have to consider two aspects. Firstly, which kind of spatial coordinates to choose in order to exploit the existing or assumed symmetries of the problem. Secondly, and far more consequential for many-body scattering, is to be aware of the limitation of the following formalism to one- and two-body scattering only.

Regarding the first point we assume spherical symmetry of the potential. The natural coordinates to choose are spherical coordinates  $(r, \theta, \phi)$  and, due to symmetry, we can eliminate the two angular variables, being left only with the radial coordinate. Another simplifying benefit is the conservation of angular momentum; the angular momentum operator commutes with the Hamiltonian  $[L, H] = 0$ , and we thus have a complete set of basis functions which we use in the partial wave expansion, see section 3.3.2.

The second point is more fundamental. Any system with two or more interacting constituents can exhibit bound states, which should not change depending on where the system is placed in space. The system has to be translationally invariant and simultaneously ensure that a scattering state in a specific configuration is truly unique with respect to the existing bound states. In the two-body case and any many-body system, which can be treated effectively as a two-body problem, this issue can be solved by going to the centre-of-mass system (CoM)

### 3. Scattering Theory – Two-Body Scattering

and using the relative distance as variable. This allows us to split the Hamiltonian into a CoM and a relative part, which enables us to solely look at the relative part and ignore the CoM contribution. This continues to work well even for systems with internal degrees of freedom, which can be excited to higher energy states, as long as there are effectively only two active scattering partners. This is *inelastic* two-body scattering. For three or more particles which form more than two subsystems, the theory described in the following sections is not unambiguously applicable. This is discussed in chapter 4.

We will restrict ourselves in this section to spinless particles. The general aspect of particles with spin will be discussed in section 3.6, together with general internal degrees of freedom and inelastic scattering.

#### 3.3.1. Coordinate Representation and Centre-of-Mass Coordinates

To combine the abstract treatment of the scattering problem in section 3.2 with the basis representation from the previous section, we bring the time-independent Lippmann-Schwinger equation (3.16) into the position basis  $|\vec{r}\rangle$ . Under the assumption of a local interaction potential, i.e.  $\langle \vec{r}' | V | \vec{r}'' \rangle = V(\vec{r}'')\delta(\vec{r}' - \vec{r}'')$ , we get

$$\begin{aligned} \langle \vec{r} | \psi \rangle &= \int d^3 r' \langle \vec{r} | \vec{r}' \rangle \langle \vec{r}' | \psi_{\text{in}} \rangle + \int \int d^3 r' d^3 r'' \langle \vec{r} | G_0^+ | \vec{r}' \rangle \langle \vec{r}' | V | \vec{r}'' \rangle \langle \vec{r}'' | \psi \rangle \\ \psi_{\vec{k}}(\vec{r}) &= \psi_{\text{in},\vec{k}}(\vec{r}) + \int d^3 r' G_0^+(\vec{r}, \vec{r}') V(\vec{r}') \psi_{\vec{k}}(\vec{r}'). \end{aligned} \quad (3.27)$$

Here,  $\vec{k}$  is the momentum wave vector, with  $k^2 = \frac{2\mu E}{\hbar^2}$ , with  $\mu$  being the reduced mass. The wave functions  $\psi_{\vec{k}}(\vec{r})$  are given at a fixed energy, traveling in the direction  $\vec{k}$ , as in equation (3.31). In this specific representation it is apparent why the Lippmann-Schwinger equation is already referred to as an integral equation in section 3.2. Using equation (3.22) together with equation (3.27) as starting points, writing  $\hbar$  again, as well as changing from energy to a short hand wave vector notation

$$|\psi_0, E', \nu\rangle \rightarrow |\vec{k}\rangle, \quad (3.28)$$

the Green's function in coordinate representation can be written as

$$\begin{aligned} G_0^\pm(\vec{r}, \vec{r}') &= \frac{2\mu}{\hbar^2} \int_0^\infty d^3 k' \frac{\langle \vec{r} | \vec{k}' \rangle \langle \vec{k}' | \vec{r}' \rangle}{k^2 - k'^2 \pm i\epsilon} \\ &= \frac{2\mu}{(2\pi)^3 \hbar^2} \int_0^\infty d^3 k' \frac{e^{i\vec{k}'(\vec{r}-\vec{r}')}}{(k+k' \pm i\epsilon)(k-k' \mp i\epsilon)} \\ &= \frac{2\mu}{(2\pi)^2 \hbar^2} \int_{-\infty}^\infty dk' k'^2 \frac{e^{i\vec{k}'|\vec{r}-\vec{r}'|}}{(k+k' \pm i\epsilon)(k-k' \mp i\epsilon)ik'|\vec{r}-\vec{r}'|}. \end{aligned} \quad (3.29)$$

Evaluating with the residue theorem, the free Green's functions are found to be

$$G_0^\pm(\vec{r}, \vec{r}') = -\frac{\mu}{2\pi\hbar^2} \frac{e^{\pm ik|\vec{r}-\vec{r}'|}}{|\vec{r}-\vec{r}'|}, \quad (3.30)$$

and the incoming solution is, in the case of  $G_0^+(\vec{r}, \vec{r}')$ , the free solution, which corresponds to plane waves. To indicate this, the subscript zero in  $|\psi_0\rangle$  is used for the wave function as well

$$\psi_{\text{in},\vec{k}}(\vec{r}) = \psi_{0,\vec{k}}(\vec{r}) = \frac{1}{(2\pi)^{\frac{3}{2}}} e^{i\vec{k}\vec{r}}. \quad (3.31)$$

To progress further in obtaining some form of a practical solution, we have to consider the boundary conditions under which the initial differential equation, that is, the Schrödinger

equation, is to be solved. The boundary conditions needed are those at large distances. We refer to them equivalently as asymptotic boundary conditions, and to the wave function that fulfils them as asymptotic solution. We did not specify these so far explicitly, but with equation (3.30) they are contained implicitly in the integral equation (3.27). We discuss them and their analytic properties in section 3.4. It is convenient to look at the long-range behaviour to give an experimental interpretation of the scattering event. When conducting such a scattering experiment, one sends in a well defined state, the incident beam, which interacts with the target on very short length scales  $r'$  and is then detected in a far away detector at distance  $r$ . This setting gives rise the approximations of the form

$$\begin{aligned} |\vec{r} - \vec{r}'| &\approx |\vec{r}| = r \\ r &\gg r' \quad \text{and} \quad kr \gg (kr')^2. \end{aligned} \quad (3.32)$$

For potentials which fall-off faster than  $r^{-1}$ , the limit for large  $r$  is unproblematic, since they drop fast enough and any solution must, therefore, be asymptotically free, i.e.  $V(R) = 0$  for some  $R \gg r'$ . Special care is required for potentials decreasing similar to  $r^{-1}$ , like the Coulomb potential, which behave distinctively different from the free solution for large  $r$ . We want to assume in this section only potentials which are well behaved in this sense. Inserting the approximations of equation (3.32) into the equations (3.27) and (3.30), we get

$$\psi_{\vec{k}}(\vec{r}) \stackrel{r \gg r'}{\cong} \psi_{\text{in}, \vec{k}}(\vec{r}) + \frac{\mu}{2\pi\hbar^2} \frac{e^{ikr}}{r} \int d^3r' V(\vec{r}') \psi_{\vec{k}}(\vec{r}') \quad (3.33)$$

$$\simeq e^{i\vec{k}\vec{r}} + f(\vec{k}', \vec{k}) \frac{e^{ikr}}{r}, \quad (3.34)$$

with  $\vec{k}' = k \frac{\vec{r}}{r}$ . This result shows that potential scattering at large enough distances reduces to being a superposition of the known incoming plane wave and an outgoing spherical wave, multiplied with the scattering amplitude  $f(\vec{k}', \vec{k})$ . Comparing equation (3.33) with the abstract notation in equations (3.20) and (3.21), we find that the scattering amplitude is the momentum-space representation of the amplitude operator  $\mathcal{T}$

$$f(\vec{k}', \vec{k}) = -\frac{(2\pi)^2 \mu}{\hbar^2} \langle \vec{k}' | \mathcal{T} | \vec{k} \rangle. \quad (3.35)$$

In spherical coordinates, the scattering amplitude is a function of the two angles  $\theta$  and  $\phi$  and of  $k$

$$f(\vec{k}', \vec{k}) \rightarrow f_k(\theta, \phi). \quad (3.36)$$

The Schrödinger equation (3.3) for two particles  $A$  and  $B$  with a central interaction potential has the form

$$H = \frac{\vec{p}_A^2}{2m_A} + \frac{\vec{p}_B^2}{2m_B} + V(\vec{r}_A - \vec{r}_B), \quad (3.37)$$

with the momenta  $\vec{p}_{A,B}$ , masses  $m_{A,B}$  and position vectors  $\vec{r}_{A,B}$ . By introducing two new variables,  $\vec{R}$  for the CoM and  $\vec{r}$  for the relative distance between  $A$  and  $B$

$$\begin{aligned} \vec{R} &= \frac{\vec{r}_A m_A + \vec{r}_B m_B}{m_A + m_B} \\ \vec{r} &= \vec{r}_A - \vec{r}_B \end{aligned} \quad (3.38)$$

and  $\vec{P}$  for the total momentum, as well as  $\vec{p}$  for the relative momentum

$$\begin{aligned} \vec{P} &= \vec{p}_A + \vec{p}_B \\ \vec{p} &= \frac{\vec{p}_A m_B + \vec{p}_B m_A}{m_A + m_B} \end{aligned} \quad (3.39)$$

### 3. Scattering Theory – Two-Body Scattering

and the total and reduced mass

$$\begin{aligned} M &= m_A + m_B \\ \mu &= \frac{m_A m_B}{m_A + m_B}, \end{aligned} \quad (3.40)$$

respectively, we can write the Hamiltonian consisting of a CoM and a relative part

$$\begin{aligned} H &= \frac{\vec{P}^2}{2M} + \frac{\vec{p}^2}{2\mu} + V(\vec{r}) \\ &= H_{\text{CoM}} + H_{\text{rel}}. \end{aligned} \quad (3.41)$$

Due to this separation, the total energy is comprised of the CoM and relative part as well

$$E_{\text{tot}} = E_{\text{CoM}} + E_{\text{rel}}. \quad (3.42)$$

Transitioning to coordinate representation, the Schrödinger equation takes the form

$$\left( -\frac{\hbar^2}{2\mu} \Delta + V(\vec{r}) \right) \psi_E(\vec{r}) = E \psi_E(\vec{r}). \quad (3.43)$$

#### 3.3.2. Radial Schrödinger Equation and Partial Wave Expansion

Motivated by the assumption of a spherically symmetric potential, we choose a spherical coordinate representation for the Schrödinger equation, resulting in a Laplacian

$$\Delta(r, \theta, \phi) = \frac{1}{r^2} \frac{\partial}{\partial r} \left( r^2 \frac{\partial}{\partial r} \right) + \frac{1}{r^2 \sin \theta} \frac{\partial}{\partial \theta} \left( \sin \theta \frac{\partial}{\partial \theta} \right) + \frac{1}{r^2 \sin^2 \theta} \frac{\partial^2}{\partial \phi^2}. \quad (3.44)$$

The angular part of the Laplacian  $\Delta(\theta, \phi)$  is actually the coordinate representation of the square of the angular momentum operator

$$\widehat{L}^2 \rightarrow \vec{L}^2 = -\hbar^2 \frac{1}{\sin \theta} \frac{\partial}{\partial \theta} \left( \sin \theta \frac{\partial}{\partial \theta} \right) + \frac{1}{\sin^2 \theta} \frac{\partial^2}{\partial \phi^2}, \quad (3.45)$$

the Laplacian can be written as

$$\Delta(r, \theta, \phi) = \frac{1}{r^2} \frac{\partial}{\partial r} \left( r^2 \frac{\partial}{\partial r} \right) - \frac{\hbar^2 \vec{L}^2}{r^2}. \quad (3.46)$$

The angular momentum has the spherical harmonics  $Y_\ell^m(\theta, \phi)$  as eigenfunctions, meaning they fulfil the eigenvalue relation

$$\Delta(\theta, \phi) Y_\ell^m(\theta, \phi) = \ell(\ell + 1) Y_\ell^m(\theta, \phi). \quad (3.47)$$

The spherical harmonics carry the angular momentum quantum number  $\ell$  and the projection  $m$ . This separation into radial and angular components in the Laplacian allows us to make an ansatz of the same kind in the wave function, by decomposing it into a product of the radial wave function  $R_{k,\ell}(r)$  and the angular wave function  $Y_\ell^m(\theta, \phi)$

$$\psi_{\vec{k}}(\vec{r}) = \sum_{\ell=0}^{\infty} \sum_{m=-\ell}^{\ell} R_{k,\ell}(r) Y_\ell^m(\theta, \phi). \quad (3.48)$$

Plugging equation (3.48) into equation (3.43), rewriting with  $k^2 = \frac{2\mu E}{\hbar^2}$ , together with equation (3.47) results in a purely radially dependent differential equation for each  $\ell$ , the radial Schrödinger equation:

$$\left( -\frac{1}{r^2} \frac{d}{dr} \left( r^2 \frac{d}{dr} \right) + \frac{\ell(\ell+1)}{r^2} + \frac{2\mu}{\hbar^2} V(r) - k^2 \right) R_{k,\ell}(r) = 0. \quad (3.49)$$

With wave number  $k = \sqrt{\frac{2\mu E}{\hbar^2}}$ , and reduced mass  $\mu$ . This can be rewritten and shortened by using

$$R_{k,\ell}(r) = \frac{u_{k,\ell}(r)}{r}, \quad (3.50)$$

meaning that the full wave function reads

$$\psi_{\vec{k}}(\vec{r}) = \sum_{\ell=0}^{\infty} \sum_{m=-\ell}^{\ell} \frac{u_{k,\ell}(r)}{r} Y_{\ell}^m(\theta, \phi). \quad (3.51)$$

We can then partially evaluate the differential, resulting in

$$\left( -\frac{d^2}{dr^2} + \frac{\ell(\ell+1)}{r^2} + \frac{2\mu}{\hbar^2} V(r) - k^2 \right) u_{k,\ell}(r) = 0. \quad (3.52)$$

Both forms are of course equivalent. The latter is used for a more compact notation.

An important aspect is the long-range behaviour of the radial solution, especially for potentials of the type

$$\int_0^{\infty} dr r V(r) < \infty. \quad (3.53)$$

In this case, the asymptotic long-range behaviour is that of the free solution, the Schrödinger equation becomes the Bessel differential equation, which has the so-called spherical Bessel functions of the first and second kind,  $j_{\ell}(kr)$  and  $n_{\ell}(kr)$ , respectively, as solutions. The general radial solution can then be written as a linear combination of the the spherical Bessel functions

$$u_{k,\ell}(r) = kr (A_{\ell}(k)j_{\ell}(kr) + B_{\ell}(k)n_{\ell}(kr)), \quad (3.54)$$

with some  $k$ -dependent coefficients  $A_{\ell}$  and  $B_{\ell}$ . For  $u_{k,\ell}(r)$  to be a meaningful physical solution, it has to fulfil the corresponding boundary conditions of the differential equation. These are defined at the origin and at infinite distance. The first demands that

$$\lim_{r \rightarrow 0} u_{k,\ell}(r) = 0, \quad (3.55)$$

meaning that the wave function has to be a regular function, see section 3.4. The second will be shown in following, resulting in equation (3.66).

With this, we can now expand the scattering amplitude (3.36) and the incoming plane wave in angular momentum eigenstates, the spherical harmonics. This is so-called partial wave expansion, or partial wave decomposition. By defining the incident direction to be the  $z$ -direction, such that  $\vec{k} = k\vec{e}_z$ , the  $\phi$ -dependency is lost, and the incoming part can be rewritten as:

$$e^{i\vec{k}\vec{r}} = \sum_{\ell=0}^{\infty} (2\ell+1) i^{\ell} j_{\ell}(kr) P_{\ell}(\cos \theta), \quad (3.56)$$

and the scattering amplitude of the outgoing wave as

$$f_k(\theta, \phi) = \sum_{\ell=0}^{\infty} (2\ell+1) f_{\ell}(k) P_{\ell}(\cos \theta). \quad (3.57)$$

### 3. Scattering Theory – Two-Body Scattering

The term  $P_\ell(\cos\theta)$  denotes the  $\ell$ -th Legendre polynomial, which depends on the product of the unit vectors  $\vec{e}_k \cdot \vec{e}_r = \cos(\theta)$ , for  $\vec{e}_k = \vec{e}_z$

$$P_\ell(\cos\theta) = \frac{4\pi}{2\ell+1} \sum_{m=-\ell}^{\ell} Y_{\ell,m}^*(\vec{k}) Y_{\ell,m}(\vec{r}) \quad (3.58a)$$

$$\vec{e}_k \equiv \vec{e}_z \quad \frac{4\pi}{2\ell+1} Y_{\ell,0}(\theta). \quad (3.58b)$$

With the asymptotic form of the spherical Bessel function for  $kr \gg 1$ , the expanded plane wave reads

$$e^{i\vec{k}\vec{r}} \xrightarrow{kr \gg 1} \sum_{\ell=0}^{\infty} (2\ell+1) i^\ell (kr)^{-1} \sin\left(kr - \frac{\pi\ell}{2}\right) P_\ell(\cos\theta). \quad (3.59)$$

The full form of the wave function, with the identities  $\sin(x) = \frac{e^{ix} - e^{-ix}}{2i}$  and  $i^\ell = e^{i\frac{\pi}{2}\ell}$ , reads

$$\begin{aligned} \psi_{\vec{k}}(\vec{r}) &\xrightarrow{r \rightarrow \infty} \sum_{\ell=0}^{\infty} (2\ell+1) P_\ell(\cos\theta) \left[ \frac{e^{ikr}}{2ikr} - \frac{e^{-ikr}}{2ikr} (-1)^\ell + f_\ell(k) \frac{e^{ikr}}{r} \right] \\ &= \sum_{\ell=0}^{\infty} (2\ell+1) \frac{P_\ell(\cos\theta)}{2ik} \left[ -(-1)^\ell \frac{e^{-ikr}}{r} + (1 + 2ikf_\ell(k)) \frac{e^{ikr}}{r} \right] \\ &= \sum_{\ell=0}^{\infty} (2\ell+1) \frac{P_\ell(\cos\theta)}{2ik} \left[ (-1)^{\ell+1} \frac{e^{-ikr}}{r} + S_\ell(k) \frac{e^{ikr}}{r} \right]. \end{aligned} \quad (3.60)$$

In the last line, we perform an important rearrangement with the partial-wave scattering amplitude into  $S_\ell(k) = (1 + 2ikf_\ell(k))$ . This is the partial-wave scattering matrix element. As a matrix, it is diagonal in all  $\ell$  values when no angular momentum coupling is allowed by the potential.

Considering only the radial part  $u_\ell$  in this expansion with equation (3.51) and equation (3.58), it is noteworthy how the reformulation introduces the interpretation of the radial wave function for fixed  $\ell$  as spherically incoming and outgoing waves

$$u_{k,\ell}(r) \sim (-1)^{\ell+1} e^{-ikr} + S_\ell(k) e^{ikr}. \quad (3.61)$$

For elastic scattering, probability must be conserved, which means that

$$|S_\ell(k)|^2 = 1. \quad (3.62)$$

This restricts  $S_\ell(k)$  to change only the phase of the outgoing wave and can, therefore, be defined to have the following form:

$$S_\ell(k) = 1 + 2ikf_\ell(k) = e^{2i\delta_\ell}. \quad (3.63)$$

Solving for the partial scattering amplitude  $f_\ell$  and reinserting into the asymptotic form (3.60) leads to

$$\psi_{\vec{k}}(\vec{r}) \xrightarrow{r \rightarrow \infty} \sum_{\ell=0}^{\infty} (2\ell+1) P_\ell(\cos\theta) i^\ell e^{i\delta_\ell(k)} \frac{\sin\left(kr - \frac{\pi\ell}{2} + \delta_\ell(k)\right)}{kr}, \quad (3.64)$$

and consequently for the radial solution we see that it behaves at large  $r$  similar to a sine function

$$u_{k,\ell}(r) \sim \sin\left(kr - \frac{\pi\ell}{2} + \delta_\ell(k)\right). \quad (3.65)$$

From equation (3.54) the radial solution must thus be of the form

$$u_{k,\ell}(r) \xrightarrow{r \rightarrow \infty} (A_\ell^2 + B_\ell^2)^{\frac{1}{2}} i^\ell e^{i\delta_\ell(k)} \sin\left(kr - \frac{\pi\ell}{2} + \delta_\ell(k)\right). \quad (3.66)$$

This has a similar form to equation (3.59), except for the phase factor  $e^{i\delta_\ell(k)}$  and the phase shift in the sine argument. This is an important observation, as it means that potential scattering leads solely to a phase difference when compared to the free solution. Comparing equations (3.54) and (3.64) together with the long-range form of the spherical Bessel functions, we get

$$\psi_{\vec{k}}(\vec{r}) \xrightarrow{r \rightarrow \infty} \sum_{\ell=0}^{\infty} (2\ell + 1) P_\ell(\cos\theta) i^\ell e^{i\delta_\ell(k)} (\cos(\delta_\ell(k)) j_\ell(kr) + \sin(\delta_\ell(k)) n_\ell(kr)), \quad (3.67)$$

giving an expression of  $u_\ell(r)$  with partial wave phase shift in sine and cosine as coefficients

$$u_{k,\ell}(r) \xrightarrow{r \rightarrow \infty} (\cos(\delta_\ell(k)) j_\ell(kr) + \sin(\delta_\ell(k)) n_\ell(kr)). \quad (3.68)$$

A visual representation of the interpretation of the effect of the phase shift relation can be seen in figure 3.1.

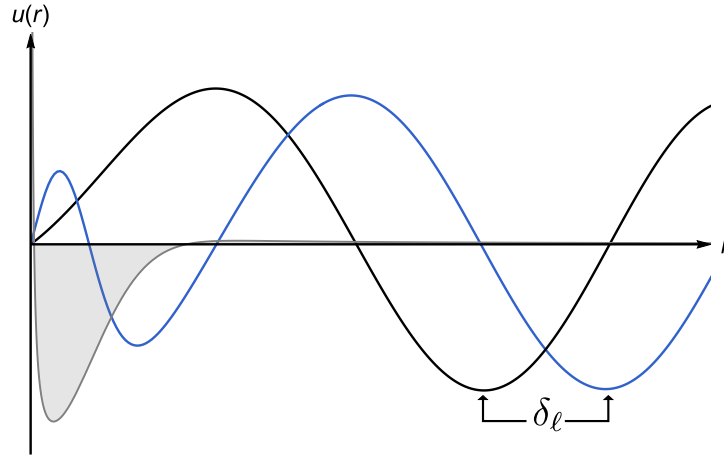


Figure 3.1.: Scattered wave function (blue) compared to the unperturbed wave (black). The scattering potential is overlaid in grey. The free solutions are Coulomb functions, as the potential is a phenomenological parametrization for a  $^{12}\text{C} + p$  scattering process. The wave function is obtained within an  $\mathcal{R}$ -matrix framework.

### 3.3.3. Coulomb Scattering

A special case of potentials are those which do not drop faster than  $1/r$  – something we normally assume to be the case to ensure converging integrals. For nuclear systems, the Coulomb interaction plays an important role. We consider the Coulomb equation as a special case of the radial Schrödinger equation:

$$\begin{aligned} \left( \frac{d^2}{dr^2} - \frac{\ell(\ell+1)}{r^2} - \frac{2Z_1 Z_2 e^2 \mu}{\hbar^2 r} + k^2 \right) u_{k,\ell}(r) &= 0 \\ \left( \frac{d^2}{dr^2} - \frac{\ell(\ell+1)}{r^2} - \frac{2k\eta}{r} + k^2 \right) u_{k,\ell}(r) &= 0, \end{aligned} \quad (3.69)$$

### 3. Scattering Theory – Two-Body Scattering

where  $e$  is the elementary charge and  $Z_{1,2}$  the charge number. We use the so-called Sommerfeld  $\eta$  parameter to rewrite the Coulomb potential

$$\eta = \frac{Z_1 Z_2 e^2 \mu}{\hbar^2 k} = \frac{\text{sgn}(Z_1 Z_2)}{a_B k}. \quad (3.70)$$

This parameter is dimensionless and conveniently expresses the strength of the interaction, where  $a_B = \frac{\hbar^2}{\mu |Z_1 Z_2| e^2}$  is the generalized Bohr radius. The Coulomb equation has the solution  $F_\ell(\eta, kr)$ , which is regular at the origin, and the solution  $G_\ell(\eta, kr)$ , which is irregular. The infinite range of the Coulomb potential affects the long-range properties of these functions, which read

$$F_\ell(\eta, kr) \xrightarrow{kr \gg 1} \sin\left(kr - \frac{1}{2}\ell\pi - \eta \log(2kr) + \sigma_\ell\right) \quad (3.71)$$

$$G_\ell(\eta, kr) \xrightarrow{kr \gg 1} \cos\left(kr - \frac{1}{2}\ell\pi - \eta \log(2kr) + \sigma_\ell\right). \quad (3.72)$$

See also appendix B for details about the Coulomb functions. The  $\sigma_\ell$  is the Coulomb phase shift

$$\sigma_\ell = \arg[\Gamma(\ell + 1 + i\eta)]. \quad (3.73)$$

With the solutions  $F_\ell(\eta, kr)$  and  $G_\ell(\eta, kr)$ , the radial solution can be again given similar to equation (3.68)

$$u_{k,\ell}(r) \xrightarrow{r \rightarrow \infty} \cos(\delta_\ell(k)) F_\ell(\eta, kr) + \sin(\delta_\ell(k)) G_\ell(\eta, kr). \quad (3.74)$$

The Coulomb functions are themselves special cases of the confluent hypergeometric functions, in turn a special case of the general hypergeometric functions. Therefore, they can be expressed by various equalities and calculation prescriptions [DLM14].

## 3.4. Analyticity and Symmetries of the Solution of the Radial Schrödinger Equation

In this section we want to highlight the regular and irregular solutions of the second-order differential equation that is the radial Schrödinger equation and their relation to the so-called Jost function. The analytic properties of these functions determine the analytic properties of the scattering matrix and show the connection between poles of the scattering matrix and resonances and bound states of the Hamiltonian. These are the key ideas for the analytic continuation in the coupling constant into the complex plane, which is discussed in chapter 8. The discussion is based on [New82, Joa76].

### 3.4.1. The Regular and Irregular Solutions

The radial Schrödinger equation equation (3.52) will be slightly modified by introducing a strength parameter, or coupling constant, in front of the interaction potential, denoted with  $\lambda$ . The Schrödinger equation then reads

$$\left(-\frac{d^2}{dr^2} + \frac{\ell(\ell+1)}{r^2} + \lambda \frac{2\mu}{\hbar^2} V(r)\right) u_{k,\ell}(r) = k^2 u_{k,\ell}(r). \quad (3.75)$$

This equation has a solution  $u_{k,\ell}(r) = \phi_\ell(k, r)$  fulfilling the boundary condition at the origin, such that under the restriction of

$$\lim_{r \rightarrow 0} r^2 V(r) = 0 \quad (3.76)$$

### 3.4. Analyticity and Symmetries of the Solution of the Radial Schrödinger Equation

$$\phi(k, 0) = 0 \quad \text{and} \quad \left. \frac{d}{dr} \phi(k, r) \right|_{r=0} = \text{const} \quad \text{for } \ell = 0 \quad (3.77a)$$

$$\lim_{r \rightarrow 0} r^{-\ell-1} \phi_\ell(k, r) = 1 \quad \text{for } \ell \neq 0. \quad (3.77b)$$

Any function satisfying the condition in equation (3.77) is called regular. No further boundary conditions are applied to  $\phi_\ell(k, r)$ , meaning that its long-range behaviour is not specified. The spherical Bessel function  $j_\ell(kr)$  is already introduced as the regular solution in the case of  $V = 0$ . At large values of  $|k|$ , the regular solution takes the form

$$\phi_\ell(k, r) = (2\ell + 1)!! k^{-\ell-1} \sin\left(kr - \frac{1}{2}\pi\ell\right) + \mathcal{O}\left(|k|^{-\ell-1} e^{|\text{Im}(k)r}\right). \quad (3.78)$$

The integral equation of the regular solution is arrived at just as in the case of the full solution, by means of the Green's function, and reads

$$\phi_\ell(k, r) = \phi_\ell^{(0)}(k, r) + \int_0^r dr' g_\ell(k; r, r') V(r') \phi_\ell(k, r'). \quad (3.79)$$

The function  $\phi_\ell^{(0)}(k, r)$  is the free (or unperturbed) regular solution. It is related to the spherical Bessel function and the Bessel function of the first kind by

$$\phi_\ell^{(0)}(k, r) = (2\ell + 1)!! k^{-\ell-1} kr j_\ell(kr) \quad (3.80)$$

$$= \Gamma\left(\ell + \frac{3}{2}\right) \sqrt{r} \left(\frac{k}{2}\right)^{-\ell-1/2} J_{\ell+1/2}(kr). \quad (3.81)$$

The Green's function  $g_\ell$  must correspond to the appropriate boundary conditions in equation (3.77), which means that

$$g_\ell(k; r, r') = 0 \quad \text{for } r < r'. \quad (3.82)$$

This is the reason why the integration domain goes from 0 to  $r$ . The equations (3.79) and (3.81), are used again in section 8.1. The regular solution satisfies certain symmetry properties, which are used to show the symmetries of the scattering matrix. For real parameters  $k$  and  $\lambda$ , we have

$$\phi_\ell(-k, r) = \phi_\ell(k, r), \quad (3.83)$$

which follows from the independence of the boundary condition (3.77) of  $k$ , and thus  $\phi_\ell(k, r)$  itself must also be real. For complex valued parameters we have

$$\phi_\ell^*(\lambda^*, k^*, r) = \phi_\ell(\lambda, k, r). \quad (3.84)$$

In the same vein, if one only takes boundary conditions for  $r$  going to infinity, one obtains the two linearly independent irregular solutions  $f_{\ell\pm}(k, r)$ . They are defined by

$$\lim_{r \rightarrow \infty} e^{\mp ikr} f_{\ell\pm}(k, r) = 1. \quad (3.85)$$

Only at the point of zero energy,  $k = 0$ , are they linear dependent. We follow with the definition in equation (3.85) the convention of [New82], meaning that  $f_{\ell+}(k, r)$  belongs to the upper half of the  $k$ -plane and  $f_{\ell-}(k, r)$  (in some works written as  $f_{\ell-}(-k, r)$ ) to the lower. The original definition is the other way round, and is followed, e.g., by [Joa76]. These functions have the symmetries

$$f_{\ell-}(k, r) = f_{\ell+}(ke^{i\pi}, r), \quad \text{for } k > 0 \quad (3.86)$$

### 3. Scattering Theory – Two-Body Scattering

which means  $f_+$  can be analytically continued to the lower half of the imaginary  $k$ -plane into  $f_-$

$$\begin{aligned} f_{\ell-}(k, r) &= f_{\ell+}^*(k, r) \text{ for } k, \lambda \in \mathbb{R} \\ f_{\ell-}(k, r) &= f_{\ell+}^*(k^*, r) \text{ for } k, \in \mathbb{C} \text{ and } \lambda \in \mathbb{R} \\ f_{\ell-}(\lambda, k, r) &= f_{\ell+}^*(\lambda^*, k^*, r) \text{ for } k, \lambda \in \mathbb{C}. \end{aligned} \quad (3.87)$$

To prove these statements, one needs to show that the integral representation converges absolutely for any  $\lambda$  and  $k$ . This is shown in chapter 8, as it is a crucial part for the method discussed there.

#### 3.4.2. The Jost Functions

From the fact that any linear combination of two linearly independent solutions to a linear differential equation must again be a solution, we can write

$$\phi_{\ell}(k, r) = a f_{\ell+}(k, r) + b f_{\ell-}(k, r). \quad (3.88)$$

The parameters  $a$  and  $b$  can be determined with the help of the Wronskian  $W(f, g) = fg' - f'g$ . If the functions  $f(x)$  and  $g(x)$  are two different solutions of the same equation, the Wronskian is constant and independent of  $x$ . In our case, we use this to define the family of Jost functions

$$\begin{aligned} W(f_{\ell+}, \phi_{\ell}) &= f_{\ell+} \phi'_{\ell} - f'_{\ell+} \phi_{\ell} \\ &\stackrel{(3.88)}{=} b W(f_{\ell+}, f_{\ell-}) \end{aligned} \quad (3.89)$$

and analogously

$$W(f_{\ell-}, \phi_{\ell}) = a W(f_{\ell-}, f_{\ell+}). \quad (3.90)$$

The value of  $W(f_{\ell+}, f_{\ell-})$  can be determined with the help of the asymptotic behaviour of  $f_{\ell+}$  and  $f_{\ell-}$  in equation (3.85)

$$W(f_{\ell+}, f_{\ell-}) = -2ik. \quad (3.91)$$

We define the first type of Jost functions as the Wronskian of  $f_{\ell+}$  and  $f_{\ell-}$  with the regular solution  $\phi_{\ell}$

$$\mathfrak{F}_{\ell\pm}(k) = W(f_{\ell\pm}, \phi_{\ell}). \quad (3.92)$$

As already mentioned, the Jost functions are independent of  $r$  and only depend on the  $k$ . This allows to rewrite the equation (3.88) as

$$\phi_{\ell}(k, r) = \frac{1}{2ik} (\mathfrak{F}_{\ell-} f_{\ell+} - \mathfrak{F}_{\ell+} f_{\ell-}), \quad (3.93)$$

and by using equation (3.85), we see it has the long-range property of the form

$$\phi_{\ell}(k, r) \simeq \frac{1}{2ik} (\mathfrak{F}_{\ell-} e^{ikr} - \mathfrak{F}_{\ell+} e^{-ikr}) \quad \text{for } r \rightarrow \infty \quad (3.94)$$

This enables us to connect the equation to the scattering matrix in section 3.5. From the definition of the Jost functions (3.92) and the boundary conditions (3.77) follows

$$\mathfrak{F}_{\ell+}(k) = (2\ell + 1) \lim_{r \rightarrow 0} r^{\ell} f_{\ell+}(k, r). \quad (3.95)$$

This, in turn, forces the same symmetries on  $\mathfrak{F}_{\ell+}(k)$  as  $f_{\ell+}(k, r)$  with respect to the energy. The Jost functions are thus analytic in  $k$  and can be continued into each other

$$\mathfrak{F}_{\ell-}(k) = \mathfrak{F}_{\ell+}(ke^{i\pi}). \quad (3.96)$$

### 3.4. Analyticity and Symmetries of the Solution of the Radial Schrödinger Equation

Their complex conjugates are

$$\mathfrak{F}_{\ell-}(k, r) = \mathfrak{F}_{\ell+}^*(k, r) \quad \text{for } k, \lambda \in \mathbb{R} \quad (3.97a)$$

$$\mathfrak{F}_{\ell-}(k, r) = \mathfrak{F}_{\ell+}^*(k^*, r) \quad \text{for } k \in \mathbb{C} \text{ and } \lambda \in \mathbb{R} \quad (3.97b)$$

$$\mathfrak{F}_{\ell-}(\lambda, k, r) = \mathfrak{F}_{\ell+}^*(\lambda^*, k^*, r) \quad \text{for } k, \lambda \in \mathbb{C}. \quad (3.97c)$$

Another aspect of the general angular momentum dependence is the difference in the high-momentum limit for the  $\ell = 0$  case as opposed to the general case. For  $\text{Im}(k) \geq 0$ , one has

$$\lim_{|k| \rightarrow \infty} \mathfrak{F}_0(k) = 1 \quad (3.98a)$$

$$\lim_{|k| \rightarrow \infty} k^\ell \mathfrak{F}_{\ell+} = (2\ell + 1)!! e^{-\frac{1}{2}i\pi\ell}. \quad (3.98b)$$

In order to have a function that approaches unity in the large  $k$  limit, we introduce a redefined Jost function

$$\mathcal{F}_{\ell\pm}(k) = \frac{1}{(2\ell + 1)!!} k^\ell e^{\frac{1}{2}i\pi\ell} \mathfrak{F}_{\ell\pm}(k), \quad (3.99)$$

which approaches unity for large  $k$  as well as being continuous at  $k = 0$ . Furthermore,  $\mathcal{F}_{\ell\pm}$  satisfy equation (3.96).

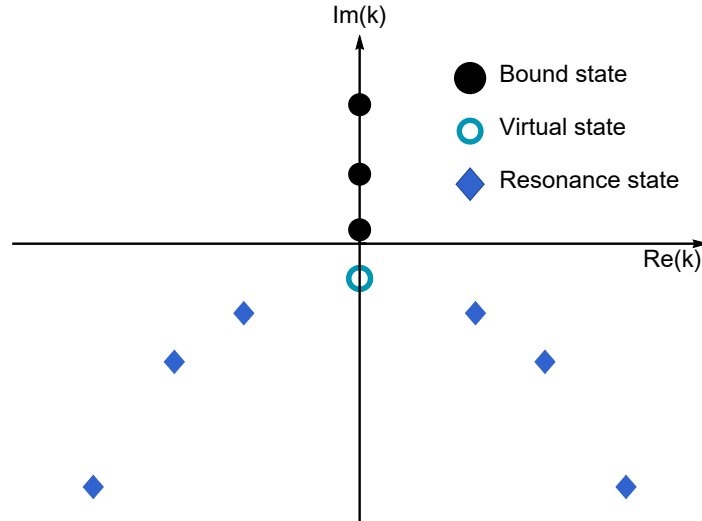


Figure 3.2.: The position of the zeros of the Jost function in the complex  $k$ -plane. Bound and virtual states lie on the positive and negative imaginary axis, respectively. Resonances lie symmetric to the left and right of the imaginary axis.

From equations (3.92) and (3.95), together with the analyticity statements in equation (3.97) follow a few important observations. First, if  $f_{\ell\pm}$  can be expanded in powers of  $\lambda$ , then so can  $\mathfrak{F}_{\ell\pm}$  and  $\mathcal{F}_{\ell\pm}$ . This is used in chapter 8 for the derivation of the method presented there. Second, if  $\mathfrak{F}_{\ell+}(k_0) = 0$ , then the *irregular* solution  $f_{\ell+}(k_0, 0)$  must necessarily become *regular*. The two functions  $f_{\ell\pm}(k, r)$  are only defined by boundary condition for large  $r$ ; while in the general case they do not fulfil the boundary conditions for regular functions, equation (3.77), this does not exclude them from ever doing so. Third, the long-range properties of  $f_{\ell+}(k, r)$  demand that the wave functions behaves like  $e^{ikr}$ . For  $\text{Im}(k) > 0$ ,  $f_{\ell+}(k, r)$  must fall off exponentially. Consequently, any zero of the Jost function in the upper half of the complex  $k$ -plane, is a square-integrable, regular solution of the radial Schrödinger equation and thus a

### 3. Scattering Theory – Two-Body Scattering

bound state. Additionally, the energy  $E$  and thus  $k^2$  must be real in this case, which means that  $\text{Re}(k_0) = 0$ , the zeros lie on the positive imaginary axis. For  $k$  on the lower half of the complex plane, no restrictions exist as to where the zeros of the Jost function have to lie.

The described properties are visualized in figure 3.2. There, the bound states are shown on the positive imaginary axis. Going to negative  $\text{Im}(k)$ , the zeros for  $\ell = 0$  can lie on the negative imaginary axis, as well as any where else. For  $\ell > 0$ , the zeros cannot lie on the negative axis. Further, all zeros lie symmetrical to the left and right of the imaginary axis.

## 3.5. Resonances

A resonance in a quantum mechanical system is a quasi-bound state, which has long enough, but a finite life time, such that an incoming particle is delayed for a certain time before leaving the system again. This picture was first proposed by Gamow [Gam28], in order to describe the newly discovered  $\alpha$ -decay. This also corresponds to demanding a purely outgoing wave as boundary condition for the Schrödinger equation, which was formulated in this way by Siegert [Sie39]. A necessary condition for this kind of behaviour is the existence of a type of barrier which is able to trap the incoming particle temporarily. A sketch of this is depicted in figure 3.3. The default case for this to occur is the presence of an angular momentum barrier. Any resonance at  $\ell = 0$  in the two-body elastic case has to be due to some other barrier effect caused by the potential. This point of view is restricted to the discussion of single channel scattering. A multi-channel system can exhibit different kinds of resonances, see section 3.6. The proper definition of a resonance is given as a pole of the scattering matrix  $S$  for complex

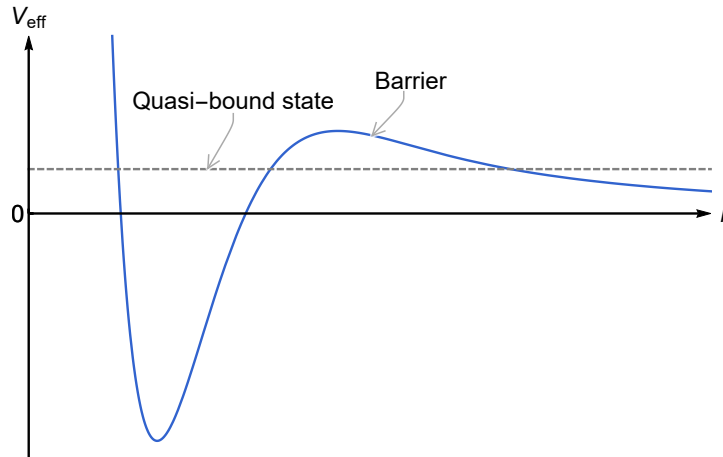


Figure 3.3.: Sketch of an effective potential with angular momentum barrier,  $V(r) + \frac{\ell(\ell+1)}{2r^2}$ . For  $\ell = 0$ , the potential has to provide some form of barrier.

wave numbers  $k$ , lying in the fourth quadrant. When going over from the wave number to the energy, we have

$$E_R - i\Gamma/2 = \frac{\hbar^2 (k_{\text{Re}} - i k_{\text{Im}})^2}{2m}, \quad (3.100)$$

as well as

$$E_R = \frac{\hbar^2 (k_{\text{Re}}^2 - k_{\text{Im}}^2)}{2m} \quad \text{and} \quad \Gamma = \frac{2\hbar^2}{m} k_{\text{Re}} k_{\text{Im}}. \quad (3.101)$$

It is apparent, when  $k_{\text{Re}}^2 < k_{\text{Im}}^2$ , the energy becomes negative. This case is usually not referred to as a resonance. We want to specify the relation of the  $S$ -matrix with the Jost function. The conventional definition of a resonance via poles of the scattering matrix  $S$  can be obtained

by rewriting the  $S$ -matrix with the help of the Jost functions. To this end, we compare the physical radial solution  $u_{k,\ell}(r)$  with the regular solution  $\phi_\ell(k, r)$ . From equation (3.55) and equation (3.65) regarding the physical solution, and from the equations (3.77) and (3.78) we see that  $u_{k,\ell}(r)$  and  $\phi_\ell(k, r)$  must be proportional

$$u_{k,\ell}(r) = \alpha_\ell(k) \phi_\ell(k, r). \quad (3.102)$$

Equation (3.61) can be compared to equation (3.94)

$$\alpha_\ell^{-1}(k) \left( -(-1)^\ell e^{-ikr} + S_\ell(k) e^{ikr} \right) = \frac{1}{2ik} \left( -\mathfrak{F}_{\ell+} e^{-ikr} + \mathfrak{F}_{\ell-} e^{ikr} \right) \quad (3.103)$$

$$= \frac{1}{2ik} \mathfrak{F}_{\ell+} \left( -e^{-ikr} + \frac{\mathfrak{F}_{\ell-}}{\mathfrak{F}_{\ell+}} e^{ikr} \right), \quad (3.104)$$

and bring the factor  $(-1)^\ell = e^{i\pi\ell}$  over, to be in accordance with equation (3.99), we get the relation

$$\begin{aligned} S(k) &= \frac{e^{i\pi\ell} \mathfrak{F}_{\ell-}(k)}{\mathfrak{F}_{\ell+}(k)} \\ &= \frac{\mathcal{F}_{\ell-}(k)}{\mathcal{F}_{\ell+}(k)}. \end{aligned} \quad (3.105)$$

This shows, that a pole of the scattering matrix corresponds to a zero of the Jost function  $\mathcal{F}_{\ell+}(k)$ . Any analytic property of the scattering matrix and its poles is thus also a consequence of the properties of the Jost functions. For example, a bound state, which is a zero of the Jost function on the positive imaginary axis, is also a pole of the  $S$ -matrix. Furthermore, the Jost function is analytic in the strength of the potential, in turn meaning the same for the scattering matrix. This fact is used in the calculation of resonance via the analytic continuation in the coupling constant in chapter 8.

### Phase Shift Behaviour Near a Resonance

The presence of a resonance and consequently an  $S$ -matrix pole has a characteristic effect on the phase shift behaviour. One can use this to check for further indications that the calculated  $S$ -matrix pole is indeed a physical resonance. Often, the  $S$ -matrix is not easily accessible, but the phase shift is. This might be the case when, e.g., the complex domain is not in the numerical scope of the computation. To give some more meaning to the phase shift, we define the infinite energy limit as

$$\lim_{E \rightarrow \infty} \delta_\ell = 0. \quad (3.106)$$

This makes the phase shift unambiguous and gives rise to the possibility of being non-zero at vanishing energy, which is used in Levinson's theorem, equation (3.110). We arrive at an interpretation for resonance phase shifts by looking at the case of a potential for which we can assume that at some point  $R$ , the potential vanishes, i.e.,  $V(R) = 0$ . For the sake of the argument, a simple square well potential is sufficient. The wave function and its derivative have to be continuous at the interface from potential to no potential

$$\begin{aligned} \psi_{\text{int}}(R) &= \psi_{\text{ext}}(R) \\ \psi'_{\text{int}}(r) \Big|_{r=R} &= \psi'_{\text{ext}}(r) \Big|_{r=R}. \end{aligned} \quad (3.107)$$

The same is true for the (inverse) logarithmic derivative of the wave function

$$\mathcal{R}(k) := \frac{\psi_{\text{int}}(R)}{\psi'_{\text{int}}(R)} = \frac{\psi_{\text{ext}}(R)}{\psi'_{\text{ext}}(R)}. \quad (3.108)$$

### 3. Scattering Theory – Two-Body Scattering

We introduce the label  $\mathcal{R}$  for the inverse logarithmic derivative of the interior wave function at the point  $r = R$  and dropped all further indices for brevity. By choosing the inverse we have recovered the definition of the so-called  $\mathcal{R}$ -matrix. Inserting the asymptotic radial wave function, equation (3.68), into equation (3.108), and solving for the phase shift, we arrive at the expression

$$\tan(\delta_\ell) = \frac{k\mathcal{R} j'_\ell(kR) - j_\ell(kR)}{k\mathcal{R} n'_\ell(kR) - n_\ell(kR)}. \quad (3.109)$$

To interpret the phase shift near a resonance, it is helpful to first introduce Levinson's theorem [Lev49], which gives a relation between the zero energy phase shift and the number of bound states

$$\delta_\ell(0) = (n + \frac{1}{2}N)\pi, \quad (3.110)$$

with  $n$  being the number of bound states and  $N = 1$  for  $\ell = 0$  and  $N = 2$  for all other  $\ell$ . The theorem provides an interpretation of quasi-bound states at energies  $E \neq 0$ , and gives insight into their appearance. This can be seen in figure 3.4; here, a bound state phase shift lies at exactly  $\pi$  for  $E = 0$  and then drops to zero with increasing energy. The other phase shift in the figure is a quasi-bound state and emulates the bound state phase shift behaviour away from the zero energy point. We thus speak of a resonance in the phase shift when it sharply increases, goes through  $\pi/2$  and then still increases, in the case of a perfectly isolated resonance up to  $\pi$  (all modulo  $\pi$ ). Conversely, a phase shift rising with increasing energy, but failing to rise above a value of  $\pi/2$ , is not a resonance phase shift.

If the phase shift rises slowly and barely passes the  $\pi/2$ , it could be due to background effects, which are not properly accounted for. This reasoning leads to a parametrization of the form

$$\delta_\ell = \delta_\ell^R + \delta_{\text{b.g.}}, \quad (3.111)$$

where the resonant part  $\delta_\ell^R$  follows the ideal phase shift behaviour as described above, and the background term  $\delta_{\text{b.g.}}$  absorbs all other contributions. This parametrization allows to write the resonant contribution as [Fri13]

$$\delta_\ell^R = -\arctan\left(\frac{\Gamma}{2(E - E_R)}\right). \quad (3.112)$$

The position  $E_R$  of a resonance extracted from a phase shift is defined as the inflection point of the resonant part of the realistic partial wave phase shift, and thus fulfils the conditions

$$\delta_\ell^R(E_R) = \frac{\pi}{2} \quad (3.113a)$$

$$\left.\frac{d^2\delta_\ell^R}{dE^2}\right|_{E=E_R} = 0. \quad (3.113b)$$

In practical applications the resonance position is often simply defined as the inflection point of the full phase shift. Taking the derivative of equation (3.112) with respect to the energy gives

$$\frac{d\delta_\ell^R}{dE} = \frac{\Gamma}{2(E - E_R)^2 + \Gamma^2/2}. \quad (3.114)$$

This leads to the Breit-Wigner formula for the partial wave cross-section

$$\sigma_\ell = \frac{4\pi}{k^2}(2\ell + 1) \sin^2(\delta_\ell) = \frac{4\pi}{k^2}(2\ell + 1) \frac{(\Gamma/2)^2}{(E - E_R)^2 + (\Gamma/2)^2}. \quad (3.115)$$

The width is then obtained from equation (3.114) by evaluating at  $E = E_R$  and rewriting it as

$$\Gamma = 2 \left( \left. \frac{d\delta_\ell}{dE} \right|_{E=E_R} \right)^{-1}. \quad (3.116)$$

This procedure is only valid for phase shifts close to the idealized case. These have relatively small widths, and are referred to as sharp resonances. If applied to broad resonances, the equations (3.113) and (3.115) can only serve as an approximation. Precise values are obtained by calculating the pole position of the  $S$ -matrix in the complex plane.

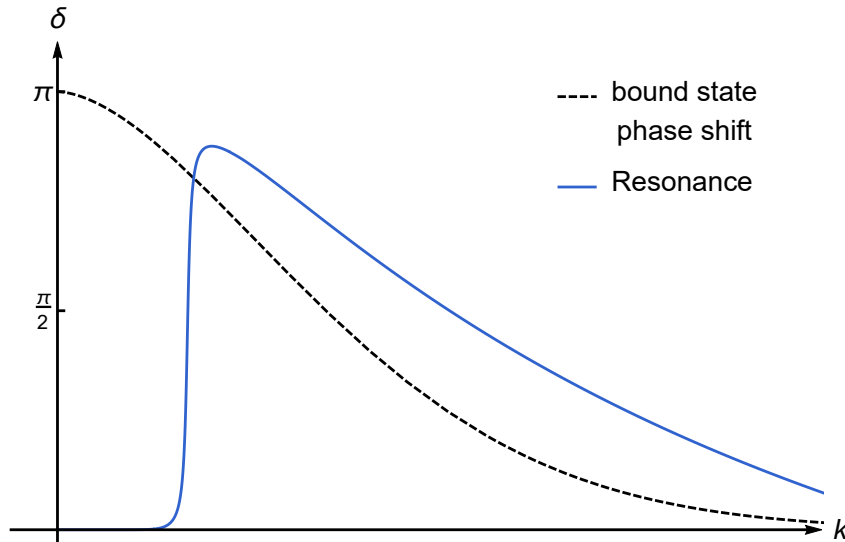


Figure 3.4.: Sketch of phase shifts. The dashed phase shift is a zero energy bound-state phase shift, according to Levinson’s theorem. In blue is a resonant phase shift corresponding to a narrow resonance, a “quasi-bound state”.

## 3.6. Spin, Inelastic and Multi-Channel Scattering

The treatment of scattering events which leave one or both scatterers with a change in the internal degrees of freedom, or excited internal states requires the formalism from the previous sections to be expanded. No new quantities have to be introduced, it is sufficient to generalize the relations introduced in the previous sections.

The terms *inelastic* and *multi-channel* scattering are closely related, but not synonymous. Inelastic scattering refers to the excitation of internal degrees of freedom

$$A + B \rightarrow A^* + B^*.$$

Multi-channel scattering implies that states of different energies couple to each other, necessitating the inclusion of energy thresholds. This gives rise to a different kind of resonance phenomenon as is discussed in sections 3.5 and 3.6.3. The introduction of new internal degrees of freedom leads to a set of coupled differential equations.

### 3.6.1. Spin Degrees of Freedom

The first additional degree of freedom we introduce is spin. We still remain in the elastic case, meaning that no energy transfer to internal excitations takes place. It serves as template for

### 3. Scattering Theory – Two-Body Scattering

the general multi-channel case. We follow reference [Fri13], for an introduction to this topic. A detailed description can be found in references [New82, Fri13]. We assume two scattering partners A and B, just as in section 3.3.1, now each carrying an generic internal angular momentum  $I_A$  and  $I_B$ , which can be either intrinsic spin, orbital or the total angular momentum, with projections  $M_A$  and  $M_B$ . We introduce the uncoupled spin state, which reads

$$\chi_{M_A, M_B} = |I_A, M_A, I_B, M_B\rangle. \quad (3.117)$$

The total relative motion wave function is case composed of a spatial and a spin wave function and reads

$$\Psi(\vec{r}, M_A, M_B) = \sum_{\nu}^{(2I_A+1)(2I_B+1)} \psi_{\nu}(\vec{r}) \chi_{\nu}, \quad (3.118)$$

where the collective index  $\nu$ , running over all  $(2I_A + 1)(2I_B + 1)$  possible spin states. The  $\psi_{\nu}(\vec{r})$  are the wave functions of each spin-channel. The total wave function must satisfy the Schrödinger equation

$$\left( -\frac{\hbar^2}{2\mu} \Delta + V \right) \Psi(\vec{r}, M_A, M_B) = E \Psi(\vec{r}, M_A, M_B). \quad (3.119)$$

The boundary conditions (in  $z$ -direction) at large distances are in analogy to equation (3.33) the incoming plane wave and outgoing spherical wave

$$\psi(\vec{r}, M_A, M_B) \xrightarrow{r \rightarrow \infty} e^{ikz} \chi_{\nu} + \sum_{\nu'}^{(2I_A+1)(2I_B+1)} f_{\nu, \nu'}(\theta, \phi) \frac{e^{ikr}}{r} \chi_{\nu'}. \quad (3.120)$$

The scattering amplitude  $f_{\nu, \nu'}(\theta, \phi)$  is not spin-sensitive and allows spin change. In the case that the interaction between the scatterers is independent of the spin, the amplitude is diagonal in spin-space  $f_{\nu, \nu'}(\theta, \phi) = \delta_{\nu, \nu'} f(\theta, \phi)$ .

We perform the partial wave expansion, which now has to be considered for each spin-channel

$$\psi(\vec{r}, \nu) = \sum_{\ell=0}^{\infty} \sum_{m=-\ell}^{\ell} \frac{u_{\nu, \ell, m}(r)}{r} Y_{\ell, m}(\theta, \phi). \quad (3.121)$$

Unlike the case in equation (3.58), the spherical harmonics have to be kept in their entirety, as we no longer have a vanishing component in the  $z$ -direction. We have not taken explicit (anti-)symmetrization into account, and equation (3.121) can formally be written as

$$\psi(\vec{r}, \nu) = \sum_{\ell=0}^{\infty} \sum_{m=-\ell}^{\ell} \mathcal{A}_{\nu} \frac{u_{\nu, \ell, m}(r)}{r} Y_{\ell, m}(\theta, \phi), \quad (3.122)$$

where  $\mathcal{A}_{\nu}$  is the relevant antisymmetrizer for fermionic systems. We arrive at the coupled radial wave functions for all spin-channels by inserting the partial wave expansion, equation (3.121), into the total wave function, equation (3.118), and this into equation (3.119), which results in the radial spin-channel Schrödinger equation

$$\left( -\frac{\hbar^2}{2\mu} \frac{d^2}{dr^2} + \frac{\ell(\ell+1)\hbar^2}{2\mu r^2} \right) u_{\nu, \ell, m}(r) + \sum_{\nu', \ell', m'} V_{\nu, \ell, m}^{\nu', \ell', m'}(r, r') u_{\nu', \ell', m'}(r) = E u_{\nu, \ell, m}(r). \quad (3.123)$$

Here,  $u_{\nu, \ell, m}(r)$  are the radial wave functions of a specific spin, and the potential being the integral over the angles  $\theta$  and  $\phi$  as well as over all spin projections  $M_A$  and  $M_B$ , indicated by the collective index  $\nu$

$$V_{\nu, \ell, m}^{\nu', \ell', m'} = \langle \chi_{\nu} Y_{\ell, m}(\theta, \phi) | \hat{V} | \chi_{\nu'} Y_{\ell', m'}(\theta, \phi) \rangle. \quad (3.124)$$

The potential can be non-local, hence the  $V(r, r')$  notation.

### 3.6.2. Coupled-Channels

The inclusion of additional degrees of freedom can be accomplished by adapting the previous treatment of spin. By considering an extension of the spin wave function to be a general wave function of that particular set of degrees of freedom. We change the notation

$$\chi_\nu \rightarrow \chi_j(\nu),$$

where  $\nu$  is representative for all relevant quantum numbers, while iterating over all possible configurations with index  $j$ .

$$\Psi(\vec{r}, \nu) = \sum_j \psi_j(\vec{r}) \chi_j(\nu). \quad (3.125)$$

The index  $\nu$  includes all internal degrees of freedom, for both scattering partners. The functions  $\chi_j(\nu)$  are the wave functions to that specific internal state. We want to assume that these states fulfil an internal/intrinsic eigenvalue relation of the form

$$H_\nu \chi_i(\nu) = E_i \chi_i(\nu). \quad (3.126)$$

The  $\psi_j(\vec{r})$  are the channel wave functions to the channel defined by  $\chi_j(\nu)$ . The Schrödinger equation takes the form

$$\left( -\frac{\hbar^2}{2\mu} \Delta + H_\nu + W \right) \Psi(\vec{r}, \nu) = E \Psi(\vec{r}, \nu). \quad (3.127)$$

The two different energies  $E$  and  $E_i$ , lead to the concept of *open* and *closed* channels. A channel is open when  $E > E_i$  and closed otherwise. This means that the wave function of a closed channel is a bound state. Inserting equation (3.126) into the Schrödinger equation leads to the coupled channel equations

$$-\frac{\hbar^2}{2\mu} \Delta \psi_i(\vec{r}) + \sum_j W_{i,j}(\vec{r}, \vec{r}') \psi_j(\vec{r}) = (E - E_i) \psi_i(\vec{r}), \quad (3.128)$$

with  $W_{i,j}(\vec{r})$  being the matrix element of the interaction between all internal degrees of freedom

$$W_{i,j}(\vec{r}) = \langle \chi_i(\nu) | W | \chi_j(\nu) \rangle, \quad (3.129)$$

similar to the case of spin scattering. The derivation of the radial Schrödinger equation is analogous to section 3.6.1. The difference is the dependence of the wave number  $k \rightarrow k_i$  on the channel

$$k_i^2 = \frac{2\mu(E - E_i)}{\hbar^2}, \quad (3.130)$$

which can make the actual computation of multi-channel scattering with realistic interaction computationally expensive. Formally, everything that follows can be written in quasi-identical form to the spin-coupled case, if the meaning of the collective index  $\nu$  is expanded to allow for all different combinations of quantum numbers, also accommodating multi-channel energies.

### 3.6.3. Resonances in Multi-Channel Scattering

The fact that states of different energy and configuration are coupled leads to a new possibility of how a resonance can occur. In the single-channel elastic scattering case we necessarily require some form of barrier, which can trap a projectile temporarily, as depicted in figure 3.3. Coupling between states allows a previously bound state to decay into the continuum, if it is energetically allowed. For example, such a case would be a bound three-body system, where one

### 3. Scattering Theory – Two-Body Scattering

particle obtains energy from a second particle, and as a result, has enough energy to leave the system. The inverse of this scenario, would be a (temporary) capture reaction. This situation is e.g. dubbed as *bound-states in the continuum* [New82]. Depending on the realization of such systems, even stable bound-states can be formed. Resonances of this kind are referred to as *Feshbach resonances* [Fes58, Fes62], see also reference [Fri13]. Formally, the Feshbach method to treat scattering is equivalent to the  $J$ -matrix approach, discussed in chapter 6. The calculation and interpretation of resonances as poles of the scattering matrix continues to be valid.

## 4. Scattering Theory – Many-Body Scattering

This chapter serves as an introduction to the limits of the two-body scattering formalism and what general steps have to be taken in order to be able to solve the many-body scattering problem exactly. Our aim is to provide the information needed to understanding why the standard scattering formalism from the two-body sector falls short, without going into too much detail, as these concepts do not enter this work directly. It is nevertheless important to be aware of them when dealing with many-body scattering with the help of other methods and what their restrictions are. The field which concerns itself with treating all possible channels that a certain system can have, nucleonic or others, is referred to as *few-body* physics. The methods developed within this field allow for treating bound as well as scattering states, with the focus on calculating the matrix elements of the transition operator  $\mathcal{T}$ , given in equation (3.21). The ability to calculate these matrix elements gives access to scattering cross-sections and allows for a close connection to scattering experiments.

Additionally, give an overview of continuum physics and scattering in *ab initio* nuclear structure, the *many-body* regime, which puts the methods presented in chapters 6 and 8 into context. In contrast to the few-body methods, the focus in the many-body application is the calculation of wave functions, primarily in the bound state-regime, with increasing interest to connect continuum and reactions with the long-standing and successful methods of *ab initio* nuclear structure. The difference in target observables in bound-state and continuum calculations make the unification of well established methods not straightforward. On overview of the current efforts to treat continuum physics consistently, and to bring *ab initio* few- and many-body methods together for a closer connection to experiment, is discussed in reference [JLA<sup>+</sup>19].

We would like to point out two things. Firstly, the motivation for the explicit  $A$ -body treatment is to find exact analytical relations of the three or even general  $A$ -body problem, but the use of approximative methods, i.e., selective treatment of one or few scattering channels, is still a viable approach. Secondly, even though the two-body formalism in deriving scattering equations is not directly applicable in the  $A \geq 3$  case, many of the interpretations or analytic continuations of the derived operators still remain in effect. In our case especially of interest are resonances. These still correspond to poles of the  $A$ -body  $S$ -matrix [New82]. The microscopic reason for the occurrence of a resonance can be of more complex nature, and must not necessarily be due to an angular-momentum barrier. In a similar fashion, this already occurs in multi-channel scattering, with, e.g., Feshbach resonances. However, it should be kept in mind that still only two scattering partners are active, with coupled-channels giving rise to other causes for resonances. This formalism still breaks down when applied to three or more scatterers.

### 4.1. Limits of Two-Body Scattering and the Three-Body Problem

We highlight the limitations of two-body scattering following the references [New82, KKH89, FM93]. When trying to solve the scattering problem, we want to find a solution to the Lippmann-Schwinger equation, given in equation (3.16) as

$$|\psi\rangle = |\psi_{\text{in}}\rangle + G_0^+ V |\psi\rangle, \quad (4.1)$$

#### 4. Scattering Theory – Many-Body Scattering

or directly for the Green's function in equation (3.17),

$$\begin{aligned} G &= G_0 + G_0 V G \\ &= G_0 + G_0 V G_0 + G_0 V G_0 V G_0 + \dots, \end{aligned} \quad (4.2)$$

where  $G_0$  is defined in equation (3.13) as

$$G_0 \equiv G_0^+ = (E - H_0)^{-1}, \quad (4.3)$$

with  $H_0$  being the kinetic energy. For the sake of simplicity, the potential  $V$  is a two-body interaction only. As the Lippmann-Schwinger equation is the integral equation of the Schrödinger equation, the term  $G_0 V$  is also referred to as the integration kernel. The failure of the Lippmann-Schwinger equation for three bodies is connected to it not belonging to a very specific class of kernels when introducing three interacting particles, which we show in following.

For a scattering system, repositioning of the whole system should not change anything, which is the requirement of translational invariance of the whole system, i.e., the Hamiltonian has to commute with the total momentum  $P$

$$[H, P] = 0. \quad (4.4)$$

The same has to be true for the kinetic energy operator and the interaction potential individually, and consequently also for  $G_0 V$

$$[H_0, P] = [V, P] = [G_0 V, P] = 0. \quad (4.5)$$

When considering the matrix element representation of the kernel in some basis containing the total momentum

$$\langle \dots P \dots | G_0 V | \dots P' \dots \rangle \propto \delta(P - P'), \quad (4.6)$$

the total momentum is naturally conserved, ensured by the appearance of a  $\delta$ -distribution. The crucial point in being able to solve the Lippmann-Schwinger equation is that the kernel  $G_0 V$  needs to be a compact operator [New82]. If that is the case, then the integral is of *Fredholm*-type, enabling the use of respective solving techniques for this class of integrals. The spectrum of a compact operator is unambiguously separated into a discrete (bound-state) and continuum part. This guarantees that the solution  $|\psi\rangle$  exists and is unique w.r.t to total momentum and energy. Being of Fredholm-type also implies square integrability [New82, AW13]. However, an operator containing a  $\delta$ -distribution cannot be compact. Even though the reverse is not necessarily true, we want to assume this to be the case in this context, i.e., if no  $\delta$ -distributions appear in the operator or within the first iterations of it in terms of an expansion, then it is compact. For proof of these statements, see e.g. references [New82, Joa76, FM93, AW13].

The appearance of a total momentum  $\delta$ -distribution is already the case in two-body scattering in section 3.3. However, every operator is conserving the total momentum, and consequently the  $\delta$ -distribution is avoidable by considering the scattering event at a fixed total momentum. Is the total momentum fixed at zero, we are in the centre-of-mass frame.

Going over to a three particle system with a two-body potential

$$\begin{aligned} V &= \sum_{i < j} V_{ij} \\ &= V_{12} + V_{13} + V_{23}, \end{aligned} \quad (4.7)$$

it is possible to fix the total momentum  $P$  again. However, the individual two-body potentials are conserving the single-particle momentum of the uninvolved particle, the spectator, as well as the relative Jacobi momentum  $\pi_i$  of the accordingly defined two-body partition. The Jacobi coordinates and momenta are introduced in equation (5.13) and equation (5.14), respectively. In some momentum representation, the interaction between particle 1 and 2, with Jacobi momentum  $\pi_1$  in a configuration  $(1+2)_{\xi_1, \pi_1} + 3$ , must be of the form

$$\langle k \pi_1 p_3 | V_{12} | k' \pi_1' p_3' \rangle \propto \delta(\pi_1 - \pi_1') \delta(p_3 - p_3'), \quad (4.8)$$

with  $p_3$  being the single-particle momentum of particle 3, and  $k$  a collective index for all other momentum like variables. In the same Jacobi configuration, at least the unaffected particle leads to another  $\delta$ -distribution

$$\langle k \pi_1 p_i | V_{kj} | k' \pi_1' p_i' \rangle \propto \delta(p_i - p_i') \quad \text{with } i \neq k, j. \quad (4.9)$$

In effect, the total potential  $V$  is a sum of parts with  $\delta$ -distribution w.r.t. to different momenta, and thus cannot simply be removed by fixing a global momentum. The potential is, therefore, a sum of non-compact operators, and as such not compact. Consequently, the standard Lippmann-Schwinger equation is not unique in its solution.

It is owed to Faddeev, who showed first that there is a way to find a kernel of Fredholm-type [Fad61], that today a variety of methods exist to construct a unique solution, e.g., references [AGS67, Wei64, HKL74].

We give the main result of the Faddeev method as found in reference [KKH89]. From the appearance of the  $\delta$ 's in equation (4.9) due to the spectator, one might try to rearrange the Lippmann-Schwinger equation in equation (4.2) in such a way that all particles are always “connected” to each other. This is the Faddeev approach. We obtain such a rearrangement by rewriting equation (4.2)

$$G = G_0 + G^{(1)} + G^{(2)} + G^{(3)}, \quad (4.10)$$

where the  $G^{(i)}$  are defined as

$$G^{(i)} = G_0 V_i G, \quad (4.11)$$

with the potential index in equation (4.7) renamed by  $V_{12} \rightarrow V_1$ ,  $V_{13} \rightarrow V_2$  and  $V_{23} \rightarrow V_3$ . The individual particle partition Green's functions, denoted with a subscript, are given by

$$G_i = (E - H_0 - V_i)^{-1} \quad (4.12)$$

$$= G_0 + G_0 V_i G_i. \quad (4.13)$$

Inserting equation (4.10) into equation (4.11) and using general indices, we have

$$\begin{aligned} G^{(i)} &= G_0 V_i \left( G_0 + G^{(1)} + G^{(2)} + G^{(3)} \right) \\ &= G_0 V_i G_0 + G_0 V_i \left( G^{(i)} + G^{(j)} + G^{(k)} \right). \end{aligned} \quad (4.14)$$

Bringing the  $G^{(i)}$  part on the right hand side in equation (4.14) over to the left hand side, one obtains the expression

$$(1 - G_0 V_i) G^{(i)} = G_0 V_i G_0 + G_0 V_i \left( G^{(j)} + G^{(k)} \right). \quad (4.15)$$

Multiplying from the left with the inverse of the new term on the left hand side, we get

$$\begin{aligned} G^{(i)} &= (1 - G_0 V_i)^{-1} G_0 V_i G_0 + (1 - G_0 V_i)^{-1} G_0 V_i \left( G^{(j)} + G^{(k)} \right) \\ &\stackrel{(4.13)}{=} G_i V_i G_0 + G_i V_i \left( G^{(j)} + G^{(k)} \right) \\ &= G_i - G_0 + G_i V_i \left( G^{(j)} + G^{(k)} \right). \end{aligned} \quad (4.16)$$

#### 4. Scattering Theory – Many-Body Scattering

These are the Faddeev equations, which can be cast into matrix form

$$\begin{pmatrix} G^{(1)} \\ G^{(2)} \\ G^{(3)} \end{pmatrix} = \begin{pmatrix} G_1 - G_0 \\ G_2 - G_0 \\ G_3 - G_0 \end{pmatrix} + \begin{pmatrix} 0 & G_1 V_1 & G_1 V_1 \\ G_2 V_2 & 0 & G_2 V_2 \\ G_3 V_3 & G_3 V_3 & 0 \end{pmatrix} \begin{pmatrix} G^{(1)} \\ G^{(2)} \\ G^{(3)} \end{pmatrix}. \quad (4.17)$$

The matrix representation highlights the initial motivation of the Faddeev approach. The missing diagonal entries show that due to this rearrangement, the isolated particle cases do not occur after one iteration of the equations (4.16) and (4.17).

From this result, we are able to compute scattering observables. For example, the earlier mentioned matrix elements of the  $\mathcal{T}$ -matrix, giving access to the amplitudes between different scattering channels and cross sections. The generalization to the  $A$ -body problem was presented by Yakubovsky [Yak67]. For an extensive introduction, we refer to, e.g. [FM93].

## 4.2. Many-Body Methods in the Continuum

The methods related to finding exact formulas for the  $A$ -body problem, like, e.g., the Faddeev method, described briefly in section 4.1, are limited in the degrees of freedom they can computationally accommodate. Calculations are limited so far to  $A = 5$  in the nucleonic sector [Laz18a, Laz18b, LHC19]. The addition of another nucleon requires substantial development efforts.

The aim of *ab initio* nuclear structure is the connection to fundamental nuclear forces rooted in QCD, with systematic improvability. It is, therefore, desirable to use the existing methods developed in this field to treat continuum effects, which both improves the description of shallow bound states, as well as allowing the computation of reaction phenomena and nuclear resonances.

Some of the most promising advancements to include continuum phenomena in *ab initio* nuclear structure are based on using the Resonating Group Method (RGM) [TLT78], the Berggren basis [Ber68], or combinations of the two. From our point of view the focus lies on extensions of the No-Core Shell Model (NCSM), introduced in chapter 5, which is a powerful tool in *ab initio* nuclear structure for the calculation of bound states, and extensively used within this work, see chapters 7 and 9.

The NCSM/RGM [QN08, QN09, NRQ11] uses the RGM to calculate relative motion wave functions of sub-clusters. The eigenstates of the sub-clusters are calculated with the NCSM. The number of included sub-clusters determines the possible scattering and reaction channels that can be described. The RGM can be combined with other methods that calculate the eigenstates of the sub-clusters, and in that way provides a unified approach to bound and continuum states. The NCSM with Continuum (NCSMC) [BNQ13a, BNQ13b] is an extension of the NCSM/RGM and constructs an overcomplete basis from the NCSM and RGM states.

The combination of the Berggren basis with the NCSM results in the so-called No-Core Gamow Shell Model (NCGSM) [PRM<sup>+</sup>13]. It explicitly includes scattering states into the many-body basis.

Another method to connect bound state calculations with the continuum is the Harmonic Oscillator Representation of Scattering Equations (HORSE), which is introduced in detail in chapter 6 and applied to the tetra-neutron in chapter 7.

Particularly well suited to obtain resonance parameters from bound state methods is the Analytic Continuation in the Coupling Constant (ACCC), which is also used to investigate the tetra-neutron. The method is described in chapter 8 and results are shown in chapter 9.

## 5. No-Core Shell Model

The No-Core Shell Model (NCSM) [ZBJ<sup>+</sup>93, PNB09, BNV13] is a powerful many-body method in the field of *ab initio* nuclear structure. It treats all nucleons as active degrees of freedom, hence the “No-Core” in the name. This separates it from the Valence-Space Shell Model, which keeps a static core and only a few valence nucleons contribute to the dynamics of the system. The NCSM is conceptually simple. It relies on a basis expansion, and subsequent diagonalization to obtain the eigenvalues and eigenvectors of the investigated system. In its more common formulation, the NCSM uses single-particle Slater determinants (SD). This allows a straightforward antisymmetrization. The simplicity comes, however, at a price. The centre-of-mass contribution is carried along until the end, and the total angular momentum is no good quantum number, leading to higher computational cost, as the matrix dimension scales factorially with the particle number. The large dimensions make the full diagonalization of the matrix unfeasible, requiring iterative approaches, like e.g., the Lanczos algorithm [Lan50].

The SD formulation is a representation of all possible configurations allowed within specified truncations. As such, the nuclear Valence-Space Shell Model, the NCSM and variations of these are part of the family of Configuration Interaction (CI) type many-body methods.

An alternative in the NCSM is the use of Jacobi coordinates, which significantly reduces model space size by explicitly separating the centre-of-mass and only treating the intrinsic part, and keeping the total angular momentum  $J$  well defined by employing an angular-momentum-coupled basis. This is counterbalanced by the costly antisymmetrization and embedding of (NN- and 3N-) interaction matrix elements into an  $A$ -body space. The NCSM is variational, thus giving an upper bound for the true eigenenergies.

The *ab initio* NCSM is constructed from the  $A$ -body Hamiltonian, which reads [PNB09]

$$H = T_{\text{rel}} + V = \frac{1}{A} \sum_{i < j} \frac{(\vec{p}_i - \vec{p}_j)^2}{2m_N} + \sum_{i < j} V_{ij}^{\text{NN}} + \sum_{i < j < k} V_{ijk}^{\text{3N}}, \quad (5.1)$$

where,  $V_{ij}^{\text{NN}}$  and  $V_{ijk}^{\text{3N}}$  denote the two and three nucleon potentials, and  $m_N$  the average nucleon mass. In theory, up to  $A$ -body interaction terms can be present. We aim to solve the stationary Schrödinger equation

$$H |\Psi_\nu\rangle = E_\nu |\Psi_\nu\rangle, \quad (5.2)$$

with eigenvectors  $|\Psi_\nu\rangle$  and energies  $E_\nu$ . The index  $\nu$  summarizes all relevant quantum numbers, the total angular momentum  $J$  and its projection  $M_J$ , parity  $\pi$ , isospin  $T$  and projection  $M_T$ ,  $\nu = (J, M_J, \pi, T, M_T)$ . The state  $|\Psi_\nu\rangle$  is expanded in a suitable orthonormal basis, which reads

$$\begin{aligned} |\Psi_\nu\rangle &= \sum_i |\Phi_i\rangle \langle \Phi_i | \Psi_\nu\rangle \\ &= \sum_i c_i^\nu |\Phi_i\rangle. \end{aligned} \quad (5.3)$$

With this expansion, the Schrödinger equation takes the form

$$\sum_j \langle \Phi_i | H | \Phi_j\rangle c_j^\nu = E_\nu c_i^\nu, \quad (5.4)$$

## 5. No-Core Shell Model

with expansion coefficient  $c_i^\nu$ . We can write the Hamiltonian as matrix element

$$\langle \Phi_i | H | \Phi_j \rangle = H_{ij}, \quad (5.5)$$

which leads to the alternative formulation in explicit matrix form

$$\begin{pmatrix} H_{11} & H_{12} & \dots \\ H_{21} & H_{22} & \dots \\ \vdots & \vdots & \ddots \end{pmatrix} \begin{pmatrix} c_1^\nu \\ c_2^\nu \\ \vdots \end{pmatrix} = E_\nu \begin{pmatrix} c_1^\nu \\ c_2^\nu \\ \vdots \end{pmatrix}. \quad (5.6)$$

The basis expansion needs to be truncated in order to obtain a finite problem. A distinguishing feature of the *ab initio* NCSM is its truncation scheme in combination with harmonic oscillator (HO) basis states. The basis is truncated by limiting the total allowed HO excitation energy, denoted with  $N_{\max}$ , meaning that the NCSM model space is spanned by all configurations with excitation energy smaller or equal to  $N_{\max} \hbar \Omega$ . This is shown schematically in figure 5.1 for two configurations of  $^{10}\text{B}$ . The  $N_{\max} = 0$  configuration for open-shell nuclei is not unique, unlike in the closed-shell case. The No-Core character is indicated by showing a configuration including excitations from all energy levels.

A very important property of the HO basis and the  $N_{\max}$ -truncation is the translation invariance of the total Hamiltonian, while simultaneously allowing the use of single-particle coordinates [PNB09]. The total wave function can be separated into the centre-of-mass and the intrinsic wave functions

$$|\Psi_\nu\rangle = |\Psi_\nu^{\text{CoM}}\rangle \otimes |\Psi_\nu^{\text{int}}\rangle. \quad (5.7)$$

Any other truncation scheme or other basis functions with single-particle coordinates do not allow this separation.

### 5.1. Single-Particle $m$ -Scheme NCSM

We refer to the standard form of the NCSM as the  $m$ -scheme. In this scheme, the basis is spanned by single-particle HO states

$$|a\rangle = |n_a, (\ell_a s_a) j_a m_{j_a}, t_a m_{t_a}\rangle, \quad (5.8)$$

with radial quantum number  $n$ , angular momentum  $\ell$  and spin  $s$ , which couple to total angular momentum  $j$  with projection  $m_j$  and the isospin  $t$  with projection  $m_t$ . In the nucleonic case in which we are interested, spin and isospin can only have the value  $s = t = \frac{1}{2}$ . The energy quantum number is given by

$$e_a = 2n_a + \ell_a. \quad (5.9)$$

An antisymmetric  $A$ -body state is realized by writing them as Slater determinants

$$|abc\dots x\rangle_a = \sqrt{A!} \mathcal{A} |a\rangle \otimes |b\rangle \otimes |c\rangle \otimes \dots \otimes |x\rangle, \quad (5.10)$$

where  $\mathcal{A}$  is the antisymmetrizer. The basis constructed from such states is diagonal in the total sum of the projection quantum numbers

$$M = \sum_i m_{j_i}, \quad M_T = \sum_i m_{t_i}, \quad (5.11)$$

and the parity  $\pi$ , where the name  $m$ -scheme originates from [PNB09].

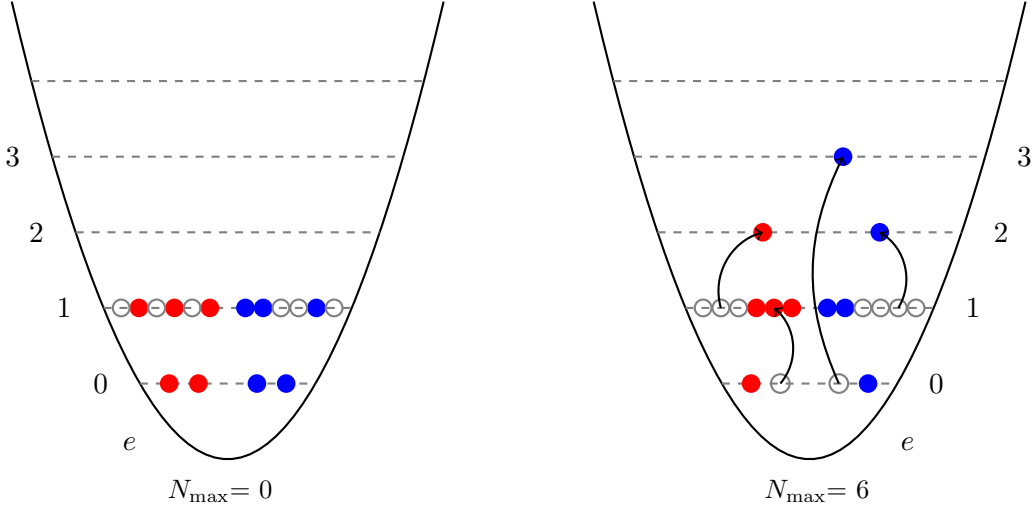


Figure 5.1.: Truncation scheme of the NCSM in the case of  $^{10}\text{B}$ . The left plot shows one possible configuration of lowest energy. On the right, one possible configuration with excitation energy of  $6\hbar\Omega$ . Neutrons and protons depicted as red and blue dots, respectively, unoccupied states depicted as open circles.

## 5.2. Jacobi-NCSM

A variant of the NCSM is the formulation with relative-coordinate HO functions, the Jacobi coordinates to be precise [Jac42]. In the low-mass sector, the Jacobi-NCSM allows for larger model spaces and full diagonalization. It is of relevance to us to obtain large model spaces and construct effective four-body potentials directly from eigenvectors, which is discussed in section 8.3.

For  $A$  particles of equal mass, the Jacobi coordinates can be constructed iteratively from the single-particle coordinates, by first defining the centre-of-mass coordinate  $\vec{\xi}_0$

$$\vec{\xi}_0 = \sqrt{\frac{1}{A}} \sum_{i=1}^A \vec{r}_i. \quad (5.12)$$

The first two particles with single-particle coordinates  $\vec{r}_1$  and  $\vec{r}_2$  define the first Jacobi coordinate  $\vec{\xi}_1$ . Between the centre-of-mass of  $\vec{r}_1$  and  $\vec{r}_2$  and the third particle is the the next Jacobi coordinate defined, and so on up to  $A$  particles and  $A - 1$  Jacobi coordinates. This reads

$$\begin{aligned} \vec{\xi}_1 &= \sqrt{\frac{1}{2}} (\vec{r}_1 - \vec{r}_2) \\ &\vdots \\ \vec{\xi}_k &= \sqrt{\frac{k}{k+1}} \left( \left( \frac{1}{k} \sum_{i=1}^k \vec{r}_i \right) - \vec{r}_{k+1} \right). \end{aligned} \quad (5.13)$$

By identical construction, one gets the Jacobi momenta

$$\vec{\pi}_k = \sqrt{\frac{k}{k+1}} \left( \left( \frac{1}{k} \sum_{i=1}^k \vec{p}_i \right) - \vec{p}_{k+1} \right). \quad (5.14)$$

Note that Jacobi coordinates can be constructed in various ways, and the particles can have different masses. The transformation from one set to another is achieved with Raynal-Revai

## 5. No-Core Shell Model

coefficients [RR70], which are related to the Talmi-Moshinsky transformations of the HO [Mos59, Smi61].

The advantage of Jacobi coordinates is the direct separation of the centre-of-mass from the intrinsic part. The matrix elements obtained in this basis do not contain any centre-of-mass contributions, which drastically reduces the number of matrix elements compared to the  $m$ -scheme. At the same time, the total HO energy must remain the same, and the form of the HO does not change between the single-particle and the relative Jacobi coordinates

$$H_{\text{HO}} = \sum_{i=1}^A \left( \frac{\vec{p}_i^2}{2m} + \frac{1}{2} m \Omega^2 \vec{r}_i^2 \right) = \sum_{i=0}^{A-1} \left( \frac{\vec{\pi}_i^2}{2m} + \frac{1}{2} m \Omega^2 \vec{\xi}_i^2 \right). \quad (5.15)$$

Harmonic oscillator matrix elements are constructed again by iteratively adding a new particle to the previously constructed ones. The disadvantage in using Jacobi coordinates is the involved antisymmetrization, which has to be redone every time a new particle is added. The antisymmetrizer has to be diagonalized in the respective  $A$ -body basis. The eigenvectors with eigenvalue 1 belong to the desired antisymmetric state. Any other eigenvectors are not of interest and can be discarded. More explicitly, starting with a two-body system, the intrinsic HO matrix elements read [NKB00, Bin10, Sch18]

$$|N_1(L_1 S_1) J_1 M_{J_1}, T_1 M_{T_1}\rangle, \quad (5.16)$$

where the HO quantum numbers  $N_1$  and  $L_1$  are defined w.r.t. to the Jacobi coordinates  $\vec{\xi}_1$  and  $\vec{\pi}_1$ , and  $L_1$  couples with the total spin  $S_1$  of the two particles to the total angular momentum  $J_1$ . The antisymmetry is obtained through particle permutation, leaving only states with

$$(-1)^{L_1+S_1+T_1} = -1, \quad (5.17)$$

to be taken into consideration for the antisymmetric states. Adding a third particle, we obtain the partially antisymmetric state (under exchange of the first two particles)

$$\begin{aligned} |N_1 N_2, [(L_1 S_1) J_1, (L_2 S_2) J_2] J_{12} M_{J_{12}}, (T_1 M_{T_1}) T_{12} M_{T_{12}}\rangle &\equiv |E_{12} \nu_{12} J_{12} M_{J_{12}} T_{12} M_{T_{12}}\rangle \\ &\equiv |E_{12} \nu_{12} J_{12} T_{12}\rangle, \end{aligned} \quad (5.18)$$

where the momenta  $L_2, S_2$  and  $J_2$  belong to the third particle, where  $L_2$  and  $S_2 = \frac{1}{2}$  couple to  $J_2$ , which in turn couples with  $J_1$  to  $J_{12}$ . In the short hand notation, with the collective index  $\nu_{12} = \{N_1, L_1, S_1, J_1, T_1, N_2, L_2, J_2\}$  and  $E_{12} = 2N_1 + L_1 + 2N_2 + L_2$ , the projection quantum numbers were dropped.

To obtain a fully antisymmetric state w.r.t. particle exchange of all three particles, the antisymmetrizer is diagonalized in the non-antisymmetric basis

$$\langle E'_{12} \nu'_{12} J'_{12} T'_{12} | \mathcal{A} | E_{12} \nu_{12} J_{12} T_{12} \rangle. \quad (5.19)$$

The matrix is block diagonal in  $E_{12}$ ,  $J_{12}$  and  $T_{12}$ . For the explicit form and derivation, see references [Bin10, NKB00]. The fully antisymmetric state is given as an expansion in the partially symmetric basis by

$$|E_{12} i_{12} J_{12} T_{12}\rangle_a = \sum_{\nu_{12}} c_{i_{12}, \nu_{12}}^{E_{12} J_{12} T_{12}} |E_{12} \nu_{12} J_{12} T_{12}\rangle. \quad (5.20)$$

The expansion coefficients  $c_{i_{12}, \nu_{12}}^{E_{12} J_{12} T_{12}}$  are the so-called coefficient of fractional parentage, as they are already *fractionally* antisymmetric under  $1 \leftrightarrow 2$  exchange. The index  $i_{12}$  labels each antisymmetric state. It does not correspond to physical quantum numbers and only counts

eigenvectors with eigenvalue 1.

Repeating the procedure, we get an antisymmetric four-body state

$$|E_{123} i_{123} J_{123} T_{123}\rangle_a = \sum_{\nu_{123}} c_{i_{123}, \nu_{123}}^{E_{123} J_{123} T_{123}} |E_{123} \nu_{123} J_{123} T_{123}\rangle. \quad (5.21)$$

We refer again to reference [NKB00] for the generalized derivation of the  $A$ -body antisymmetrizer matrix elements and references [Sch18, Sch13] for the explicit treatment of the four-body case. In practice, the diagonalization of the antisymmetrizer becomes prohibitively expensive at  $A \sim 6$ , which limits the Jacobi-NCSM to the lightest nuclei.

In this work, we employ the Jacobi-NCSM up to large  $N_{\max}$  model spaces to obtain the required states for the analysis performed in chapters 7 and 9.



## 6. J-Matrix and Harmonic Oscillator Representation of Scattering Equations

The description of continuum states usually requires the capability to accurately treat the long-range behaviour of the wave functions. To be able to compute any kind of interacting system, the problem has to be discretized with the help of a basis. Hence, the solving method of choice should naturally incorporate adequate basis functions which can provide the correct asymptotic behaviour, if not completely, in a systematically improvable approximation. This requirement seems to make the treatment of scattering states within Configuration Interaction (CI) methods, discussed in chapter 5, which span the Hamilton matrix on a  $L^2$  basis set, impossible. Contrary to this, the so-called stabilization method [HT70], exploited the quasi-stationary character of resonance states to expand them in a  $L^2$  basis and obtain precise results. This can be considered to be the precursor to the  $J$ -matrix method discussed in this chapter.

The  $J$ -matrix, short for Jacobi-matrix, was first introduced in atomic physics in 1973 [HY73, YF75]. The name derives from the fact that a matrix  $J = T - E$ , where  $T$  is the kinetic energy, becomes tridiagonal in a specific  $L^2$ -basis representation [HY73]. This is the Jacobi-matrix of linear algebra, not to be confused with the first-order partial derivative matrix.

The application of the  $J$ -matrix method to problems of nuclear physics was first reported in the 1980's [Fil81, SN82, JRZ85]. It was also combined with the Resonating Group Method, which leads to algebraic expressions, hence it is referred to as Algebraic RGM [VNAB01]. The  $J$ -matrix has also been used in the reverse scattering formalism to construct effective (two-body) interactions [SVMW07]. A summary and reprint of the fundamental papers contributing to the evolution of the  $J$ -matrix is given as a textbook [AYHA08]. A defining aspect of the  $J$ -matrix is reminiscent of the  $\mathcal{R}$ -matrix method, discussed in the following. It is important to note that formally, the  $J$ -matrix is equivalent to the Feshbach method [Fes62], as has been shown in reference [Yam82].

Following the collection of papers in reference [AYHA08], the underlying principle of the  $J$ -matrix and its different special cases, arises from the general idea that the exact solution, in abstract eigenvalue notation

$$(T + V - E) |\psi\rangle = 0, \quad (6.1)$$

can be brought into a matrix representation by choosing some basis functions. The expansion in the most general bound state basis  $|\phi_n\rangle$  of the form

$$|\psi\rangle = \sum_{n=0}^{\infty} b_n |\phi_n\rangle, \quad (6.2)$$

where  $b_n = \langle \phi_n | \psi \rangle$  are the expansion coefficients, leads to the matrix representation

$$\sum_{n=0}^{\infty} \langle \phi_m | T + V - E | \phi_n \rangle b_n = 0. \quad (6.3)$$

Equation (6.3) is in the general case not fulfilled by scattering states, due to the bound state basis lacking the correct asymptotics. Evidently, this is not the case when considering only

## 6. *J*-Matrix and Harmonic Oscillator Representation of Scattering Equations

bound states, as this is precisely the approach of CI methods, which arrive at their results by truncating the infinite sum at some parameter. In the example of the No-Core Shell Model, this would be  $N_{\max}$ .

Considering as bound state basis the special case of Laguerre or Hermite (HO) polynomials, the expansion

$$|\psi^0\rangle = \sum_{n=0}^{\infty} b_n^0 |\phi_n\rangle, \quad (6.4)$$

solves the free problem of the kinetic energy  $H_0 = T$

$$\langle \phi_m | T - E | \psi^0 \rangle = 0, \quad (6.5)$$

with the special property that the solution takes the form of a tridiagonal matrix. To obtain a solution when considering an interaction, the potential is only taken up to a finite range in the  $\mathcal{N} \times \mathcal{N}$  matrix, where  $\mathcal{N}$  is the truncation parameter. This is shown schematically in figure 6.1.

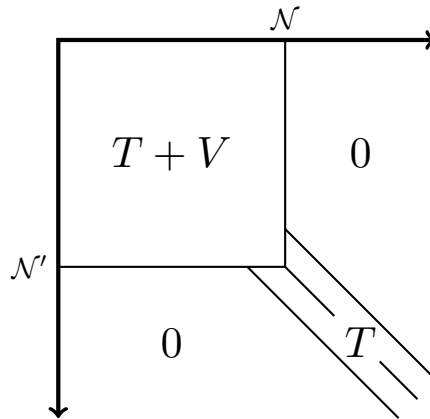


Figure 6.1.: Truncation scheme cartoon. The inner region consists of the truncated kinetic term plus the potential term.

The eigenvalue problem with the truncated potential  $V^{\mathcal{N}}$  reads

$$\langle \phi_m | T + V^{\mathcal{N}} - E | \psi^0 \rangle = 0, \quad (6.6)$$

and is exactly solvable, due its finite model space.

The sought solution to this equation must be of the usual form of a scattering solution, that is it can be written in terms of incoming and outgoing waves, denoted with  $I_n$  and  $O_n$  respectively. The solutions are related by the scattering matrix  $S$ , and are linear combinations of the regular and irregular free solution, and the scattering matrix, see equation (3.61) and equation (3.67). The general solution reads

$$\begin{aligned} |\psi^0\rangle &\sim N(k) (I_n + S O_n) \\ &= N(k) ((c_n - i s_n) + S(c_n + i s_n)). \end{aligned} \quad (6.7)$$

Here,  $N(k)$  is some normalizing function. The  $s_n$  and  $c_n$  are the expansion coefficient of the regular (sine like) and irregular (cosine like) in the tridiagonal  $L^2$ -integrable basis, respectively. Analogous to the discussion in section 3.5, we can obtain an expression for the Green's function and the scattering matrix, which takes the form

$$S(E) = \frac{I_N + G_{\mathcal{N}\mathcal{N}} T_{\mathcal{N},\mathcal{N}+1} I_{\mathcal{N}+1}}{O_N + G_{\mathcal{N}\mathcal{N}} T_{\mathcal{N},\mathcal{N}+1} O_{\mathcal{N}+1}}. \quad (6.8)$$

The Green's function matrix representation is given by  $G_{n,n'}$ ,  $I_n$  and  $O_n$  as above. Alternatively, the kinetic part can be absorbed into the Green's function

$$S(E) = \frac{I_N + G_{NN} I_{N+1}}{O_N + G_{NN} O_{N+1}}. \quad (6.9)$$

This is solely a matter of convention for ease of readability and to remain consistent with the usual definition. In the following section, we derive the relevant expression for the case of harmonic oscillator functions.

## 6.1. Harmonic Oscillator Representation of Scattering Equations

The  $J$ -matrix formalism in the harmonic oscillator basis is called the Harmonic Oscillator Representation of Scattering Equations, or HORSE, for short. The use of HO functions, together with the  $J$ -matrix truncation scheme, makes this approach an ideal candidate for combining it with NCSM-type methods. First applications of the HORSE method in nuclear physics were published in the 1980's, e.g., [Fil81, SN82, JRZ85], and have been further developed in, and used in conjunction with, nuclear CI calculations [BMS<sup>+</sup>00, ZSS98, SMZ<sup>+</sup>04].

Following the above mentioned papers, we start with the full solution, equation (3.48), as presented in in section 3.3

$$\psi_{\vec{k}}(\vec{r}) = \sum_{\ell=0}^{\infty} \sum_{m=-\ell}^{\ell} \bar{R}_{k,\ell}(r) Y_{\ell}^m(\theta, \phi), \quad (6.10)$$

where  $\bar{R}_{k,\ell}(r)$  is the radial wave function, and  $Y_{\ell}^m(\theta, \phi)$  are the spherical harmonics, depending on the angles  $\theta$  and  $\phi$ , with  $k$  as the relative motion momentum, the angular momentum  $\ell$  and its projection quantum number  $m$ . The overline  $\bar{R}$  solely serves to better differentiate it from the radial HO function. We are interested in the radial part, fulfilling the radial Schrödinger equation (3.49)

$$\left( -\frac{1}{r^2} \frac{d}{dr} \left( r^2 \frac{d}{dr} \right) + \frac{\ell(\ell+1)}{r^2} + \frac{2\mu}{\hbar^2} V(r) - k^2 \right) \bar{R}_{k,\ell}(r) = 0. \quad (6.11)$$

Expanding the relative motion radial wave function  $\bar{R}_{k,\ell}$  in an infinite series of radial HO functions  $R_{n\ell}$ , depending on the radial quantum number  $n$  and the relative angular momentum  $\ell$ , we have

$$\bar{R}_{k,\ell}(r) = \sum_{n=0}^{\infty} a_{n\ell}(k) R_{n\ell}(r) \quad (6.12)$$

$$= \sum_{N=N_{\min}, N_{\min}+2, \dots, \infty} a_{N\ell}(E) R_{N\ell}(r). \quad (6.13)$$

Here,  $N$  is the principle quantum number

$$N = 2n + N_{\min}. \quad (6.14)$$

In the case of a single particle in an harmonic oscillator potential, we have

$$N_{\min} = \ell, \quad (6.15)$$

## 6. J-Matrix and Harmonic Oscillator Representation of Scattering Equations

otherwise  $N_{\min}$  corresponds to the minimal HO configuration. The new unknowns are the expansion coefficient  $a_{n\ell}(k)$ . The form of equation (6.13) is given to already make the connection to the NCSM visible. The HO radial function has the explicit form

$$R_{n\ell}(r) = (-1)^n \sqrt{\frac{2\Gamma(n+1)}{a_{\text{HO}}\Gamma(n+\ell+3/2)}} \left(\frac{r}{a_{\text{HO}}}\right)^{\ell+1} \exp\left[-\frac{r^2}{2a_{\text{HO}}^2}\right] L_n^{\ell+1/2}\left(\frac{r^2}{a_{\text{HO}}^2}\right), \quad (6.16)$$

where  $L_n^\alpha(z)$  is the associated Laguerre polynomial, the HO length  $a_{\text{HO}} = \sqrt{\frac{\hbar}{\mu\Omega}}$ ,  $\mu$  is the reduced mass. This direct relation of the angular momentum dictating the lowest possible energy configuration no longer holds in the many-body case. There, we have to evaluate  $N_{\min}$  for each investigated system. We, therefore, continue to use the formulation with the radial quantum number only, as it is more accessible, leads to more compact notation, and the derived equations can easily be translated to the energy quantum number by proper substitution, taking the correct  $N_{\min}$  into account.

The unknowns to be determined are the expansion coefficients  $a_{n\ell}(k) \rightarrow a_{n\ell}(E)$  of equation (6.12), where we change to an energy notation. They can be obtained by scalar multiplication of the radial solution  $\bar{R}_{k,\ell}(r)$  with the radial HO function

$$\begin{aligned} \int_0^\infty dr r^2 \bar{R}_{k,\ell}(r) R_{n\ell}(r) &= \int_0^\infty dr r^2 \sum_{n'=0}^\infty a_{n'\ell}(E) R_{n'\ell}(r) R_{n\ell}(r) \\ &= \sum_{n'=0}^\infty a_{n'\ell}(E) \delta_{nn'} = a_{n\ell}(E). \end{aligned} \quad (6.17)$$

We arrive at the equations which will define our new problem to solve by inserting the expansion of equation (6.12) into the full Schrödinger equation, which then reads

$$\int d^3r \sum_{n'=0}^\infty R_{n\ell}(r) Y_\ell^{m*}(\theta, \phi) H a_{n'\ell}(E) R_{n'\ell}(r) Y_\ell^m(\theta, \phi) = E \int d^3r \sum_{n'=0}^\infty R_{n\ell}(r) Y_\ell^{m*}(\theta, \phi) \quad (6.18)$$

$$\begin{aligned} &\times a_{n'\ell}(E) R_{n'\ell}(r) Y_\ell^m(\theta, \phi) \\ &= E a_{n\ell}(E), \end{aligned} \quad (6.19)$$

where relation (6.17) is used in the last line. Here, we write in analogy to  $H_{nn'} = \langle n\ell m | H | n'\ell m \rangle$  the same for the potential  $V_{nn'}$ .

The left hand side is the expansion of the Hamiltonian in the HO basis

$$\begin{aligned} \int d^3r \sum_{n'=0}^\infty R_{n\ell}(r) Y_\ell^{m*}(\theta, \phi) H a_{n'\ell}(E) R_{n'\ell}(r) Y_\ell^m(\theta, \phi) &= E a_{n\ell}(E) \\ \sum_{n'=0}^\infty H_{nn'} a_{n'\ell}(E) &= E a_{n\ell}(E), \end{aligned} \quad (6.20)$$

and using

$$\langle \vec{r} | n\ell m \rangle = \langle r\theta\phi | n\ell m \rangle = R_{n\ell}(r) Y_\ell^m(\theta, \phi). \quad (6.21)$$

To solve is then a system of infinitely many algebraic equations

$$\sum_{n'=0}^\infty (H_{nn'} - \delta_{nn'} E) a_{n'\ell}(E) = 0 \quad (6.22)$$

$$\sum_{n'=0}^\infty (T_{nn'} + V_{nn'} - \delta_{nn'} E) a_{n'\ell}(E) = 0. \quad (6.23)$$

### 6.1. Harmonic Oscillator Representation of Scattering Equations

The matrix elements of the kinetic energy operator in harmonic oscillator basis read

$$T_{n,n} = \frac{\hbar\Omega}{2} \left( 2n + \ell + \frac{3}{2} \right) \quad (6.24a)$$

$$T_{n,n+1} = -\frac{\hbar\Omega}{2} \sqrt{(n+1)(n + \ell + \frac{3}{2})} \quad (6.24b)$$

$$T_{n,n-1} = -\frac{\hbar\Omega}{2} \sqrt{n(n + \ell + \frac{1}{2})} \quad (6.24c)$$

$$T_{n,n'} = 0, \quad \text{for } |n' - n| > 1. \quad (6.24d)$$

With these, the coupled equations of (6.22) become

$$a_{n-1\ell}(k)T_{n,n-1} + a_{n\ell}(E)T_{n,n} + a_{n+1\ell}(k)T_{n,n+1} + \sum_{n'=0}^{\infty} (V_{nn'} - \delta_{nn'}E) a_{n'\ell}(E) = 0. \quad (6.25)$$

The equations 6.24 are the eponymous relations of the  $J$ -matrix condition of the kinetic energy being tridiagonal. The next step is to separate the function space into an inner and outer region at which the potential is sufficiently small. The HO quantum number at which this happens is denoted with  $\mathcal{N}$ . In other words, we have

$$H_{nn'} = \begin{cases} T_{nn'} + V_{nn'} & \text{for } n, n' \leq \mathcal{N} \\ T_{nn'} & \text{for } n \text{ or } n' > \mathcal{N}. \end{cases} \quad (6.26)$$

The matrix around line and column  $(\mathcal{N}, \mathcal{N})$  looks schematically like equation (6.27).

$$\left( \begin{array}{ccc|ccc} \dots & \dots & V_{\mathcal{N}-2\mathcal{N}} & \dots & \dots & \dots & \dots & \dots \\ \dots & H_{\mathcal{N}-1\mathcal{N}-1} & H_{\mathcal{N}-1\mathcal{N}} & 0 & 0 & \dots & \dots & \dots \\ V_{\mathcal{N}\mathcal{N}-2} & H_{\mathcal{N}\mathcal{N}-1} & H_{\mathcal{N}\mathcal{N}} & T_{\mathcal{N}\mathcal{N}+1} & 0 & \dots & \dots & \dots \\ \hline \dots & 0 & T_{\mathcal{N}+1\mathcal{N}} & T_{\mathcal{N}+1\mathcal{N}+1} & T_{\mathcal{N}+1\mathcal{N}+2} & 0 & \dots & \dots \\ \dots & 0 & 0 & T_{\mathcal{N}+2\mathcal{N}+1} & T_{\mathcal{N}+2\mathcal{N}+2} & T_{\mathcal{N}+2\mathcal{N}+3} & 0 & \dots \\ \dots & \dots & \dots & 0 & \dots & \dots & \dots & \dots \end{array} \right) \quad (6.27)$$

The truncation at  $\mathcal{N}$  and assuming the potential to vanish appears analogous to the same procedure for potential of finite reach in position space. However, the potential does not vanish, but compared to the kinetic term, which grows linearly in  $n$ , as can be seen in equation (6.24), the potential decreases similar to  $1/n$  [SMMV16].

After neglecting the potential for  $n > \mathcal{N}$ , only the tridiagonal kinetic energy remains. This is the analogue case to the vanishing potential in spatial coordinates, where only the long-range, effectively free wave function remains. This fact can be written as a three term recurrence relation for the asymptotic solution

$$T_{n,n'-1} a_{n'-1,\ell}^{\text{asy}}(k) + (T_{n,n'} - E) a_{n',\ell}^{\text{asy}}(k) + T_{n,n'+1} a_{n'+1,\ell}^{\text{asy}}(k) = 0 \quad \text{for } n > \mathcal{N}. \quad (6.28)$$

This relation has two solutions, a regular one,  $s_{n\ell}$ , and an irregular solution,  $c_{n\ell}$ , whose explicit forms are known – see equations (6.39) and (6.41).

The continuity at truncation  $\mathcal{N}$  requires a matching condition, we thus combine the inner and outer region results by demanding that they are equal at  $n = \mathcal{N}$ . We obtain

$$\sum_{n'=0}^{\mathcal{N}} (H_{\mathcal{N}n'} - \delta_{\mathcal{N}n'}E) a_{n'\ell}(E) = -\delta_{\mathcal{N}\mathcal{N}} T_{\mathcal{N},\mathcal{N}+1} a_{\mathcal{N}+1,\ell}^{\text{asy}}(E). \quad (6.29)$$

## 6. $J$ -Matrix and Harmonic Oscillator Representation of Scattering Equations

With the steps above, the similarity to the  $\mathcal{R}$ -matrix is apparent. At first glance, this seems to be even identical to the  $\mathcal{R}$ -matrix approach – a truncation due to the negligible potential contributions, with  $\mathcal{N}$  being the analogue to the channel radius, which separates the position space in the radial coordinate into an outer and an inner region. While the HORSE method and the  $\mathcal{R}$ -matrix are conceptually strongly related, the space in which the separation is performed, results in a more fundamental difference. The separation in the HORSE method is done in the functional (basis) space and not in a coordinate. The position space in the  $\mathcal{R}$ -matrix is itself again expanded in a basis to obtain a mesh on which one can solve the radial Schrödinger equation. This difference in the underlying defining spaces makes it, therefore, possible to derive the  $\mathcal{R}$ -matrix equation in the HORSE formalism [BMS<sup>+</sup>00].

The matching of the inner and outer solutions allows us to express the unknown solution  $a_{n\ell}(E)$  in terms of the known asymptotic solutions  $a_{\mathcal{N}+1,\ell}^{\text{asy}}(E)$ . From the discussion in chapter 3, it follows from the equations (3.16) and (3.20), that the relation of the inner and the asymptotic solution is given by the Green's function. From equation (3.22)

$$G_0(E) = \int_0^\infty dE' \frac{\sum_\nu |\psi_0, E', \nu\rangle \langle \psi_0, E', \nu|}{E - E'}, \quad (6.30)$$

which gives the Green's function expanded in a complete basis, we already know the general form.

First, the truncation of the potential at point  $\mathcal{N}$ , while ignoring the asymptotic part, is the usual matrix eigenvalue problem, already mentioned previously, and reads

$$H |\psi_\nu\rangle = E_\nu |\psi_\nu\rangle, \quad (6.31)$$

which is similar to equation (6.4) expanded in the harmonic oscillator basis  $|n\ell m\rangle$ . For the eigenvector  $|\psi_\nu\rangle$  we have

$$\sum_{n'=0}^{\mathcal{N}} (H_{nn'} - \delta_{nn'} E_\nu) \langle n'\ell m | \psi_\nu \rangle = 0. \quad (6.32)$$

We use this relation by multiplying equation (6.29) from the left with

$$\sum_{n=0}^{\mathcal{N}} \langle \psi_\nu | n\ell m \rangle, \quad (6.33)$$

giving

$$\sum_{n=0}^{\mathcal{N}} \sum_{n'=0}^{\mathcal{N}} \langle \psi_\nu | n\ell m \rangle (H_{nn'} - \delta_{nn'} E) a_{n'\ell}(E) = - \sum_{n=0}^{\mathcal{N}} \langle \psi_\nu | n\ell m \rangle \delta_{n\mathcal{N}} T_{\mathcal{N},\mathcal{N}+1} a_{\mathcal{N}+1,\ell}^{\text{asy}}(E) \quad (6.34a)$$

$$\Rightarrow \sum_{n'=0}^{\mathcal{N}} \langle \psi_\nu | n'\ell m \rangle (E_\nu - E) a_{n'\ell}(E) = \langle \psi_\nu | \mathcal{N}\ell m \rangle T_{\mathcal{N},\mathcal{N}+1} a_{\mathcal{N}+1,\ell}^{\text{asy}}(E) \quad (6.34b)$$

$$\Rightarrow \sum_{n'=0}^{\mathcal{N}} \langle \psi_\nu | n'\ell m \rangle a_{n'\ell}(E) = \frac{\langle \psi_\nu | \mathcal{N}\ell m \rangle T_{\mathcal{N},\mathcal{N}+1} a_{\mathcal{N}+1,\ell}^{\text{asy}}(E)}{(E_\nu - E)}$$

$$\Rightarrow a_{n'\ell}(E) = \sum_{n'=0}^{\mathcal{N}} \frac{\langle n'\ell m | \psi_\nu \rangle \langle \psi_\nu | \mathcal{N}\ell m \rangle T_{\mathcal{N},\mathcal{N}+1} a_{\mathcal{N}+1,\ell}^{\text{asy}}(E)}{(E_\nu - E)}. \quad (6.34c)$$

Comparing the right hand side of equation (6.34c) with the known form of the expanded Green's function (6.30), we can write it as

$$G_{nn'} = - \sum_{\nu=0}^{\mathcal{N}} \frac{\langle nlm | \psi_{\nu} \rangle \langle \psi_{\nu} | n'lm \rangle}{E_{\nu} - E}, \quad (6.35)$$

leading to the connecting equation for the inner and asymptotic solution

$$a_{n\ell}(E) = G_{n\mathcal{N}} T_{\mathcal{N}\mathcal{N}+1} a_{\mathcal{N}+1,\ell}^{\text{asy}}(E). \quad (6.36)$$

Having an expression for the Green's function allows us to write down the  $S$ -matrix, which reads

$$S(E) = \frac{I_{\mathcal{N}\ell}(E) - G_{\mathcal{N}\mathcal{N}}(E) T_{\mathcal{N}\mathcal{N}+1} I_{\mathcal{N}+1,\ell}(E)}{O_{\mathcal{N}\ell}(E) - G_{\mathcal{N}\mathcal{N}}(E) T_{\mathcal{N}\mathcal{N}+1} O_{\mathcal{N}+1,\ell}(E)}, \quad (6.37)$$

and alternatively the phase shift

$$\tan(\delta_{\ell}(E)) = - \frac{s_{\mathcal{N}\ell}(E) - G_{\mathcal{N}\mathcal{N}}(E) T_{\mathcal{N}\mathcal{N}+1} s_{\mathcal{N}+1,\ell}(E)}{c_{\mathcal{N}\ell}(E) - G_{\mathcal{N}\mathcal{N}}(E) T_{\mathcal{N}\mathcal{N}+1} c_{\mathcal{N}+1,\ell}(E)}.$$

### Regular and Irregular Solutions

The regular and irregular (free) solutions have explicit forms, which are obtained from calculating the integrals of the usual regular and irregular solution. In the absence of Coulomb forces, the free solutions are the Bessel functions. The regular solution reads

$$\begin{aligned} s_{n\ell}(E) &= \int_0^{\infty} dr r^2 j_{\ell}(kr) R_{n\ell}(r) \\ &= (-1)^n \sqrt{\frac{\pi}{2k}} \sqrt{\frac{2n!}{a_{\text{HO}}^3 \Gamma(n + \ell + \frac{3}{2})}} a_{\text{HO}}^{-\ell} \int_0^{\infty} dr r^{\ell + \frac{1}{2}} \exp\left(-\frac{r^2}{2a_{\text{HO}}^2}\right) L_n^{\ell + \frac{1}{2}}\left(\frac{r^2}{a_{\text{HO}}^2}\right) J_{\ell}(kr). \end{aligned} \quad (6.38)$$

The lower case  $j_{\ell}$  is the spherical Bessel function of the first kind, the upper case  $J_{\ell}$  is the ordinary Bessel function of the first kind. With the abbreviation  $q = \sqrt{\frac{2E}{\hbar\Omega}}$ , we get for the regular solution

$$s_{n\ell}(q) = \sqrt{\frac{2n!}{\lambda\Gamma(n + \ell + 3/2)}} q^{\ell+1} \exp\left(\frac{-q^2}{2}\right) L_n^{\ell + \frac{1}{2}}(q^2). \quad (6.39)$$

For the irregular solution, we obtain

$$c_{n\ell}(E) = (-1) \int_0^{\infty} dr r^2 \sqrt{\frac{\pi}{2rk}} J_{-\ell - \frac{1}{2}}(kr) R_{n\ell}(r), \quad (6.40)$$

and again with the abbreviation  $q$

$$\begin{aligned} c_{n\ell}(q) &= \frac{\Gamma[\ell + \frac{1}{2}]}{\pi} \sqrt{\frac{2n!}{\lambda\Gamma(n + \ell + 3/2)}} q^{-\ell} \exp\left(\frac{-q^2}{2}\right) {}_1F_1\left(-n - \ell - 1/2; -\ell + \frac{1}{2}; q^2\right) \\ &= \frac{(-1)^{\ell}}{\Gamma(-\ell + 1/2)} \sqrt{\frac{2n!}{\lambda\Gamma(n + \ell + 3/2)}} q^{-\ell} \exp\left(\frac{-q^2}{2}\right) {}_1F_1\left(-n - \ell - 1/2; -\ell + \frac{1}{2}; q^2\right). \end{aligned} \quad (6.41)$$

The function  ${}_1F_1$  is the confluent hypergeometric function [DLM14], see also appendix B. The derivation for the case of Coulomb interaction can be found in [BMS<sup>+</sup>00].

### 6.1.1. Connection to the No-Core Shell Model

The discussion of the No-Core Shell Model in chapter 5 introduced the truncation parameter  $N_{\max}$  to obtain a finite matrix, which is diagonalized, giving the eigenvalues as (bound-state) energies of the many-body problem. The connection of the HORSE method with the NCSM on a conceptual level is given by the use of the same basis expansion and truncation of the model space. In this sense, the HORSE method can be understood as the NCSM with continuum boundary conditions in its model space. The truncation used so far is based on the radial quantum number  $n$ , which solely needs to be translated into the main HO quantum number  $N$ , and from there to the energy excitation quantum number  $N_{\max}$

$$n = \frac{N - N_{\min}}{2} = \frac{(N_{\max} + N_{\min}) - N_{\min}}{2} = \frac{N_{\max}}{2}, \quad (6.42)$$

and consequently

$$\mathcal{N} + 1 = \frac{N_{\max} + 2}{2}, \quad (6.43)$$

which can be substituted in the relevant equations to obtain the desired  $N_{\max}$  dependency. For example, the phase shift reads with main quantum number

$$\tan(\delta_{\ell}(E)) = -\frac{s_{N\ell}(E) - G_{NN}(E)s_{N+2,\ell}(E)}{c_{N\ell}(E) - G_{NN}(E)c_{N+2,\ell}(E)}. \quad (6.44)$$

In order to be able to calculate the phase shift, one needs the complete Green's function, equation (6.35). This requires performing a sum over all eigenvectors and eigenenergies obtained from the NCSM diagonalization. For the most common implementation of the NCSM in the so-called  $m$ -scheme, this implies the computation of up to  $10^{10}$  eigenenergies and corresponding vectors. This is computationally unfeasible, due to the extreme memory demand. The sum in equation (6.35) can itself not be truncated again, as even high lying eigenvalues can contribute significantly, and therefore, have to be taken into account. The use of the relative coordinate Jacobi-NCSM, on the other hand, makes it theoretically possible, as the matrix dimension drastically reduces compared to the  $m$ -scheme. However, one is limited to the very lightest nuclei with  $A \leq 4$ .

## 6.2. Single-State Harmonic Oscillator Representation of Scattering Equations

The aforementioned limitations make the use of the “full” HORSE together with the  $m$ -scheme NCSM prohibitive. Fortunately, for the use of the HORSE method, the expansion in the discrete basis leads to a very simple expression of the scattering matrix and hence the phase shift [YA93], when inserting the precise eigenvalue  $E_{\nu}$  into relation (6.37). When this is done, one obtains the Single-State HORSE. With the abbreviation

$$\langle nlm|\psi_{\nu}\rangle = \gamma_{\nu}, \quad (6.45)$$

### 6.3. True Many-Particle Scattering in the Oscillator Representation

when the energy takes on the exact eigenenergy  $E_\mu$ , we get

$$\lim_{E \rightarrow E_\mu} S(E) = \lim_{E \rightarrow E_\mu} \frac{I_{N\ell}(E) - G_{NN}(E) T_{NN+1}}{O_{N\ell}(E) - G_{NN}(E) T_{NN+1}} \quad (6.46)$$

$$= \lim_{E \rightarrow E_\mu} \frac{I_{N\ell}(E) + \left( \sum_{\nu \neq \mu}^N \frac{\gamma_\nu \gamma_\nu^*}{E_\nu - E} + \frac{\gamma_\mu \gamma_\mu^*}{E_\mu - E} \right) T_{NN+1} I_{N+1,\ell}(E)}{O_{N\ell}(E) + \left( \sum_{\nu \neq \mu}^N \frac{\gamma_\nu \gamma_\nu^*}{E_\nu - E} + \frac{\gamma_\mu \gamma_\mu^*}{E_\mu - E} \right) T_{NN+1} O_{N+1,\ell}(E)} \frac{E_\mu - E}{E_\mu - E} \quad (6.47)$$

$$= \frac{I_{N+1,\ell}(E_\mu)}{O_{N+1,\ell}(E_\mu)}. \quad (6.48)$$

The phase shift in the Single-State HORSE is obtained in the same way and reads

$$\tan \delta_\ell(E_\nu) = -\frac{s_{N+2,\ell}}{c_{N+2,\ell}} \quad (6.49)$$

$$\begin{aligned} &= -\frac{\Gamma(-\ell + 1/2) \left( \sqrt{\frac{2E_\nu}{\hbar\Omega}} \right)^{\ell+1} \exp \left[ \frac{-E_\nu}{\hbar\Omega} \right] L_{(N-\ell)/2}^{\ell+\frac{1}{2}} \left( \frac{2E_\nu}{\hbar\Omega} \right)}{(-1)^\ell \left( \sqrt{\frac{2E_\nu}{\hbar\Omega}} \right)^{-\ell} \exp \left[ \frac{-E_\nu}{\hbar\Omega} \right] {}_1F_1 \left( -(N + \ell + 1)/2; -\ell + 1/2; \frac{2E_\nu}{\hbar\Omega} \right)} \\ &= -\frac{\Gamma(-\ell + 1/2) \left( \sqrt{\frac{2E_\nu}{\hbar\Omega}} \right)^{2\ell+1} L_{(N-\ell)/2}^{\ell+\frac{1}{2}} \left( \frac{2E_\nu}{\hbar\Omega} \right)}{(-1)^\ell {}_1F_1 \left( -(N + \ell + 1)/2; -\ell + 1/2; \frac{2E_\nu}{\hbar\Omega} \right)}. \end{aligned} \quad (6.50)$$

This is an important finding, as it means that the phase shift at an energy corresponding to an exact eigenvalue of the truncated matrix can be obtained from only the ratio of the asymptotic solutions at this energy.

The practical application of this is that we perform NCSM calculations at a fixed  $N_{\max}$  and vary the oscillator length or frequency over a wide range to obtain the sought energies, see chapter 7.

### 6.3. True Many-Particle Scattering in the Oscillator Representation

The description of a many-particle scattering system requires some further modification to the  $J$ -matrix HORSE formalism. The treatment of such system can be done with the help of scattering amplitudes of each of the possible sub-clusters that can be formed by all the constituents of the scattering partners. This is done in some form, e.g. in the Faddeev-Yakubovsky method [Fad61, FM93] or in the Resonating Group Method [TLT78]. One of the sub-clusters that can be formed is the true  $A$ -body to  $A$ -body scattering, without any bound sub-systems

$$A \rightarrow A,$$

e.g., we assume this to be true for the tetra-neutron

$$n + n + n + n \rightarrow n + n + n + n.$$

This scattering channel is referred to as *true many-particle* scattering, *democratic* scattering or *democratic* decay [ZSS98, LS04]. It can serve as a good approximation for a more complex system with bound sub-structures, where the excitation energies are large compared to the scattering energies. This democratic decay approximation has been used, e.g. on  $^{11}\text{Li} = {}^9\text{Li} + n + n$ , among others [LS04], and more specifically in the case of the tetra-neutron [SPM<sup>+</sup>16, SMMV16].

## 6. *J*-Matrix and Harmonic Oscillator Representation of Scattering Equations

The true many-particle scattering asymptotic wave function is a spherical wave in a  $3A - 3$  dimensional space, with  $A$  being the number of particles. It can, therefore, be described with an appropriate set of coordinates in  $3A - 3$  dimensions with the help of the  $(A - 1)$  Jacobi coordinates  $\vec{\xi}_i$ , see section 5.2 about Jacobi coordinates. The form of the asymptotic wave function can be obtained using hyperspherical harmonics, which are an extension of the spherical harmonics to  $3A - 3$  dimensions. This gives a partial wave expansion in this multi-dimensional space. We introduce the unifying hyperspherical radius  $\rho$  and the set of angles  $\bar{\Omega}$ . The hyperradius is given as [BLO00]

$$\rho = \sqrt{\sum_{i=1}^{A-1} (\vec{r}_i - \vec{\xi}_0)^2} \quad (6.51)$$

$$= \sqrt{\sum_{i=1}^{A-1} \xi_i^2}. \quad (6.52)$$

The  $\vec{r}_i$  are the single-particle coordinates and  $\vec{\xi}_i$  is the centre-of-mass coordinate. The hyper-radius is symmetric with respect to permutation in the single-particle coordinates. The pair of angles  $(\theta_i, \phi_i)$  belonging to each Jacobi coordinate  $\vec{\xi}_i$  are extended via the hyperangle  $\alpha$ , defined by the relation

$$\sin \alpha_i = \frac{\xi_i}{\rho_i}, \quad (6.53)$$

where  $\xi_i$  is the radial part of the Jacobi coordinate,  $\rho_i$  is the hyperradius constructed up to the  $i$ -th coordinate. The angular coordinates are collected in  $\bar{\Omega}$ . The bar is used to distinguish it from the HO frequency  $\Omega$ .

We introduce the hyperspherical oscillator basis, which consists of the eigenfunctions of the harmonic oscillator in the hyperspherical coordinates. In abstract notation, we write it as any basis expansion

$$|Ei\alpha\rangle = \sum_{n'K\gamma} \langle n'K\gamma | Ei\alpha \rangle |n'K\gamma\rangle, \quad (6.54)$$

where  $|Ei\alpha\rangle$  can, for example, be the Jacobi basis as in section 5.2, with  $E$  being the total energy quantum,  $i$  a collective index for antisymmetric states, the hyperspherical principal HO number  $n$ , the hypermomentum  $K$ , and the collective indices  $\alpha$  and  $\gamma$ , which represent all other relevant quantum numbers, in the respective coordinates. In the general case, the sum is infinite, if the expanded state is not bounded and discrete. In the special case of a state which is itself formed or part of a truncated basis, like the HO basis we use in the NCSM and HORSE method, the sum is finite as well and limited in the values  $K$  can reach. The states in the hyperspherical harmonics (HH) expansion must be orthonormal

$$\langle n'K'\gamma' | nK\gamma \rangle = \delta_{n'n} \delta_{K'K} \delta_{\gamma'\gamma}. \quad (6.55)$$

The basis can be written in coordinate representation as [ZSS98]

$$|nK\gamma\rangle = \mathfrak{R}_{nK}(\rho) \mathfrak{Y}_{K\gamma}(\bar{\Omega}). \quad (6.56)$$

The first part of this basis,  $\mathfrak{R}_{nK}(\rho)$ , is the hyperspherical radial function and  $\mathfrak{Y}_{K\gamma}$  is a collective function, incorporating the hyperspherical harmonics as well as any other functions with relevant degrees of freedom, e.g. spin. The hyperspherical radial function reads

$$\mathfrak{R}_{nK}(\rho) = \mathfrak{R}_n^{\mathcal{L}}(\rho) = \rho^{-(3A-4)} \mathfrak{r}_{nK}(\rho), \quad (6.57)$$

with

$$\mathfrak{r}_{nK}(\rho) = \mathfrak{r}_n^{\mathcal{L}}(\rho) = (-1)^n \sqrt{\frac{\lambda 2n!}{\Gamma(n + \mathcal{L} + \frac{3}{2})}} (\lambda\rho)^{\mathcal{L}+1} e^{-\frac{\rho^2}{2}} L_n^{\mathcal{L}+\frac{1}{2}}(\lambda\rho^2), \quad (6.58)$$

where  $\lambda$  is the oscillator length  $\sqrt{\hbar/m\Omega}$ . Due to the orthonormalization, equation (6.55), it follows that

$$\int d\rho \mathfrak{r}_{n'K}^*(\rho) \mathfrak{r}_{nK}(\rho) = \delta_{n'n}. \quad (6.59)$$

Here,  $L_n^{\mathcal{L}+\frac{1}{2}}(\rho^2)$  is the generalized Laguerre function, with hyperspherical angular momentum

$$\mathcal{L} = K + \frac{3(A-2)}{2}. \quad (6.60)$$

The energy levels are given by the analogue relation of a  $3(A-1)$  dimensional harmonic oscillator

$$E_{nK} = \left(2n + K + \frac{3(A-1)}{2}\right) \hbar\Omega = \left(N + \frac{3(A-1)}{2}\right) \hbar\Omega. \quad (6.61)$$

The expansion in equation (6.54), together with the relations of the two momenta in equation (6.60) as well as the total energy in equation (6.61), indicates that the hypermomentum  $K$  can be truncated. From the large values of the centrifugal barrier  $\mathcal{L}(\mathcal{L}+1)$ , we can introduce both a minimal value for the momentum,  $K_{\min}$ , as well as an upper truncation  $K_{\max}$ , if, e.g., a study with increasing  $K$  is desirable.

The differential equation which is solved by the function  $\mathfrak{r}_{nK}(\rho)$  is the analogue to the radial Schrödinger equation, in hyperspherical coordinates [DB10]

$$\left(\frac{\hbar^2}{2\mu} \left(-\frac{d^2}{d\rho^2} + \frac{(K + \frac{3(A-2)}{2})(K + \frac{3(A-2)}{2} + 1)}{\rho^2}\right) - E\right) \mathfrak{r}_{nK}(\rho) + \sum_{n'K'\gamma'} V_{\gamma K\gamma'K'}(\rho) \mathfrak{r}_{n'K'}(\rho) = 0 \quad (6.62a)$$

$$\left(\frac{\hbar^2}{2\mu} \left(-\frac{d^2}{d\rho^2} + \frac{\mathcal{L}(\mathcal{L}+1)}{\rho^2}\right) - E\right) \mathfrak{r}_{nK}(\rho) + \sum_{n'K'\gamma} V_{\gamma K\gamma'K'}(\rho) \mathfrak{r}_{n'K'}(\rho) = 0. \quad (6.62b)$$

The term  $V_{\gamma K\gamma'K'}(\rho)$  is some two-body interaction matrix element expanded in hyperspherical harmonics

$$V_{\gamma K\gamma'K'}(\rho) = \langle \mathfrak{Y}_{K\gamma}(\bar{\Omega}) | \sum_{i<j} V_{ij}(\vec{r}_i - \vec{r}_j) | \mathfrak{Y}_{K'\gamma'}(\bar{\Omega}) \rangle. \quad (6.63)$$

Due to the HH expansion of the potential, we have by construction a set of coupled differential equations. The replacement of  $K \rightarrow \mathcal{L}$  in equations (6.62a) and (6.62b) highlights the interpretation of  $\mathcal{L}$  as the analogue to the usual angular momentum. Equation (6.62), in the absence of a potential, has two fundamental solutions, which are almost identical to the non-hyperspherical case. The regular and irregular solution  $s_{n\mathcal{L}}$  and  $c_{n\mathcal{L}}$  read, in terms of the HH HO radial quantum number  $n$ , the hyperspherical angular momentum  $\mathcal{L}$ , and the momentum  $q = \sqrt{\frac{2E}{\hbar\Omega}}$  [ZSS98]

$$s_{n\mathcal{L}}(q) = \sqrt{\frac{2n!}{\lambda\Gamma(n + \mathcal{L} + 3/2)}} q^{\mathcal{L}+1} \exp\left(\frac{-q^2}{2}\right) L_n^{\mathcal{L}+\frac{1}{2}}(q^2), \quad (6.64)$$

and

$$\begin{aligned}
 c_{n\mathcal{L}}(q) &= \frac{\Gamma[\mathcal{L} + \frac{1}{2}]}{\pi} \sqrt{\frac{2n!}{\lambda\Gamma(n + \mathcal{L} + 3/2)}} q^{-\mathcal{L}} \exp\left(\frac{-q^2}{2}\right) {}_1F_1\left(-n - \mathcal{L} - 1/2; -\mathcal{L} + \frac{1}{2}; q^2\right) \\
 &= \frac{(-1)^\mathcal{L}}{\Gamma(-\mathcal{L} + 1/2)} \sqrt{\frac{2n!}{\lambda\Gamma(n + \mathcal{L} + 3/2)}} q^{-\mathcal{L}} \exp\left(\frac{-q^2}{2}\right) {}_1F_1\left(-n - \mathcal{L} - 1/2; -\mathcal{L} + \frac{1}{2}; q^2\right).
 \end{aligned} \tag{6.65}$$

The change in the prefactor in equation (6.65) corresponds to the equation as used in reference [SMMV16]. The phase shift in the Single-State HORSE approximation is given by

$$\begin{aligned}
 \tan(\delta_l(q)) &= -\frac{s_{n+1,\mathcal{L}}(q)}{c_{n+1,\mathcal{L}}(q)} \\
 &= -\frac{\Gamma(-\mathcal{L} + 1/2) q^{2\mathcal{L}+1} L_{(n+1)}^{\mathcal{L}+\frac{1}{2}}(q^2)}{(-1)^\mathcal{L} {}_1F_1(-n - 1 - \mathcal{L} - 1/2; -\mathcal{L} + \frac{1}{2}; q^2)}.
 \end{aligned} \tag{6.66}$$

This allows us calculate phase shifts for the tetra-neutron in the Single-State HORSE democratic decay approximation, see chapter 7.

## 6.4. Construction of Hyperspherical States from Jacobi-NCSM Eigenstates

Part of this work is to exploit the advantages of the Jacobi-NCSM to construct the full HORSE matrix in terms of increasing hyperspherical momentum  $K$ . The limiting factor in the more common  $m$ -scheme NCSM is two-fold. Firstly, the extremely large basis space, with linear dimension in the order of  $10^7$  to  $10^{10}$ , would have to be diagonalized completely, and all eigenvectors and eigenvalues would have to be written to disc, requiring up to a petabyte of storage space. This is computationally unfeasible. The only way to obtain eigenvalues and vector for matrices of this size is with iterative schemes, like the Lanczos algorithm [BNV13]. This returns only the lowest eigenstates. Secondly, even if the whole matrix could be diagonalized and stored in memory or on disc in the  $m$ -scheme, it would require multiple Talmi-Moshinsky transformations to obtain the desired scattering channel with good total angular momentum  $J$ , and getting rid of any centre-of-mass contaminations [SMMV16]. The Jacobi-NCSM, on the other hand, is by construction free of centre-of-mass contributions and the Hamiltonian in this basis can be fully diagonalized.

It is possible to use the eigenvectors obtained from the Jacobi-NCSM in the expansion of equation (6.54), and further obtain the Green's function, given in equation (6.35). We want to apply the true many-particle boundary conditions to the Green's function, so instead of using the vectors given in the usual HO, we are interested in the HH expanded formulation, which reads

$$G_{nn'} = - \sum_{\nu, K, \gamma} \frac{\langle nK\gamma | \psi_\nu \rangle \langle \psi_\nu | n'K\gamma \rangle}{E_\nu - E}. \tag{6.67}$$

This requires the computation of the overlap of the HH state with the Jacobi-NCSM eigenstate, which in turn is constructed from antisymmetric Jacobi basis states, given in equation (5.21)

$$|E_{123} i_{123} J_{123} T_{123}\rangle_a \equiv |E_{123} i \alpha\rangle, \tag{6.68}$$

#### 6.4. Construction of Hyperspherical States from Jacobi-NCSM Eigenstates

where we introduce a short-hand notation of the basis states for this section. The index  $i$  runs over all antisymmetric basis and does not correspond to physical quantum numbers. The index  $\alpha = \{J_{123}, T_{123}, P_{123}\}$  collects all other quantum numbers. We change from the explicit antisymmetrization to an implicit notation, by omitting the subscript  $a$ .

The vector product of state  $|nK\gamma\rangle$  with the state  $|\psi_\nu\rangle$  can be expanded in the Jacobi basis

$$\langle nK\gamma|\psi_\nu\rangle = \sum_{i,\alpha} \langle nK\gamma|E_{123} i \alpha\rangle \langle E_{123} i \alpha|\psi_\nu\rangle. \quad (6.69)$$

The  $\langle nK\gamma|E_{123} i \alpha\rangle$  are unknown expansion coefficients. We obtain these, without having to resort to an explicit representation in a hyperspherical basis, by utilizing the fact that the minimal energy configuration has to be identical in both coordinate systems. We must have the equality

$$\begin{aligned} N_K &= 2n + K \\ \rightarrow 2\mathcal{N}_K + K &= N_{\max} + N_{\min} = E_{123}, \end{aligned} \quad (6.70)$$

where  $N_K$  is the principle hyperspherical HO quantum number,  $n$  the hyperspherical radial quantum number,  $\mathcal{N}_K$  is the maximal possible hyperspherical HO radial quantum number conforming to the total possible energy, analogous to equation (6.26). This means that the smallest possible  $K$  value  $K_{\min}$  at  $n = 0$  and the corresponding states

$$|n = 0, K_{\min}, \gamma\rangle \quad (6.71)$$

must be contained within the lowest possible energy configuration of  $N_{\max} = 0$ . We, therefore, write the  $K_{\min}$  states as a linear combination of the basis states belonging to the  $N_{\max} = 0$  space

$$|n = 0, K_{\min}, \gamma\rangle = \sum_{i,\alpha \subseteq N_{\max}=0} c_i^\alpha |E_{123} i \alpha\rangle, \quad (6.72)$$

where the coefficients  $c_i$  are determined by orthonormalization of the states, but other than that, can be chosen freely. As we have no information about their relative amplitudes, we can choose them to be of equal absolute value, or directly identify the basis states with the hyperspherical states in a one-to-one relation. From this starting point, we can construct all further HH states in an iterative scheme, where we utilize the tridiagonality of the kinetic energy, both in the Jacobi basis and in the hyperspherical basis, which is tridiagonal in  $n$ , while being diagonal in  $K$  and  $\gamma$ . By letting the kinetic energy act upon a Jacobi basis-state, we excite it into the next higher energy quantum

$$T |E_{123} i \alpha\rangle = |E_{123} + 2, i \alpha\rangle = |n = 1, K_{\min}, \gamma\rangle, \quad (6.73)$$

without changing the value of  $K = K_{\min}$ . We can, therefore, write for the hyperspherical states a relation of the form

$$T |n = 0, K_{\min}, \gamma\rangle = \beta_0 \underbrace{|n = 0, K_{\min}, \gamma\rangle}_{N_{\max}=0} + \beta_1 \underbrace{|n = 1, K_{\min}, \gamma\rangle}_{N_{\max}=2}, \quad (6.74)$$

which gives the  $K_{\min}$  states at  $n = 1$ , belonging to the next higher  $N_{\max}$  space. The coefficients  $\beta$  should be chosen such that they ensure orthonormalization. By iteration, we obtain all further states of the same  $K$  in the next higher lying space, for  $K = K_{\min}$  this reads

$$T |n, K_{\min}, \gamma\rangle = \beta_1 |n - 1, K_{\min}, \gamma\rangle + \beta_2 |n, K_{\min}, \gamma\rangle + \beta_3 |n + 1, K_{\min}, \gamma\rangle. \quad (6.75)$$

## 6. *J*-Matrix and Harmonic Oscillator Representation of Scattering Equations

All other higher  $K$  states follow in the same fashion, by first identifying the  $K_{\min}$  states within the  $N_{\max} = 0$  space, constructing the next  $K_{\min}$  states within  $N_{\max} = 2$  space with the help of equation (6.74). Within the  $N_{\max} = 2$  space, all remaining basis states, which are not part of  $K_{\min}$  must then be part of  $K_{\min} + 2$  states. The procedure of equation (6.75) then generalizes to

$$T |n, K, \gamma, j\rangle = \beta_1 |n-1, K, \gamma\rangle + \beta_2 |n, K, \gamma\rangle + \beta_3 |n+1, K, \gamma\rangle. \quad (6.76)$$

In this way, all hyperspherical states up to a desired  $K$  within the total available  $N_{\max}$  space can be constructed with equation (6.72) as a starting point. The orthogonalization of the states has to be ensured, both to obtain the sought hyperspherical expansion coefficient, as well to account for numerical inaccuracy, which means in practical application, that this has to be done after each time a new set of states is obtained, e.g., via a Gram-Schmidt procedure.

As a practical example, we consider the tetra-neutron, which has two states at  $N_{\max} = 0$ , nine at  $N_{\max} = 2$ , and 29 states  $N_{\max} = 4$ . Or, equivalently

$$\begin{aligned} |E_{123} = 2, i \alpha\rangle & \quad i = 1, 2 \\ |E_{123} = 4, i \alpha\rangle & \quad i = 1, 2, \dots, 9 \\ & \dots \end{aligned}$$

The minimal  $K$  in this case is  $K_{\min} = 2$ . That means we have also two  $K_{\min}$  states in equation (6.72), meaning

$$|n = 0, K_{\min} = 2, \gamma\rangle = \sum_{i=1}^2 c_i^\alpha |E_{123} = 2, i \alpha\rangle \quad (6.77)$$

$$|n = 0, K_{\min} = 2, \gamma'\rangle = \sum_{i=1}^2 \tilde{c}_i^\alpha |E_{123} = 2, i \alpha\rangle. \quad (6.78)$$

Applying the kinetic energy operator as in equation (6.75) gives two additional  $K_{\min}$  states in the  $N_{\max} = 2$  space. The remaining five states must consequently belong to  $K = 4$ . Continuing in this way, we obtain two  $K = 2$  states at each higher  $N_{\max}$  value, and applying the kinetic energy operator to the  $K = 4$  states, we obtain five new states of the same  $K$  for each  $N_{\max}$ . This leaves 13 states at  $N_{\max} = 4$  which must belong to  $K = 6$ , and so on.

The hyperspherical states thus obtained can then be inserted into equation (6.69) to get the sought expansion coefficients

$$\begin{aligned} \langle nK\gamma|\psi_\nu\rangle &= \sum_{i,\alpha} \langle nK\gamma|E_{123} i \alpha\rangle \langle E_{123} i \alpha|\psi_\nu\rangle \\ &= \sum_{i,\alpha} \sum_{j,\alpha'} c_j^{\alpha'} \langle E_{123} j \alpha'|E_{123} i \alpha\rangle \langle E_{123} i \alpha|\psi_\nu\rangle \\ &= \sum_{i,\alpha} c_i^\alpha \langle E_{123} i \alpha|\psi_\nu\rangle. \end{aligned} \quad (6.79)$$

With the coefficients  $c_i^\alpha$  and thus  $\langle nK\gamma|\psi_\nu\rangle$ , we obtain the Green's function in equation (6.67). It should be noted that the Green's function contains a sum over all hyperspherical  $K$ , which makes the computation computationally expensive.

# 7. Tetraneutron in the Single-State Harmonic Oscillator Representation of Scattering Equations

The interest in the four-neutron system in the more recent past has first been kindled by the possibility of experimental evidence of a weakly bound state [MLO<sup>+</sup>02]. Most theoretical studies could not substantiate the existence of a bound state [BZ03, Pie03], with one exception [MLP14], and also a resonance was disfavoured [LC05]. A recent experiment sparked renewed interest in a possible tetraneutron resonance in the  $J^\pi = 0^+$  state, proposing a position at  $0.83 \pm 0.65(\text{stat}) \pm 1.25(\text{syst})$  MeV and giving an upper limit for the width of 2.6 MeV [KSM<sup>+</sup>16]. The theoretical studies that followed disagree whether a resonance exists, let alone what its parameters are. While some come to the conclusion that it exists, with varying results regarding position and width [SPM<sup>+</sup>16, FRMP17, GHK<sup>+</sup>17, LMH<sup>+</sup>19], others find no evidence to support a resonance [HLCK16, LCH17, CLHK17, Del18, DL19b, HGKV20].

One important aspect in this endeavour is the role of the nuclear interaction. Studies investigating necessary modifications in the interaction, e.g., the isospin  $T = 3/2$  channel [HLCK16], find these modifications to be incompatible with other system in close proximity on the nuclear chart, breaking theoretically and experimentally well established observables. Realistic nuclear interactions aim for an accurate description the nuclear chart, and the most advanced interactions are based on Chiral Effective Field Theory ( $\chi$ EFT). The correct reproduction of tetraneutron parameters, is, therefore, an ideal test. Most of the studies using realistic potentials report that their findings do not depend too strongly on the employed interaction. The different results thus have to be related to some degree to the used methods.

In this chapter, we present the work performed to further expand the studies presented in reference [SPM<sup>+</sup>16]. We employ the Single-State Harmonic Oscillator Representation of Scattering Equations (HORSE), described in section 6.2, applied to the tetraneutron in the democratic decay approximation, discussed in section 6.3, together with the Jacobi No-Core Shell Model (NCSM) to solve the many-body problem. The extensions are of two kinds. Firstly, we greatly expand the NCSM model space, from previously  $N_{\text{max}} = 18$  to  $N_{\text{max}} = 26$  for most of the SRG evolved interaction, and even up to  $N_{\text{max}} = 30$  in the case of the bare two-body chiral interaction.

Secondly, we present the first systematic study of a range of state-of-the-art  $\chi$ EFT NN and 3N and realistic inverse scattering NN interactions, and their impact on tetraneutron phase shifts. The effect of the SRG is studied in comparing the bare, unevolved NN interaction to its SRG counterparts, as well as comparing two different flow parameter values. We present the impact of the SRG evolved NN-only, NN with induced three-body terms and initial 3N interactions. In the case of the 3N interaction, we also use two different values for the regulator cut-off. The systematic approach of the chiral interaction also allows us to study the phase shifts order-by-order in the two-body sector. The interactions are listed in table 7.1.

To this end, we first present the main findings in the form of a comparative plot, followed by individual aspects of the different interactions and SRG parameters.

## 7. Tetraneutron in the Single-State HORSE

Name	Type	Year	Reference	SRG $\alpha$ [fm <sup>4</sup> ]
JISP16	ISP NN	2007	[SVMW07]	-
DAEJEON16	ISP NN	2016	[SSK <sup>+</sup> 16]	-
N <sup>3</sup> LO <sub>EM</sub>	$\chi$ EFT NN	2003	[EM03]	bare, 0.04 & 0.08
N <sup>3</sup> LO <sub>EM</sub> + N <sup>2</sup> LO <sub><math>\Lambda</math>,L</sub>	$\chi$ EFT NN + 3N	2007	[Nav07]	0.04 & 0.08
N <sup>2</sup> LO <sub>SAT</sub>	$\chi$ EFT NN	2015	[EJW <sup>+</sup> 15]	0.04 & 0.08
N <sup>x</sup> LO <sub>EMN</sub>	$\chi$ EFT NN	2017	[EMN17]	0.04 & 0.08

Table 7.1.: Interactions used in this work. Interaction constructed from inverse scattering potentials are denoted ISP.

### 7.1. Identifying Resonances

The characteristics of a system in the continuum can be inferred from their (partial waves) phase shifts. We obtain the needed energies to calculate these for the  $J^\pi = 0^+$  state as described in section 7.2.

The deduction of the existence of a resonance in the four-neutron system within the Single-State HORSE method follows from the discussion in section 3.5. According to the statements made in section 3.5, a resonance phase shift is characterized by a sudden and sharp increase when coming from lower and going to higher energies, passing 90° and going to almost 180°, after which it declines again. We infer resonance character from the general shape of the phase shifts in the way just described. The phase shifts are calculated via equation (6.66) and read

$$\begin{aligned} \tan(\delta_l(E)) &= -\frac{s_{n+1,\mathcal{L}}(E)}{c_{n+1,\mathcal{L}}(E)} \\ &= -\frac{\Gamma(-\mathcal{L} + 1/2) \sqrt{\frac{2E}{\hbar\Omega}}^{2\mathcal{L}+1} L_{\left(\frac{N_{\max}+2}{2}\right)}^{\mathcal{L}+\frac{1}{2}}\left(\frac{2E}{\hbar\Omega}\right)}{(-1)^\mathcal{L} {}_1F_1\left(-\left(\frac{N_{\max}+2}{2}\right) - \mathcal{L} - 1/2; -\mathcal{L} + \frac{1}{2}; \frac{2E}{\hbar\Omega}\right)}. \end{aligned} \quad (7.1)$$

From the inflection point of the phase shift we gain an approximate value for the resonance position equation (3.113b)

$$E_R \rightarrow \left. \frac{d^2\delta_l(E)}{dE^2} \right|_{E=E_R} = 0. \quad (7.2)$$

The width is approximated with the Breit-Wigner distribution, see equations (3.115) and (3.116),

$$\Gamma = 2 \left( \left. \frac{d\delta_l}{dE} \right|_{E=E_R} \right)^{-1}. \quad (7.3)$$

Within this work, the tetraneutron is assumed to be true  $4 \rightarrow 4$  scattering with no sub-clusters. This is also referred to as *democratic* decay [SPM<sup>+</sup>16], see section 6.3. A pure neutron bound-state is currently deemed unlikely by almost all recent publication on the topic, which makes the democratic decay approximation reasonable. How a trineutron resonance, should it exist, would affect the tetraneutron, remains to be investigated. We are operating with hyperspherical coordinates, and therefore, we have for the hypermomentum  $K$  and the hyperspherical angular momentum in the case of the tetraneutron

$$\mathcal{L} = K + \frac{3(A-2)}{2} = K + 3. \quad (7.4)$$

We use the minimal approximation of

$$K = K_{\min} = 2, \quad (7.5)$$

due to the large centrifugal barrier

$$\frac{\mathcal{L}(\mathcal{L} + 1)}{\rho^2} \rightarrow \frac{5(5 + 1)}{\rho^2}. \quad (7.6)$$

We note that a phase shift can be broadened due to back groundcontributions, leading to a parametrization as given in equation (3.111). The resonance position in reference [SPM<sup>+</sup>16] for the tetraneutron resonance candidate was determined by fitting the phase shift data points to a function parametrized as in equation (3.111), where the resonant contribution was further parametrized as

$$\delta_\ell^R(E) = -\tan^{-1} \left( \frac{a\sqrt{E}}{E - b^2} \right), \quad (7.7)$$

which gives the resonance position  $E_R$  and width  $\Gamma$  via

$$E_R = b^2 - \frac{a^2}{2} \quad \text{and} \quad \Gamma = 2a\sqrt{b^2 - \frac{a^2}{4}}, \quad (7.8)$$

which is a rewritten form of the relations given in equations (3.100) and (3.101), within this parametrization. The results are for the position  $E_R \approx 0.8$  MeV and for the width  $\Gamma \approx 1.4$  MeV. A study to extract the resonance parameters in analogy to the one in reference [SPM<sup>+</sup>16] from a selection of the newly generated data was part of a bachelor's thesis [Der17].

## 7.2. Data Generation

The data for the tetraneutron are generated within the framework of the Jacobi-NCSM. The target state for this is a  $J^\pi = 0^+$  state. To calculate phase shifts according to equation (6.66), we generate relative coordinate matrix elements in a broad range in the HO length  $a_{\text{HO}}$ . The NCSM calculations are then performed with successively increasing  $N_{\text{max}}$ . This gives the relevant input for equation (6.66) as data triplets  $(E, a_{\text{HO}}, N_{\text{max}})$ , or alternatively with the HO frequency  $(E, \hbar\Omega, N_{\text{max}})$ . For the plots, we choose to use the frequency. The obtained energies decrease with decreasing frequency, as opposed to increasing oscillator lengths. The use of the frequency, therefore, allows for consistent plot layout when plotting the phase shifts  $\delta(E)$  and  $\delta(\hbar\Omega)$ , respectively.

## 7.3. Main Findings

The combined comparison of the investigated interactions is shown in figure 7.1. All interactions shown are given at a consistent  $N_{\text{max}} = 26$ , where each data point corresponds to a set of  $(E, \hbar\Omega, N_{\text{max}} = 26)$ . The plot shows the JISP16 potential for comparison to reference [SPM<sup>+</sup>16], alongside the DAEJEON16 and various SRG evolved  $\chi$ EFT interactions.

The phase shifts generally agree with each other. They all show the same distinct behaviour of rising sharply coming from low energies, crossing  $90^\circ$  around 1.2 MeV, continuing to varying maximal phase shift values between  $100^\circ$  and  $110^\circ$ , and they slowly decrease for  $E > 5$  MeV, showing some slight differences going to larger energies. The phase shifts have inflection points at approximately

$$E_R \approx 0.7 \text{ MeV},$$

and a width, via equation (3.116), of

$$\Gamma \approx 1.2 \text{ MeV}.$$

## 7. Tetraneutron in the Single-State HORSE

These values are arrived at by interpolating the data points with a third degree polynomial. We conclude, that the gross properties of the phase shifts obtained in the Single-State HORSE formalism for the tetraneutron are independent of the interaction used in the NCSM calculation, excluding the bare interaction, which is not shown in this plot.

The differences that can be seen are on the one hand due to the way the in interaction were constructed in the first place; at the high energy end, the  $\chi$ EFT based ones show a phase shift of a few degrees lower than the ISP based interactions, i.e. JISP16 and DAEJEON16. The important energy range of 5 MeV and lower to around 1 MeV has the most spread in the phase shifts, of around 10 degrees. In the lowest energy region, the phase shifts tend to agree, with the noticeable exception of the DAEJEON16 potential.

These results corroborate the findings published in [SPM<sup>+</sup>16], and expand the analysis with different state-of-the-art  $\chi$ EFT interactions. The inferred existence of a four-neutron resonance from the phase shift analysis within the Single-State HORSE formalism does not depend on the interaction, while details such as exact position and width might be affected.

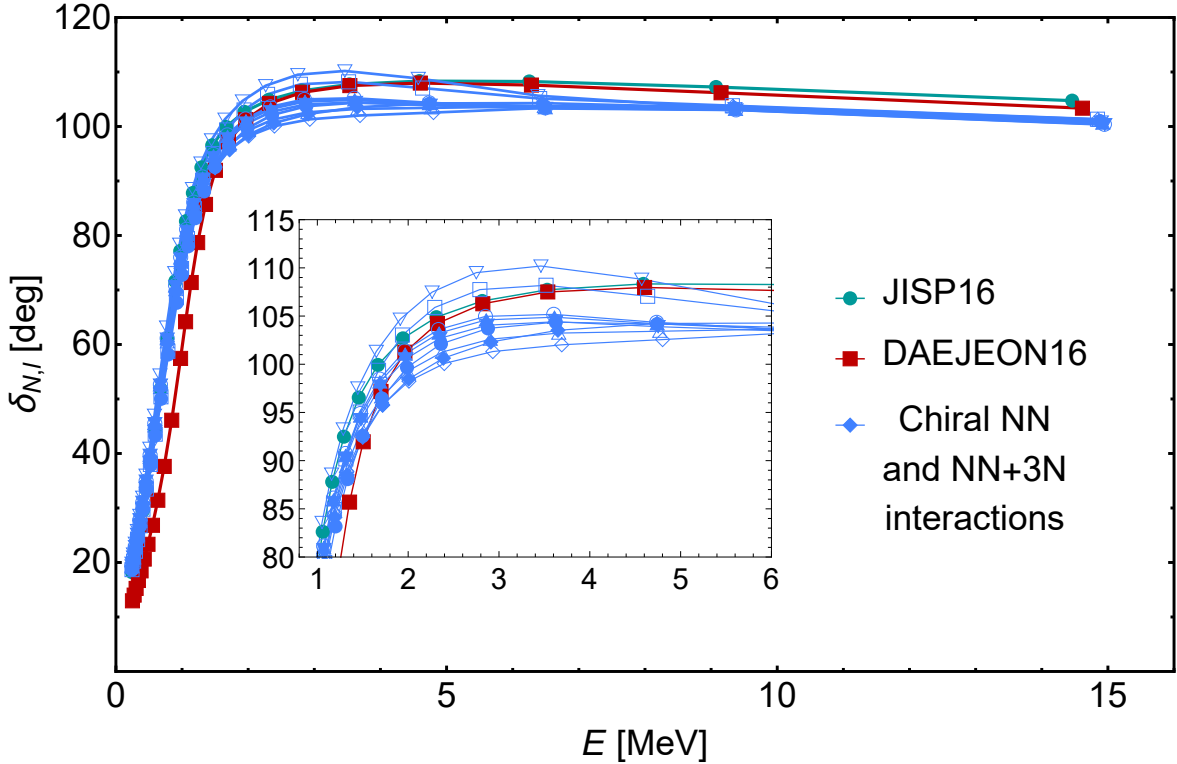


Figure 7.1.: Tetraneutron Single-State HORSE phase shifts, comparison of various interactions. All data shown are  $N_{\max} = 26$ , as well as all blue lines SRG flow parameter  $\alpha = 0.08 \text{ fm}^4$ . See table 7.1 as well as the text for details on the used interactions. The plot markers represent calculated data points, the lines connecting the markers are linear interpolations and only serve to guide the eye.

### 7.3.1. NCSM Model Space Dependence

We discuss the  $N_{\max}$  dependence of the data first with the energy as a function of the oscillator frequency, which represents the raw data used as input for the phase shift relation of equation (6.66). Additionally, we investigate the phase shift as a function of the frequency, as well

as a function of the energy.

To demonstrate the  $N_{\max}$  sequences, we choose the interaction  $N^3\text{LO}_{\text{EM}} + N^2\text{LO}_{500,\text{L}}$  SRG evolved with  $\alpha = 0.08 \text{ fm}^4$  [EM03, Nav07]. This  $\chi\text{EFT}$  potential is a common choice in *ab initio* nuclear structure calculations. The complete  $N_{\max}$  sequences of the phase shift for all other interactions can be found in appendix C.

Figure 7.2 shows the eigenenergy from the NCSM calculations as a function of harmonic oscillator frequency. With higher HO frequencies, the energy at each model space size parameter  $N_{\max}$  increases. For fixed frequency, the energy decreases with increasing  $N_{\max}$ . Unlike the bound ground-state case, where a fixed-frequency gives an upper limit in the energy, which can be improved by frequency variation, this is not the case in the pseudo-continuum. The eigenenergy at a given frequency is not an upper bound for energies obtained with different frequencies. The approach of choosing a favourable frequency for best convergence is thus not possible. On the contrary, the Single-State HORSE method relies on this energy-frequency relation in the continuum. The pattern of the  $N_{\max}$  sequence appears to be better converged at lower frequencies. Nevertheless, going to larger model spaces of  $N_{\max} = 26$  has a visible impact on the energies.

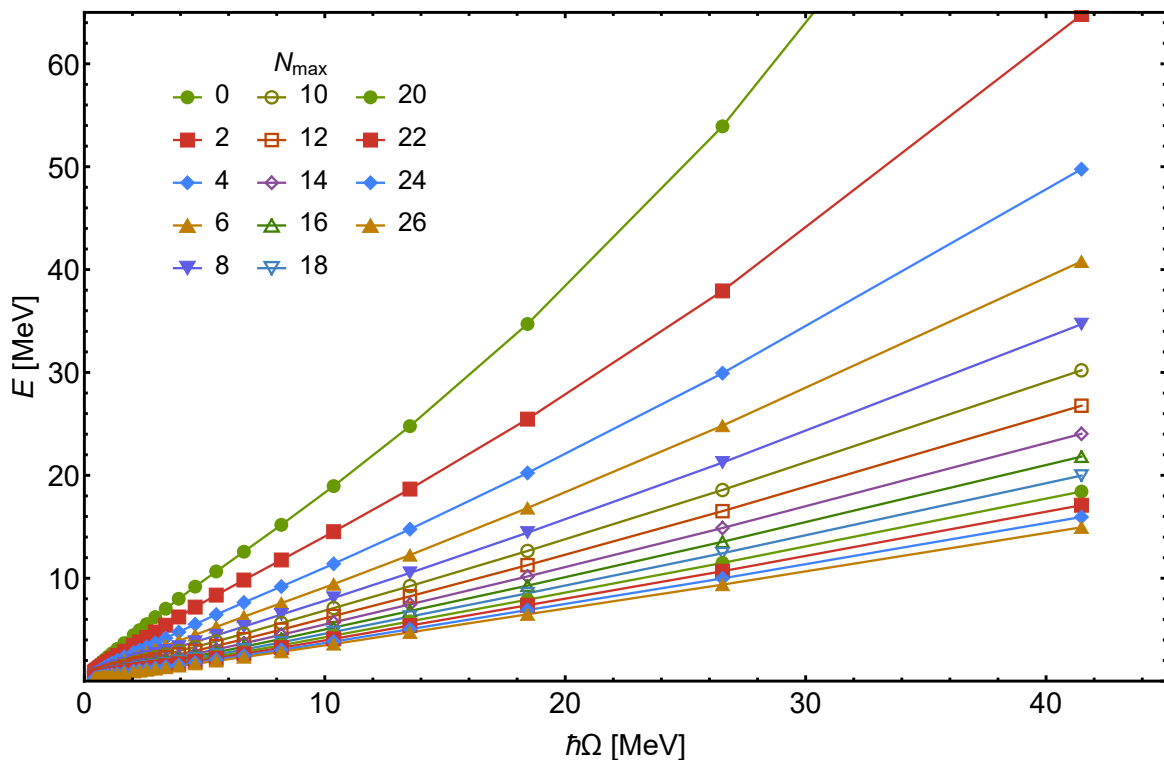


Figure 7.2.: Tetra-neutron NCSM eigenenergies as function of the HO frequency  $\hbar\Omega$ . Interaction  $N^3\text{LO}_{\text{EM}} + N^2\text{LO}_{500,\text{L}}$  SRG evolved with  $\alpha = 0.08 \text{ fm}^4$ .

The data as shown in figure 7.2 are used as input to obtain phase shifts. To better illustrate the data relation further and better see the  $N_{\max}$  convergence in the phase shift than in the  $\delta(E)$  plot, we keep  $\hbar\Omega$  as a variable in figure 7.3. At larger frequencies, the phase shift is approached from below, going to larger angles, with increasing  $N_{\max}$ . At approximately  $\hbar\Omega = 1.5 \text{ MeV}$  and below, this trend is inverted and the phase shift value is approached from above with increasing  $N_{\max}$ .

Finally, going over to the energy as a variable for the phase shift, depicted in figure 7.4, whose overall behaviour resembles figure 7.3, we see that the phase shift values for the largest  $N_{\max}$  lie

## 7. Tetraneutron in the Single-State HORSE

on top of each other in the resolution of the plot, at least at higher energies. In the physically most interesting region of 5 MeV and below, the convergence is not perfect. Overall, the larger model spaces show some improvement in all three considered cases for the convergence of the phase shifts.

The resonance energy and width as a function of  $N_{\max}$ , determined via equations (7.2) and (7.3), are shown in figure 7.5. The positions show a clear trend towards lower energies and widths with increasing  $N_{\max}$ . The given error bars are solely the difference to the previous datum. They give no information about the applicability of equations (7.2) and (7.3). By the definition of an ideal resonance, which lies exactly at  $\delta = 90^\circ$ , see equations (3.112) and (3.113a), the distance of the inflection point to the energy where the phase shift crosses the  $90^\circ$  might give some indication, however, we do not know of any prescription which allows the extraction of uncertainties from this relation in a meaningful way. The exact values of figure 7.5 are listed in table 7.2.

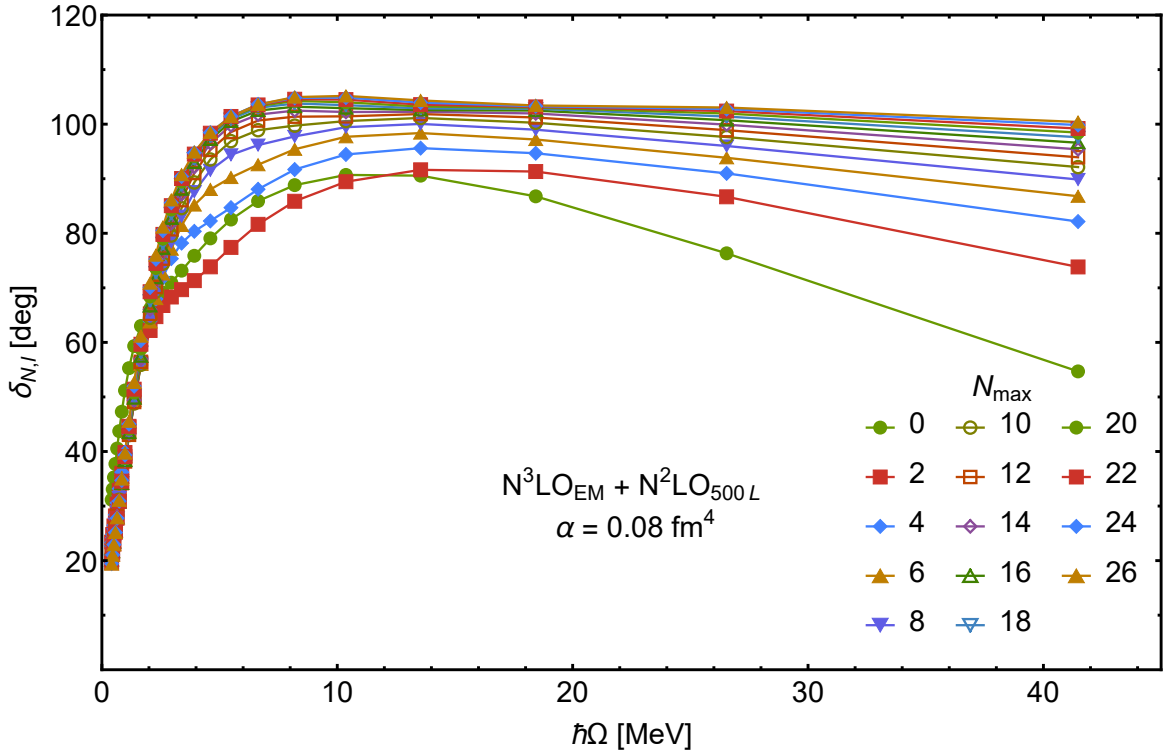


Figure 7.3.: Tetraneutron Single-State HORSE phase shifts as function of the HO frequency  $\hbar\Omega$ . Interaction  $N^3LO_{EM} + N^2LO_{500,L}$  SRG evolved with  $\alpha = 0.08 \text{ fm}^4$ .

$N_{\max}$	16	18	20	22	24	26
$E_R$	0.99	$0.93 \pm 0.06$	$0.85 \pm 0.09$	$0.78 \pm 0.07$	$0.72 \pm 0.06$	$0.65 \pm 0.07$
$\Gamma$	2.28	$2.02 \pm 0.27$	$1.82 \pm 0.20$	$1.64 \pm 0.18$	$1.49 \pm 0.15$	$1.36 \pm 0.13$

Table 7.2.: Resonances and widths as function of  $N_{\max}$ , as shown in figure 7.5. Interaction  $N^3LO_{EM} + N^2LO_{500,L}$ . Uncertainties give difference to previous smaller  $N_{\max}$ .

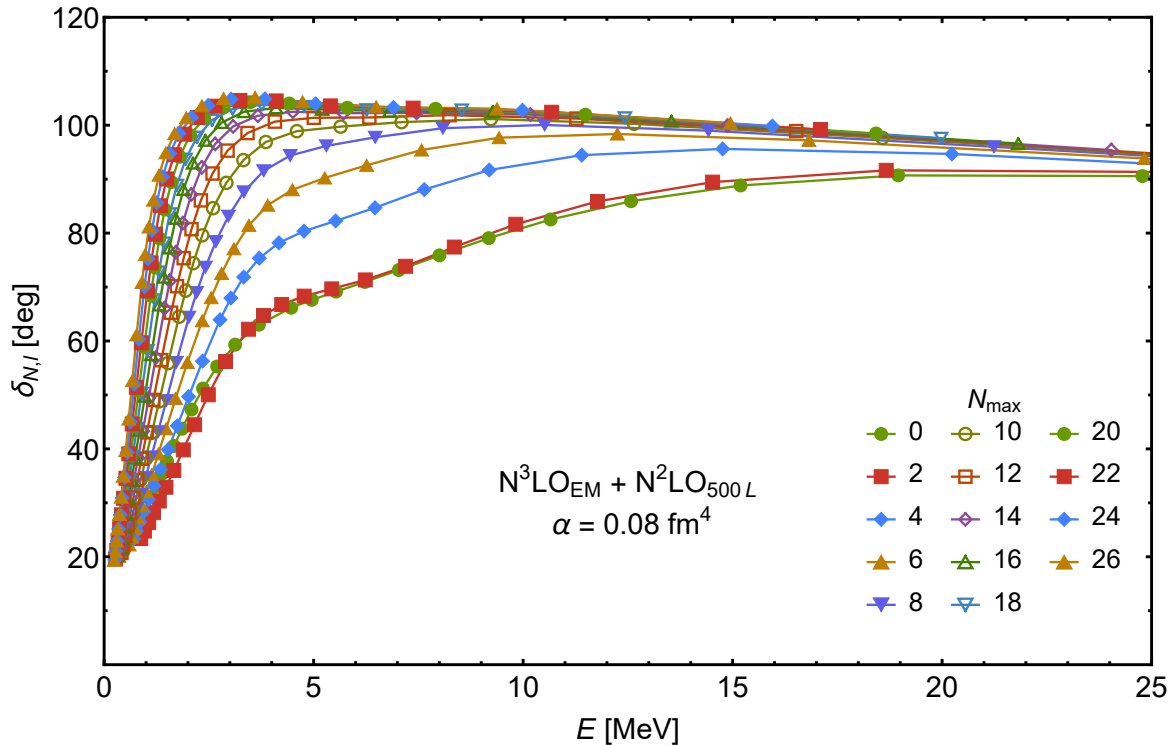


Figure 7.4.: Tetra-neutron phase shift as function of the energy. Interaction  $N^3\text{LO}_{\text{EM}} + N^2\text{LO}_{500,L}$  SRG evolved with  $\alpha = 0.08 \text{ fm}^4$ .

### 7.3.2. Similarity Renormalization Group Dependence

The largest impact on the energy eigenvalue obtained from the diagonalization in a finite model space has the SRG treatment of the interaction. In NCSM many-body calculations, the use of the SRG (or other convergence improving methods) is indispensable. The tetra-neutron is no exception.

The full  $N_{\text{max}}$  sequence of the phase shift as a function of  $E$  with the bare two-body  $N^3\text{LO}_{\text{EM}}$  interaction is depicted in figure 7.6, up to  $N_{\text{max}} = 30$ . Here, the convergence is clearly not reached. The behaviour of the phase shift is also noticeably different from the SRG evolved interactions. The phase shifts exhibit a noticeably different convergence rate in the energy around 3 MeV. In the direct comparison, which can be seen in figure 7.7, one can see how different the phase shifts of the bare and SRG evolved interactions are in the energy region between 1 and 5 MeV, making the terrible convergence of the bare interaction even more apparent. It is only at energies above 6 MeV where the bare interaction approaches the SRG evolved ones in a fashion where a few further steps in  $N_{\text{max}}$  would suffice to reach the same phase shift values.

Additionally, figure 7.7 shows the effect of two different choices of the SRG flow parameter. We used the values of  $\alpha = 0.04 \text{ fm}^4$  and  $\alpha = 0.08 \text{ fm}^4$ . This is done with the NN interaction  $N^3\text{LO}_{\text{EM}}$  as well as the NN+3N interactions  $N^3\text{LO}_{\text{EM}} + N^2\text{LO}_{400,L}$  and  $N^3\text{LO}_{\text{EM}} + N^2\text{LO}_{500,L}$ , to further compare the effects of the cut-off parameter  $\Lambda$ . The maximal differences between the  $\alpha$  values at both  $\Lambda$  are three degrees. The differences between the  $\Lambda = 400$  and  $\Lambda = 500$  at consistent  $\alpha$  is less than one degree. We find that the flow parameter as well as the three-body regulator cut-off have minor impact.

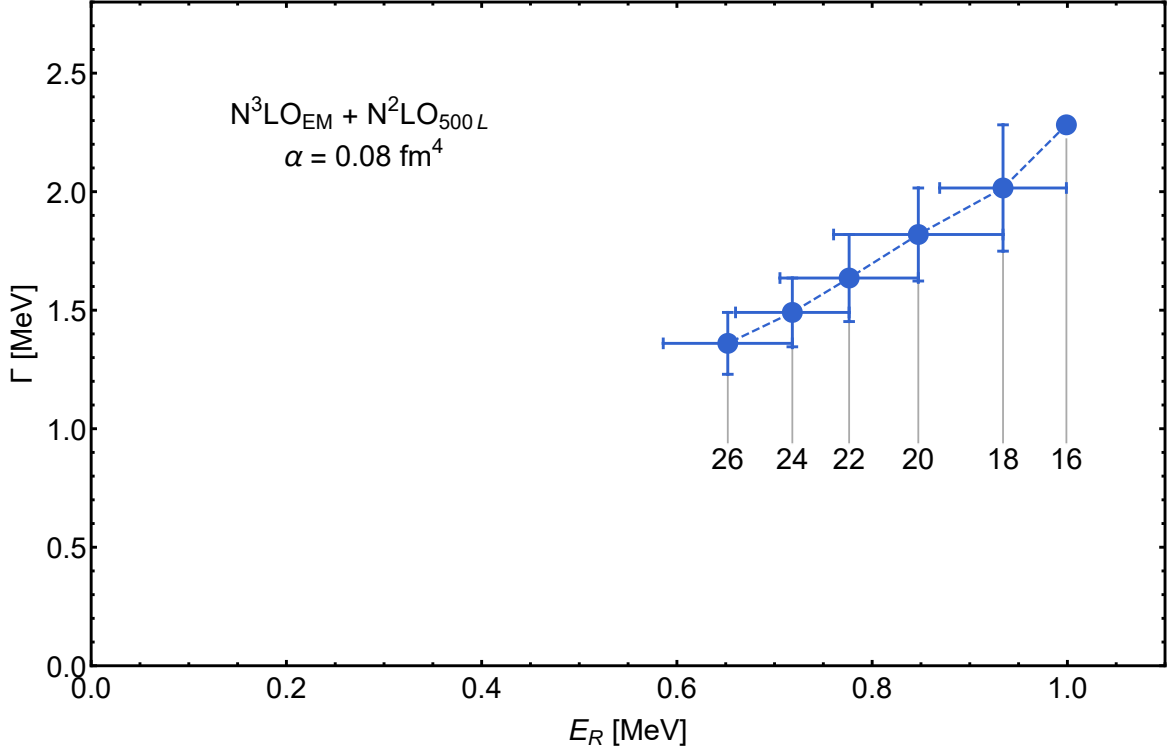


Figure 7.5.: Resonance position  $E_R$  and width  $\Gamma$  for the largest six  $N_{\max}$ , labelled accordingly. The position and width were determined via equations (7.2) and (7.3), respectively. The error bars give the difference to the previous value.

### 7.3.3. Two- and Three-body Interaction Effects

The inclusion of many-body interactions has either been neglected, by stressing the minor impact on other four-body systems, as well as the dominant contribution of the  $^1S_0$  partial wave in the two nucleon interaction, or only been used in a very limited fashion [SPM<sup>+</sup>16, HLCK16, FRMP17, Del18]. To this end, we use the chiral three-body force  $N^2LO_{\Lambda,L}$  [Nav07]. The effect of the three-body interaction on the phase shifts is shown in figure 7.8. The biggest difference can be observed when comparing the SRG evolved NN interaction without the induced 3N with the NN interaction with induced 3N part. The next step of including an initial full 3N interaction has only minor contributions to the phase shift.

This suggest that within the Single-State HORSE method, initial three-body forces have little impact on the existence of the tetraneutron as a nuclear resonance. Whereas SRG induced many-body forces should not be neglected when inquiring about precise resonance parameters.

### 7.3.4. Chiral Order Dependence

The two-body interaction  $N^xLO_{EMN}$  [EMN17] is constructed up to fifth order, that means  $N^4LO_{EMN}$ , and can be investigated for each order separately. It is, therefore, well suited for analyzing the impact of the chiral order on the phase shifts. We compare each chiral order with two SRG flow parameter values,  $\alpha = 0.04 \text{ fm}^4$  and  $\alpha = 0.08 \text{ fm}^4$ , respectively. The calculations were performed including SRG induced three-body interactions. The phase shifts can be seen in figure 7.9. The different orders appear to follow a staggered pattern, where  $N^2LO_{EMN}$  delivers the highest lying phase shift. The next order,  $N^3LO_{EMN}$  provides the lowest, and  $N^4LO_{EMN}$  gives a phase shift between the previous two.

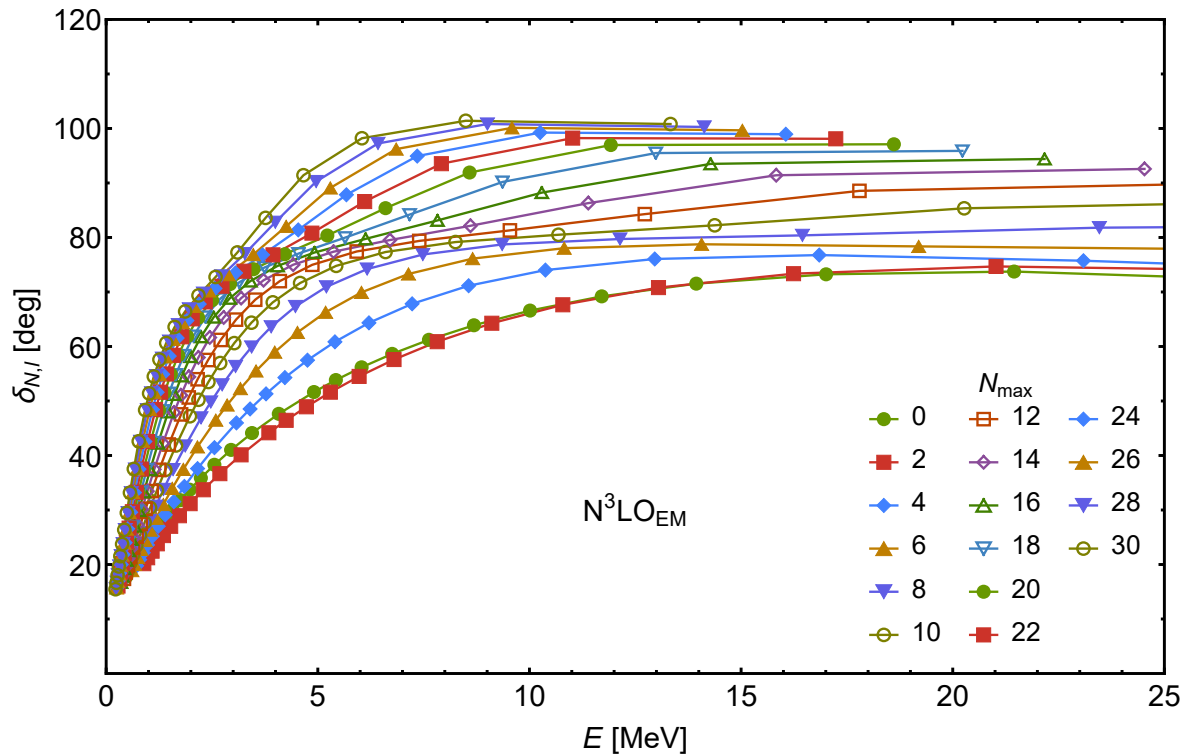


Figure 7.6.: Tetra-neutron phase shift of the NN bare (non-SRG evolved)  $N^3LO_{EM}$  interaction. The  $N_{max}$  sequence is not converged, even with a large model space of  $N_{max} = 30$ .

$T_{lab}$ bin (MeV)	No. of data	LO	NLO	NNLO	N3LO	N4LO
0-100	1975	283	11.9	1.74	1.03	1.00
0-190	2903	235	31.6	3.27	1.35	1.08
0-290	4853	206	51.5	6.30	1.63	1.15

Table 7.3.:  $\chi^2/datum$  for  $pp$ - plus  $np$ -scattering for the 2016 NN data base of the interaction  $N^xLO_{EMN}$ . Values taken from [EMN17].

As the two-nucleon interaction contributes the most to the overall system, it appears reasonable that a systematic increase in the chiral order has a notably bigger impact than, e.g., the inclusion of the initial 3N force. Similarly to the observed effects in the induced versus the initial three-body interaction, going from  $N^2LO$  to  $N^3LO$  leads to the strongest changes in the phase shift, with slightly less changes going to  $N^4LO$ . Considering the  $\chi^2/datum$  of the  $N^xLO_{EMN}$  interaction, the changes in the phase shifts going to higher chiral orders are not surprising. The  $\chi^2/datum$  for each order are shown in table 7.3. The difference between  $N^2LO_{EMN}$  and  $N^3LO_{EMN}$ , are still significant, whereas the change going  $N^4LO_{EMN}$  is smaller.

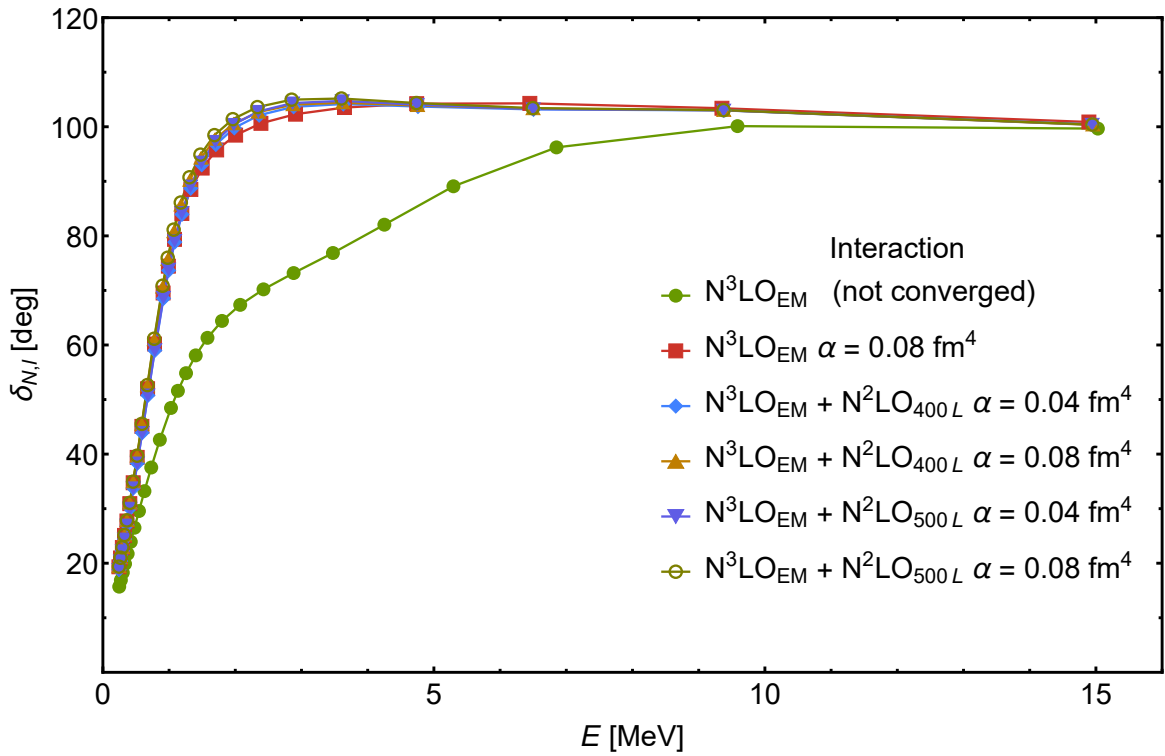


Figure 7.7.: Tetraneutron phase shift comparison of bare interaction with SRG evolved interactions at  $N_{\max} = 26$ . Further comparison of two different SRG flow parameters  $\alpha$ , as well as two values of  $\chi$ EFT three-body cut-off parameter  $\Lambda$ . Note that the bare interaction is far from convergence.

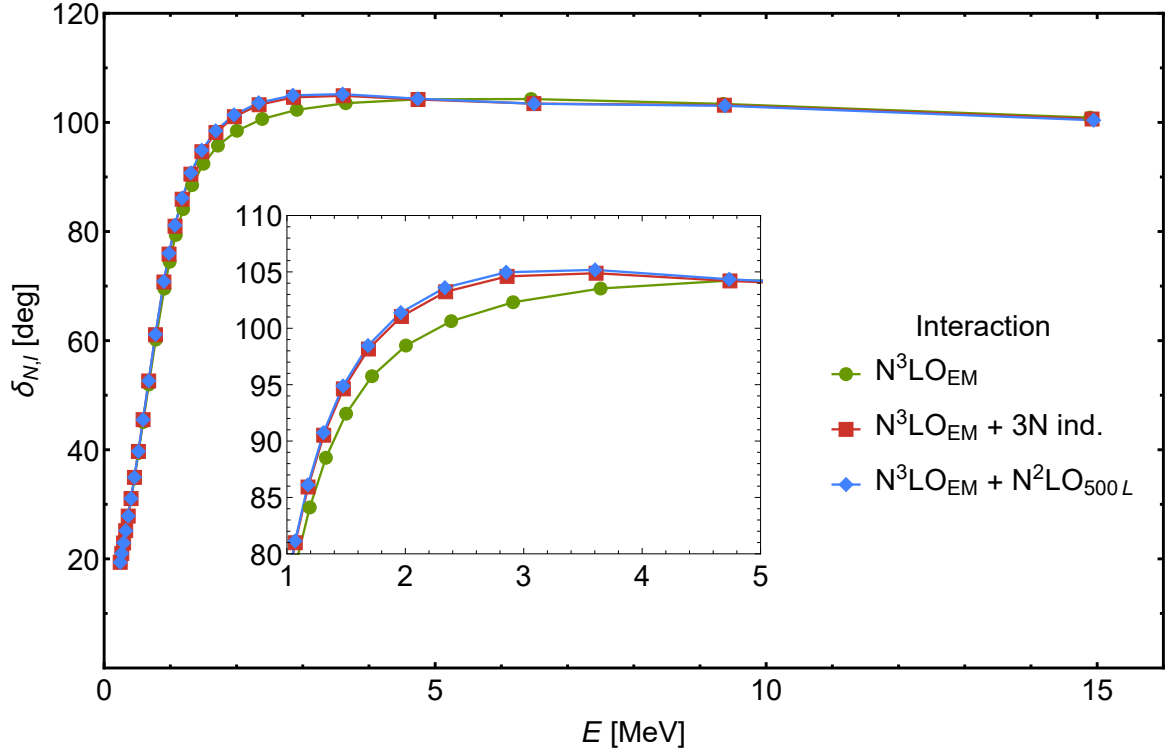


Figure 7.8.: Tetraneutron phase shift comparison of the effect of NN vs. NN+3N induced vs. initial 3N interaction. Shown interactions are  $N^3LO_{EM}$  and  $N^2LO_{500L}$ . SRG parameter  $\alpha = 0.08 \text{ fm}^4$ ,  $N_{\text{max}} = 26$ .

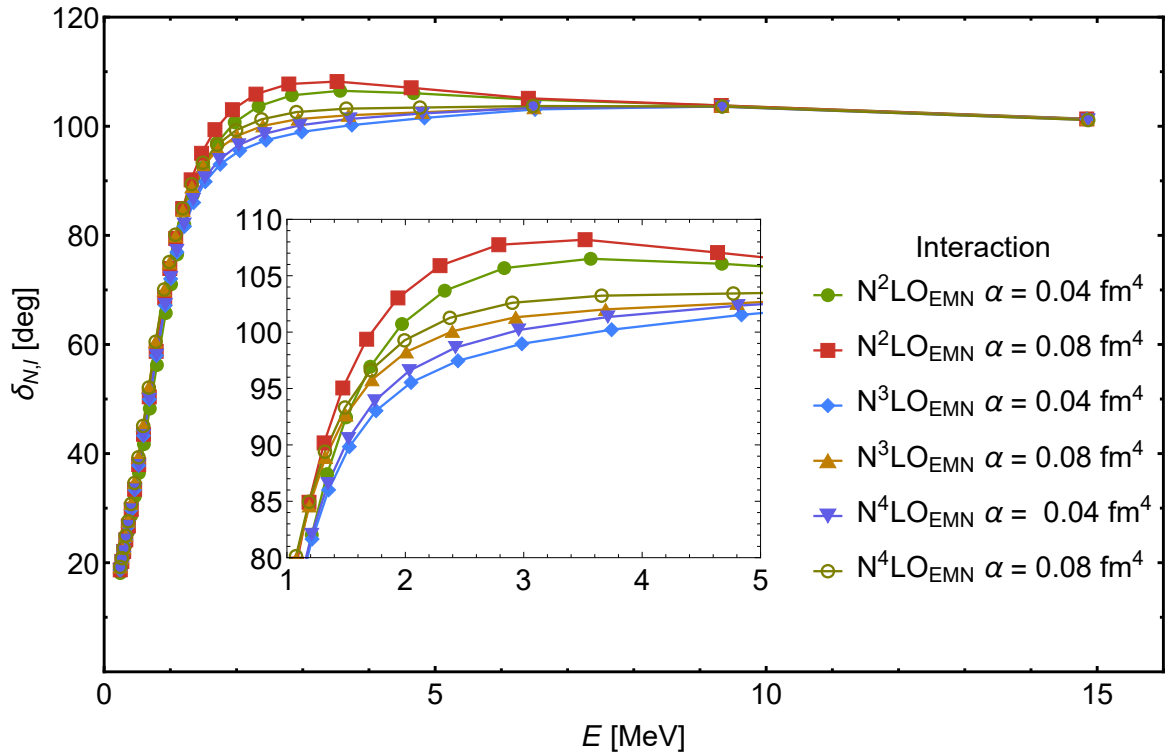


Figure 7.9.: Tetraneutron phase shift dependence of the phase shift on the chiral order. The interaction is  $N^zLO_{EMN}$  including SRG induced three-body forces. All at  $N_{\text{max}} = 26$ .

## 7.4. Conclusion

Considering the differences in the employed interaction, it is quite remarkable that they still produce such similar phase shifts. Similarities in the phase shifts with different interactions in the Single-State HORSE are due to delivering almost the same eigenenergies at the same frequency  $\hbar\Omega$  and same model space  $N_{\max}$  in the pseudo-continuum of the NCSM. That this should be the case is not self-evident.

The use of SRG evolved  $\chi$ EFT interaction results in good  $N_{\max}$  convergence in the higher lying end of the energy that can be reached with the available sets of  $\hbar\Omega$  or  $a_{\text{HO}}$ , respectively.

We find the resonance energy and width for all interactions to be  $E_R \approx 0.7$  MeV and  $\Gamma \approx 1.4$  MeV, however, a stabilization in the inflection points with respect to increasing model space size  $N_{\max}$  is not reached. This can be seen in figure 7.5 and table 7.2, judging by the almost constant difference to the previous values. Considering that the inflection point criterion is only valid for sharp resonances, which is clearly not the case here, the results are a crude approximation. Overall, the presented results extend the published results of reference [SPM<sup>+</sup>16] to larger model spaces, showing a slight adjustment in the resonance position and width. The differences are, considering the mostly unknown uncertainties in this case, small. The robust phase shifts with respect to variation in the input interaction are remarkable. We show that the inclusion of initial three-body forces has small impact compared to the inclusion of SRG induced three-body forces. The increase in chiral order behaves as expected, showing order-by-order convergence, in the sense that the next higher orders has less impact than the previous one.

## 8. Analytic Continuation in the Coupling Constant

The properties of resonances can be inferred from the knowledge of the scattering  $S$ -matrix as is discussed in section 3.4 and section 3.5. Unfortunately, it is computationally demanding to obtain solutions directly in the continuum, when using modern, realistic interactions. There exist various methods to obtain resonance parameters, that treat bound and scattering states on the same footing. However, they have to contend themselves with drastically reduced reach in terms of accuracy or size of the system etc., compared to what is possible for pure bound-state calculation. Among them are the  $J$ -matrix based HORSE method [AYHA08, SMVM12, SMMV16], discussed chapter 6, and the No-Core Shell Model with RGM (NCSM/RGM) [QN08, QN09, NRQ11], and the NCSM with Continuum (NCSMC) [BNQ13b, HQN15]. Though the latter method is very promising, calculations are not continued onto the complex plane on which resonance are best understood. The extension of the basis within the NCSM with explicit scattering states is referred to as NCGSM [PRM<sup>+</sup>13, FRMP17], and results in a complex eigenvalue problem. Regardless the method of choice, the most reliable and accurate ones have to provide access to the complex plane by some form of analytic continuation.

One approach to obtain access to the complex plane is the Analytic Continuation in the Coupling Constant (ACCC). Even though the properties of the solutions to the Schrödinger equation as a function of the interaction strength were investigated by R. Newton in the 1960's [New60, New82], the proposition to also use them to obtain resonance parameters is due to the work presented by Kukulin, Krasnopol'sky, and Hóráček in the references [KK77, KK78, KKH89]. The ACCC has the appeal of only requiring bound-state calculations to be performed. The continuum is accessed by finding a fit to the bound-state energies (or wave numbers), as a function of the coupling strength of a modified interaction potential. Some examples of its more recent application in nuclear physics include the excited states of  ${}^6\text{He}$  and  ${}^6\text{Li}$  as three-body systems [TSV97], two- and three-body cluster approximations for  ${}^5\text{He}$ ,  ${}^5\text{Li}$ ,  ${}^9\text{Be}$ , and  ${}^9\text{B}$  [TSVL99], the soft-dipole resonance in  ${}^6\text{He}$ , combined with the Complex Scaling method [Aoy03], a self-consistent relativistic mean field approach with  ${}^{60}\text{Ca}$  and  ${}^{122}\text{Zr}$  [ZMZH04], the tetraneutron [LC05], and the second  $2^+$  state of  ${}^{12}\text{C}$  [FHT06]. Even more recently, various studies of the use of the ACCC in quantum chemistry were published [HSPT09, PvMM<sup>+</sup>13, ČPH16, WHGM17, SMHE17]. They are of interest for this work, because they successfully demonstrate the combination of the ACCC with Configuration Interaction (CI) based many-body solvers.

We have established that a resonance as well as a bound state are singularities in the  $S$ -matrix, which in turn corresponds to a zero in the Jost function  $\mathcal{F}_{\ell+} \equiv \mathcal{F}_{\ell}$ . Proving that the Jost function is analytic in the coupling constant provides the basis by which we can track the  $S$ -matrix singularity of a bound state into the continuum by changing the coupling strength. The location of the singularity in the bound-state regime is directly determined by the energy of the bound state. Solving the Schrödinger equation for a Hamiltonian with a modified potential

$$H = T + \lambda V, \tag{8.1}$$

## 8. Analytic Continuation in the Coupling Constant

at different values of  $\lambda$  then should allow us to, e.g., find a fit which can be extrapolated into the unbound energy range and provide the location of the  $S$ -matrix pole in the continuum and thus the resonance. Finding an expression for the energy as function of the coupling constant,  $E(\lambda)$ , is the goal of the analytic continuation in the coupling constant, though it is advantageous to use the wave number  $k = \sqrt{\frac{2\mu E}{\hbar^2}}$ . The reason being that the Jost function and its zeros lie in the complex plane, see figure 3.2. Inserting (negative) bound-state energies into the  $E$ - $k$ -relation puts the solution in the correct domain. This also means that the continuation in the energy does not give information about the width of the scattering state in the form of an imaginary part. The wave-number can provide this information. The purpose of this chapter and the ACCC is, therefore, to construct an expression of the wave number

$$k \equiv k_\ell(\lambda), \quad (8.2)$$

for a partial wave with angular momentum  $\ell$ , which uses bound-state calculations to allow us to extrapolate into the unbound regime. To obtain such an expression, we first want to prove that the Jost function is analytic in the coupling constant. After that, we need to find the general form a low energy expansion of  $k_\ell(\lambda)$  has, allowing us to choose appropriate parametrization or fit functions.

### 8.1. Proof of Analyticity

A resonance, as well as a bound state is defined via the relation of the two Jost functions, see equation (3.105). The Jost functions are analytic both in going from  $k \in \mathbb{R}$  to  $k \in \mathbb{C}$  as well as in the interaction strength.

Any analytic property of the Jost function  $\mathcal{F}_\ell$  follows directly from the same properties of its defining constituents, the regular and irregular solution  $\phi_\ell$  and  $f_{\ell+}$ , respectively. They solve the (radial) Schrödinger equation with strength parameter  $\lambda$ , with their defining boundary conditions

$$\left( -\frac{d^2}{dr^2} + \frac{\ell(\ell+1)}{r^2} + \lambda V(r) \right) u_\ell(r) = k^2 u_\ell(r), \quad (8.3)$$

where the potential has absorbed other constants  $\hbar^2/2\mu V \rightarrow V$ . To show that  $\mathcal{F}_\ell$  is analytic in the strength parameter of either the full interaction or a perturbative potential, one needs to show this for  $\phi_\ell$  and  $f_{\ell+}$ . We sketch the proof of this in the following way:

- Transform differential equation into integral equation with the help of Green's function with appropriate boundary conditions
- Exploit that the integral is of the Volterra type, thus solvable by iteration
- Show that the iteration converges absolutely for any  $\lambda$  and  $k$ , if the potential fulfils certain conditions

We do this by casting the differential equations for the two functions to integral equations. The proof is taken from reference [New82], where more details are found. The regular solution in integral form, see equation (3.79), reads

$$\phi_\ell(k, r) = \phi_\ell^{(0)}(k, r) + \int_0^r dr' g_\ell(k; r, r') V(r') \phi_\ell(k, r'). \quad (8.4)$$

The integral only goes up to  $r$ . The boundary conditions in equation (3.77) are defined at  $r = 0$ . Consequently, casting the differential equation into an integral equation requires the

corresponding boundary conditions and Green's function  $g_\ell(k; r, r')$  for these boundary conditions. We use a lower case  $g$  to differentiate the Green's functions belonging to different boundary conditions. For the case of  $\ell = 0$ , the first iteration free solution, also referred to as zero-order function, reads

$$\phi_0^{(0)}(k, r) \equiv \phi^{(0)}(k, r) = \frac{\sin(kr)}{k}, \quad (8.5)$$

and the Green's function

$$g(k; r, r') = \begin{cases} \frac{\sin(k(r-r'))}{k} & \text{for } r > r' \\ 0 & \text{for } r < r'. \end{cases} \quad (8.6)$$

For arbitrary  $\ell \neq 0$ , these functions read

$$\phi_\ell^{(0)}(k, r) = r^{\frac{1}{2}} \left(\frac{k}{2}\right)^{-\ell-\frac{1}{2}} \Gamma\left(\ell + \frac{3}{2}\right) J_{\ell+\frac{1}{2}}(kr), \quad (8.7)$$

and for  $r > r'$

$$g_\ell(k; r, r') = k r' r (j_\ell(k, r') n_\ell(k, r) - j_\ell(k, r) n_\ell(k, r')) \quad (8.8)$$

$$= \frac{(r r')^{\frac{1}{2}} \pi}{2 \cos(\pi \ell)} \left( J_{\ell-\frac{1}{2}}(kr) J_{-\ell-\frac{1}{2}}(kr') - J_{\ell+\frac{1}{2}}(kr') J_{-\ell-\frac{1}{2}}(kr) \right), \quad (8.9)$$

with  $j_\ell(k, r')$  and  $n_\ell(k, r)$  being the spherical Bessel functions and  $J_n(kr)$  being the Bessel functions of the first kind. We arrive at a proof for the analyticity of the regular and irregular solution by first exploiting the fact that equation (8.4) is of the Volterra-type [LP12, New82], allowing us to iteratively construct a solution. Considering  $\ell = 0$ , we write the power series ansatz

$$\phi(k, r) = \sum_{n=0}^{\infty} \lambda^n \phi^{(n)}(k, r) \quad (8.10)$$

$$\phi^{(0)}(k, r) = \frac{\sin(kr)}{k} \quad (8.11)$$

$$\phi^{(n)}(k, r) = \frac{1}{k} \int_0^r dr' \sin(k(r-r')) V(r') \phi^{(n-1)}(k, r'). \quad (8.12)$$

The above ansatz remains the same for  $\ell \neq 0$ . For the sake of readability, we only treat the  $\ell = 0$  case in the following. With this power series, we are able to show that they converge absolutely with the following inequalities. For all  $k$  and all  $r \in \mathbb{R}, r \geq 0$ , there exists a constant  $C$ , such that the inequalities hold

$$|\sin(kr)| \leq C e^{|\operatorname{Im}k|r} \frac{|k|r}{1 + |k|r}, \quad (8.13)$$

and for all  $k$  and all  $r \in \mathbb{R}, r \geq r' \geq 0$

$$|\sin(k(r-r'))| \leq C e^{|\operatorname{Im}k|(r-r')} \frac{|k|r}{1 + |k|r}. \quad (8.14)$$

Introducing the definition

$$\left| \phi^{(n)}(k, r) \right| = e^{|\operatorname{Im}k|r} \frac{r}{1 + |k|r} \psi^{(n)}(k, r), \quad (8.15)$$

## 8. Analytic Continuation in the Coupling Constant

allows us to write

$$\psi^{(n)}(k, r) \leq C \int_0^r dr' |V(r')| \frac{r'}{1 + |k|r} \psi^{(n-1)}(k, r') \quad (8.16)$$

$$\leq C^{n+1} \int_0^r dr_n \dots \int_0^{r_2} dr_1 |V(r_1)V(r_2) \dots V(r_n)| \frac{r_1}{1 + |k|r_1} \dots \frac{r_n}{1 + |k|r_n} \quad (8.17)$$

$$\leq C^{n+1} \frac{1}{n!} \left( \int_0^r dr' |V(r')| \frac{r'}{1 + |k|r'} \right)^n, \quad (8.18)$$

we arrive at (still for  $\ell = 0$ )

$$|\phi(k, r)| \leq \sum_{n=0}^{\infty} |\lambda|^n |\phi^{(n)}(k, r)| \quad (8.19)$$

$$= e^{|\text{Im}k|r} \sum_{n=0}^{\infty} |\lambda|^n \psi^{(n)}(k, r) \quad (8.20)$$

$$\leq C e^{|\text{Im}k|r} \frac{r}{1 + |k|r} \exp \left( |\lambda| C \int_0^r dr' |V(r')| \frac{r'}{1 + |k|r'} \right). \quad (8.21)$$

This converges absolutely for all  $\lambda$  and  $k$  under the condition that

$$\int_0^{\infty} dr r |V(r)| < \infty. \quad (8.22)$$

Similarly, we can write for the irregular solution an iterative approach

$$f_{\pm}(k, r) = \sum_{n=0}^{\infty} \lambda^n f_{\pm}^{(n)}(k, r) \quad (8.23)$$

$$f_{\pm}^{(0)}(k, r) = e^{\pm ikr} \quad (8.23)$$

$$f_{\pm}^{(n)}(k, r) = -\frac{1}{k} \int_r^{\infty} dr' \sin(k(r - r')) V(r') f_{\pm}^{(n-1)}(r'). \quad (8.24)$$

introducing a definition in analogy to equation (8.15)

$$h_{\pm}^{(n)(k, r)} = f_{\pm}^{(n)}(k, r) e^{\mp ikr}, \quad (8.25)$$

and using equation (8.14), we arrive at the inequality

$$|f_{\pm}(k, r)| \leq C e^{\mp \text{Im}kr} \exp \left( |\lambda| C \int_r^{\infty} dr' |V(r')| \frac{r'}{1 + |k|r'} \exp((|\text{Im}k| \mp \text{Im}k)(r' - r)) \right). \quad (8.26)$$

The irregular solution is thus absolutely convergent for power series in the coupling constant  $\lambda$ , if

$$\int_0^{\infty} dr |V(r)| e^{(|\text{Im}k| \mp \text{Im}k)r} < \infty. \quad (8.27)$$

The above discussion only treats the case of  $\ell = 0$ , which does not impact the condition put upon the potential in equations (8.22) and (8.27). The inequalities in equation (8.13) and equation (8.14) have to be adapted accordingly, see reference [New82] for a detailed treatment.

Having shown that the Jost function is analytic in the interaction strength parameter, we want to track the zeros of the Jost function as they go from the bound to the unbound regime with the help of an expression for the wave number  $k_{\ell}(\lambda)$ . To be able to do that, we need to know

how the Jost function depends on  $k$ , which also provides the form how  $k$  depends on  $\lambda$  close to the continuum threshold. To that end, we introduce the integral representation of the Jost function [Dru87, New82]

$$\mathcal{F}_\ell(\lambda, k) = 1 + \frac{i\lambda k^\ell}{(2\ell + 1)!!} \int_0^\infty dr \sqrt{\frac{1}{2}\pi kr} H_{\ell+1/2}^{(1)}(kr) V(r) \phi_\ell(k, r). \quad (8.28)$$

Here,  $H_{\ell+1/2}^{(1)}(kr)$  is the Hankel function of the first kind, also known as Bessel function of the third kind [DLM14]. From the integral representation, we can see how  $\mathcal{F}_\ell(\lambda, k)$  depends on  $k$ , by considering the individual constituents. We use that the Hankel function can be written as [DLM14]

$$H_\nu^{(1)}(z) = i \csc(\nu\pi) (e^{-\nu\pi i} J_\nu(z) - J_{-\nu}(z)), \quad (8.29)$$

and the Bessel functions in turn read [DLM14]

$$J_\nu(z) = \left(\frac{1}{2}z\right)^\nu \sum_{k=0}^{\infty} (-1)^k \frac{\left(\frac{1}{4}z^2\right)^k}{k! \Gamma(\nu + k + 1)}. \quad (8.30)$$

From equation (3.81), which is also given in equation (8.7), together with the Green's function for the regular boundary conditions, equation (8.9), as well as the Volterra-type nature of  $\phi_\ell(k, r)$ , discussed in the previous paragraphs, we infer the  $k$  dependence of  $\phi_\ell(k, r)$  must be of the same kind as the Bessel function. The same conclusion for  $\phi_\ell(k, r)$  can be reached when considering the boundary conditions in equation (3.77) and the resulting symmetry in equation (3.83). The regular solution must, therefore, be an even function in  $k$ . We insert the schematic  $k$  dependences into equation (8.28), where we drop all other parts not dependent on  $k$ , and have

$$\mathcal{F}_\ell(\lambda, k) \sim 1 + \frac{i\lambda k^\ell}{(2\ell + 1)!!} \int_0^\infty dr \dots \sqrt{k} \left( k^{\ell+1/2} \sum_{n=0}^{\infty} \dots k^{2n} + k^{-\ell-1/2} \sum_{n=0}^{\infty} \dots k^{2n} \right) \dots \sum_{n=0}^{\infty} \dots k^{2n} \quad (8.31)$$

$$\sim \left( k^{2\ell+1} \sum_{n=0}^{\infty} \dots k^{2n} + \sum_{n=0}^{\infty} \dots k^{2n} \right) \sum_{n=0}^{\infty} \dots k^{2n}. \quad (8.32)$$

We see that the Jost function is dependent of  $k$  only in even powers, except for the first  $k^{2\ell+1}$ . As a consequence, we are able to parametrize the Jost function at fixed values of  $\lambda$

$$\mathcal{F}_\ell(\lambda_{\text{const}}, k(\lambda)) = A_\ell(k) + ik^{2\ell+1} B_\ell(k), \quad (8.33)$$

where the terms  $A_\ell(k)$  and  $B_\ell(k)$  are of the type

$$\mathcal{F}_\ell(\lambda_{\text{const}}, k) = (a_0 + a_2 k^2 + a_4 k^4 + \dots) + ik^{2\ell+1} (b_0 + b_2 k^2 + b_4 k^4 + \dots), \quad (8.34)$$

meaning they absorb all other, non- $k$ -dependent parts in the coefficients  $a_i$  and  $b_j$ . Comparing with the integral representation in equation (8.28), it is apparent that they also are integrals over the radial variable. This corresponds to the result given in references [Dru87, OS72, New82].

In conjunction with the analytic properties of the Jost function w.r.t. to  $\lambda$ , this leads to an expansion of  $k$  around the bound-state-continuum-threshold  $\lambda_0$ , with  $x = \sqrt{\lambda - \lambda_0}$  [OS72]

$$k_\ell(\lambda) = \sum_{j=1}^{\ell} A_j x^{2j-1} + \sum_{j=2\ell}^{\infty} B_j x^j. \quad (8.35)$$

## 8. Analytic Continuation in the Coupling Constant

An alternative approach to arrive at this expression is given in appendix D. Only considering the leading terms, one arrives at the relation

$$k_0(\lambda) \sim (\lambda - \bar{\lambda}_0), \quad (8.36)$$

with  $\bar{\lambda}_0$  such that  $k_0(\bar{\lambda}_0) = 0$ . For  $\ell \neq 0$ , we have

$$k_\ell(\lambda) \sim \pm c \sqrt{\lambda - \lambda_0}, \quad (8.37)$$

with some constant  $c$ . Any parametrization for the analytic continuation needs to incorporate this behaviour close to the continuum threshold.

### 8.2. Using Padé Approximants

The analytic properties of the Jost functions under variation of the coupling constant allow us to modify the Hamiltonian by means of varying the interaction strength and study the evolution of its eigenenergies as a function of this binding parameter. To actually achieve this binding, two general methods are possible. Binding the initial Hamiltonian  $H$  with an external potential  $V_{\text{ext}}$

$$H(\lambda) = H + \lambda V_{\text{ext}}, \quad (8.38)$$

or modifying the initial interaction either completely by a prefactor

$$H(\lambda) = T + \lambda V_{\text{init}}, \quad (8.39)$$

or in partially, if the potential can be separated accordingly, e.g., in an primarily attractive and repulsive part

$$H(\lambda) = T + (V - V^p) + \lambda V^p, \quad (8.40)$$

where  $V^p$  is either the attractive part, which is increase with  $\lambda$ , or the repulsive part, being decreased with  $\lambda$ . Which method to choose can be a matter of practicality, e.g. one might be more complicated to implement, etc. The use of an external potential can be used to only bind specific  $A$ -body substructures, while leaving others untouched. We discuss this with a focus on the application within the Jacobi-NCSM in section 8.3.

With a properly bound system, we can exploit the threshold behaviour of the wave number by using the relations from the previous section, i.e., equation (8.35) and the resulting equations (8.36) and (8.37),

$$k_\ell \sim \sqrt{\lambda - \lambda_0} \quad \text{for } \ell \neq 0 \quad (8.41a)$$

$$k_0 \sim \lambda - \bar{\lambda}_0 \quad \text{for } \ell = 0. \quad (8.41b)$$

The term  $\bar{\lambda}_0$  accommodates the branch point relation for  $s$ -waves

$$k_0 = i\kappa = k_0(\lambda_0). \quad (8.42)$$

A distinct feature of the ACCC as proposed in references [KK77, KKH89], is the use of Padé approximants to describe the  $k(\lambda)$  trajectories, instead of, e.g., equation (8.35), or some similar Taylor expansion.

The use of Padé approximants in this case has some clear advantages, among them being

1. Convergence on the whole domain of analyticity, as opposed to divergence of equation (8.35) at points far away from the threshold [KKH89, BGM96].

2. Padé approximants fulfil the unitarity condition of the  $S$ -matrix, equation (3.26) and equation (A.5).
3. Poles are described easily, due to the fractional nature of the Padé approximants.

We introduce the Padé approximation of a function  $f(z)$ , which is representable as power series of the form

$$f(z) = \sum_{j=0}^{\infty} f_j x^j. \quad (8.43)$$

The Padé approximant of the function  $f(z)$  is given as a rational fractional of two polynomials [BGM96]

$$f^{[N,M]}(z) = \frac{P_N(z)}{Q_M(z)} = f(z) + \mathcal{O}(z^{N+M+1}), \quad (8.44)$$

with  $N$  and  $M$  being the order of the respective polynomials. A further overview of properties of Padé approximants is given appendix A.

We discuss the parametrization of the wave number via Padé approximants. Introducing the variable  $x = \sqrt{\lambda - \lambda_0}$  for the case of  $\ell \neq 0$ , we can write the wave number as

$$k_\ell(x) \approx k_\ell^{[N,M]}(x) = \frac{P_N(x)}{Q_M(x)} = i \frac{c_0 + c_1 x + \dots + c_N x^N}{1 + d_1 x + \dots + d_M x^M} \quad (8.45a)$$

$$k_\ell(x) \approx \dots = i \frac{c_1 x + \dots + c_N x^N}{1 + d_1 x + \dots + d_M x^M}. \quad (8.45b)$$

We can choose to include or exclude the parameter  $c_0$ , to either provide a stabilizing constant for the fit or to enforce the  $k_\ell(0) = 0$  criterion. The parameters of the Padé approximation are obtained by minimization of  $\chi^2$  type problem

$$\chi^2 = \frac{1}{L} \sum_{i=1}^L \frac{1}{\sigma_i^2} \left| \frac{P_N(x)}{Q_M(x)} - k_i \right|^2. \quad (8.46)$$

The quantity  $L$  is the number of data points and  $\sigma_i$  denotes the weights corresponding to the (numerical) uncertainty of the  $i$ -th data point  $k_i$ . In the case of unknown uncertainties, they are chosen as  $\sigma_i = 1$ .

We want to emphasize the important detail, that all calculations and fits are performed with real parameters, both the input data and the fit parameters themselves. It is by virtue of going over to the wave number  $k$  and the variable  $x = \sqrt{\lambda - \lambda_0}$  that we have access to the complex plane, where  $k$  allows the continuation and  $x$  determines how the trajectories of the resonance pole move through the complex plane.

The function obtained in this way can be evaluated at any  $\lambda$ , especially at the value of  $\lambda$  corresponding to the unmodified Hamiltonian (in most instances this would be  $\lambda = 0$  or 1). Resonance parameters are obtained via equation (3.100)

$$E_R - i\Gamma/2 = \frac{\hbar^2 (k_{\text{Re}} - i k_{\text{Im}})^2}{2\mu}, \quad (8.47)$$

with  $\mu$  being the reduced mass. Consequently, the position and width read

$$E_R = \frac{\hbar^2 (k_{\text{Re}}^2 - k_{\text{Im}}^2)}{2\mu} \quad \text{and} \quad \Gamma = \frac{2\hbar^2}{\mu} k_{\text{Re}} k_{\text{Im}}. \quad (8.48)$$

## 8. Analytic Continuation in the Coupling Constant

The treatment of many-body systems requires to account for the formation of possible sub-structures. As a simple example, consider the break-up of an  $A$ -body system into a two-cluster configuration, e.g., of the type

$$A \rightarrow (A - b) + b,$$

where any other many-body threshold lies far enough away. For example, if the  $A$ -body Hamiltonian can be written as

$$H(\lambda_p) = \sum_{i=1}^A h_0(i) + \sum_{i<j}^A (V_{ij} - V_{ij}^p) + \lambda_p \sum_{i<j}^A V_{ij}^p, \quad (8.49)$$

with some primarily attractive (or repulsive) potential term  $V_{ij}^p$ , and the single-particle energies  $h_0(i)$ . The analytic continuation via Padé fit is then performed with respect to the break-up threshold

$$k(\lambda_p) = \sqrt{E_A(\lambda_p) - E_{\text{thr}}(\lambda_p)} = \frac{P_N(\lambda_p)}{Q_M(\lambda_p)}. \quad (8.50)$$

Though viable, this procedure introduces further computational effort and uncertainties, which propagate, e.g., to the threshold parameter. An  $A$ -body system can exhibit complex sub-structures, which are all affected by a modification of this kind. It is best to avoid this approach, if it is possible. This is the motivation to the binding method introduced in section 8.3.2.

### 8.2.1. Inverse ACCC

The inverse analytic continuation in the coupling constant, or IACCC for short, is the Padé fit of the coupling constant  $\lambda$  as a function of the wave number  $k$ . Considering the  $\ell \neq 0$  case, we write

$$\lambda^{[N,M]}(k) = i \frac{\lambda_0 + \lambda_2 k^2 + \dots + \lambda_N k^N}{1 + \mu_2 k^2 + \dots + \mu_M k^M}. \quad (8.51)$$

The linear term is absent, which is the consequence of the square root relation in the low energy behaviour of  $k \propto \sqrt{\lambda - \lambda_0}$ . Analogous to equation (8.46), we minimize the function

$$\chi^2 = \frac{1}{L} \sum_{i=1}^L \frac{1}{\sigma_i^2} \left| \frac{P_N(k)}{Q_M(k)} - \lambda_i \right|^2. \quad (8.52)$$

The use of the inverse approach becomes clear when looking at the first term of equation (8.51), which is  $\lambda_0$ . In this setting, there is no need to determine the threshold value  $\lambda_0$  beforehand, as it is the first coefficient of the fit. The IACCC can be either used to obtain the value of  $\lambda_0$ , or the resonance parameters can be extracted directly. The resonance parameters are obtained by finding the roots of the nominator, while simultaneously ensuring that the denominator is non-zero,

$$P_N(k) = 0 \quad \text{and} \quad Q_M(k) \neq 0. \quad (8.53)$$

This gives up to  $N$  roots, grouped in pairs of two, symmetrical along the imaginary axis. In the absence of any numerical uncertainties in the data to be fitted, the roots appearing at higher orders correspond to other resonances and virtual states [HPČ14].

## 8.3. Using the ACCC with the Jacobi-NCSM

In this section, we discuss how the binding of a physical system within the Jacobi-NCSM, discussed in chapter 5, can be achieved.

Incorporating a binding scheme in a many-body bound-state method is a question of the physical consequences the binding has on sub-structures, and how they have to be treated to correctly describe the physical system. The equations (8.38) and (8.39), give the two ways a system can be bound artificially, that is either by some additional potential  $V_{\text{ext}}$ , or by modification of the initial interaction  $V_{\text{init}}$ . Though, theoretically equivalent, the latter can complicate the ACCC by introducing bound sub-clusters, each with thresholds which have to be treated, when applied to the NN- and 3N-interaction. This increases computational cost and uncertainties, and is thus best avoided. An additional potential  $V_{\text{ext}}$ , on the other hand, can be formulated in such a way, that it is an irreducible  $a$ -body operator, with, e.g.,  $2 \leq a \leq A$ , depending on the requirements. An additional benefit is the capability to fine tune  $V_{\text{ext}}$ , to, e.g., result in smooth transitions from unbound to bound states [SMHE17].

The advantages are counterbalanced with the increased difficulty to implement such an additional potential. The inclusion of irreducible four-body interaction into the NCSM is a laborious undertaking, as well as significantly increasing the computational cost. Other methods related to Jacobi-Faddeev implementations, or having a direct connection to a hyperspherical formulations, do not suffer the same difficulties and can implement such an additional binding potential relatively easily. On the other side, the implementation of a simple factor in front of the interaction is easily done. Nevertheless, As works in other fields of physics have shown, the ACCC can be successfully used with Configuration Interaction (CI) type methods and additional binding potentials [HP10, SMHE17, WHGM17]. However, these application from theoretical chemistry do not suffer from the same restrictions in computational cost as the ones in nuclear structure. In other, modern applications of the ACCC, the use of an external potential is the method of choice, see e.g. references [TSVL99, Aoy03, LC05].

We are thus interested to find a way to bind the four-body system, without binding the three- and two-body sub-systems. This is the motivation for the approach we dubbed eigenvector binding, presented in section 8.3.2, giving a additional “quasi-external” potential, constructed from smaller NCSM model space eigenvectors. This avoids the difficult task of implementing a new four-body interaction. Due to the ease of implementation, we also present the modification of interaction matrix elements.

### 8.3.1. Modification of Matrix Elements

To achieve binding, it is possible to modify the strength of the initial interaction, either completely or in parts. The use of a prefactor in the form of

$$H_\lambda = T + \lambda V, \quad (8.54)$$

in an  $A$ -body system, where  $V$  contain two- and three-body interactions, has the drawback of increasing all contributions indiscriminately of being repulsive or attractive, thus not necessarily being practical, and possibly creating bound substructures. For some phenomenological potentials, the distinction into attractive and repulsive parts is possible, and can be used in the ACCC, as was already demonstrated in [KKH89]. Realistic nuclear interaction cannot be split up in this form in any way. To use any interaction in the Jacobi-NCSM, they are expanded into relative coordinates harmonic oscillator matrix elements and exist as partial waves of the total orbital angular momentum  $L$ , for a given total angular momentum  $J$ . It is possible to modify the interaction on both the two- and three-body level separately

$$H_\lambda = T + \lambda_{2b} V_{NN} + \lambda_{3b} V_{3N}, \quad (8.55)$$

or in their individual partial waves.

The modification of the complete NN and 3N interaction applied to the tetra-neutron is discussed in section 9.3.1. The modification of the NN and 3N interaction excluding the  $^1S_0$  partial

## 8. Analytic Continuation in the Coupling Constant

wave applied to the tetra-neutron is discussed in section 9.3.2. A modification of the 3N force exclusively fails due to the relatively weak contribution to the binding energy. The required changes to even achieve binding are so drastic, that it becomes impossible to extrapolate back to the unbound state with any meaningful result.

### 8.3.2. Eigenvector Binding

In the desire to use an external potential, we are faced with the complications of constructing a finite-range many-body interaction which only acts on the Hilbert space of a given particle rank, and as such does not act upon any sub-systems of fewer constituents. For methods which are formulated in hyperspherical coordinates or can be easily combined with them, such an  $A$ -body ( $A \geq 4$ ) effective interaction is easier to implement, see e.g. reference [LC05]. Introducing an additional interaction in the (Jacobi-)NCSM is accompanied with a long chain of steps to perform, where we refer to, e.g., reference [Sch18] for a detailed treatment of this topic.

To circumvent this, we chose to construct an additional potential from the previously in a small model space diagonalized initial four-body Hamiltonian. This ensures all symmetries of the  $TJP$  block, which have to be specified beforehand, are respected, as well as being a true four-body interaction only, such that bound two- and three-body systems are avoided. The construction of this potential goes as follows: Within the Jacobi-NCSM framework, the initial Hamiltonian is embedded into the four-body space. Then, a first diagonalization is performed in a small model space. The  $N_{\max}$  of this model space is denoted by  $N_{\max}^{\text{bin}}$ , e.g.,  $N_{\max}^{\text{bin}} = 0, 2, 4$  for natural parity, as is the case for the tetra-neutron  $J^\pi = 0^+$  state. From the diagonalization we obtain the eigenvectors

$$H_{N_{\max}^{\text{bin}}} \left| \Psi_{\nu}^{N_{\max}^{\text{bin}}} \right\rangle = E_{\nu} \left| \Psi_{\nu}^{N_{\max}^{\text{bin}}} \right\rangle, \quad (8.56)$$

which are then used to form a dyadic product and subtracted from the initial Hamiltonian

$$\begin{aligned} H_{\lambda} &= H - \lambda \sum_{\nu=0}^{n_{\text{ev}}} \left| \Psi_{\nu}^{N_{\max}^{\text{bin}}} \right\rangle \left\langle \Psi_{\nu}^{N_{\max}^{\text{bin}}} \right| \\ &= H - \lambda W. \end{aligned} \quad (8.57)$$

The index  $\nu$  runs from the state with the lowest eigenenergy in the  $N_{\max}^{\text{bin}}$  model space up to the one specified by the number  $n_{\text{ev}}$ . The maximum of  $n_{\text{ev}}$  is the matrix dimension of the model space. We refer to this scheme as eigenvector binding, owing to its construction from eigenvectors within the  $N_{\max}^{\text{bin}}$  model space.

## 8.4. Obtaining the Fit and Parameters

This section is dedicated to the set of parameters that impact the accuracy and reliability of the fits to the Padé approximants. The parameters are discussed in section 8.4.1. The concrete realization of the fit routines is discussed in section 8.4.2. The chiral interaction we use are not investigated as variational parameter. We restrict ourselves to two chiral interactions with NN and NN+3N forces in the application to the dineutron and the tetra-neutron, respectively.

### 8.4.1. Parameters

To give an overview, we classify the parameters influencing the analysis by their origin and where they come into play. Parameters that stem from the many-body method, the NCSM, are the model space size parameter  $N_{\max}$  and the HO length  $a_{\text{HO}}$ , or equivalently, the HO frequency  $\hbar\Omega$ . They are directly connected to the eigenenergies.

Parameters related to the binding method are  $N_{\max}^{\text{bin}}$  and  $n_{\text{ev}}$  when using eigenvector binding, and e.g. the modification of only selected partial waves versus modification of all matrix element. Directly related to the fit routine are the choice of minimization algorithm, the determination and choice of starting parameters, the numerical accuracy goal  $\sigma_{\text{rel}}^{\text{fit}}$  (how many effective digits of accuracy should be sought in the final result), and the interplay of the total number of digits available in the raw data set. In general, non-linear fits can be strongly dependent on the start values of the fitting parameters. This feeds back to the used algorithm to minimize the  $\chi^2$  function. An overview of the parameters than can be varied is given in table 8.1. For the analysis of the data presented in chapter 9, the fit accuracy  $\sigma_{\text{rel}}^{\text{fit}}$  within the fits is chosen to provide converged results and non-stalling fits.

We want to distinguish several aspects when referring to accuracy, precision, exactness and similar terms. The NCSM, as a many-body method, yields a numerically exact result within the given model space, with respect to all approximations and assumption made *a priori*. This result is of a certain numerical accuracy, determined by the floating point accuracy, the rounding errors during calculation etc., and how many digits are written into the results file. The first items listed, the numerical noise, is not something we consider to be of any importance to the reliability of the subsequent fits of the ACCC. Previously, the numerical noise was considered as a relevant problem [KKH89]. We assume this not to be an issue with modern high performance computers, that handle double floating point precision. Of importance to the ACCC is the total number of available digits in the result, together with the relative accuracy, as this has a potential impact on the fit routine. To be precise, the results are generally of order 1, and stored with an accuracy of six digits after the decimal point, where the last digit has to be considered as rounded.

Further relevant is the difference in convergence towards this numerically exact result of the NCSM as a function of  $N_{\max}$  for different strengths in the coupling constant. Increasing the model space size could have a bigger impact on states close to the threshold than those further away, or vice versa. This is, e.g., shown in figure 9.8. This is related to the question of which and how many data points to take into account, and how close to the threshold they should be allowed to lie.

These considerations of numerical exactness have to be further distinguished from physical exactness. How well we describe real physics can only be asserted *post factum*.

Parameter	Remarks
Interaction	Two $\chi\text{EFT NN}+3\text{N}$ considered
$N_{\max}$	Systematically increased. Analysis performed at largest $N_{\max}$
$a_{\text{HO}}$	Chosen in range of $\sim [1, 4]$ fm
$N_{\max}^{\text{bin}}$	0,2 or 6
$n_{\text{ev}}$	Either one or full sub-model space
Padé orders	$(N, M) = (1,1)$ to $(6,6)$
Data points	Variable
Algorithm	Newton, Broyden-Fletcher-Goldfarb-Shanno, Levenberg-Marquardt
Starting values	See section 8.4.2
$\sigma_{\text{rel}}^{\text{fit}}$	Relative numerical fit error during fitting routine
Determination of $\lambda_0$	Interpolation, IACCC, simultaneously fitted
Inclusion of $c_0$	See equation (8.45)

Table 8.1.: List of parameters considered in this work.

### 8.4.2. Fit Protocol and Data Collection

The first step in the process is data collection. We describe in the following the procedure for Jacobi-NCSM calculations. The threshold value  $\lambda_0$  is approximately determined with a few initial calculations at the largest  $N_{\max}$ , approaching the threshold from above and below, with no more than two decimal digits precision for the position of the threshold. The two closest points above and below the threshold are linearly interpolated to obtain  $\lambda_0$  via  $E(\lambda) = 0$ . We do this to establish the values  $\lambda$  must take to obtain a specific  $x = \sqrt{\lambda - \lambda_0}$  range and to be able to calculate data sets equidistant in  $x$ . We aim for a range of  $x \approx [0, 4]$ , with somewhere between 100 and 250 points, motivated by references [PvMM<sup>+</sup>13, SMHE17]. The raw data, which is a set of pairs of binding strength and energy at a fixed  $N_{\max}$  and  $a_{\text{HO}}$ ,  $(\lambda, E)$ , is translated into the wave number

$$k = \sqrt{\frac{2\mu E}{\hbar^2}} \equiv i\kappa.$$

The binding energy under the square root is negative. We choose the sign such that we have a real, positive  $\kappa$ , which lies on the positive imaginary axis when multiplied with the imaginary number  $i$ . The data that is used for the fit are consequently the pairs  $(\lambda, \kappa)$ .

The starting value for  $\lambda_0$  is once more determined by linear interpolation between the two points closest above and below the threshold. If no point is available above the threshold, then the first two bound states are linearly extrapolated to zero energy. This value is then used for all subsequent fits as a starting value.

The choices of fits are the IACCC, section 8.2.1, to either obtain a new threshold parameter value or use it for calculation of resonance parameters, given by equation (8.51)

$$\lambda(k) = i \frac{\lambda_0 + \lambda_2 k^2 + \dots + \lambda_N k^N}{1 + \mu_2 k^2 + \dots + \mu_M k^M}.$$

The ACCC with fixed  $\lambda_0$ , where the  $(\lambda, \kappa)$  pairs are put into the relation (8.46) and the parameters thus obtained are inserted in equation (8.45), which gives the trajectory of the wave number as a function of the coupling constant

$$k_\ell^{[N,M]}(x) = \frac{P_N(x)}{Q_M(x)} = i \frac{c_0 + c_1 x + \dots + c_N x^N}{1 + d_1 x + \dots + d_M x^M},$$

or the ACCC with simultaneous fitting of  $\lambda_0$

$$k_\ell^{[N,M]}(\lambda) = \frac{P_N(\lambda)}{Q_M(\lambda)} = i \frac{c_0 + c_1 \sqrt{\lambda - \lambda_0} + \dots + c_N \sqrt{\lambda - \lambda_0}^N}{1 + d_1 \sqrt{\lambda - \lambda_0} + \dots + d_M \sqrt{\lambda - \lambda_0}^M}. \quad (8.58)$$

In practice, the fits are done as follows. As start value for  $\lambda_0$  we always use the one obtained by linear interpolation. The first two Padé orders are obtained with starting values

$$c_0 = c_1 = c_2 = d_1 = d_2 = 0.$$

The first two orders have proven to be very stable w.r.t. to all parameter variations almost all of the time. Beginning with the third order, the default protocol is to obtain the starting values for the fit parameters from the previously performed lower order fits. At each new Padé order  $p$ , two new parameters  $c_p, d_p$  appear, and are at first set to zero. Should the fit either not converge within the step limit of  $\approx 4000$ , or stall due to insufficient decrease in the norm of the residual, then the values are randomly chosen in half-integer steps from a range between  $[-19, 19]$ , until a fit is found or up to 60 tries. This approach and the specific numbers developed empirically, often enough finding a fit, while not searching too long for new parameter values.

Other settings, e.g., the accuracy goal  $\sigma_{\text{rel}}^{\text{fit}}$ , are not changed dynamically.

One approach to overcome and quantify the dependence on some of the parameters is the so-called statistical ACCC [PvMM<sup>+</sup>13], not to be confused with the statistical Padé approximation, see appendix A. In this method, we randomly select a subset of size  $L$  from all available data points,  $L_{\text{tot}}$ . The fits are performed with  $\lambda_0$  as a free fit parameter. Starting values are first enforced up to a specified order, which have been determined from a low precision fit to the complete data set  $L_{\text{tot}}$ . After that, the previous lower order fits serve as starting points, with the same procedure as described above. Should a data set not deliver a fit, then a new subset is randomly chosen, repeating the procedure. If no fit is found at a certain Padé order after 100 new set were chosen, the routine ends and returns all fits found up to the previous order.

In reference [PvMM<sup>+</sup>13], they select up to 3000 subsets consisting of 20 points, from a total of 30 points. We present results obtained from set ranging in size between 500 and 1000 subsets, consisting of 30 points, out of a total of 100 to 250 points. We found the limitation to 1000 subsets to be sufficient. Tests with 5000 sets yielded no adequate improvement in stabilizing the mean of the distribution while justifying the increase in computation time.

This approach leads to a spread in the extrapolated results. We quantify this by using the mean value and the standard deviation of the distribution in the resonance position and width as the result. To further account for the different quality of the fits and extrapolations, we use the estimated fit error variance of each fit as a weight in the calculation of the mean and the standard deviation. An example of the statistical ACCC, the layout of the plot and how to interpret it, can be seen figure 8.6.

In the following, we discuss an example analysis with the described fit routines.

## 8.5. Example Discussion With Phenomenological Gaussian Potential

We introduce a simple Gaussian potential to introduce the fitting routines discussed in section 8.4.2. We use two different methods to achieve the necessary binding. The first is an additional external potential that varies smoothly from the given depth to zero as a function of the relative distance. The second is a prefactor in front of the initial potential.

The toy potential also uses a modified Coulomb interaction, and reproduces the first few states of positive parity of  ${}^8\text{Be}$  [BFW77]. We pick the second excited state, a  $J^\pi = 4^+$  state, which is resonant at  $E_R = (11.35 \pm 0.15) \text{ MeV}$  and a width  $\Gamma \approx 3.5 \text{ MeV}$  [TKG<sup>+</sup>04]. The potential has the form

$$\begin{aligned} V(r) &= V_N(r) + V_C(r) \\ &= -122.6225 \exp\left(\left(-\frac{r}{2.132}\right)^2\right) + 4e^2 \frac{\text{erf}(r/1.33)}{r}. \end{aligned} \quad (8.59)$$

Calculations are performed with the values of  $e^2 = 1.44 \text{ MeV fm}$  and  $\frac{\hbar^2}{m_N} = 41.472 \text{ MeV fm}^2$ . The Schrödinger equation is solved in a single-channel  $\mathcal{R}$ -matrix framework on a Lagrange mesh with 200 points and a channel radius of 80 fm. The external potential we use for binding is taken from [SMHE17] (referred to as Voronoi potential) and is defined by

$$\begin{aligned} V^{\text{ext}} &= V(r) + \lambda V_{\text{ext}}(a, b, r) \\ &= V(r) + \lambda (s(a, b, r) - 1), \end{aligned} \quad (8.60)$$

## 8. Analytic Continuation in the Coupling Constant

where the external potential is a soft box potential and is defined piecewise as

$$s(a, b, r) = \begin{cases} 0 & r \leq a \\ \rho^3(10 - \rho(15 - 6\rho)) & a < r < b, \\ 1 & b \leq r \end{cases} \quad (8.61)$$

with

$$\rho = \frac{r - a}{b - a}.$$

The second form is defined via a prefactor  $(1 + \lambda)$ , to let the extrapolated  $\lambda$  value always be consistently zero when comparing two different binding methods:

$$V^{\text{fac}} = (1 + \lambda)V(r). \quad (8.62)$$

The form of the potentials is shown in figure 8.1, in three different cases: The unmodified potential and the two binding mechanism, each at approximately the value of  $\lambda \approx \lambda_0$ . Comparing  $V^{\text{ext}}$  and  $V^{\text{fac}}$  in this plot shows that the potential  $V^{\text{ext}}$  is shallower, broader and not as steep as  $V^{\text{fac}}$  at the threshold to a bound state. The shape of the potential has an impact on the trajectory of the  $S$ -matrix pole, which also depends on the fitting algorithm and  $\sigma_{\text{rel}}^{\text{fit}}$ . This is shown in figure 8.5.

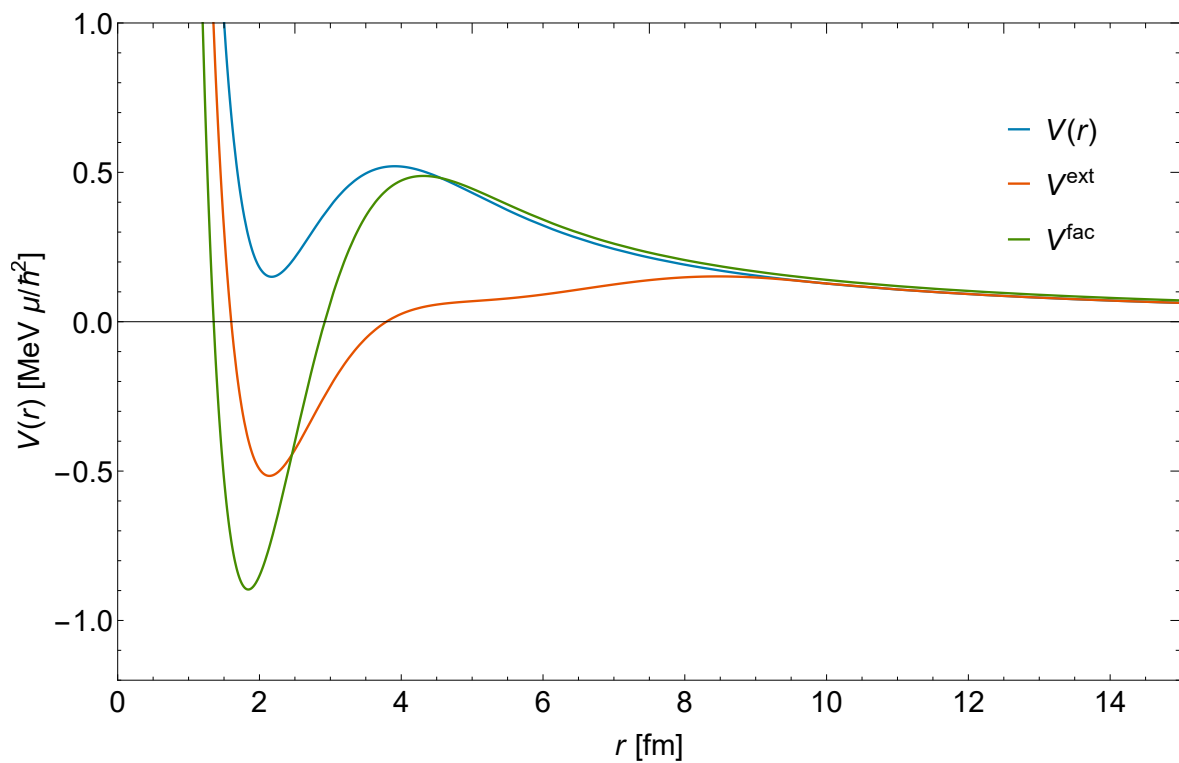


Figure 8.1.: Gaussian  $\alpha + \alpha$  potential for  $\ell = 4$  in units of the reduced mass  $\mu = 2m_N$ . The unmodified potential is blue. The external potential in orange at a value  $\lambda = 0.712$ , the prefactor modification in green with  $\lambda = 0.445$ . These  $\lambda$  are the approximate threshold values to achieve binding.

This translates, in some sense, to the bound states which we fit to. In figure 8.2, the binding energies generated with  $V^{\text{ext}}$  and  $V^{\text{fac}}$  are shown as a function of the coupling constant  $\lambda$ . The prefactor modification  $V^{\text{fac}}$  shows a clear bend when approaching the threshold, whereas the

external potential  $V^{\text{ext}}$  appears almost linear. A linear and a quadratic fit to all data points help to both visualize this and give a first idea on the resonance position.

Quadratic fits to the energy as function of the binding potential depth are used in reference [GHK<sup>+</sup>17] to extrapolate tri- and tetra-neutron resonance parameters. The results from these fits are given in table 8.2. These procedure can be of some use, if a resonance is actually present. Then, the missing imaginary part only restricts the prediction to an approximate resonance position, without a width. In this phenomenological example, the potential  $V^{\text{ext}}$  is already very close to the experimental value. The fits obtained with  $V^{\text{fac}}$  are far away from the expected result. If this approach is applied to a non resonant system, one cannot hope to learn anything from this, as the complex continuation is vital to actually be able to determine the absence of such a resonance. This can be seen in section 9.1.

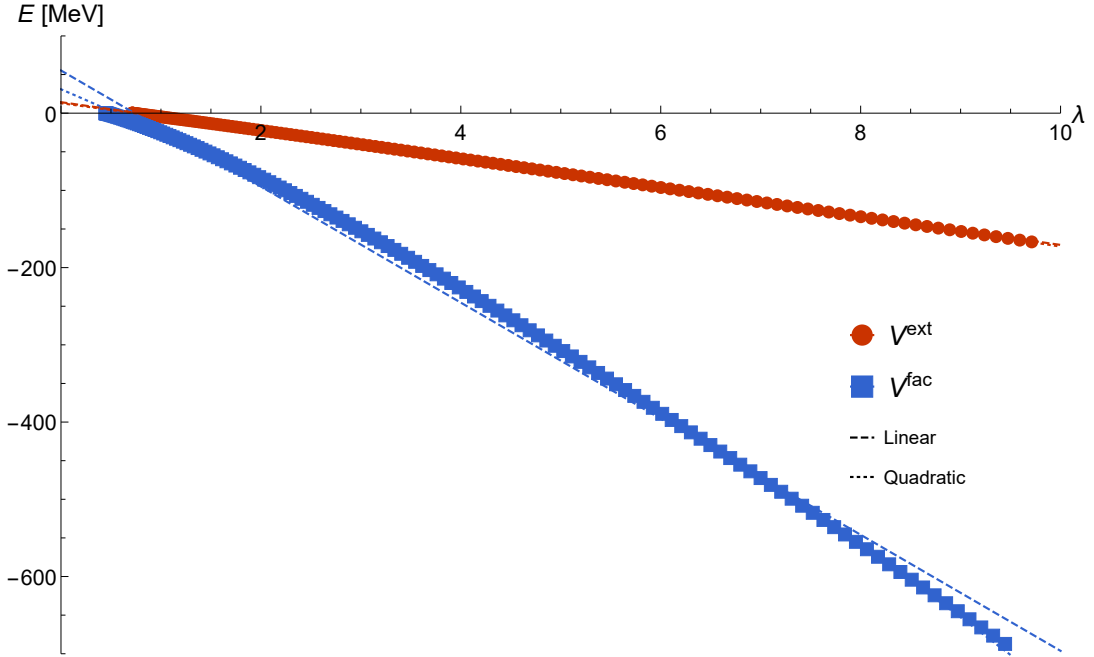


Figure 8.2.: Gaussian  $\alpha + \alpha$ : Binding energies which are used to perform the Padé fits, 151 points each. In red, data obtained from binding with the external potential in equation (8.60) and (8.61). In blue the modification as in equation (8.62). The dashed lines are linear fits, the dotted lines quadratic fits to the energy.

	$V^{\text{ext}}$ [MeV]	$V^{\text{fac}}$ [MeV]	Reference [MeV]
Linear	14.24	55.28	$11.35 \pm 0.15$
Quadratic	12.89	30.95	

Table 8.2.: Resonance position by extrapolation from linear and quadratic fits to the energy as a function of the binding parameter.

### 8.5.1. Inverse ACCC – $\lambda_0$ and Resonance

The determination of the root branch cut and thus the threshold value  $\lambda_0$  is of vital importance to the correct analytic continuation to the complex plane. With the IACCC, we can obtain  $\lambda_0$  by fitting the data, as discussed in 8.2.1. The fit protocol is discussed in 8.4.2. In this

## 8. Analytic Continuation in the Coupling Constant

example, we can perform bound-state calculations as close to the threshold as is needed. For this potential,  $\lambda_0$  obtained from linear interpolation of bound and unbound states and from fitting with the IACCC do coincide, depending on the fitting algorithms, however. This is shown in figure 8.3, for a sample size of 38 approximately equidistant points in the unifying variable  $x = \sqrt{\lambda - \lambda_0}$ , over a range  $x = [0.1, 3.0]$ . The value of  $\lambda_0$  is given for four different algorithms as a function of Padé order. The two binding potentials are shown side by side.

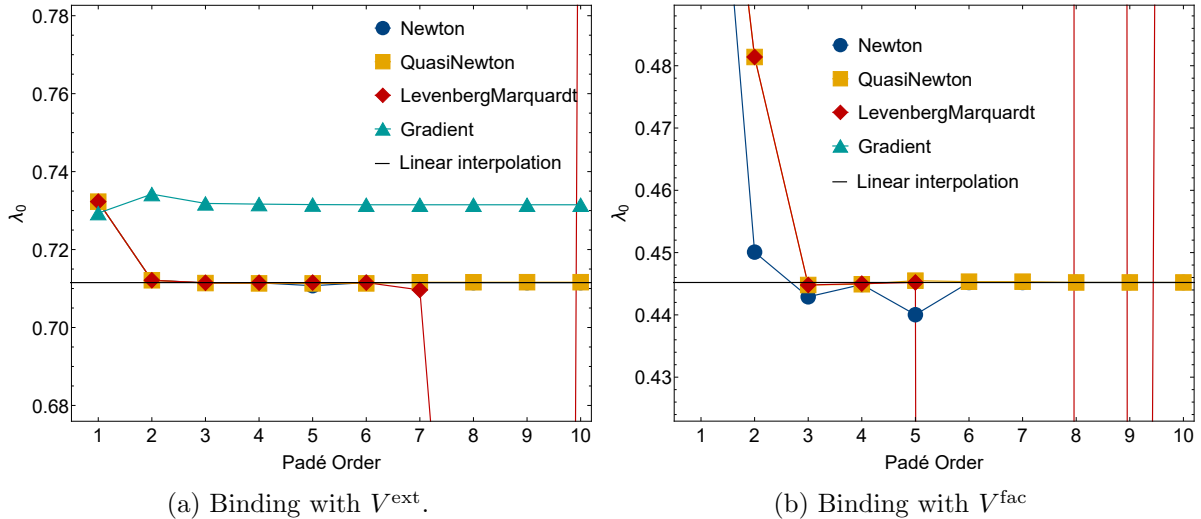


Figure 8.3.: Gaussian  $\alpha + \alpha$  scattering potential: Threshold value  $\lambda_0$ , obtained by fitting to 38 points, up to tenth Padé order. Four different fitting algorithms with  $\sigma_{\text{rel}}^{\text{fit}} = 6$ . The erratic behaviour of Levenberg-Marquardt method might indicate the overshooting of the optimal Padé order.

The three Newton-based algorithms, Newton, BFGS (Quasi-Newton) and Levenberg-Marquardt, produce similar results and lie on top of or close to the linear interpolation result, with some deviations. The Newton method does not always find a fit for orders starting at (5,5) as it does either not converge or stalls in a local minimum. Different starting values impact the obtained maximal Padé order, leading to different results when repeating the fit, see 8.4.2 for details. The Quasi-Newton BFGS algorithm is, similarly to the Newton method, dependent on the choice of starting values and requires multiple iterations to reach higher Padé orders. Contrasting to this is the Levenberg-Marquardt algorithm. As long as the starting values are reasonably good, it finds the same fit with the same parameter values in most cases, at the cost of longer computation time. However, the fit parameters can in some cases reach values of up to  $10^{11}$ , making it difficult to gauge their reliability. The Gradient method fails completely to reproduce accurate results. It is, therefore, not considered when drawing conclusions.

From the same fit we can also obtain the resonance position by solving for the root of the nominator in the Padé parametrization, as described in section 8.2.1. The result of that is given in table 8.3 for only three of the four algorithms, excluding the Gradient method. Even though the value for  $\lambda_0$  obtained with Levenberg-Marquardt shown in figure 8.3 takes very different values compared to the reference line in some orders, the resonance position at these orders is still reasonable. The BFGS (QN) results do not reproduce the experimental resonance width (to which the potential is fitted), even jumping in value after order (7,7). This contrasts with the stable appearance of  $\lambda_0$  in figure 8.3.

Alg.		(2,2)	(3,3)	(4,4)	(5,5)	(6,6)	(7,7)	(8,8)	(9,9)	(10,10)
NE	$E_R$	12.913	11.411	11.077	10.72	11.855	11.873	11.873	11.873	11.873
	$\Gamma$	0.	1.901	2.015	2.393	2.792	3.701	3.701	3.701	3.701
QN	$E_R$	12.913	11.411	11.343	11.363	11.363	11.363	11.914	11.914	11.9
	$\Gamma$	0.	1.901	2.386	2.517	2.517	2.517	1.531	1.531	1.511
LM	$E_R$	12.913	11.411	11.077	11.707	11.49	11.885	11.8	11.8	11.8
	$\Gamma$	0	1.901	2.015	2.954	3.411	3.767	3.611	3.611	3.612

Table 8.3.: Gaussian  $\alpha+\alpha$  scattering potential: Resonance position and width for  $V^{\text{ext}}$  obtained from solving for the roots of the numerator of the inverse ACCC. Selection of which root of the polynomial is the correct one has to be performed “by hand”.

### 8.5.2. ACCC

The trajectories of the  $S$ -matrix pole from a bound state to a resonant state are shown in figures 8.4 and 8.5, where also the BFGS and the Levenberg-Marquardt algorithm are compared. Each line corresponds to a different Padé order. The pole moves from the positive imaginary axis down, where it corresponds to a bound state, towards the origin. At this point the root branch cut occurs. We follow the branch cut into the fourth quadrant, see also figure 8.4 for an example of pole trajectory in the complex plane. The binding potential has an impact on the trajectory of the pole that is being tracked by the fit. The comparison between figure 8.5a and 8.5b shows not only different trajectories for different potentials, but also for different fitting algorithms. In the case of  $V^{\text{ext}}$ , the BFGS and Levenberg-Marquardt algorithm result in different widths, but with good agreement in the resonance position. In contrast, the use of  $V^{\text{fac}}$  shows agreement between the algorithms, but higher Padé orders are needed to arrive at the correct resonance position in the case of the BFGS algorithm.

The application of the statistical ACCC, described in section 8.4.2, is depicted in figure 8.6 with the Levenberg-Marquardt algorithm and in figure 8.7 for BFGS. In the plots showing the results of the statistical ACCC, the data is presented with the resonance energy (the position) on the abscissa. The ordinate corresponds directly to the width  $\Gamma$ , from the relation given in equation (3.101)

$$E_R = \frac{\hbar^2 (k_{\text{Re}}^2 - k_{\text{Im}}^2)}{2m} \quad \text{and} \quad \Gamma = \frac{2\hbar^2}{m} k_{\text{Re}} k_{\text{Im}}. \quad (8.63)$$

Each point corresponds to a fit to a randomly chosen subset, where same colours are of the same Padé order. All points at each order are used for calculating the mean value and the standard deviation in resonance position  $\overline{E}_R$  and width  $\overline{\Gamma}$ . The mean position and width is indicated with a larger dot and  $\overline{E}_R$  is further highlighted with as line down to the abscissa. The standard deviation is given as a box around the mean value.

Figure 8.6 shows the two different approaches to binding the Hamiltonian in combination with the effect of data point choice for the fit and how the binding potential affects the Padé order-by-order behaviour. Looking at the data point dependence in form of the standard deviation, given by the size of the boxes around the mean value, the external potential  $V^{\text{ext}}$  has a preferable behaviour, as all sets lead to similar extrapolations. The simple prefactor method shows a larger spread in comparison. Regarding the Padé orders, the use of  $V^{\text{ext}}$  leads to smaller jumps, as opposed to the prefactor method, where the first two orders are far away from the next higher ones and the experimental result.

The same protocol together with the BFGS algorithm shows more spread in the individual

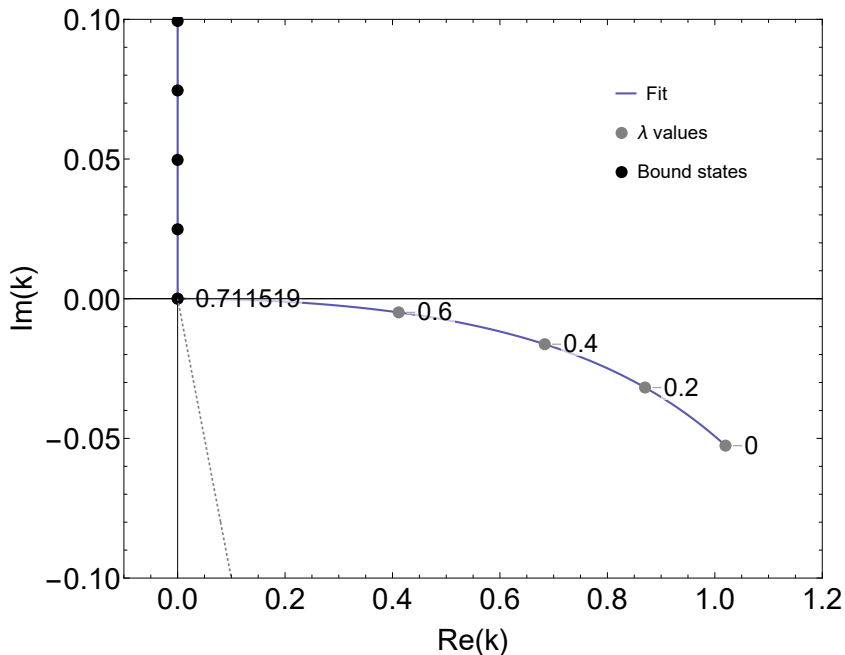


Figure 8.4.: Example of how the  $S$ -matrix pole moves through the complex plane with specific values of the coupling constant. The black dots are the data obtained from a Jacobi-NCSM calculation and are fitted to. The grey dashed line indicates where  $\text{Re}(k) = \text{Im}(k)$ . Order (5,5) of  $V^{\text{ext}}$  with BFGS algorithm, shown in figure 8.5a.

points and at all orders. Consequently, the standard deviation is much larger. The statistical ACCC result shows the same too small resonance width as the individual fit results shown in table 8.3 and figure 8.6. However, BFGS requires less computational effort, returning fits to 1000 subsets in a fraction of the time that it takes to perform the fits for 200 points with Levenberg-Marquardt.

### 8.5.3. Conclusion

The ACCC analysis of a potential of simple Gaussian form, which has been fitted to reproduce experimental data, both shows what to expect of the ACCC and serves as an introduction to the the fitting protocols we use in this work.

Even in this simple case, some differences in the comparison of the external and prefactor potential can be observed. Different modifications in large scale calculations might show stronger deviations from each other.

The determination of the the threshold value  $\lambda_0$  via IACCC has to be done with care. The prescribed approach of reference [KKH89] to use the  $\lambda_0$  converged w.r.t. the Padé orders as the correct one does not lead to the best results. Firstly, they tend to the directly determined threshold value, and secondly, the best converged result, in this case obtained with BFGS, fails to reproduce the resonance width provided by the reference.

The interplay of the fit algorithm, starting parameter values, fit accuracy goal and desired Padé order are problems to be aware of. They can be treated with the statistical ACCC, which gives a measure for the spread caused by choosing different data points for the fit. Within this, the starting parameter value dependence and the absolute fit error can be absorbed, due to the probable repetition of fits to similarly distributed data points, but with potentially different starting values, supposing a large enough set size is used.

The result show that the Padé orders (1,1) and (2,2) are not accurate in reproducing the

### 8.5. Example Discussion With Phenomenological Gaussian Potential

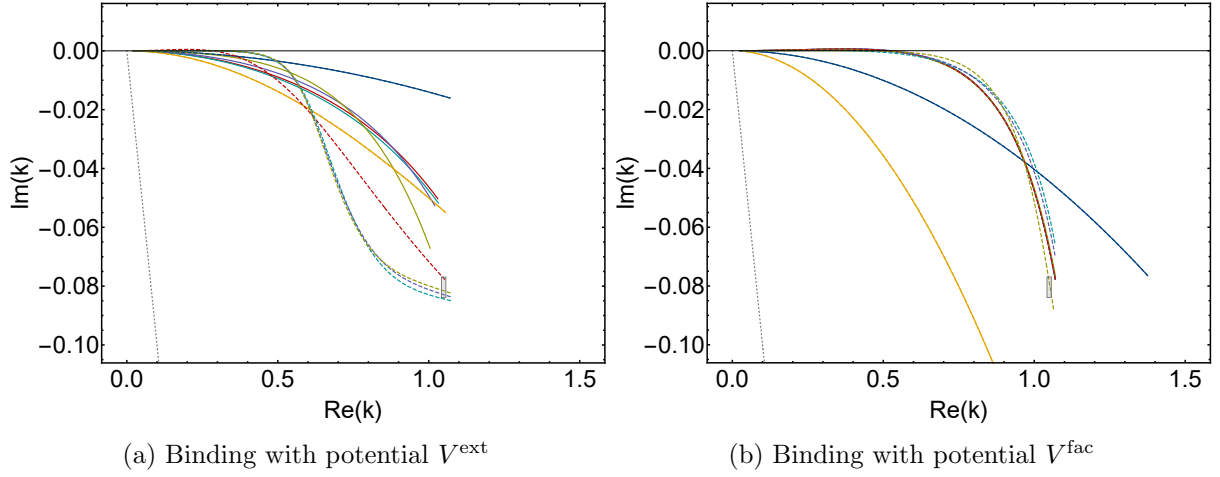


Figure 8.5.: Gaussian  $\alpha + \alpha$  scattering potential: ACCC for fixed  $\lambda_0$  for the two different binding approaches, full data set of 150 points.  $\lambda_0$  determined by linear interpolation. BFGS in solid lines, dashed lines Levenberg-Marquardt and  $\sigma_{\text{rel}}^{\text{fit}} = 6$ . Parametrization as in equation (8.45b). Experimental reference is the grey box, the width uncertainty is set to arbitrary 5%.

resonance parameters, but are very stable with respect to set selection and starting values. Realistic results are obtained with order (3,3).

## 8. Analytic Continuation in the Coupling Constant

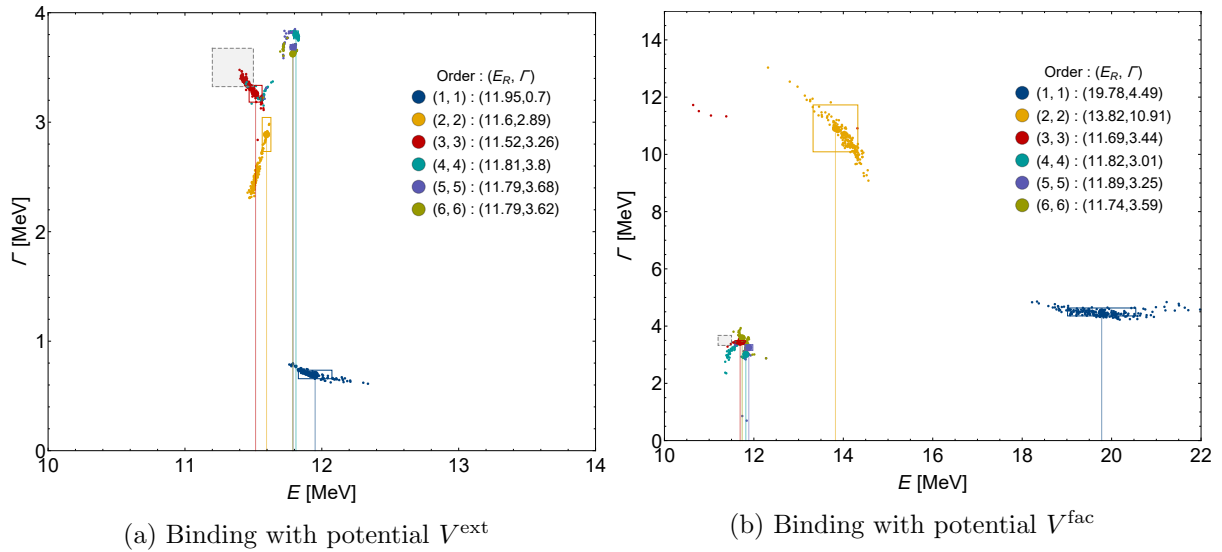


Figure 8.6.: Gaussian  $\alpha + \alpha$  scattering potential: Statistical ACCC for the two different binding approaches. 200 sets each. Parametrization as in equation (8.45b). The large dots with a line to the axis are the mean values of all points, the boxes give the standard deviation from the mean. Experimental reference is the grey box, the width uncertainty is set to arbitrary 5% for better visibility. Levenberg-Marquardt algorithm.

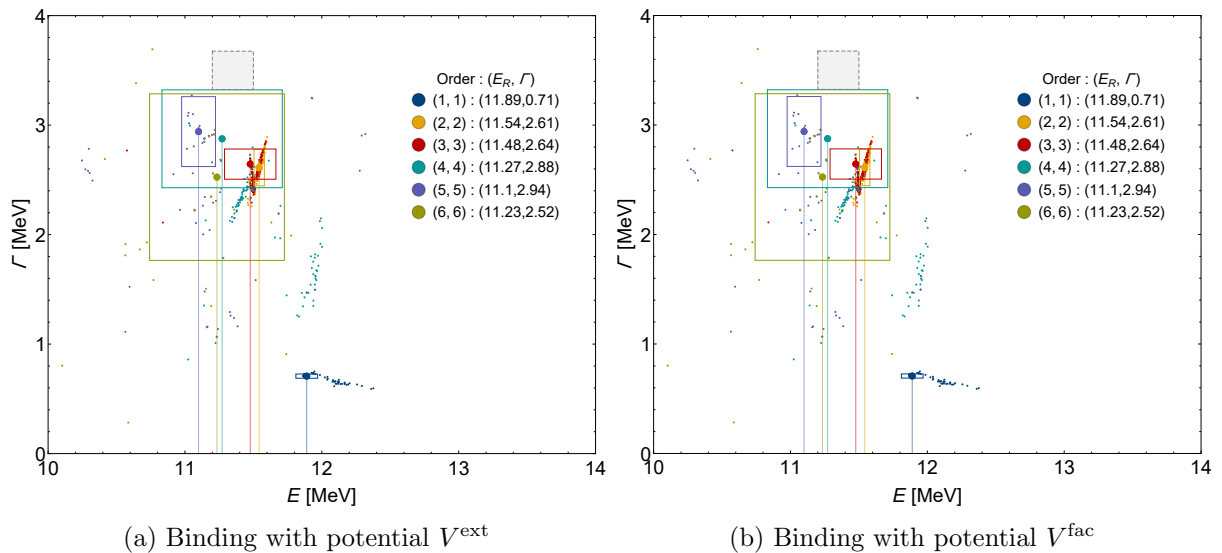


Figure 8.7.: Gaussian  $\alpha + \alpha$  scattering potential: Statistical ACCC for the two different binding approaches. 1000 sets each. Parametrization as in equation (8.45b). The large dots with a line to the axis are the mean values of all points, the boxes give the standard deviation from the mean. Experimental reference is the grey box, the width uncertainty is set to arbitrary 5% for better visibility. BFGS algorithm.

## 9. Results Analytic Continuation in the Coupling Constant

Interest in the four-neutron system was renewed recently due to the proposed resonance candidate by Kisamori et al. [KSM<sup>+</sup>16], with an energy position of  $0.83 \pm 0.65(\text{stat}) \pm 1.25(\text{syst})$  MeV and upper limit for the width of 2.6 MeV, at a significance level of  $4.9\sigma$ . It has since then been the motivation for new and further investigations into the matter [SPM<sup>+</sup>16, HLCK16, CLHK17, LCH17, GHK<sup>+</sup>17, FRMP17, Del18, LMH<sup>+</sup>19], see also the introduction to chapter 7. There is no consensus among theorist whether a tetra-neutron resonance should exist, and if so, what its resonance parameters are. Further experiments are still ongoing, and a final verdict from the experimental side has yet to be made.

In this chapter we present the results of the application of the Analytic Continuation in the Coupling Constant to the two- and four-neutron system. The focus of our investigation lies on the tetra-neutron.

We use state-of-the-art Chiral Effective Field Theory ( $\chi$ EFT) interactions, which have been Similarity Renormalization Group (SRG) transformed, together with the No-Core Shell Model (NCSM) as many-body method, see chapter 2 and 5 for details on  $\chi$ EFT and the NCSM, respectively. We achieve binding of the systems by direct strength increase in the interaction matrix elements as well with a novel approach we call eigenvector binding. The ideas behind these two methods are described in section 8.3. The dineutron is first investigated and serves as an example for the response of the ACCC to a non-resonant system and the use of the eigenvector binding method.

The tetra-neutron is studied exhaustively under variation of different parameters. These are introduced in section 8.4.1. The parameters that are investigated fall into different categories. These are either related to the interaction, the many-body method, the specifics of obtaining a bound system, or the fitting routine. Details on the fit protocols are discussed in section 8.4 and section 8.5.

For the dineutron, we use a bare (not SRG evolved) NN-interaction. For the tetra-neutron study, we utilize two  $\chi$ EFT interactions, both with full NN + 3N forces. They are listed in table 9.1.

Name	Reference	SRG
$N^3LO_{EM}$	[EM03]	–
$N^3LO_{EM} + N^2LO_{500,L}$	[EM03, Nav07]	SRG evolved with $\alpha = 0.12 \text{ fm}^4$
$N^3LO_{EMN} + N^3LO_{500,NL}$	[EMN17, HVH <sup>+</sup> 19]	SRG evolved with $\alpha = 0.08 \text{ fm}^4$

Table 9.1.: Chiral interactions used in this study.

The role of the interaction is the primarily investigated parameter in the Single-State HORSE study in chapter 7. From our conclusions drawn in this chapter, the gross properties of a tetra-neutron resonance, whether it even exist, and if so, where it approximately lies, should not change between  $\chi$ EFT interactions. We, therefore, leave interaction properties fixed.

## 9. Results Analytic Continuation in the Coupling Constant

We further investigate different harmonic oscillator (HO) lengths  $a_{\text{HO}}$ . However, the eigenvector binding is by construction not independent of the HO length parameter.

The way the binding of the Hamiltonian is achieved has consequences for the fit stability and prediction of resonance positions. Variations to investigate for the prefactor binding are modifications of only the NN matrix elements, exclusion of specific partial waves, and the complete NN+3N interaction matrix elements. The 3N interaction alone is too weak that any sufficiently strong exclusive three-body interaction modification results in unusual behaviour in the eigen-energies and is, therefore, not further investigated. The eigenvector binding requires investigation into the NCSM model-sub-space size  $N_{\text{max}}^{\text{bin}}$  and number of used eigenvector  $n_{\text{ev}}$ , at which the external binding potential is constructed.

The fact that we fit a highly non-linear model to data of unknown adequacy, raises the question of the sensitivity to the fit routines. The choice of which data points to use, the starting values of the fit parameters, the minimization algorithm and their cross-dependencies all lead to different extrapolated results.

The chapter is structured as follows: The dineutron system is investigated for two binding approaches, to show the application of the ACCC to a non-resonant system.

Our main objective is the study of the tetra-neutron, bound with the eigenvector method, which is introduced in section 8.3.2. We first present the input data and their dependence on the NCSM parameters. The subsequent subsections comprise an extensive parameter study. Our main findings with the eigenvector binding method are presented at the end of the section. Further, as a separate binding method, we increase the potential contribution to the tetra-neutron many-body Hamiltonian in order to bind the system, which is discussed in the end, before we concluding this study.

### 9.1. Dineutron

The dineutron is our first application of the ACCC with a realistic Hamiltonian, constructed from the state-of-the-art  $\chi\text{EFT}$  interaction  $\text{N}^3\text{LO}_{\text{EM}}$  [EM03]. It is a well-known, non-resonant system, providing a reference as to what a non-resonant systems looks like in the ACCC, and to make sure we do not falsely produce a resonance with the yet unproven eigenvector binding. The two-neutron system is pure  $s$ -wave scattering, and hence cannot be a two-body shape resonance, see section 3.5. The branch point is given for  $\ell = 0$  by equation (8.42)

$$k_0(\lambda) = i\kappa + (\lambda - \lambda_0). \quad (9.1)$$

A proper treatment of the  $S$ -matrix poles to also extract the virtual state properties requires the knowledge of the branching point  $\kappa_0$ , as described in chapter 8. Within this investigation of the dineutron, we want to make sure that we are not producing a resonance by construction, and not accurately track the pole. We neglect the beforehand calculation of  $\kappa$ . However, it is important to accommodate this circumstance by only fitting to the Padé parametrization including the zero order, variable independent, parameter  $c_0$ , as in equation (8.45a).

The raw data for the dineutron is obtained from a NCSM calculation with  $E_{\text{max}} = 300$ , with the bare two-body chiral interaction  $\text{N}^3\text{LO}_{\text{EM}}$ , at HO lengths  $a_{\text{HO}} = 2.5$  and  $3.5$  fm. Each  $a_{\text{HO}}$  set consists of 400 data points in a  $\lambda$  range of approximately  $\lambda = [0, 10]$  for the prefactor binding and  $\lambda = [0, 16]$  for the eigenvector binding. The data set for the prefactor binding is obtained with the form

$$H(\lambda) = T + \bar{\lambda}V.$$

To have the same extrapolation value of  $\lambda = 0$ , the values are shifted by  $\lambda = \bar{\lambda} - 1$  to

$$H(\lambda) = T + (1 + \lambda)V.$$

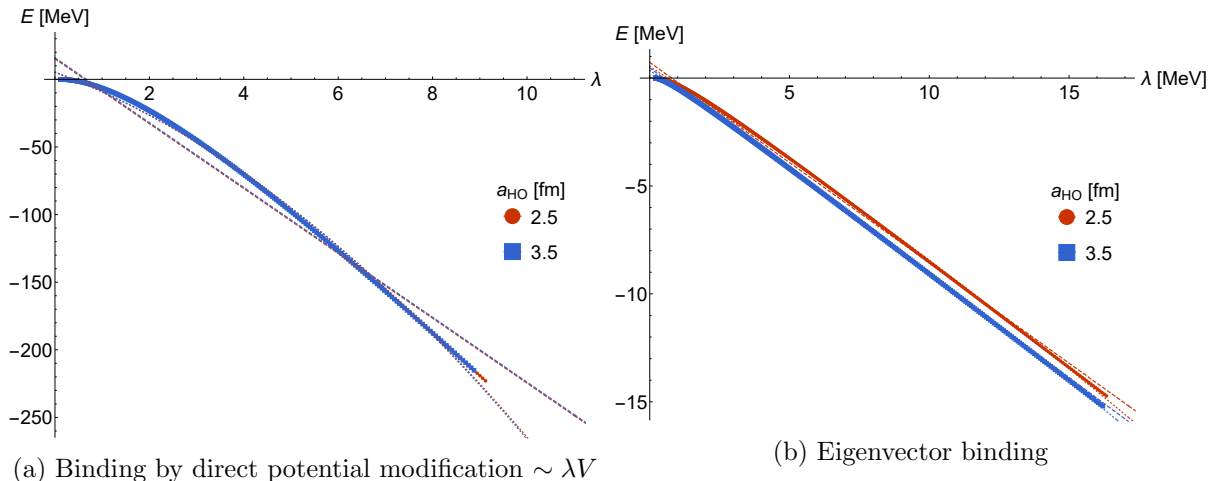


Figure 9.1.: Dineutron bound state produced with two different harmonic oscillator lengths  $a_{\text{HO}} = 2.5$  and  $a_{\text{HO}} = 3.5$  fm. Note the difference in binding energies. Dashed lines are linear fits, dotted lines quadratic fits to the full data set of 402 points.

	$\sim \lambda V$		$\sim \lambda W$	
$a_{\text{HO}}$ [fm]	2.5	3.5	2.5	3.5
$\lambda_0$	0.12096	0.11421	0.33902	0.20794

Table 9.2.: Threshold positions for the different binding methods.

The eigenvector binding is performed as described in section 8.3.2, which reads

$$\begin{aligned}
 H_\lambda &= H - \lambda \sum_{\nu=0}^{n_{\text{ev}}} \left| \Psi_\nu^{N_{\text{max}}^{\text{bin}}} \right\rangle \left\langle \Psi_\nu^{N_{\text{max}}^{\text{bin}}} \right| \\
 &= H - \lambda W.
 \end{aligned}$$

The energy as a function of the binding parameter is shown in figure 9.1a and figure 9.1b, for the matrix element and eigenvector modification, respectively. On the resolution provided by the two plots, the two  $a_{\text{HO}}$  lines lie on top of each other for the matrix element modification, whereas the eigenvector binding data are clearly distinguishable, but approaching each other close to the threshold. The form of the matrix element modification is also distinctly differently shaped than with the pseudo-external binding potential. The matrix element modification shows a strong curvature, the eigenvector binding appears almost linear at larger  $\lambda$ . The matrix element modification shows a slightly flatter curve at low  $\lambda$  values over the same range of  $\lambda \approx [0, 1]$  compared to the eigenvector binding. This difference in appearance as well as the near-threshold behaviour is also observable in the benchmark case discussed in section 8.5, displayed in figure 8.2. We perform a linear and quadratic fit to the energy as a function of  $\lambda$  to highlight the different curvature of the two binding methods. Additionally, the quadratic fit is a possibility to obtain an estimate of the resonance position, but only if a resonance is present in the first place. With this in mind, these two fits serve as counter examples of the limitation of fitting to the energy as a function of  $\lambda$ , without proper analytic continuation. The linear and quadratic fits and extrapolation to the unmodified Hamiltonian are shown in table 9.3.

Lacking the information of the precise root branch cut position  $\kappa$ , we refrain from performing the IACCC. We perform the statistical ACCC (SACCC) with three different algorithms, motivated by the findings presented in section 8.5, Levenberg-Marquardt in figure 9.2, BFGS in figure 9.3,

## 9. Results Analytic Continuation in the Coupling Constant

$a_{\text{HO}}$ [fm]	Linear [MeV]	Quadratic [MeV]
2.5	15.168	5.092
3.5	15.974	5.430
2.5	0.7275	0.5329
3.5	0.473	0.3543

Table 9.3.: Fits to the energy as function of  $\lambda$ . Direct matrix element modification on top, eigenvector on the bottom. The two fits serve to better highlight the differences in behaviour with increasing  $\lambda$ . The fits also serve as counter examples to the direct extrapolation without analytic continuation.

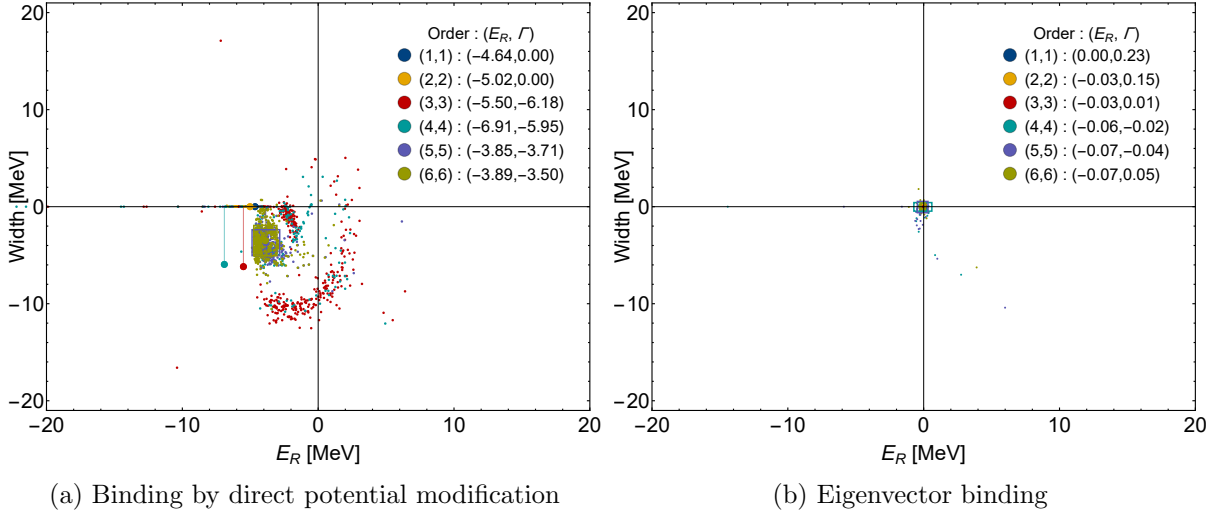


Figure 9.2.: Statistical ACCC for two binding methods. Performed with Levenberg-Marquardt with  $\sigma_{\text{rel}}^{\text{fit}} = 8$ ,  $a_{\text{HO}} = 3.5$  fm, 500 subsets of 30 points, unitary weights.

and Newton in figure 9.4. We limit this analysis to only one oscillator length,  $a_{\text{HO}} = 3.5$  fm. A total of 500 subsets, consisting of 30 out of 400 points, is randomly selected. Each subset serves as fit data, whose extrapolation result is shown as dot in the figures 9.2 to 9.4. The SACCC is introduced in section 8.4.2 and further described in section 8.5.

From the six plots depicted, five show considerable spread in the individual subset results, with the exception of the eigenvector binding fitted with Levenberg-Marquardt, figure 9.2b. This spread is most pronounced in the matrix element modification in combination with the Newton and BFGS fits. Common feature of the matrix element modification is the negative average position  $\bar{E}_R$ , with heterogeneous widths. The eigenvector binding results lie close to the  $y$ -axis. The most stable extrapolations, with respect to the data point selection, are the Levenberg-Marquardt fits, figure 9.2. The mean values of each order lie in the same region, with small standard deviations. The exceptions are the standard deviation boxes of the Padé orders (3,3) and (4,4) in figure 9.2a, being larger than the plotting range. The eigenvector binding gives zero energy and zero width.

## Conclusion

We conclude that no resonance is present, for both binding approaches, primarily supported by the findings shown in figure 9.2. Within all investigated cases, the mean values of the

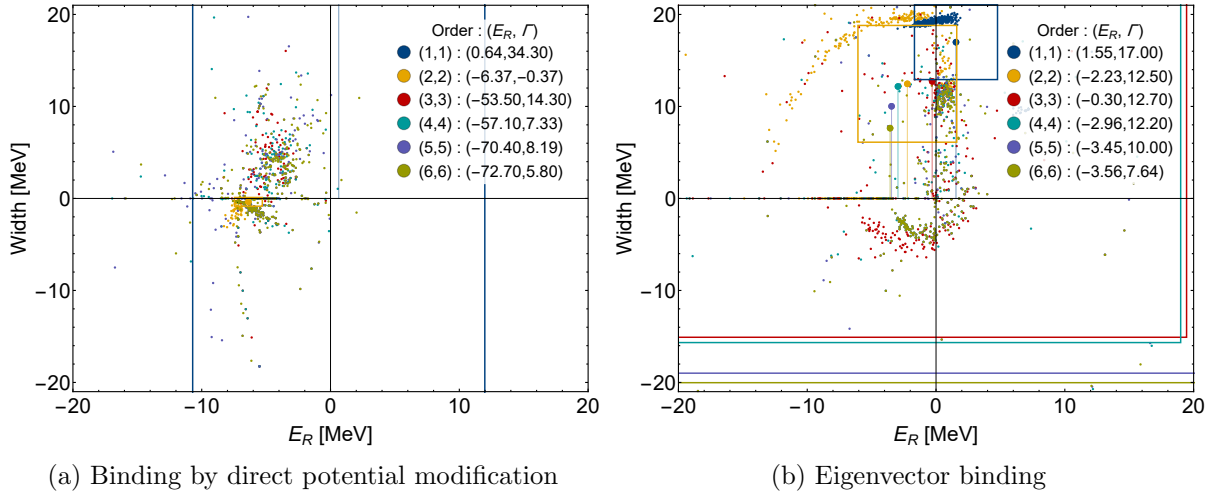


Figure 9.3.: Statistical ACCC for two binding methods. Performed with BFGS with  $\sigma_{\text{rel}}^{\text{fit}} = 8$ ,  $a_{\text{HO}} = 3.5$  fm, 500 subsets of 30 points, unitary weights.

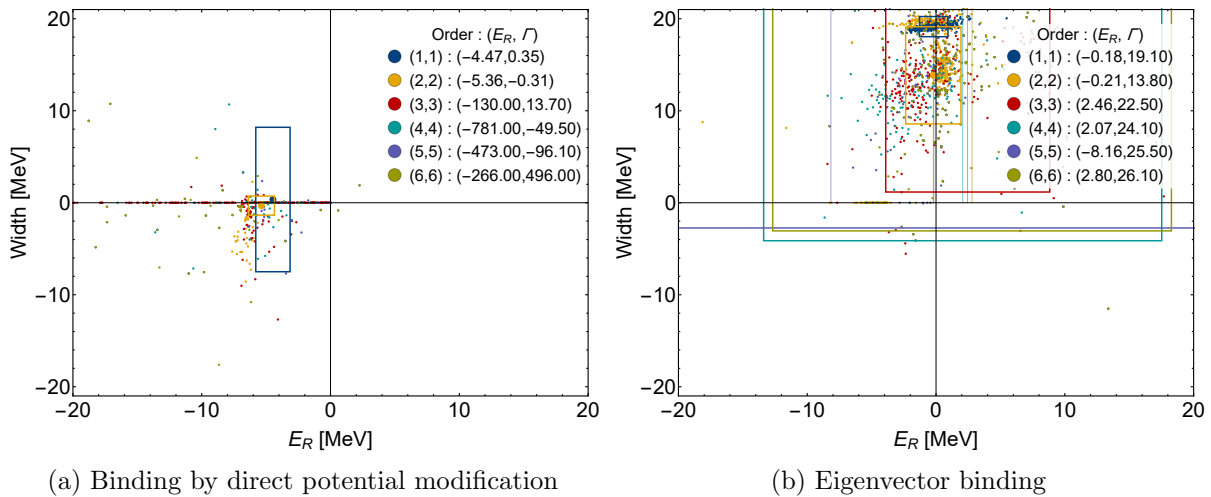


Figure 9.4.: Statistical ACCC for two binding methods. Performed with Newton with  $\sigma_{\text{rel}}^{\text{fit}} = 8$ ,  $a_{\text{HO}} = 3.5$  fm, 500 subsets of 30 points, unitary weights.

SACCC are counter-indicative to the existence of a resonance in the dineutron system. This is as expected in this case. The eigenvector binding shows less dependence on data point selection with different fit algorithms than the matrix element modification. We attribute this to the almost linear dependence in  $\lambda$ . That this linearity in the  $E(\lambda)$  plane is not problematic can also be observed in figure 8.2, where a truly external potential shows similar features. The findings shown figure 9.2 are promising for potentially enabling the calculation of virtual states with data obtained with the NCSM, if the determination of the  $s$ -wave root branch point is performed. The observable differences in the employed fitting algorithms give further motivation to investigate their effect on the ACCC applied to the tetraneutron. We discuss this in section 9.2.2.

## 9.2. Tetraneutron: Eigenvector Binding

### 9.2.1. Input Data

For our investigation of the tetraneutron, we choose two state-of-the-art chiral interactions with two- and three-body forces, denoted by  $N^3\text{LO}_{\text{EM}} + N^2\text{LO}_{500,\text{L}}$  and  $N^3\text{LO}_{\text{EMN}} + N^3\text{LO}_{500,\text{NL}}$  see table 9.1 for SRG parameters and references. The bound-state energies required for the ACCC are obtained by solving the many-body problem in the framework of the Jacobi-NCSM, up to large model spaces of  $N_{\text{max}} = 28$ . See chapter 5 for the introduction of the NCSM. The Jacobi-NCSM enables the calculation of a great number of data points ( $\sim 150$ ) for a fixed set of parameters within a few hours of wall-time on a high performance cluster. We use the so-called Padé-III approximants, which means we use more input data points for the fit than we have degrees of freedom in the Padé parametrization, see also appendix A.

With the use of an elaborate solving method, such as the NCSM, comes necessarily the question about the dependencies of the data from the truncation parameters inherent to the interaction, the solver and the employed basis. The interaction truncation parameters and their effects onto a possible tetraneutron resonance are not part of this work. The parameters that are investigate are the model space size  $N_{\text{max}}$  and the harmonic oscillator length  $a_{\text{HO}}$ . Regarding  $N_{\text{max}}$  we have to check if the eigenenergies are converged with respect to that parameter. This is done in section 9.2.4. The behaviour under variation of  $a_{\text{HO}}$  is usually shown to become independent for sufficiently large model spaces. Why this is not the case here is discussed in section 9.2.3.

With the two chiral interactions, a large set of different harmonic oscillators lengths  $a_{\text{HO}}$  is produced, though not all are shown with individual analysis.

For the  $N^3\text{LO}_{\text{EM}} + N^2\text{LO}_{500,\text{L}}$  interaction, a range of  $a_{\text{HO}}$  between [2.0, 10] fm is computed. For the  $N^3\text{LO}_{\text{EMN}} + N^3\text{LO}_{500,\text{NL}}$  interaction, we use matrix elements with  $a_{\text{HO}} = 2.5, 3.5$  and 4.5 fm.

If the tetraneutron exists as a resonance, we assume it to be in a spatially sparse configuration. In the context of the eigenvector binding, we, therefore, have to consider this when choosing the oscillator lengths. We focus on two different  $a_{\text{HO}}$  for the main parameter studies,  $a_{\text{HO}} = 2.5$  fm and 3.5 fm, in section 9.2.2.

The  $N_{\text{max}}$  sequence of the lowest lying energy of the unmodified Hamiltonian with the interaction  $N^3\text{LO}_{\text{EM}} + N^2\text{LO}_{500,\text{L}}$  is shown in figure 9.5, for the interaction  $N^3\text{LO}_{\text{EMN}} + N^3\text{LO}_{500,\text{NL}}$ , see figure 9.6. This depicts the expected behaviour for a system with positive energy eigenvalues in the NCSM as a function of  $N_{\text{max}}$ . The “ground state” energy drops with increasing model space size. Unlike the bound-state case, a reasonable extrapolation of  $N_{\text{max}} \rightarrow \infty$  can not be made. From figure 9.5, we see that the larger the oscillator length is, the less the absolute energy changes with increasing  $N_{\text{max}}$ .

Considering the  $N_{\text{max}}$  sequences for the bound states at three different coupling constants in figure 9.8, we observe the typical convergence behaviour in the input data as we would expect it from a bound system. At the shown length of 3.5 fm, the convergence looks reasonable for purely bound-state observables. How this affects the extrapolation to unbound energies is discussed in section 9.2.4.

Owing to the nature by which we construct the external potential to bind the tetraneutron, we have the two parameters  $N_{\text{max}}^{\text{bin}}$  and  $n_{\text{ev}}$ , which specify the subspace and the number of eigenvectors from this subspace to use.

The effect the external binding potential has on the Hamiltonian and its lowest lying states is shown in figure 9.7. The higher lying energy states within the same  $J^\pi = 0^+$  block exhibit level crossing, as depicted in figure 9.7, but not so the lowest one, denoted  $E[0]$ . This state

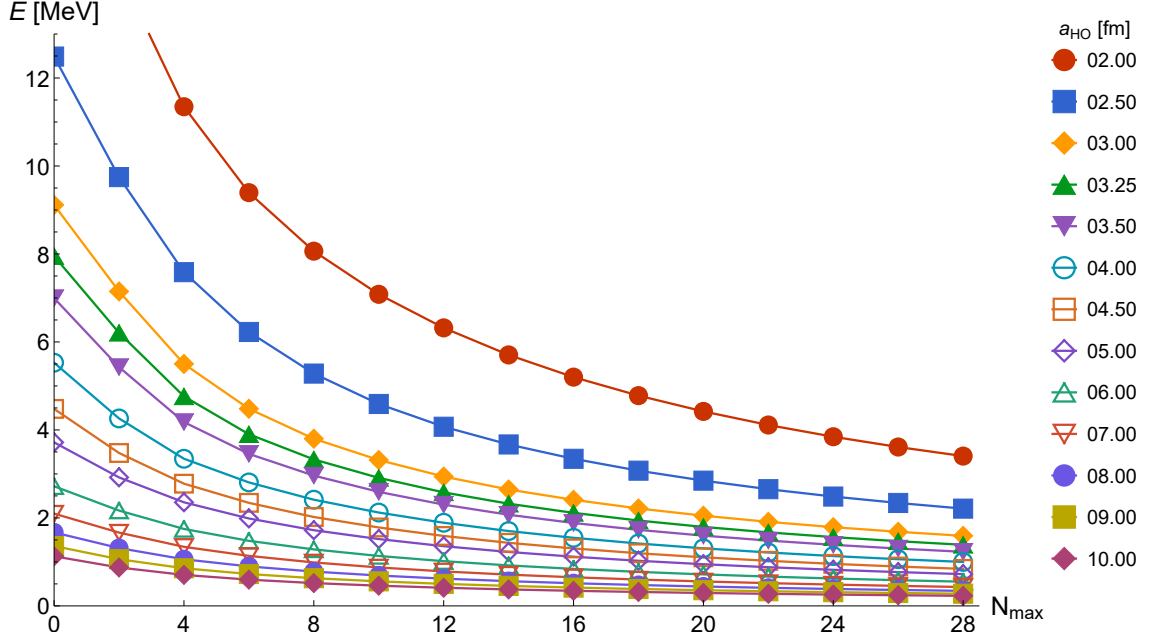


Figure 9.5.:  $N_{\max}$  sequence for the interaction  $N^3\text{LO}_{\text{EM}} + N^2\text{LO}_{500,\text{L}}$  at different oscillator lengths in the pure, unmodified pseudo continuum.

moves continuously from the unbound regime at  $\lambda = 0$  into the bound regime. The second energy state, denoted by  $E[1]$ , undergoes a crossing with the next higher  $E[2]$ , which undergoes level crossing with next, and so on. From the point of view of tracking a certain bound state over the threshold into the continuum, e.g. the second lowest in the bound-state case, is not the same state as the second lowest in the unmodified case, due to the crossings. The state labelled  $E[1]$  actually remains in the continuum up to larger values of  $\lambda$ . We only extrapolate the lowest energy state, where all level crossing should be far enough away from  $\lambda = 0$ , to which we extrapolate. This is also discussed in reference [FHT06], see also the *avoided* level crossings for finite volume calculations introduced in reference [Wie89]. The extrapolations with different  $N_{\max}^{\text{bin}}$  and  $n_{\text{ev}}$  is discussed in section 9.2.5.

## 9. Results Analytic Continuation in the Coupling Constant

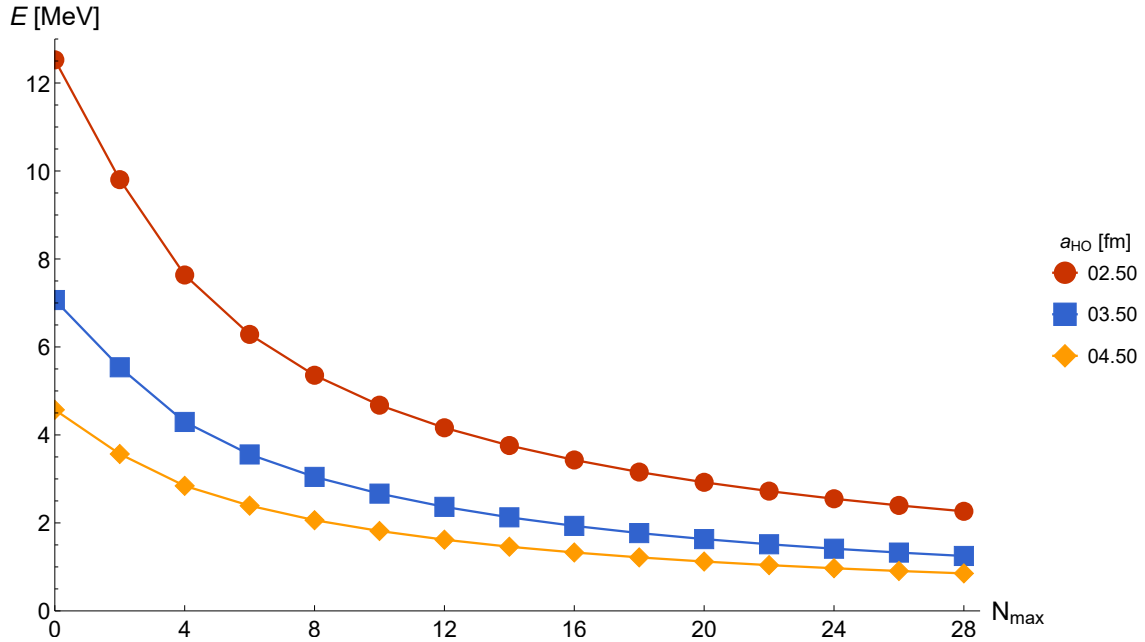


Figure 9.6.:  $N_{\max}$  sequence for the interaction  $N^3\text{LO}_{\text{EMN}} + N^3\text{LO}_{500,\text{NL}}$  for three different oscillator lengths in the pure, unmodified pseudo continuum.

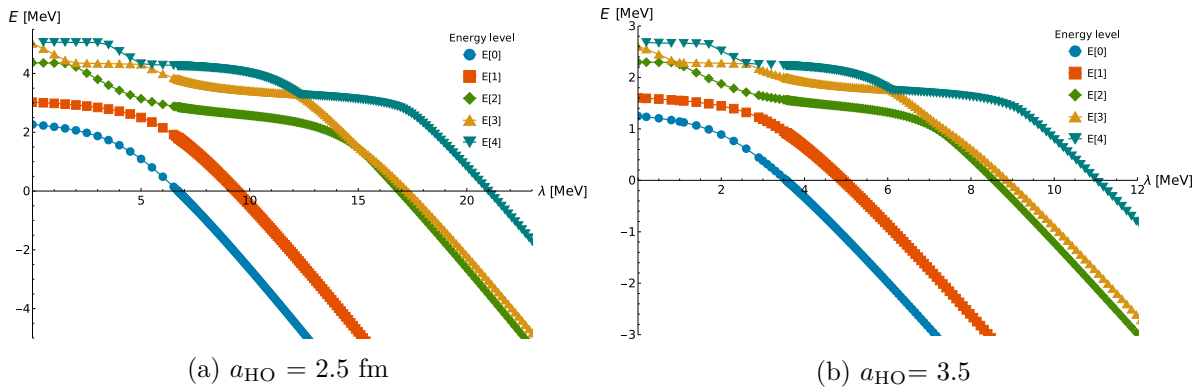


Figure 9.7.: First four energy levels with  $J^\pi = 0^+$  as a function of the coupling constant. Interaction  $N^3\text{LO}_{\text{EMN}} + N^3\text{LO}_{500,\text{NL}}$  Eigenvector binding with  $N_{\max}^{\text{bin}} = 2$  and  $n_{\text{ev}} = 9$ . The data used for extrapolation is denoted with  $E[0]$ . Note the different scales used on the plots.

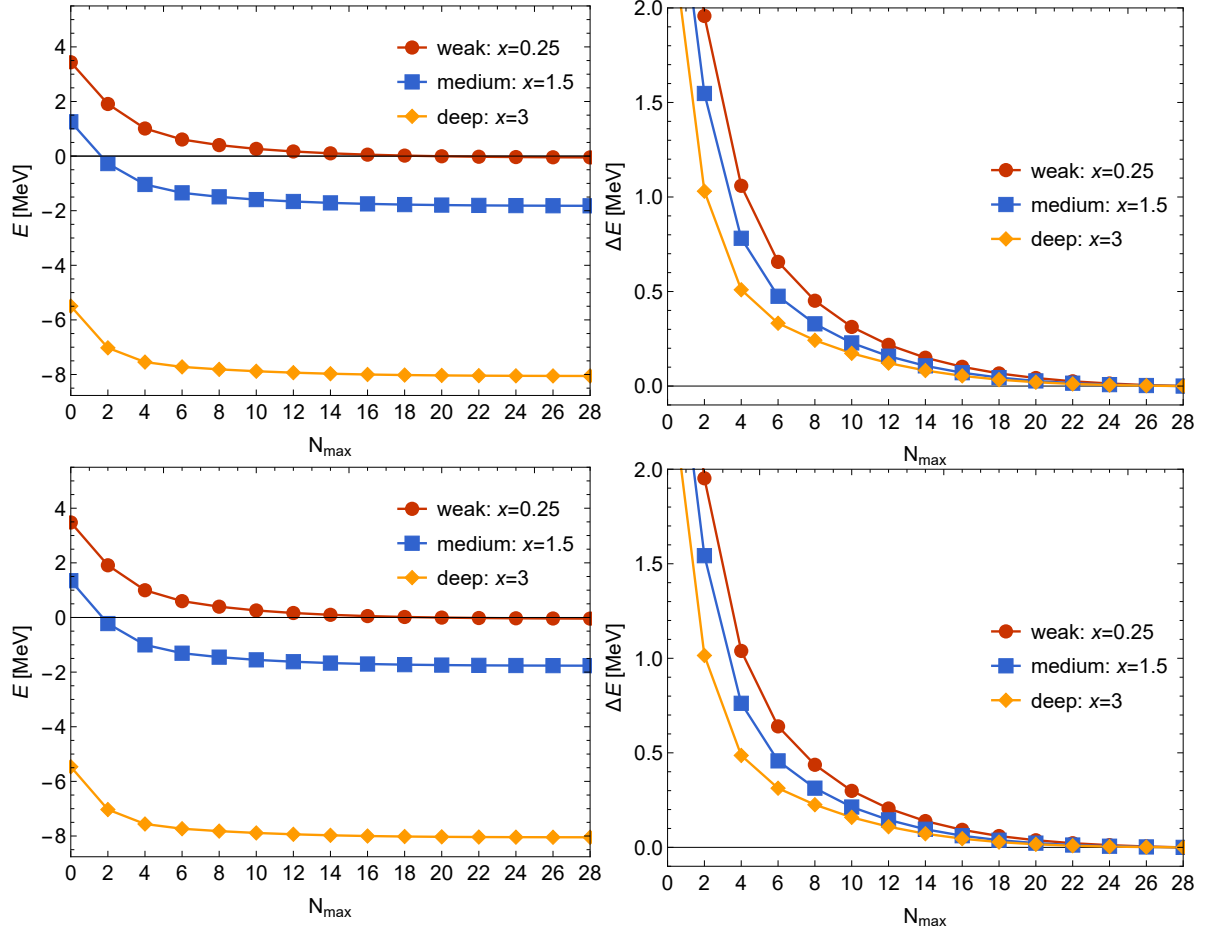


Figure 9.8.:  $N_{\max}$  sequence for the interactions  $N^3\text{LO}_{\text{EM}} + N^2\text{LO}_{500,\text{L}}$  on the top and  $N^3\text{LO}_{\text{EMN}} + N^3\text{LO}_{500,\text{NL}}$  at the bottom row at  $a_{\text{HO}} = 3.5$ . On the left the absolute energies obtained for three different  $x$  values,  $x \approx 0.25, 1.5, 3$ . On the right, the difference ( $E_{N_{\max} < 28} - E_{N_{\max} = 28}$ ). Threshold determined by linear interpolation.

### 9.2.2. ACCC and IACCC Analysis, Algorithm-, Start Value- and Data Point Dependence

The discussions in sections 8.5, 9.1 and 9.3, demonstrate that the used algorithm in combination with the selection of the data points, used in the fit, has an effect on the extrapolation. To not have to deal with the choice of data points and start values over and over again, we use the statistical ACCC [PvMM<sup>+</sup>13], which is described in section 8.4.2. Within this approach, we simultaneously fit the value of  $\lambda_0$ . This requires less manual input to choose a presumably good  $\lambda_0$ , but also increases fit instability.

In this section, we want to justify the use of the already introduced statistical ACCC and its application within the hereafter following tetra-neutron study.

To this end, we use the IACCC to determine the threshold parameter  $\lambda_0$  which is then used in the regular ACCC. This approach is the originally recommended procedure [KKH89]. The difficulties arising in this framework, when applied to the data that we have available, motivate the use of the statistical ACCC together with the Levenberg-Marquardt algorithm as primary fit method.

#### Minimization Algorithm and Start Parameter Dependence with Fixed Data Sets

The stability of fits is dependent on the starting values of the fit parameters, to varying degrees. Tightly bound to the choice of good starting points is the performance of the algorithm used to minimize the  $\chi^2$  problem. Additionally, different methods might be better or suited than others.

The algorithms which we compared are the Mathematica implementations of the Newton method (NE), the Quasi-Newton Broyden-Fletcher-Goldfarb-Shanno algorithm (BFGS), also referred to as Quasi-Newton (QN), the Levenberg-Marquardt algorithm (LM), which is a so-called Gauss-Newton method, and nonlinear Gradient (GR).

These methods make different approximations to compute the Hessian matrix. Assuming the complexity of the problem one wants to solve is within the scope of each method, as well as being suitable to actually be solved with a given method, they should arrive at the same result, within the errors made in the initial assumption on which a specific method is based. The computational costs, the number of steps needed to converge, and the required memory can vary. For details on the specific implementation of the algorithms within Mathematica, see reference [Mat20].

When applied to a specific problem with varying compatibility to different minimization algorithms, it comes as no surprise that, e.g., the sensitivity of starting values of the fit parameters can have a stronger influence.

In the case of the ACCC, we fit to a non-linear model of Padé approximants, either to

$$k_\ell^{[N,M]}(x) = \frac{P_N(x)}{Q_M(x)} = i \frac{c_0 + c_1 x + \dots + c_N x^N}{1 + d_1 x + \dots + d_M x^M}, \quad (9.2)$$

or without parameter  $c_0$

$$k_\ell^{[N,M]}(x) = \frac{P_N(x)}{Q_M(x)} = i \frac{c_1 x + \dots + c_N x^N}{1 + d_1 x + \dots + d_M x^M}, \quad (9.3)$$

or with additional fit parameter  $\lambda_0$

$$k_\ell^{[N,M]}(\lambda) = i \frac{c_0 + c_1 \sqrt{\lambda - \lambda_0} + \dots + c_N \sqrt{\lambda - \lambda_0}^N}{1 + d_1 \sqrt{\lambda - \lambda_0} + \dots + d_M \sqrt{\lambda - \lambda_0}^M}, \quad (9.4)$$

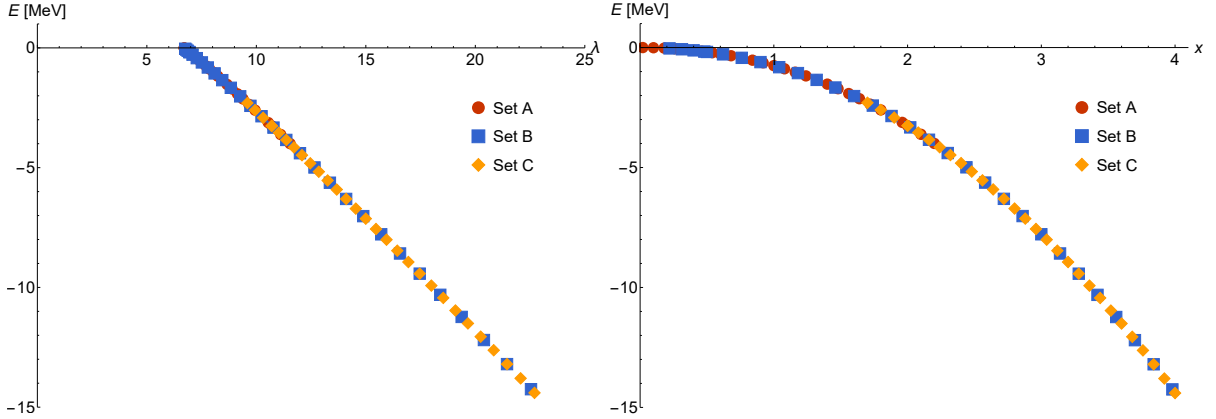


Figure 9.9.: The three data sets to compare the algorithm dependence from interaction  $N^3\text{LO}_{\text{EMN}} + N^3\text{LO}_{500,\text{NL}}$ ,  $a_{\text{HO}}=2.5$  fm. Each set consists of 30 points. The threshold value is determined via linear interpolation  $\lambda_0 \approx 6.702$ .

and

$$k_\ell^{[N,M]}(\lambda) = i \frac{c_1 \sqrt{\lambda - \lambda_0} + \dots + c_N \sqrt{\lambda - \lambda_0}^N}{1 + d_1 \sqrt{\lambda - \lambda_0} + \dots + d_M \sqrt{\lambda - \lambda_0}^M}, \quad (9.5)$$

which emphasizes the non-linearity further. Furthermore, the parameters are highly correlated. We are thus generally looking for a global minimum in a landscape of many local minima, which can be additionally degenerate w.r.t. the fit parameters.

An effort to reduce the degrees of freedom is presented in [ČPH16], called the Regularized Analytic Continuation. We do not employ this approach, limiting ourselves to the use of the ACCC, the inverse ACCC, and the statistical ACCC.

We observe differences in the Padé extrapolations when using different minimization techniques, seen in figures 8.3, 8.5 to 8.7 and 9.2 to 9.4, and leaves the case of ill-posed problems for the applied Newton, Quasi-Newton, and Gauss-Newton methods. A statement of which method to use is given e.g., in [SMHE17], where they advocate the use of the BFGS algorithm when performing a non-linear fit that simultaneously optimizes the threshold parameter  $\lambda_0$ . In the results of the  $\alpha + \alpha$  scattering with a phenomenological potential, see section 8.5, we noted different behaviour in the algorithms when using an external potential versus manipulation of the initial interaction to bind the system.

We perform a fitting sequence on three data sets sampled from the same initial set, with the mentioned methods and different starting parameters. The sets are obtained with  $N^3\text{LO}_{\text{EMN}} + N^3\text{LO}_{500,\text{NL}}$  at  $a_{\text{HO}} = 2.5$  fm, with all results shown with  $N_{\text{max}} = 28$ ,  $N_{\text{max}}^{\text{bin}} = 2$  and  $n_{\text{ev}} = 9$ .

The sample sets are divided in  $x = \sqrt{\lambda - \lambda_0}$  as follows:

- Set A has 30 points in the region  $x = [0, 2.3]$ .
- Set B has 30 points in the region  $x = [0.2, 3.9]$ .
- Set C has 30 points in the region  $x = [1.7, 4.0]$ .

The three sets as a function of  $\lambda$ , as well as a function of  $x$ , are shown in figure 9.9. To give ranges roughly equidistant in the variable  $x$ , the threshold value is determined via linear interpolation from the two closest points above and below the threshold from the complete available data set.

## 9. Results Analytic Continuation in the Coupling Constant

Set	Algo.	(2,2)	(3,3)	(4,4)	(5,5)	(6,6)	(7,7)	(8,8)
A	NE	6.7117	6.66884	–	–	–	–	–
	QN	6.7117	6.70164	6.70214	6.70202	6.70196	6.70183	6.7017
	LM	6.7117	6.70164	6.70213	6.70216	6.70216	6.70216	6.70216
	GR	6.71373	6.72498	6.74403	6.753	6.72522	6.75911	6.72257
B	NE	6.76678	6.60807	6.70193	6.70218	–	–	–
	QN	6.76678	6.69649	6.69939	6.70150	6.70014	6.69893	6.70142
	LM	6.76678	6.69649	6.70193	6.70218	6.70216	6.70216	6.70216
	GR	–	–	–	–	–	–	–
C	NE	6.97824	6.46543	–	–	–	–	–
	QN	6.97824	6.6986	6.84708	6.74094	6.68301	6.69306	6.72643
	LM	6.97824	6.6986	6.67734	-816284.	-1.33131	6.70648	42.0862
	GR	–	–	–	–	–	–	–

Table 9.4.: Threshold values  $\lambda_0$  obtained via IACCC for three different sets consisting of 30 points, see text for details. Interaction  $N^3LO_{EMN} + N^3LO_{500,NL}$  with  $a_{HO}=2.5$  fm. Start values at all orders set to 0, except for  $\lambda_0 = 6.70216$ . Note that the first IACCC Padé order starts at (2,2). NE = Newton, QN = Quasi-Newton (BFGS), LM = Levenberg-Marquardt, GR = gradient.

Performing the IACCC, we compare the obtained threshold values  $\lambda_0$  for each set between the three methods and different starting parameters. The first comparison is done with a starting parameter for  $\lambda_0$  and the rest all set to 0 and is listed in table 9.4. The second comparison is with all  $\lambda_0$  as before and starting values set to 1 at all orders, see table 9.5.

The third method is to use the results from the previous lower order fit as start values for the next higher order. This leaves two new parameters, whose start values are first set to 0. Should this not lead to a converged result, then, in a first step, the parameter in the nominator,  $\lambda_N$ , is randomly chosen from a range of  $[-15,15]$  in half integer steps, while the denominator  $\mu_M$  is kept at 0. If this still is not sufficient after 8 tries, then  $\mu_M$  is also randomly chosen to be either -1, 0 or 1. This procedure is repeated either until a fit is found, or aborted after 60 tries. This approach is admittedly arbitrary and solely based on the observation, that the different combinations in the sign of the undetermined starting parameters have a bigger impact on if a fit is found than the precise value. The results for this are listed in table 9.6.

Comparing the results, we find that the Levenberg-Marquardt algorithm shows proper convergence behaviour in the Padé orders, for the data sets A and B for all three starting parameter value choices, ending up at what was the initial guess by linear interpolation. On the other hand, for data set C, the same method results in unrealistic values, especially in the case of using the previous lower order fit as input. The fact that the results show little variation with the starting parameter values, provided the data set is good, qualifies the Levenberg-Marquardt algorithm to be the primary method. The Newton approach often does not converge or needs lengthy searches for suited starting values, which increases calculation time; but when it does converge, which is in this instance only the case for starting values from the previous lower order fits, the results agree with the other methods. The Quasi-Newton BFGS algorithm shows little variation with different starting values between the different data sets. In these examples, it is the middle ground in terms of reliability and calculation time – not really showing a converged parameter value in the Padé orders, but also not returning off-the-chart results. The disadvantage in this is that also inadequate fits are found, possibly skewing the conclusion one might draw from such fits.

The Gradient method is the least flexible in escaping a local minimum, thus resulting in converged Padé orders, but not necessarily finding the global minimum. It should not be used. We only show it for reference.

The inverse ACCC is the recommended approach in reference [KKH89] to determine the correct threshold value  $\lambda_0$ . The presented results do not reveal what the correct values to use are. Focusing on a data set which would be a reasonable choice when being limited in the amount of data points one can calculate, set B, as it spans a broad range of  $x$  values, the results obtained from the IACCC with the Levenberg-Marquardt algorithm suggest that in this particular example the value  $\lambda_0 = 6.70216$  should be used, as it is converged in the Padé orders. It is not clear how to choose  $\lambda_0$  in the case of non-converging values. In the common literature, e.g., references [KKH89, TSVL99, Aoy03], no recommendations are made regarding the handling of this scenario, if  $\lambda_0$  is to remain constant, apart from demanding that a good  $\lambda_0$  shows Padé order convergence to a reasonable amount within the expected numerical accuracy of the data. This raises further questions. The Padé approximants have an optimal order at finite accuracy data, after which the description of the data worsens with growing order [KKH89]. Finding the best  $\lambda_0$  fit combination by that stability argument thus requires the knowledge of the “break-down” order. How this is determinable from some calculable criterion is not clear.

This question is avoided when simultaneously fitting  $\lambda_0$ . The drawback is a potentially more unstable fit, due to the strong non-linearity, as well as worse Padé order agreement, since each order has a different threshold value. Though, as is shown for a simple example in section 8.5, as well as in reference [SMHE17], the simultaneous fit result in reasonable data.

To further illustrate the difficulties going the way of first performing the IACCC to obtain  $\lambda_0$  and subsequently performing the regular ACCC, we take each  $\lambda_0$  from each IACCC Padé order and perform the ACCC fit with the same algorithm, limiting us to the BFGS and Levenberg-Marquardt methods. We choose the set B as an example. The same procedure with set A and C can be found in appendix E.

The parameter values are based on the previous lower order fits. The results of this are shown in figures 9.10 and 9.11. These plots show the  $S$ -matrix pole trajectories in the complex  $k$ -plane. How to interpret this type of plot is discussed in figure 8.4. On the positive imaginary axis lie the bound states which are fitted. The fit is then extrapolated by decreasing  $\lambda$  below the threshold, with  $\lambda = 0$  corresponding to the end of the line. A resonance has its ending point in the fourth quadrant,  $\text{Re}(k) > 0, \text{Im}(k) < 0$  and  $|\text{Im}(k)| < \text{Re}(k)$ . Each figure shows the ACCC fits with the  $\lambda_0$  from the IACCC with the corresponding order given in the lower left corner of each window.

The BFGS method in figure 9.10 has remarkable agreement in the Padé orders, for most  $\lambda_0$  values, even for very high orders of up to (8,8). However, at IACCC orders (4,4) to (7,7), the ACCC orders (3,3) and higher move into the first quadrant. In the last two panels, they change the direction, going to regions that correspond to negative resonance positions  $E_R$ .

In contrast, the Levenberg-Marquardt results in figure 9.11 exhibit no real order by order convergence, generally being unstable in this regard. The fit lines do, however, end in many cases in a region that would correspond to a resonance, though at very different positions and widths.

9. Results Analytic Continuation in the Coupling Constant

Set	Algo.	(2,2)	(3,3)	(4,4)	(5,5)	(6,6)	(7,7)	(8,8)
A	NE	6.7117	6.66654	6.70213	–	–	–	–
	QN	6.7117	6.70164	6.70214	6.70202	6.70195	6.70183	6.7017
	LM	6.7117	6.70164	6.70213	6.70216	6.70216	6.70216	6.70216
	GR	6.71908	6.73101	6.74441	6.75437	6.75706	6.7579	6.75787
B	NE	6.76678	6.69649	6.70193	6.70218	–	–	–
	QN	6.76678	6.69649	6.69944	6.7015	6.70015	6.70175	6.70143
	LM	6.76678	6.69649	6.70193	6.70218	6.70216	6.70216	6.70216
	GR	–	–	–	–	–	–	–
C	NE	6.97824	6.4535	6.6685	6.63892	–	–	–
	QN	6.97824	6.6986	6.83325	6.73869	6.68093	6.69248	6.72682
	LM	6.97824	6.6986	6.67734	-197987	-179.258	6.70648	–
	GR	–	–	–	–	–	–	–

Table 9.5.: Threshold values  $\lambda_0$  obtained via IACCC for three different sets consisting of 30 points,  $a_{\text{HO}} = 2.5$  fm. Start values at all orders set to 1, except for  $\lambda_0 = 6.70216$ . See also table 9.4.

Set	Algo.	(2,2)	(3,3)	(4,4)	(5,5)	(6,6)	(7,7)	(8,8)
A	NE	6.7117	6.70164	6.70213	6.70215	6.70217	6.70215	6.70217
	QN	6.7117	6.70164	6.70214	6.702133	6.70218	6.70217	6.70216
	LM	6.7117	6.70164	6.70213	6.70216	6.70216	6.70216	6.72069
	GR	6.71373	6.70278	6.7028	6.70177	6.70171	6.70178	6.70176
B	NE	6.76678	6.69649	6.70193	6.69689	6.70216	6.70213	6.70213
	QN	6.76678	6.69649	6.70193	6.7019	6.70211	6.70211	6.7021
	LM	6.76678	6.69649	6.70193	6.70218	6.70216	6.70216	6.70216
	GR	6.74406	6.76914	6.72593	6.72493	6.70371	6.70711	6.70004
C	NE	6.97824	6.6986	6.66919	6.64561	6.69681	6.6282	6.66101
	QN	6.97824	6.6986	6.67325	6.67309	6.67357	6.67348	6.67215
	LM	6.97824	6.6986	6.67734	-579142	$-2.8 \cdot 10^7$	$-2.5 \cdot 10^7$	$-1.1 \cdot 10^7$
	GR	6.84137	6.94414	6.8679	6.87059	6.80217	6.79886	6.80037

Table 9.6.: Threshold values  $\lambda_0$  obtained via IACCC for three different sets consisting of 30 points,  $a_{\text{HO}} = 2.5$  fm. Start values are taken from the previous order. For details, see text as well as table 9.4.

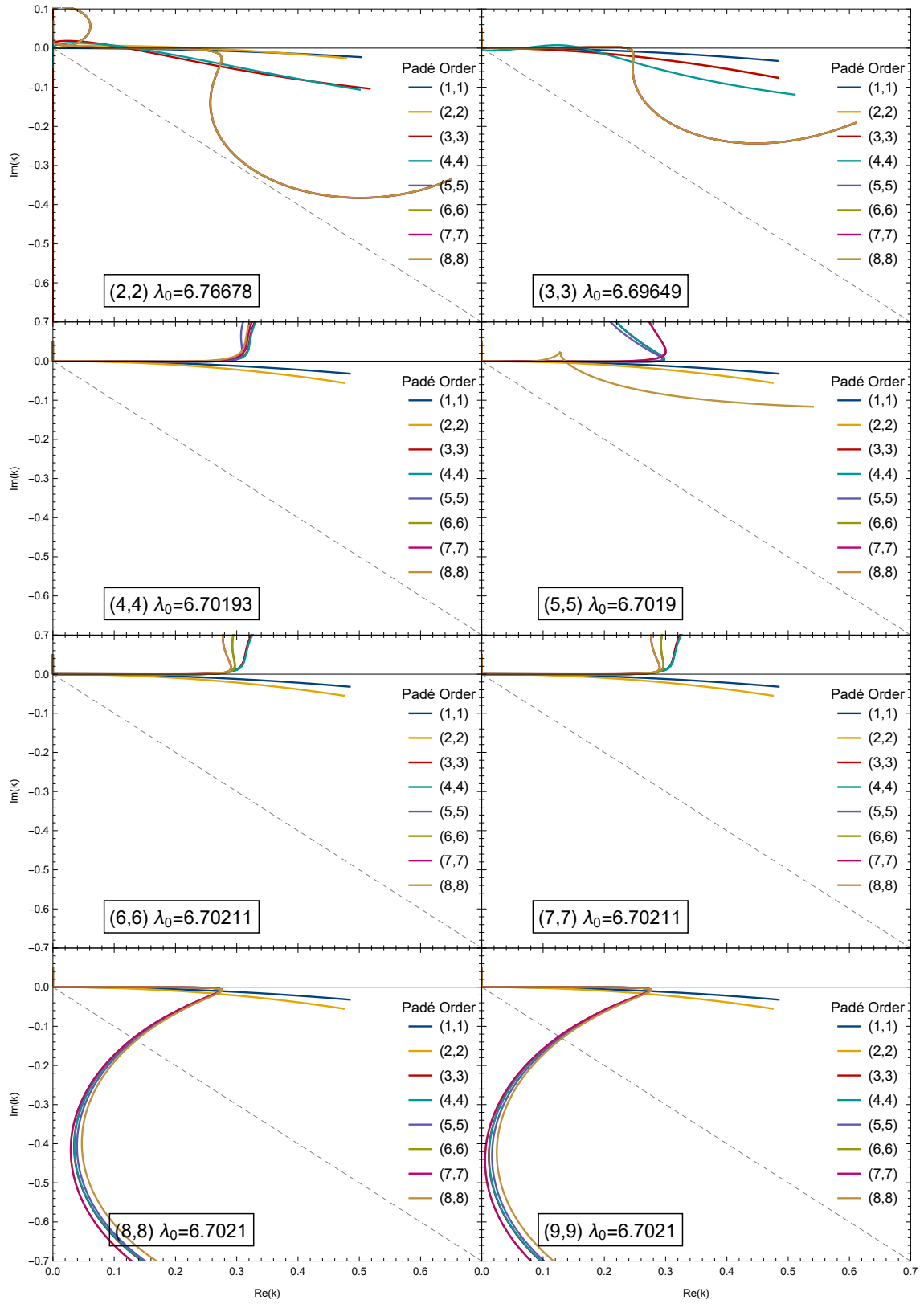


Figure 9.10.: Tetraneutron  $S$ -matrix pole trajectories. Data set B,  $\lambda_0$  determination and fit performed with Quasi-Newton BFGS.  $N_{\max} = 28$ ,  $a_{\text{HO}} = 2.5$  fm.

## 9. Results Analytic Continuation in the Coupling Constant

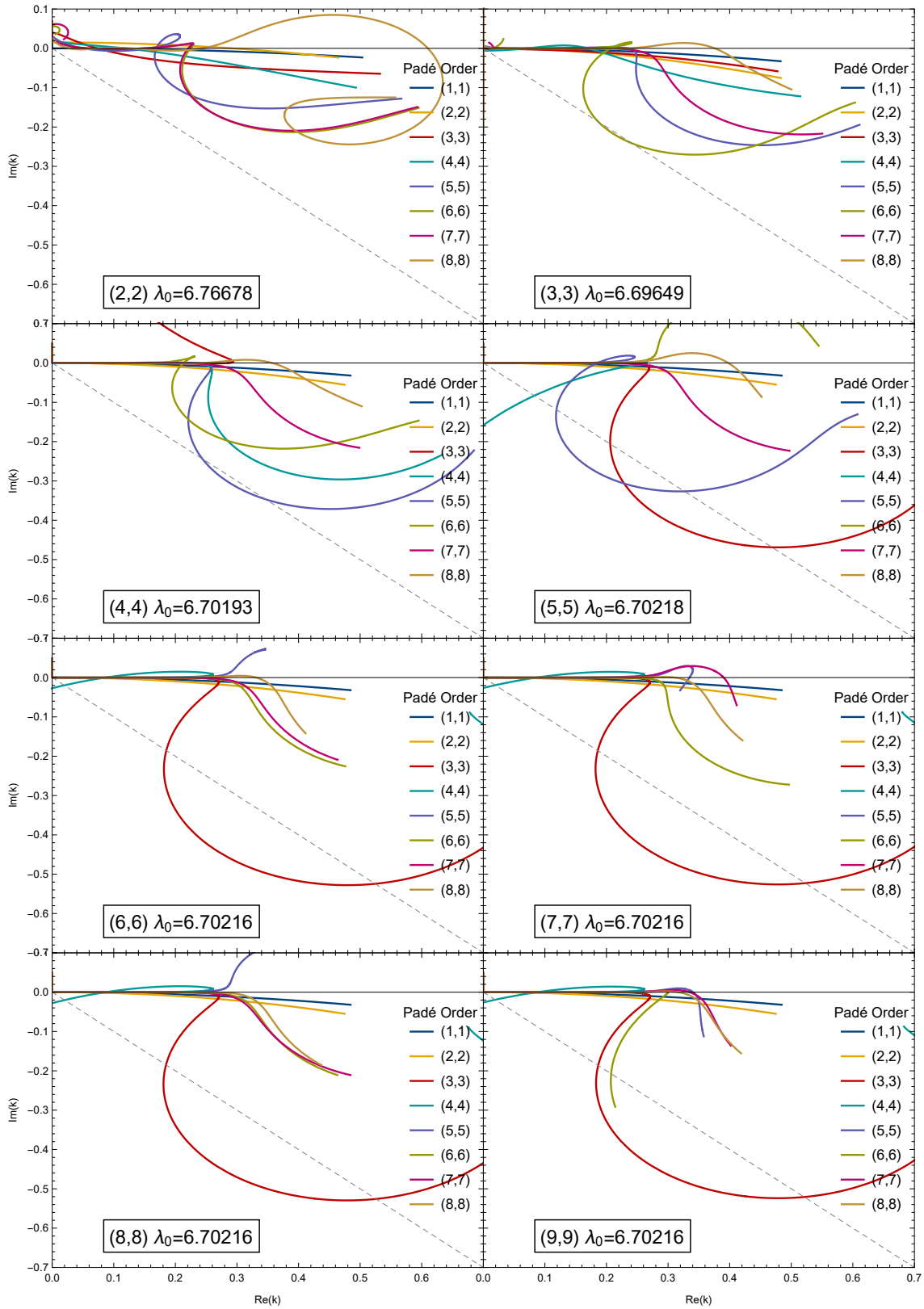


Figure 9.11.: Tetra-neutron  $S$ -matrix pole trajectories. Data set B,  $\lambda_0$  determination and fit performed with Levenberg-Marquardt.  $N_{\max} = 28$ ,  $a_{\text{HO}} = 2.5$  fm.

### Minimization Algorithm and Start Parameter Dependence with Variable Subsets

The choice of which points are used to fit data has some impact on the outcome of the extrapolation, but also on the stability of the fit. This can already be seen in the previous subsection 9.2.2. To obtain a measure of the impact of data point choice, we use the statistical ACCC [PvMM<sup>+</sup>13], introduced in section 8.4, where also the fit protocol is explained. From the mean value and standard deviation of the distribution, we gain an estimate for the dependence of the fit to the data point selection. We assume that at the same time, some effects of the start value dependence can be absorbed, with a large enough number of sampled sets. The standard deviations, shown as boxes around the mean value, do not give an error estimate in a statistical sense. This means that they do not yield a probability of finding the correct value within that region. They can only provide information about the sensitivity to data selection and the reliability of the mean value of the statistical ACCC (SACCC) to be a good approximation to an ordinary ACCC.

To both demonstrate the data point and the fit algorithm dependency, we discuss the results of three SACCC calculations with a small sample size of 100 subsets. The Newton method is shown in figure 9.12, the BFGS algorithm in figure 9.13, and the Levenberg-Marquardt algorithm in figure 9.14. The plots illustrate the (resonance-) energy-width plane. Each dot corresponds to one subset. The larger dots indicate the mean value, surrounded by the standard deviation boxes. The left hand side of each plot gives the mean and standard deviation with equally weighted points, the right hand side uses the estimated fit error variance of the fit routine to weight each point accordingly in the determination of mean and standard deviation. The same interaction and  $a_{\text{HO}}$  is used as in section 9.2.2. All fits are performed with the parametrization as in equation (8.45b). Further, the Padé order is shown up to large orders of (9,9).

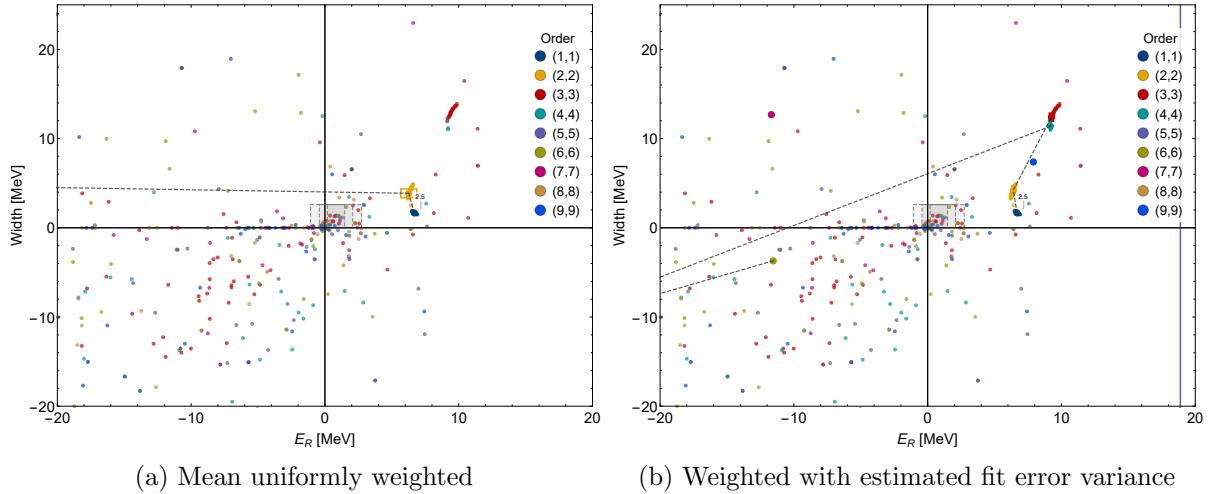


Figure 9.12.: Statistical ACCC, 100 sets of 30 points, Newton algorithm with  $\sigma_{\text{rel}}^{\text{fit}} = 8$ ,  $\text{N}^3\text{LO}_{\text{EMN}} + \text{N}^3\text{LO}_{500,\text{NL}}$ ,  $a_{\text{HO}} = 2.5$  fm. Comparison of two weightings. The grey box gives the experimental range [KSM<sup>+</sup>16].  $N_{\text{max}}^{\text{bin}} = 0$ ,  $n_{\text{ev}} = 2$ . Parametrization as in equation (8.45b). The grey dashed lines connect the mean values of each order to guide the eye.

Considering at the Newton and BFGS fits in figures 9.12 and 9.13, the far spread of the individual points is immediately apparent. The first two Padé orders are consistent between all methods and do not spread. The unweighted means are accordingly far out, and are not in the shown region of the plots. However, the majority of the fits have large estimated fit error variances, according to the analysis of variance (ANOVA). Calculating the mean and

## 9. Results Analytic Continuation in the Coupling Constant

standard deviation with the inverse fit error variance as weights for each point, the locations shift drastically to a position where all algorithms are roughly compatible up to the (4,4) order. A very different outcome is presented when using the Levenberg-Marquardt algorithm, shown in figure 9.14. Here, the spread of the individual fits is contained to a moderate region, compared to the other two fit methods. Each point is also associated with an estimated fit error variance of similar magnitude to the others, leading to relatively small changes when comparing the differently weighted means.

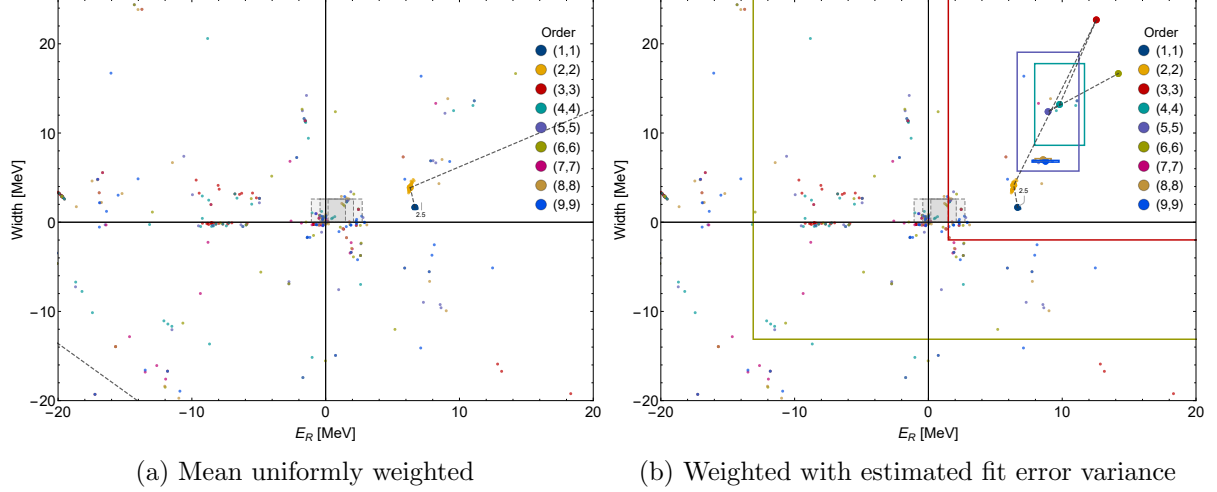


Figure 9.13.: Statistical ACCC, 100 sets of 30 points, Quasi-Newton BFGS with  $\sigma_{\text{rel}}^{\text{fit}} = 8$ ,  $N^3\text{LO}_{\text{EMN}} + N^3\text{LO}_{500,\text{NL}}$ ,  $a_{\text{HO}} = 2.5$  fm. Comparison of different weightings. The grey box gives the experimental range [KSM<sup>+</sup>16].

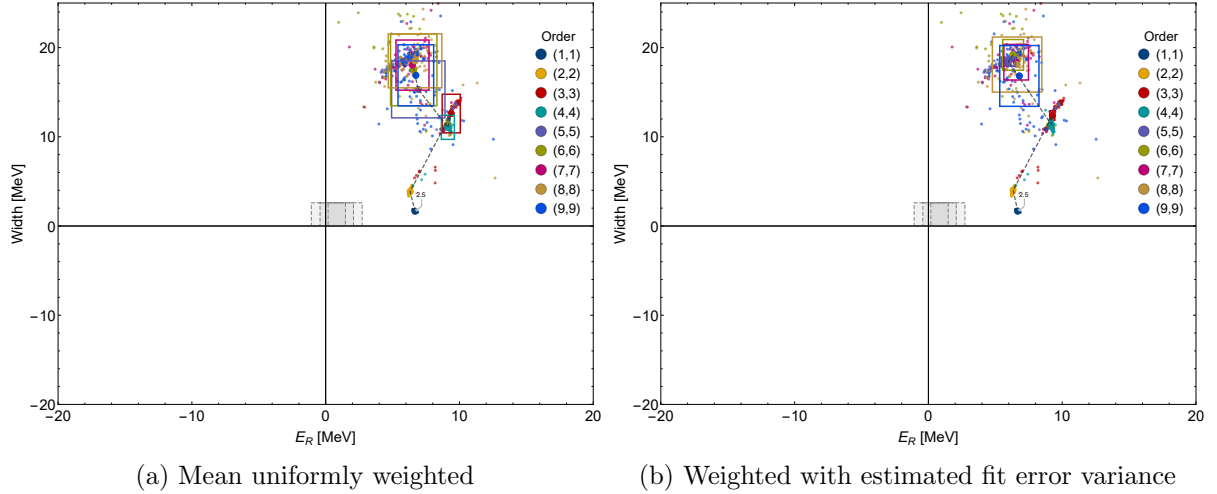


Figure 9.14.: Statistical ACCC, 100 sets of 30 points, Levenberg-Marquardt with  $\sigma_{\text{rel}}^{\text{fit}} = 8$ ,  $N^3\text{LO}_{\text{EMN}} + N^3\text{LO}_{500,\text{NL}}$ ,  $a_{\text{HO}} = 2.5$  fm. Comparison of different weightings. The grey box gives the experimental range [KSM<sup>+</sup>16].

To illustrate how the fit parametrization of equation (8.45), also given in equations (9.4) and (9.5), affects the extrapolations, we perform calculations as in figures 9.12 to 9.14 for 1000 subsets of 30 points, each with the three presented algorithms and parametrization as in equation (8.45b), as well as in equation (8.45a). The results of this is given in tables 9.7 and 9.8 for an oscillator length of  $a_{\text{HO}} = 2.5$  fm and in tables 9.9 and 9.10 for  $a_{\text{HO}} = 3.5$  fm. Listed

are the mean values with standard deviation, where the results for the Newton and BFGS are weighted with the estimated fit error variance. The effect on the mean values at each Padé order is overall comparatively small, with a few exceptions. However, the standard deviation is noticeably reduced with the Newton method at orders (4,4) and above. With the BFGS and Levenberg-Marquardt method, the impact is much smaller, but tending to smaller standard deviations at lower orders when including  $c_0$ , but not necessarily leading to a reduction at higher orders.

The findings presented here are an argument for the use of the Levenberg-Marquardt algorithm in the statistical ACCC.

Mean resonance position $E_R$ [MeV] excluding $c_0$ , $a_{\text{HO}} = 2.5$ fm					
	(2,2)	(3,3)	(4,4)	(5,5)	(6,6)
NE	$6.42 \pm 0.17$	$9.20 \pm 0.15$	$9.18 \pm 0.16$	$5.21 \pm 1150$	$8.50 \pm 237$
QN	$6.38 \pm 0.12$	$9.52 \pm 4.01$	$9.31 \pm 0.88$	$8.23 \pm 1.22$	$8.42 \pm 0.64$
LM	$6.39 \pm 0.13$	$9.24 \pm 0.17$	$8.91 \pm 0.49$	$5.93 \pm 0.77$	$6.54 \pm 0.92$

Mean resonance width $\Gamma$ [MeV] excluding $c_0$					
NE	$4.26 \pm 0.53$	$12.2 \pm 0.48$	$11.1 \pm 0.53$	$18.2 \pm 149$	$-30.2 \pm 338$
QN	$4.13 \pm 0.49$	$12.0 \pm 11.4$	$11.6 \pm 1.48$	$12.8 \pm 1.77$	$12.9 \pm 0.95$
LM	$4.16 \pm 0.45$	$12.3 \pm 0.52$	$11.8 \pm 0.74$	$18.4 \pm 1.10$	$18.7 \pm 2.31$

Table 9.7.: Tetraneutron resonance energy position  $E_R$  and width  $\Gamma$  in MeV, rounded to two significant for values  $> 1$ , three significant digits otherwise. Interaction  $\text{N}^3\text{LO}_{\text{EMN}} + \text{N}^3\text{LO}_{500,\text{NL}}$ , at  $a_{\text{HO}} = 2.5$  fm,  $N_{\text{max}}^{\text{bin}} = 0$ ,  $n_{\text{ev}} = 2$ . Levenberg-Marquardt results correspond to those depicted in figure 9.22.

Mean resonance position $E_R$ [MeV] including $c_0$ , $a_{\text{HO}} = 2.5$ fm					
	(2,2)	(3,3)	(4,4)	(5,5)	(6,6)
NE	$7.03 \pm 0.42$	$9.09 \pm 0.13$	$8.72 \pm 0.25$	$6.16 \pm 1320$	$6.28 \pm 899000$
QN	$6.90 \pm 0.35$	$9.17 \pm 0.34$	$8.60 \pm 0.42$	$8.79 \pm 0.90$	$8.44 \pm 0.34$
LM	$6.76 \pm 0.25$	$9.18 \pm 0.07$	$8.52 \pm 0.44$	$6.39 \pm 0.66$	$6.84 \pm 0.92$

Mean resonance width $\Gamma$ [MeV] including $c_0$					
NE	$5.93 \pm 0.59$	$11.52 \pm 0.63$	$10.7 \pm 0.31$	$4.09 \pm 8.53$	$4.74 \pm 96.6$
QN	$5.76 \pm 0.64$	$11.7 \pm 0.85$	$11.14 \pm 0.94$	$10.2 \pm 3.25$	$6.84 \pm 0.51$
LM	$5.60 \pm 0.53$	$11.7 \pm 0.34$	$10.8 \pm 0.32$	$18.8 \pm 0.90$	$19.0 \pm 2.16$

Table 9.8.: See description of table 9.7. Levenberg-Marquardt results correspond to those depicted in figure 9.22.

9. Results Analytic Continuation in the Coupling Constant

Mean resonance position $E_R$ [MeV] excluding $c_0$ , $a_{\text{HO}} = 3.5$ fm					
	(2,2)	(3,3)	(4,4)	(5,5)	(6,6)
NE	$3.61 \pm 0.15$	$4.51 \pm 0.04$	$4.62 \pm 0.03$	$4.53 \pm 99.4$	$11.0 \pm 678$
QN	$3.61 \pm 0.17$	$4.46 \pm 0.11$	$4.60 \pm 0.17$	$4.46 \pm 0.31$	$4.40 \pm 0.19$
LM	$3.65 \pm 0.16$	$4.49 \pm 0.03$	$4.38 \pm 0.048$	$4.20 \pm 0.214$	$4.19 \pm 0.15$

Mean resonance width $\Gamma$ [MeV] excluding $c_0$					
NE	$2.47 \pm 0.26$	$6.29 \pm 0.14$	$6.07 \pm 0.08$	$3.00 \pm 58.7$	$-21.2 \pm 196$
QN	$2.46 \pm 0.27$	$6.40 \pm 0.52$	$6.24 \pm 0.41$	$5.24 \pm 1.59$	$6.11 \pm 0.80$
LM	$2.53 \pm 0.28$	$6.33 \pm 0.14$	$5.82 \pm 0.10$	$5.82 \pm 0.23$	$5.99 \pm 0.27$

Table 9.9.: See description of table 9.7. Levenberg-Marquardt results correspond to those depicted in figure 9.22.

Mean resonance position $E_R$ [MeV] including $c_0$ , $a_{\text{HO}} = 3.5$ fm					
	(2,2)	(3,3)	(4,4)	(5,5)	(6,6)
NE	$3.94 \pm 0.18$	$4.43 \pm 0.08$	$3.90 \pm 0.52$	$3.55 \pm 4.11$	$3.34 \pm 336$
QN	$3.91 \pm 0.18$	$4.37 \pm 0.29$	$4.24 \pm 0.26$	$4.00 \pm 0.85$	$4.82 \pm 0.54$
LM	$3.86 \pm 0.17$	$4.52 \pm 0.07$	$4.30 \pm 0.07$	$4.14 \pm 0.15$	$4.29 \pm 0.13$

Mean resonance width $\Gamma$ [MeV] including $c_0$					
NE	$3.10 \pm 0.19$	$6.37 \pm 0.14$	$3.25 \pm 1.02$	$2.48 \pm 3.03$	$3.56 \pm 478$
QN	$3.06 \pm 0.22$	$6.22 \pm 0.19$	$5.64 \pm 0.68$	$5.38 \pm 3.33$	$4.76 \pm 0.54$
LM	$3.02 \pm 0.21$	$6.20 \pm 0.10$	$5.70 \pm 0.06$	$5.82 \pm 0.23$	$6.19 \pm 0.22$

Table 9.10.: See description of table 9.7. Levenberg-Marquardt results correspond to those depicted in figure 9.22.

### 9.2.3. Harmonic Oscillator Length Dependence

The dependence on the oscillator length, or equivalently the frequency, in a usual bound-state calculation is something that is only an artefact of the finite model space, and thus becomes less and less as  $N_{\max}$  increases [PNB09]. It is, therefore, common to perform the calculation of an observable whose harmonic oscillator dependency is yet unknown, with a few different frequencies, compare their  $N_{\max}$  convergence behaviour, chose the frequency with the best convergence, and stick with it for the remaining calculations [PNB09]. Not so in the case of eigenvector binding. Here, the binding potential is constructed from the  $a_{\text{HO}}$  dependent Hamiltonian, and thus the extrapolated result is dependent on this as well. Not being stationary under variation of the external potential means one is model dependent, and thus diminishes the predictive power. The oscillator length takes on the role of the spatial extension of the potential. For an outspread system, an appropriate  $a_{\text{HO}}$  is needed to accommodate the wave function. The choice of  $a_{\text{HO}}$  causes a systematic uncertainty due to the a model-dependence and the spatial restriction of the system.

The  $a_{\text{HO}}$  dependence of the unmodified data for the two different chiral interactions used is shown in figures 9.5 and 9.6, and discussed in section 9.2.1.

In figure 9.15 and figure 9.16, we show the binding energy as a function of  $\lambda$ , corresponding to the interactions  $N^3\text{LO}_{\text{EM}} + N^2\text{LO}_{500,\text{L}}$  and  $N^3\text{LO}_{\text{EMN}} + N^3\text{LO}_{500,\text{NL}}$ , respectively. The bound-state energies at different oscillator lengths behave analogously to the unbound scheme, that is that smaller lengths, which lie higher in energy, require more binding energy in the form of  $\lambda$ . In other words, this means that the threshold value  $\lambda_0$  must lie at larger values for smaller  $a_{\text{HO}}$ . Not all  $a_{\text{HO}}$  are calculated over a wider range in the unbound regime. This is the reason for the distinct kinks visible in figure 9.15. In figure 9.16, additionally two different ( $N_{\max}^{\text{bin}}, n_{\text{ev}}$ ) are shown, which is discussed in section 9.2.5.

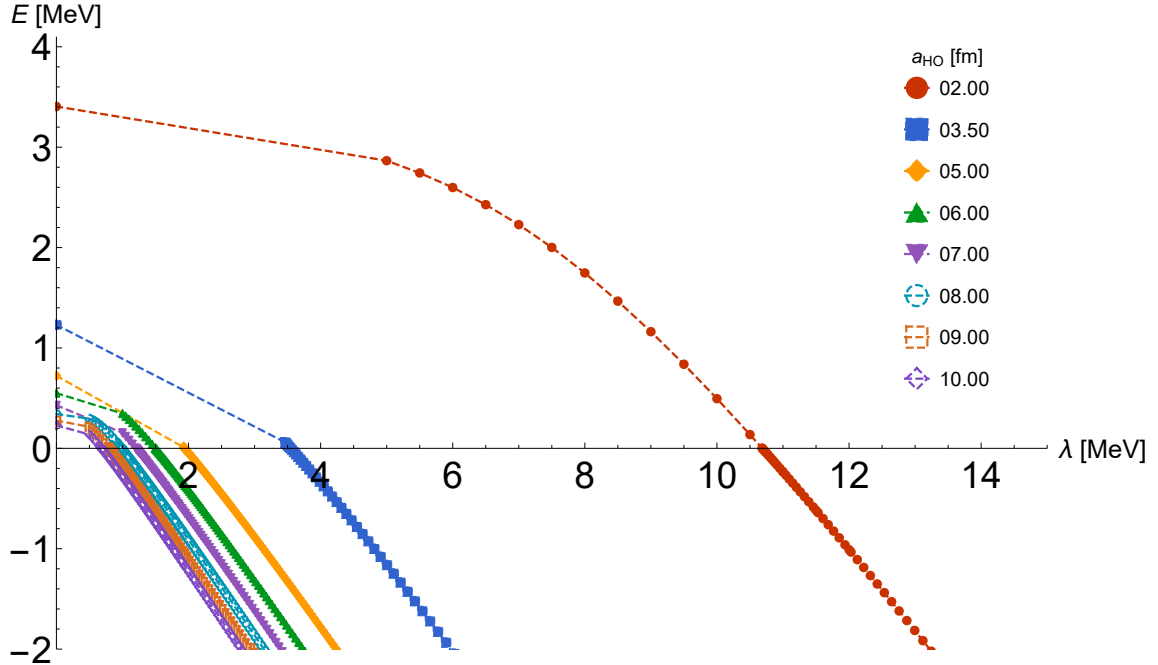


Figure 9.15.: Tetraneutron binding energies close-up for different oscillator lengths near the threshold. Interaction  $N^3\text{LO}_{\text{EM}} + N^2\text{LO}_{500,\text{L}}$ ,  $N_{\max}^{\text{bin}} = 2$ ,  $n_{\text{ev}} = 1$ .

Considering the Padé extrapolations in figures 9.17 and 9.22 (see sections 8.4.2 and 8.5 for the introduction of the SACCC), there are obvious differences in how one would interpret the

## 9. Results Analytic Continuation in the Coupling Constant

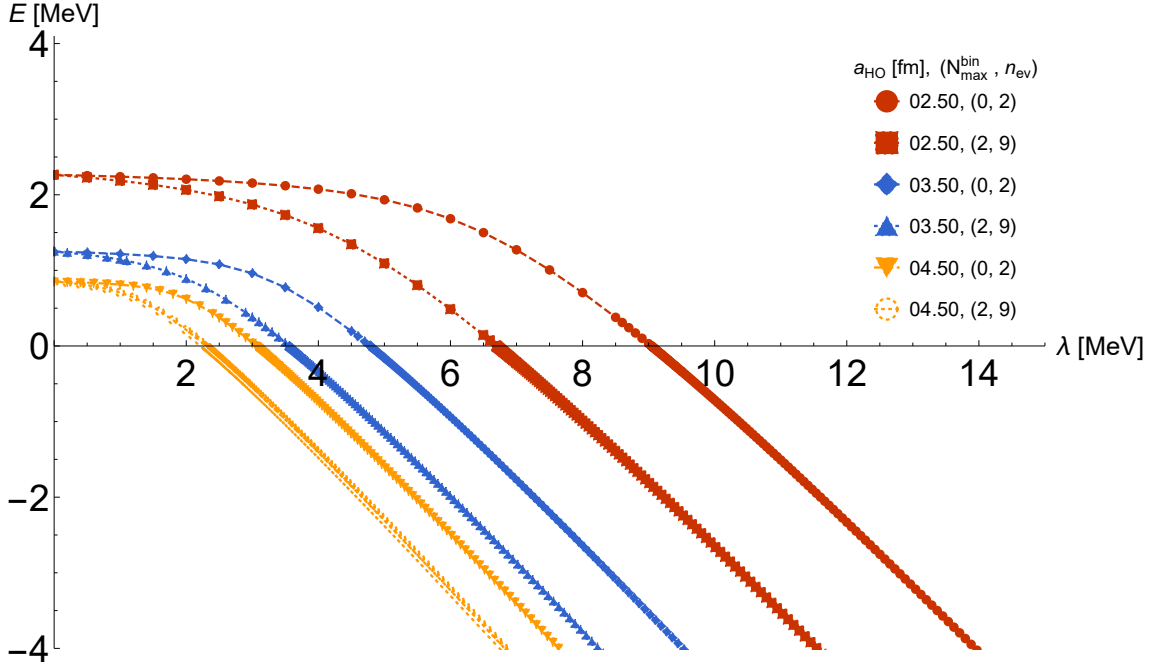


Figure 9.16.: Tetra-neutron binding energies close-up for three oscillator lengths near the threshold, combined with different  $N_{\max}^{\text{bin}}$  and  $n_{\text{ev}}$  values, see also section 9.2.5. Interaction  $\text{N}^3\text{LO}_{\text{EMN}} + \text{N}^3\text{LO}_{500,\text{NL}}$ .

results depending on the oscillator length  $a_{\text{HO}}$ . For both interactions, the  $a_{\text{HO}} \leq 2.5$  fm behave significantly different than the larger lengths regarding the Padé orders. In the case of the data obtained from  $\text{N}^3\text{LO}_{\text{EM}} + \text{N}^2\text{LO}_{500,\text{L}}$ , in figure 9.17, the  $a_{\text{HO}} = 2.0$  fm fit is inconsistent in the Padé orders. From order (2,2), the mean value jumps from a value of  $(E_R, \Gamma) \approx (7.4, 3.6)$  MeV to  $(E_R, \Gamma) \approx (19.4, 9.0)$  MeV, and continuing in a unsystematic pattern going to higher orders. The relatively consistent clustering of the individual extrapolations at orders (3,3) and (4,4), together with the spread in extrapolation results in the next higher orders, indicates the limit of the Padé approximation to describe this data set.

For the oscillator length 2.5 fm with the interaction  $\text{N}^3\text{LO}_{\text{EMN}} + \text{N}^3\text{LO}_{500,\text{NL}}$  in figure 9.22, the Padé orders do not agree in the width, but are more moderate in their overall Padé order-by-order behaviour, compared to the  $a_{\text{HO}} = 2.0$  fm case, and agree reasonably well w.r.t the resonance position, see also table 9.12.

At oscillator lengths above 3.5 fm, the Padé orders are agreeing with each other and could be considered broad resonances, at this specific length. Furthermore, the larger oscillator lengths approach the experimentally proposed candidate region, indicated by the grey shaded area. The behaviour of the resonance energy and width as a function of  $a_{\text{HO}}$  is shown in figure 9.18. The plot illustrates the difficulty in assessing if some form of stabilization with further increasing HO length takes place. The energy and width lie on top of each other starting with  $a_{\text{HO}} = 3.5$  fm, and continue to decrease. To see what limit of  $a_{\text{HO}} \rightarrow \infty$  under the heuristic assumption of exponential decay is, two fits are shown. The result in a range for  $E_R$  of 0.86 to 0.58 MeV.

Nevertheless, the result looks significantly different from the dineutron case. Thus, even with the uncertainty of the decreasing resonance energy and width prediction with increasing  $a_{\text{HO}}$ , the overall results do support the existence of a resonance. Further, under the assumption diffuse system, larger HO length should be favoured. This gives an upper limit to the parameters,

whereas the extrapolation to  $a_{\text{HO}} \rightarrow \infty$  leads to a tentative lower bound. For the interaction with eigenvector binding parameters  $N_{\text{max}}^{\text{bin}} = 2$ ,  $n_{\text{ev}} = 1$ , taking the first  $a_{\text{HO}}$  with stable Padé orders as upper limit, which is  $a_{\text{HO}} = 3.5$  fm, we find  $(0.58 \leq E_R \leq 3.75 \pm 0.3)$  MeV and  $(0.5 \leq \Gamma \leq 3.6 \pm 0.5)$  MeV.

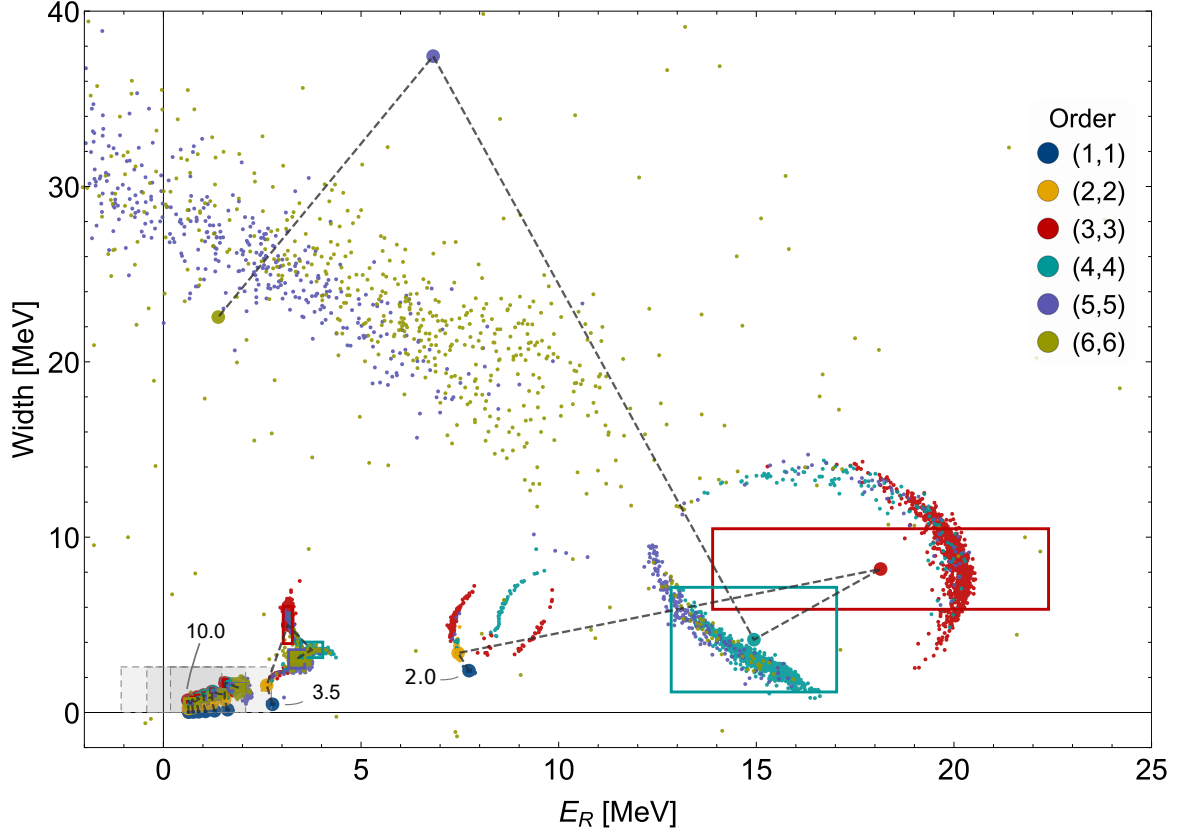


Figure 9.17.: Tetraneutron statistical ACCC extrapolation results for the data sets from figure 9.15,  $N^3\text{LO}_{\text{EM}} + N^2\text{LO}_{500,\text{L}}$  interaction. 1000 subsets of 30 points, Levenberg-Marquardt with  $\sigma_{\text{rel}}^{\text{fit}} = 8$ , mean and standard deviation not weighted.  $N_{\text{max}} = 28$ ,  $N_{\text{max}}^{\text{bin}} = 2$ ,  $n_{\text{ev}} = 1$ . Parametrization as in equation (8.45b). Experimental candidate indicated by grey box. The labels denote the first two and the last corresponding  $a_{\text{HO}}$  in fm.

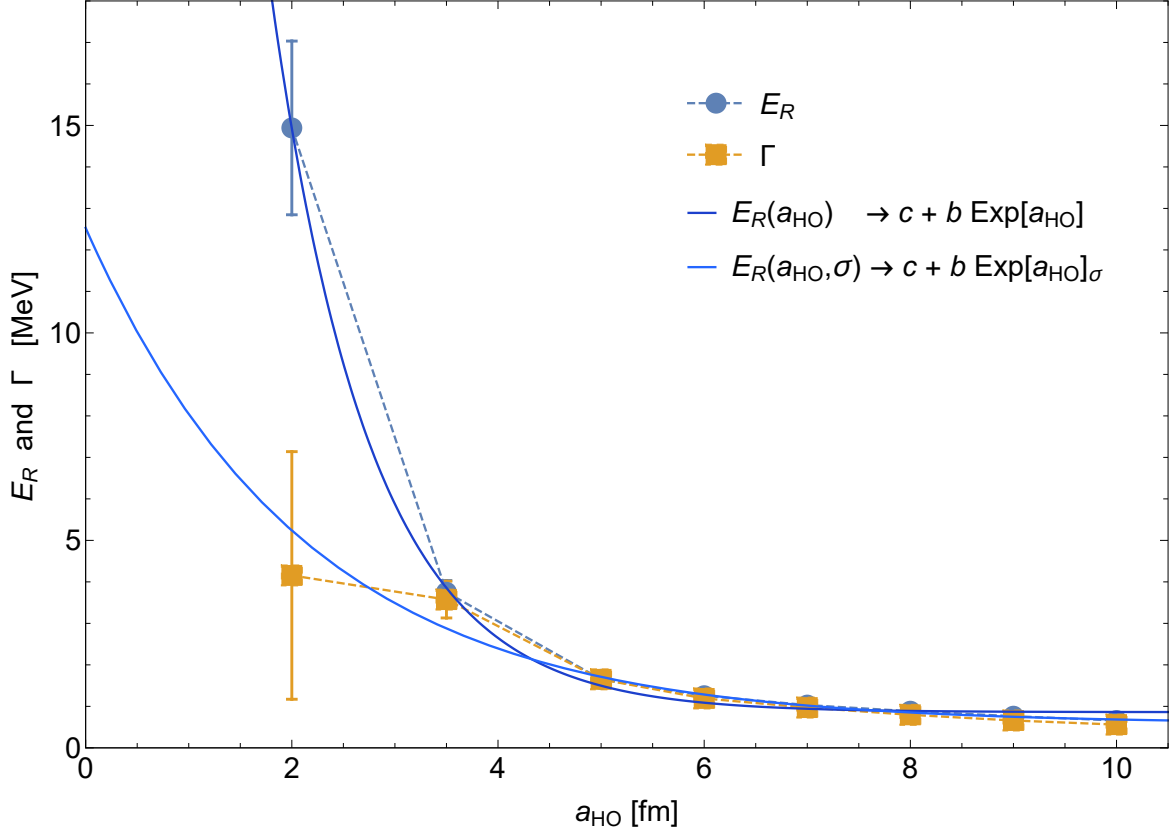


Figure 9.18.: The resonance and width as a function of  $a_{\text{HO}}$  for the (4,4) Padé order, corresponding to results shown in figure 9.17. Interaction  $\text{N}^3\text{LO}_{\text{EM}} + \text{N}^2\text{LO}_{500,\text{L}}$ ,  $N_{\text{max}}=28$ . The exponential fits are purely heuristic and are no prediction. One fit is performed with given errors as weights.

#### 9.2.4. $N_{\text{max}}$ Behaviour

The  $N_{\text{max}}$  behaviour of the bound data for different binding strengths in figure 9.8 suggests something akin to convergence at  $N_{\text{max}}=20$ . And indeed, the  $N_{\text{max}}$  behaviour for the extrapolation becomes more robust with increasing model space size, in the sense that the Padé orders agree with each other.

Figure 9.19 shows the  $N_{\text{max}}$  sequence of the mean values at each Padé order for the statistical ACCC, with  $a_{\text{HO}} = 3.5$  fm and the interaction  $\text{N}^3\text{LO}_{\text{EMN}} + \text{N}^3\text{LO}_{500,\text{NL}}$ . The individual fits to the subsets have been omitted for better visibility. The first two orders are robust with increasing  $N_{\text{max}}$  and change comparatively little. The orders (3,3) and above show strong changes when going from  $N_{\text{max}} = 10$  up to  $N_{\text{max}} = 28$ . With increasing  $N_{\text{max}}$ , the mean values approach each other. Though not shown, to not overload the plot, the fits are performed up to order (6,6), which has a similar behaviour to order (5,5). From these results, we assume the  $N_{\text{max}}$ -dependence of the extrapolation not to be the dominating uncertainty, especially when compared to the oscillator length, data point, starting values, and minimization algorithm choice.

The good agreement already at  $N_{\text{max}} \approx 20$  could potentially open up the use of the ACCC to the  $m$ -scheme NCSM, both for further investigations into the tetra-neutron with on-the-fly constructed phenomenological four-body interactions to use as external binding potential, as well as slightly heavier systems with mass number  $A \sim 6$ .

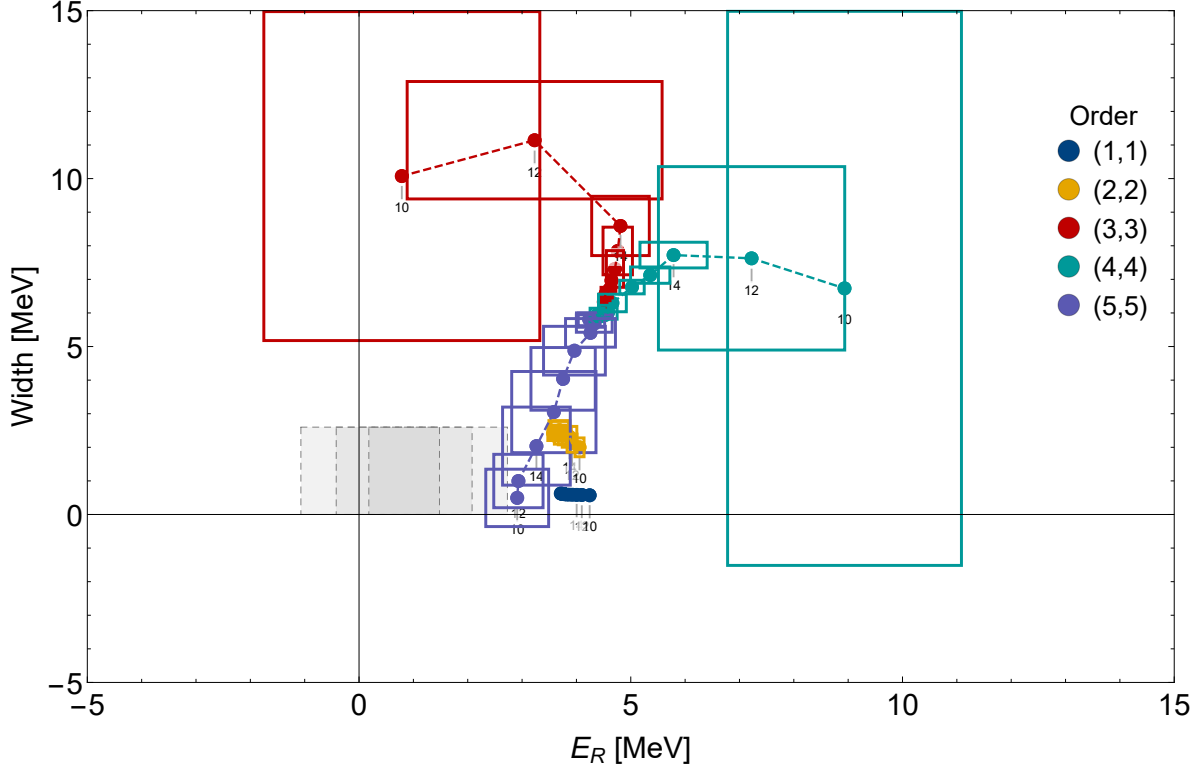


Figure 9.19.:  $N_{\max}$  sequence of the mean values of statistical ACCC. 1000 subsets out of at least 221 total data points at  $N_{\max} = 10$ .  $N_{\max}^{\text{bin}} = 0$ ,  $n_{\text{ev}} = 2$ , for the interaction  $N^3\text{LO}_{\text{EMN}} + N^3\text{LO}_{500,\text{NL}}$  at  $a_{\text{HO}} = 3.5$  fm. The lowest three  $N_{\max}$  values are labelled for identification. The dashed lines connect points of the same order to guide the eye. Mean and standard deviation weighted with estimated fit error variance. The grey box gives the experimental range from [KSM<sup>+</sup>16].

### 9.2.5. Dependence on $N_{\max}^{\text{bin}}$ and $n_{\text{ev}}$

In this subsection, we study the effect the choice of the binding model space size  $N_{\max}^{\text{bin}}$  has on the eigenenergy, and how it affects the fits. For some diagonalizable matrix  $A$  with normalized eigenvectors  $|x\rangle$  and eigenvalue  $\epsilon$ , we have the relation

$$(A - \lambda |x\rangle\langle x|) |x\rangle = (\epsilon - \lambda) |x\rangle. \quad (9.6)$$

It is to expect that calculations performed with  $N_{\max}^{\text{bin}}$  very close to  $N_{\max}$  behave almost like a trivial linear shift in the energy, as in equation (9.6), see section 8.3.2 for the construction of the eigenvector binding potential. We, therefore, restrict the analysis to the smallest  $N_{\max}^{\text{bin}} = 0, 2, 4, 6$ , with the two- and three-body interaction by  $N^3\text{LO}_{\text{EM}} + N^2\text{LO}_{500,\text{L}}$ . These are shown in figure 9.20, with the corresponding minimal and maximal amount of eigenvectors  $n_{\text{ev}}$  taken into account to achieve the binding. With increasing  $N_{\max}^{\text{bin}}$ , the threshold value approaches the linear relation, indicated by the grey line in the plots. The difference in the threshold position  $\lambda_0$  between  $\min(n_{\text{ev}})$  and  $\max(n_{\text{ev}})$  for the same  $N_{\max}^{\text{bin}}$  becomes more pronounced with the growing number of total eigenvectors of the model space. The difference in the threshold position between  $N_{\max}^{\text{bin}} = 0$  and  $N_{\max}^{\text{bin}} = 6$  is already substantial, requiring approximately half the energy.

To illustrate the differences further, as well as to gauge the Padé extrapolation, a simple linear and quadratic fit to all bound data points is performed and extrapolated to  $\lambda = 0$ , shown in

## 9. Results Analytic Continuation in the Coupling Constant

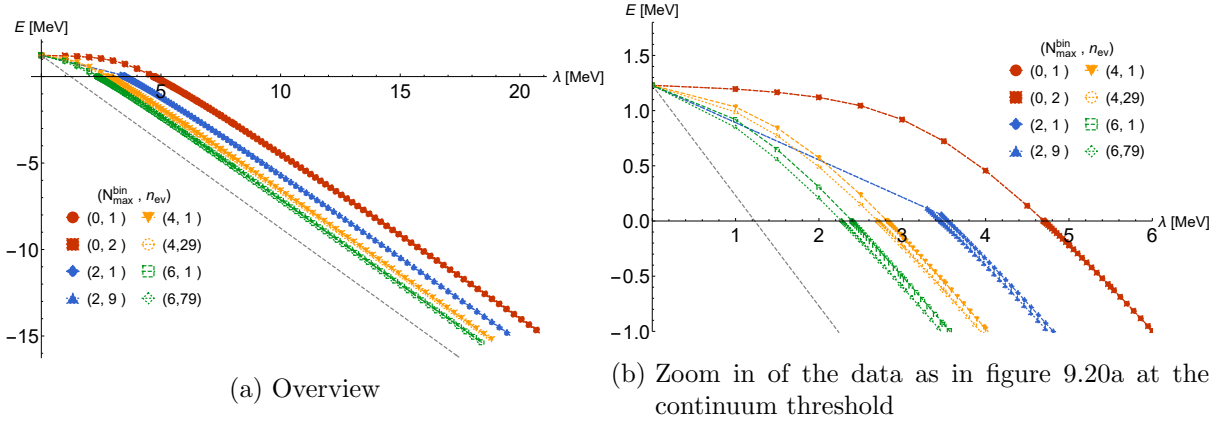


Figure 9.20.: The energy as a function of the binding parameter  $\lambda$  for binding model spaces  $N_{\max}^{\text{bin}} = 0, 2, 4, 6$  and  $n_{\text{ev}}$  values of only one eigenvector and all eigenvectors contained in the corresponding  $N_{\max}^{\text{bin}}$ . The grey line is a shift by a constant as it would be the case for  $N_{\max}^{\text{bin}} = N_{\max}$ . The HO length is  $a_{\text{HO}} = 3.5$  fm, interaction  $N^3\text{LO}_{\text{EMN}} + N^3\text{LO}_{500,\text{NL}}$ ,  $N_{\max} = 28$ .

table 9.11. As expected, the difference between linearly and quadratically extrapolated results become smaller and the fractions get closer to unity. Interestingly, the inclusion of all available eigenvectors leads to less “linearity” than only taking one vector into account. However, the bound states produced, and thus the fits, can benefit from the smooth, almost linear behaviour as a function of  $\lambda$ , in the bound-state regime [SMHE17], compare also to the behaviour of the bound-state data with an external potential, delivering similarly looking data in figure 8.2.

The majority of fits are performed with  $N_{\max}^{\text{bin}} = 0, 2$  or  $4$ , with either just the lowest eigenstate, or the corresponding maximal  $n_{\text{ev}} = 2, 9$  and  $29$ , respectively, to remain as far as possible from the linear shift by a constant.

Note that considerations of potentially being too close to trivial linearity are not the only factor in the choice of how many eigenvectors to use. It is dictated first by the energy as a function of  $\lambda$  behaviour above the threshold, while still in the continuum. Should the lowest lying eigenstate in the unmodified case already undergo level crossings when binding several energy states, then exclusively binding the lowest state would lead to a spurious extrapolated result. Fortunately for us, as shown in figure 9.7, the state that is the lowest one at  $\lambda = 0$  is also the first to cross the threshold without level crossing and becomes the “ground state” of the newly bound system. This allows modification with only one eigenvector.

The effect of the binding subspace on the Padé fits and extrapolation is depicted in figure 9.21, and is easy to follow for the lowest two Padé orders  $(1, 1)$  and  $(2, 2)$ . The smallest  $N_{\max}^{\text{bin}}$  shows practically no difference between the two modifications, as only two HO configurations even exist at this level, with minimal differences in the bound-state energies. Considering larger  $N_{\max}^{\text{bin}}$  values, the extrapolated values decrease in energy  $E_R$  as well as width  $\Gamma$ . This trend should naturally approach the unmodified NCSM result of  $E \approx 1.23$  MeV at  $a_{\text{HO}} = 3.5$  fm for  $N_{\max}^{\text{bin}} = N_{\max}$ , with undetermined width. Unlike the first two orders, the higher lying orders are difficult to assign to a clear trend, both in regards of the  $(N_{\max}^{\text{bin}}, n_{\text{ev}})$  dependence as well as order-by-order convergence, except for the  $N_{\max}^{\text{bin}} = 0, 2$  case, where the Padé orders show the most resemblance of order-by-order convergence, with simultaneous small dependence on the used data points, indicated by the significantly smaller boxes around the mean values. Though only orders up to  $(4, 4)$  are shown in figure 9.21, for the sake of clarity, the orders  $(5, 5)$  and  $(6, 6)$  behave as erratically for  $N_{\max}^{\text{bin}} > 2$  as the orders  $(3, 3)$  and  $(4, 4)$ .

The closeness of the  $N_{\max}^{\text{bin}} = 6$  continuum threshold to the direct linear modification, which

$(N_{\max}^{\text{bin}}, n_{\text{ev}})$	linear	quadratic	$\Delta$	lin. / quad.
(0, 1)	4.499	3.855	0.644	1.167
(0, 2)	4.498	3.854	0.644	1.167
(2, 1)	3.502	3.074	0.428	1.139
(2, 9)	3.380	2.932	0.448	1.153
(4, 1)	2.831	2.550	0.281	1.11
(4,29)	2.721	2.417	0.304	1.126
(6, 1)	2.435	2.229	0.206	1.093
(6,79)	2.313	2.085	0.228	1.109

Table 9.11.: Extrapolation result for a linear and quadratic fit to zero binding strength of the data set shown in figure 9.20. Units in MeV, around 100 points in each set.

would correspond to  $N_{\max}^{\text{bin}} = 28$ , with only approximately 1 MeV difference, is disconcerting. The effect of  $n_{\text{ev}}$  can not be observed to be of great importance at these  $N_{\max}^{\text{bin}}$  values.

When applying the data to the ACCC, the increased instability in the Padé orders with growing  $N_{\max}^{\text{bin}}$  is another indicator to use the smallest binding subspaces. The fact that the dependence on the selection of input points for the fit is increased with larger  $N_{\max}^{\text{bin}}$  is counter intuitive, when expecting the data to be more linear. However, it has to be considered, that the linearity directly in the continuum is the problem in that aspect, not necessarily in the bound states.

## 9. Results Analytic Continuation in the Coupling Constant

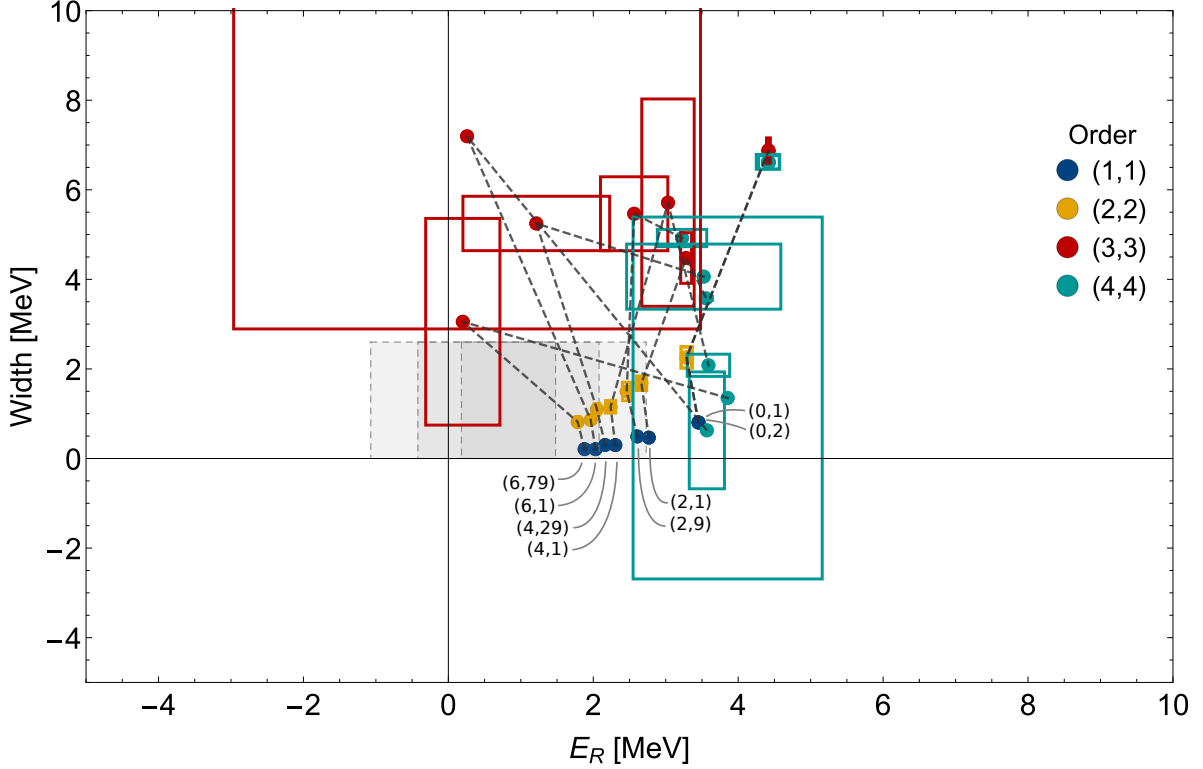


Figure 9.21.: Statistical ACCC of the four-neutron system, for the  $(N_{\max}^{\text{bin}}, n_{\text{ev}})$  pairs (0,1), (0,2), (2,1), (2,9), (4,1), (4,29), (6,1) and (6,79), indicated by the corresponding labels. Only the weighted mean values are shown.  $N_{\max}=28$ , 1000 sets, 30 data points per set. Levenberg-Marquardt,  $\sigma_{\text{rel}}^{\text{fit}}=8$ , with weighted mean and standard deviation. Excluding  $c_0$ , equation (8.45b). Interaction  $N^3\text{LO}_{\text{EM}} + N^2\text{LO}_{500,\text{L}}$ ,  $a_{\text{HO}} = 3.5$  fm. The grey lines connect each  $(N_{\max}^{\text{bin}}, n_{\text{ev}})$  pair to guide the eye.

### 9.2.6. Main Findings and Comparison to Other Works

We present the main findings of our investigation into the tetra-neutron with the eigenvector binding method in the form of a statistical ACCC plot, a table giving the results shown in the plot for each Padé order, and a table comparing our results with the resonance candidate given in reference [KSM<sup>+</sup>16], and other works which find a resonance. The SACCC is introduced in sections 8.4.2 and 8.5.2, where the underlying fit protocols are explained.

Figure 9.22 shows our extrapolation results in the energy-width plane, of 1000 randomly chosen sets consisting of 30 points, from a total of 270 data points, in a range of  $x = \sqrt{\lambda - \lambda_0} \approx [0, 4]$ . The model space size is  $N_{\max} = 28$ . The larger dots and boxes are the mean values with standard deviation for the 1000 ACCC extrapolation per Padé order. The interaction is  $N^3\text{LO}_{\text{EMN}} + N^3\text{LO}_{500,\text{NL}}$  [EMN17, HVH<sup>+</sup>19]. The plot includes three different HO lengths  $a_{\text{HO}}$ , indicated with a label on the Padé order  $(N, M) = (1, 1)$ . The eigenvector binding parameter pairs are  $(N_{\max}^{\text{bin}} = 0, n_{\text{ev}} = 2)$ . For details on  $N_{\max}^{\text{bin}}$  and  $n_{\text{ev}}$ , see section 8.3, for the analysis of the impact of the eigenvector binding parameters, see section 9.2.5.

The Padé orders do not appear to converge in the width at  $a_{\text{HO}} = 2.5$  fm. Convergence w.r.t. the Padé order appears at  $a_{\text{HO}} \geq 3.5$  fm. Even so, the resonance position  $E_R$  is relatively stable also for  $a_{\text{HO}} = 2.5$  fm. The Padé order (5,5) and (6,6) at  $a_{\text{HO}} = 2.5$  fm split up into two distinct clusters, which leads to the larger standard deviation compared to the lower orders. To a lesser extent, this is also the case for order (3,3), for all three  $a_{\text{HO}}$  lengths. This is an effect of the

parameter start value and subset dependence, indicating that different local minima exist for different starting values, assigned by the previous lower order fit.

We find a resonance for the three presented HO lengths. The resonance parameter at Padé order (4,4) are compared to the findings from chapter 7 and other works in table 9.13. Note that the table only includes references where a resonance candidate is found. The complete list of values for each Padé order are listed in table 9.12. See also the main ACCC conclusion in section 9.4.

$a_{\text{HO}}$	2.5 fm		3.5 fm		4.5 fm	
Order	$E_R$ [MeV]	$\Gamma$ [MeV]	$E_R$ [MeV]	$\Gamma$ [MeV]	$E_R$ [MeV]	$\Gamma$ [MeV]
(1,1)	$6.68 \pm 0.07$	$1.66 \pm 0.07$	$3.71 \pm 0.05$	$0.63 \pm 0.03$	$2.49 \pm 0.04$	$0.29 \pm 0.02$
(2,2)	$6.32 \pm 0.07$	$3.88 \pm 0.31$	$3.52 \pm 0.07$	$2.28 \pm 0.15$	$2.36 \pm 0.05$	$1.41 \pm 0.10$
(3,3)	$9.06 \pm 1.07$	$11.79 \pm 2.97$	$4.38 \pm 0.23$	$6.09 \pm 1.35$	$2.46 \pm 0.05$	$3.96 \pm 0.56$
(4,4)	$9.14 \pm 0.40$	$11.32 \pm 1.22$	$4.56 \pm 0.09$	$6.1 \pm 0.46$	$2.52 \pm 0.07$	$3.91 \pm 0.43$
(5,5)	$7.53 \pm 1.84$	$13.92 \pm 3.33$	$4.26 \pm 0.30$	$5.93 \pm 0.25$	$2.59 \pm 0.07$	$3.65 \pm 0.33$
(6,6)	$6.69 \pm 1.37$	$17.77 \pm 3.56$	$4.13 \pm 0.21$	$5.91 \pm 0.28$	$2.56 \pm 0.05$	$3.71 \pm 0.14$

Table 9.12.: Resonance parameters at each Padé order, from SACCC with standard deviation, corresponding to data shown in figure 9.22. Results are rounded to two decimals.

Ref.	$E_R$ [MeV]	$\Gamma$ [MeV]
[KSM <sup>+</sup> 16]	$0.83 \pm 0.65 \pm 1.25$	2.6
[SPM <sup>+</sup> 16]	0.8	1.4
[GHK <sup>+</sup> 17]	2.1	–
[FRMP17]	7.3	3.7
[LMH <sup>+</sup> 19]	2.64	2.38
Single-State HORSE	0.7	1.2
(4,4) at $a_{\text{HO}}=2.5$ fm	$9.14 \pm 0.40$	$11.32 \pm 1.22$
(4,4) at $a_{\text{HO}}=3.5$ fm	$4.56 \pm 0.09$	$6.1 \pm 0.46$
(4,4) at $a_{\text{HO}}=4.5$ fm	$2.52 \pm 0.07$	$3.91 \pm 0.43$

Table 9.13.: Comparison of resonance parameters from other references with our work. The presented values are approximated to be reasonably comparable. They are intended to reflect the main findings of the respective references, without claiming to be complete. See the original works for precise values.

Our results are partly compatible to resonance parameters found by the presented references. However, we note this with reservation. The visible dependence on the harmonic oscillator length, which is analysed in detail in section 9.2.3, is reason for caution in giving a definitive resonance position and width. From the arguments presented section 9.2.3, we take the  $a_{\text{HO}} = 3.5$  fm as an upper limit for the energy and width, we find ( $E_R \leq 4.56 \pm 0.09$ ) MeV and ( $\Gamma \leq 6.1 \pm 0.46$ ) MeV. Note that the eigenvector binding parameters are  $N_{\text{max}}^{\text{bin}} = 0$  in this case, compared to  $N_{\text{max}}^{\text{bin}} = 2$  used in section 9.2.3, causing different resonance parameters at the same HO length. Under this aspect, broader parameter studies in possible future investigations with other methods, either those among the already presented, or not yet applied, could help in identifying the origin of the observed differences.

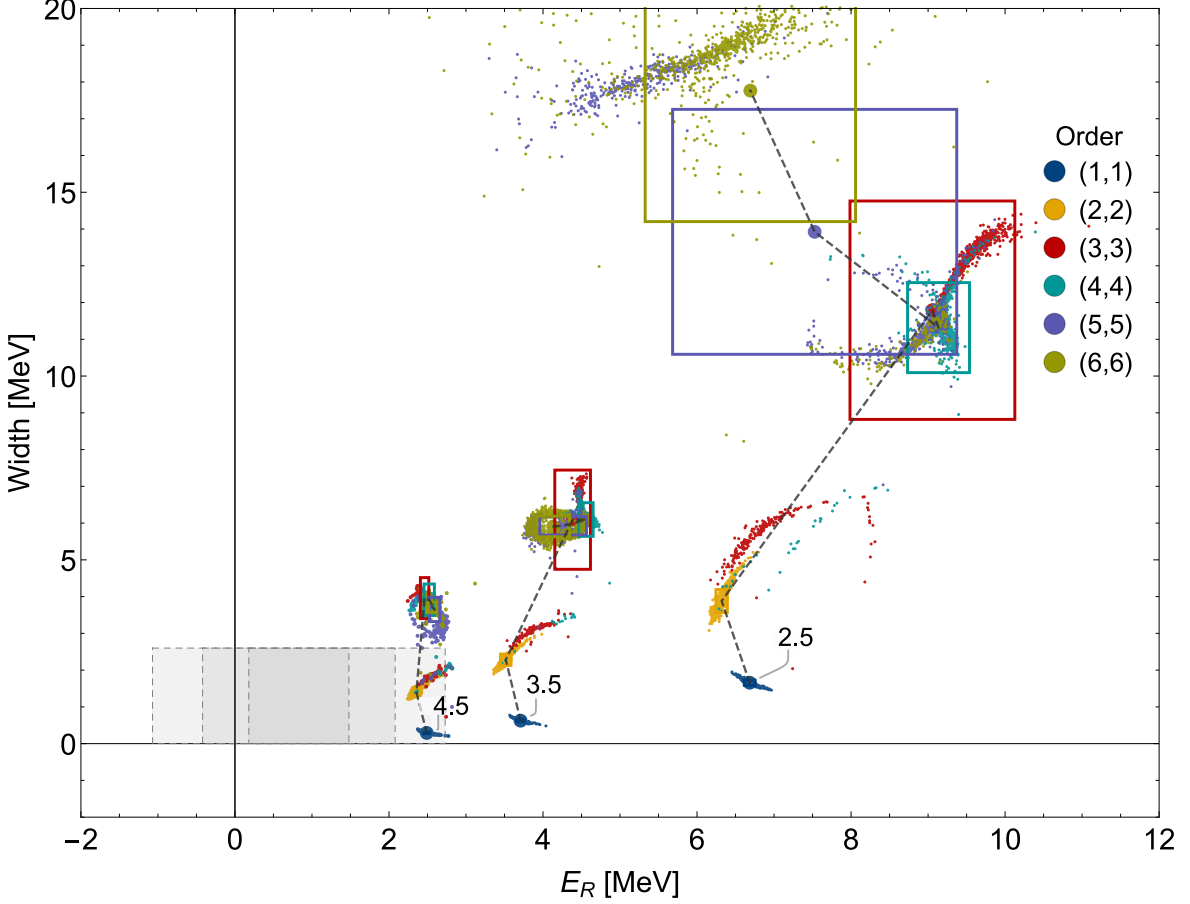


Figure 9.22.: Tetra-neutron SACCC extrapolation results for the data sets from figure 9.16. HO lengths of 2.5, 3.5, and 4.5 fm,  $N_{\max} = 28$ ,  $N_{\max}^{\text{bin}} = 0$ ,  $n_{\text{ev}} = 2$ . Interaction  $N^3\text{LO}_{\text{EMN}} + N^3\text{LO}_{500,\text{NL}}$ , 1000 subsets of 30 points, Levenberg-Marquardt algorithm with  $\sigma_{\text{rel}}^{\text{fit}} = 8$ , points weighted equally for mean and standard deviation. Parametrization as in equation (8.45b). The experimental result [KSM<sup>+</sup>16] is given as grey boxes, corresponding to uncertainty regions (stat.), (syst.) and (stat. + syst.).

### 9.3. Tetra-neutron: Modification of $\chi\text{EFT}$ Matrix Elements

The main goal of this work is to find out if a tetra-neutron resonance exists, and if so, to determine the resonance position and width. To apply the ACCC, we are faced with the challenge is how to achieve binding of the system in a proper way, such that we either avoid bound substructures or treat them correctly. In section 9.2, we constructed a quasi-external potential in four-body space to bind the system. In this section, we modify the NN- and 3N-interaction matrix elements to achieve binding. This means to perform the ACCC relative to the dineutron threshold, possibly even to the trineutron threshold as well, as claimed, e.g. by references [GHK<sup>+</sup>17, LMH<sup>+</sup>19], if bound substructures occur. However, we first only consider the direct extrapolation as done with the dineutron, i.e.

$$k(\lambda) = \sqrt{\frac{2m}{\hbar^2} E_{4n}}, \quad (9.7)$$

as opposed to the wave number with respect to the dineutron or even trineutron threshold

$$k(\lambda) = \sqrt{\frac{2m}{\hbar^2}(E_{4n} - E_{2n})} \quad (9.8)$$

$$k(\lambda) = \sqrt{\frac{2m}{\hbar^2}(E_{4n} - E_{3n} - E_{2n})}. \quad (9.9)$$

The simultaneous treatment of multiple thresholds increases the uncertainty to unknown degrees. We do not pursue this approach within this work.

### 9.3.1. 2N + 3N Modification

We modify the whole interaction by multiplying all two- and three-body interaction matrix elements with the same factor

$$H(\lambda) = T + \lambda \left( \sum_{i,j} V_{ij} + \sum_{i,j,k} V_{ijk} \right), \quad (9.10)$$

where  $V_{ij}$  and  $V_{ijk}$  are the two- and three-body matrix elements, respectively. This binds the dineutron as well, we are, however, not taking this into account and consequently extrapolate over the dineutron threshold.

The data sets obtained with this binding approach are shown in figure 9.23. The four depicted HO lengths are moving apart from each other with increasing  $\lambda$ . This is different from the similar comparison done for the dineutron in figure 9.1a. However, all  $a_{\text{HO}}$  approach the threshold at close proximity to each other, with  $\lambda_0 \sim 1.34$ . Note that the coupling constant is dimensionless, unlike in the eigenvector binding case.

The value of the prefactor is in this case of special importance. In table 9.2, the value of the dineutron threshold is determined to be  $\lambda_0(^2\text{n}) = 1.12096$  for  $a_{\text{HO}} = 2.5$  fm (shifted by a constant of ‘1’). This means that, when relaxing the binding strength, the neutron-neutron separation threshold is reached before the “true” four-neutron channel opens up, in the sense of the so-called democratic decay, see section 6.3. In references [DL19a, DL19b], this procedure is denied to be applicable to the tetraneutron. However, in the combination of an external two-body potential, which also binds the dineutron, this approach is used in references [GHK<sup>+</sup>17, GHK<sup>+</sup>19].

The  $N_{\text{max}}$  sequence for an example data set with  $a_{\text{HO}} = 3.0$  fm in figure 9.24 depicts three different points at constant  $\lambda$ , corresponding to a weakly bound, intermediately bound, and a strongly bound state, determined at the largest available  $N_{\text{max}} = 28$ . The plot shows that the data is clearly not converged in terms of  $N_{\text{max}}$  and that the larger  $\lambda$  or  $x$  becomes, the slower the convergence rate is.

The energy behaviour as a function of  $N_{\text{max}}$  at strong coupling constants is reason for caution. The combination together with the extrapolation over the dineutron threshold makes the reliability of obtained results questionable. An exhaustive investigation into the various parameter dependencies is, therefore, not performed. We limit the discussion in this case to the results of the statistical ACCC results for two different minimization algorithms.

The Padé fit and extrapolation performed with the Levenberg-Marquardt algorithm can be seen in figure 9.25. The Levenberg-Marquardt method does not converge when forcing the fit through the origin by not using the  $c_0$  parameter as in equation (8.45b). We employ the parametrization of equation (8.45a) and further compare the mean values with equal weighting

## 9. Results Analytic Continuation in the Coupling Constant

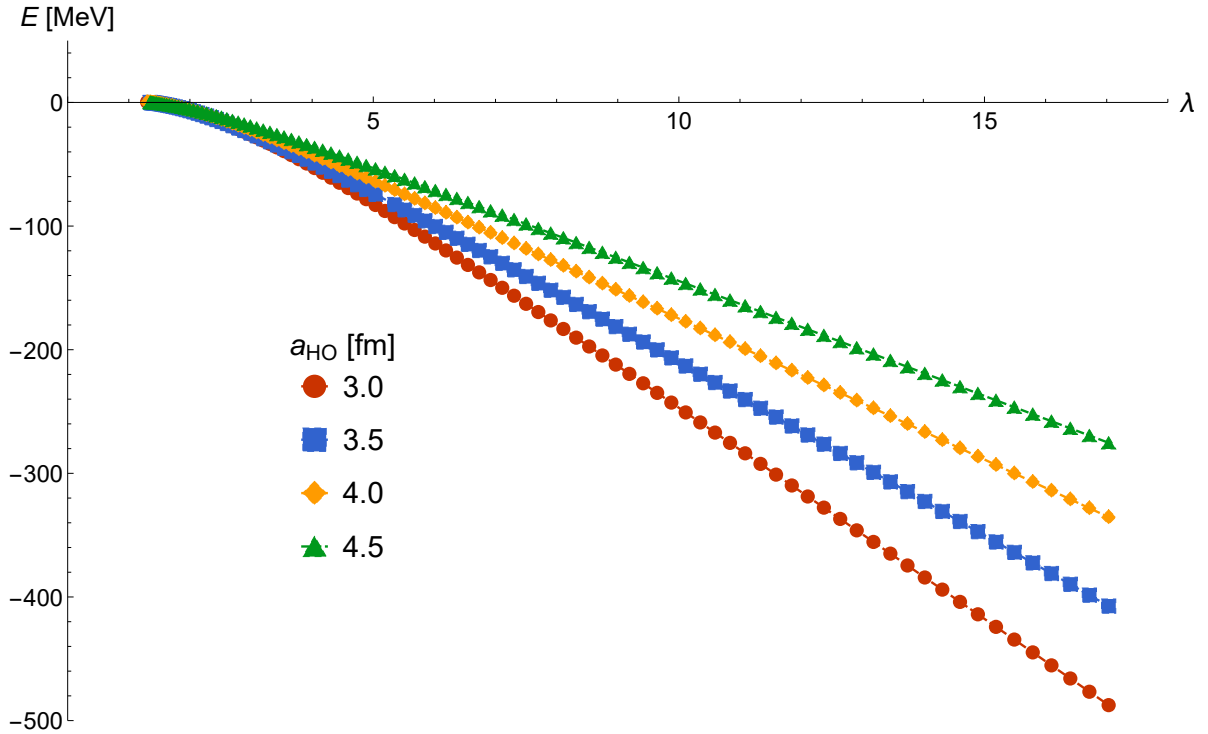


Figure 9.23.: Comparison of four different HO lengths  $a_{\text{HO}}$  of the total binding energy as a function of the coupling constant. Interaction  $\text{N}^3\text{LO}_{\text{EM}} + \text{N}^2\text{LO}_{500,\text{L}}$ .

and estimated error variance. A significant dependence on the data point selection is apparent, with the mean values lacking consistency w.r.t. the Padé orders. The weighting with the error variance does not improve mean Padé order consistency. Judging by these values, a resonance is not present. Especially the location of the first two orders, which are robust in the eigenvector analysis, raise serious doubts about the applicability of the procedure.

The fit with the Newton method is performed without the  $c_0$  parameter as in equation (8.45b), thus forcing the extrapolation through the origin in the  $k(\lambda)$  plane. The SACCC is shown in figure 9.26. The spread in the extrapolated results for the different subsets is quite significant, although with some clustering around the origin and the experimentally predicted region for both methods shown. Similar to the results of the Levenberg-Marquardt fit, the first two orders lie in different regions. The orders (3,3) and (4,4) cluster around the region of  $E_R \approx 2.5$  MeV, and the (5,5) order is left of the width-axis at negative energies.

The presented results are not clear in their interpretation. The erratic behaviour in the Padé orders, especially the lower ones, and, e.g., the difficulties to obtain fits with otherwise successful Levenberg-Marquardt algorithm, are at least not indicative to the existence of resonance, at least within this binding approach, with mentioned shortcomings. On the other hand, these findings are also not ruling out a resonance. In the discussion in section 8.5, we point out the inadequacy of the Padé orders (1,1) and (2,2) to reproduce a known result, while still being consistent in the subset sampling. The dineutron discussed in section 9.1, is, together with the Levenberg-Marquardt as minimizer, consistent in order (1,1) and (2,2), and again consistent in the higher orders. This is not the case for the matrix element modification. Together with the worsened  $N_{\text{max}}$  convergence rate for strongly bound states, we conclude the binding scheme to be inadequate for the application of the ACCC.

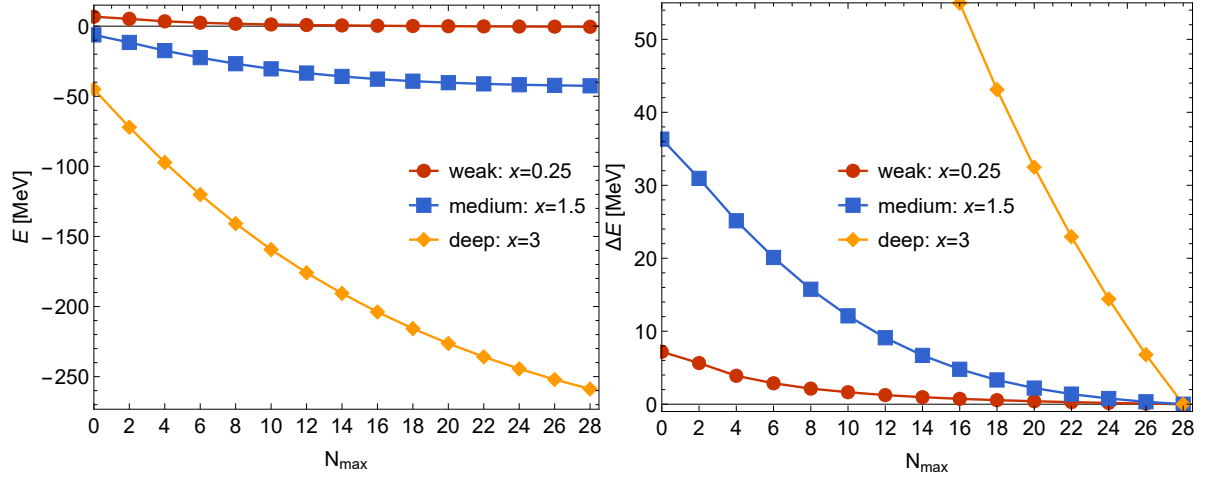


Figure 9.24.: Tetraneutron  $N_{\max}$  sequence for three different points, corresponding to  $x \approx 0.25, 1.5, 3$  at  $N_{\max} = 28$ . On the left the absolute values, on the right the difference at each  $N_{\max}$  to  $N_{\max} = 28$ . Interaction  $N^3\text{LO}_{\text{EM}} + N^2\text{LO}_{500,\text{L}}$   $\alpha = 0.08 \text{ fm}^4$  and  $a_{\text{HO}} = 3.0 \text{ fm}$ .

Speculatively, the clustering observed in the Padé (3,3), and partly the (4,4) order in figures 9.25 and 9.26, could correspond to the findings of [GHK<sup>+</sup>17].

## 9. Results Analytic Continuation in the Coupling Constant

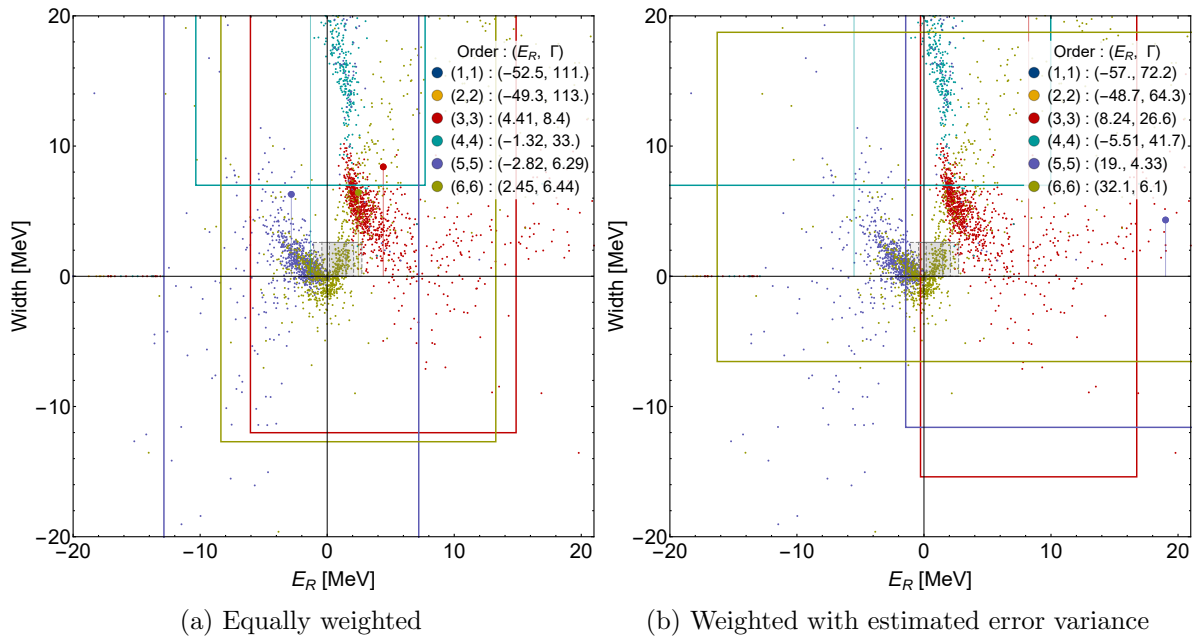


Figure 9.25.: Tetraneutron statistical ACCC for the matrix element manipulation. Parametrized as in equation (8.45a).  $N_{\max} = 28$ , 1000 sets, 30 data points, Levenberg-Marquardt method with  $\sigma_{\text{rel}}^{\text{fit}} = 8$ . In grey the experimental range from [KSM<sup>+</sup>16].

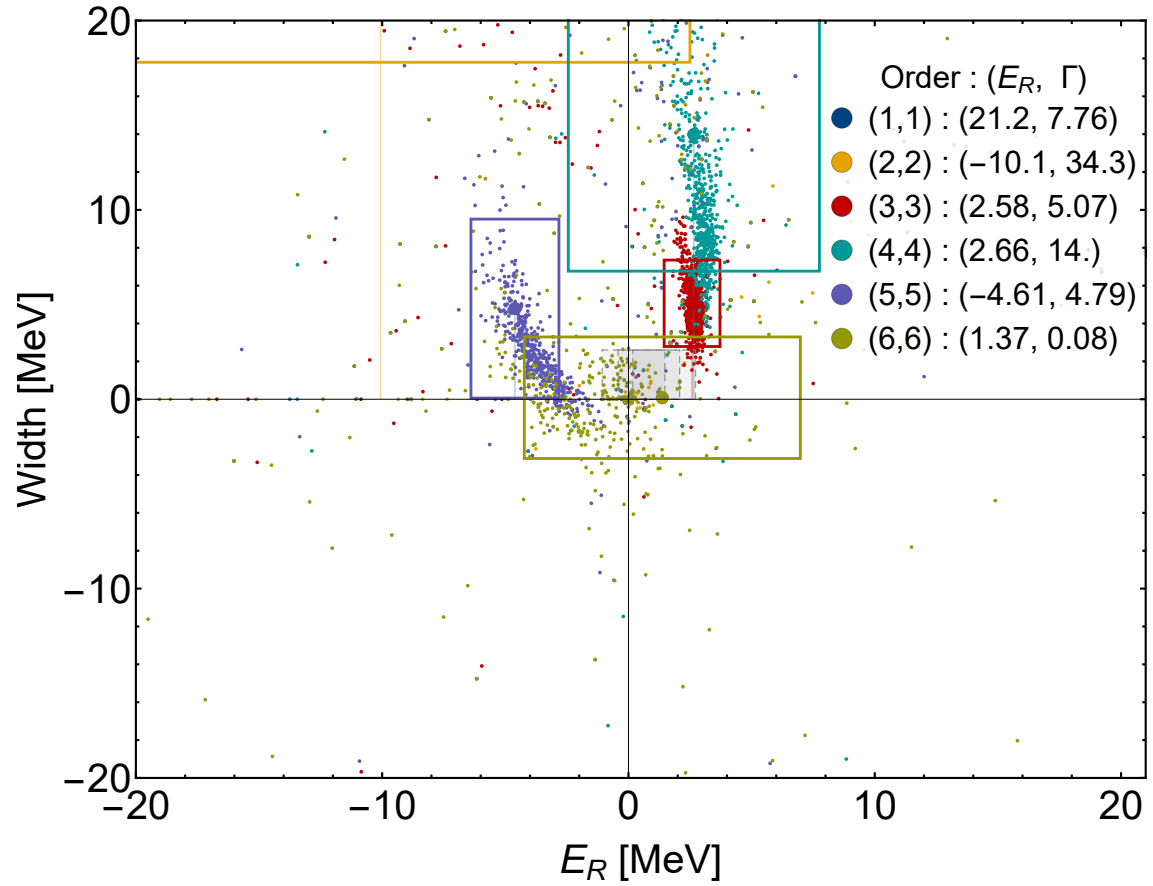


Figure 9.26.: Tetraneutron statistical ACCC for the matrix element modification. Parametrization as in equation (8.45b). 1000 subsets of 30 points. Newton method with  $\sigma_{\text{rel}}^{\text{fit}} = 8$ .

### 9.3.2. 2N + 3N Excluding $^1S_0$ Partial Wave

In order to avoid binding the dineutron subsystem, we exclude the  $^1S_0$  partial wave from being enhanced by a prefactor. The resulting extrapolations for the statistical methods with a subset size of 1000 set can be seen in figure 9.27. The interaction is  $N^3\text{LO}_{\text{EM}} + N^2\text{LO}_{500,\text{L}}$ . The obtained energies and width located at very large energies and widths of  $E_R \approx 90$  MeV and  $\Gamma \approx 250$  MeV. Contrary to the modification including the  $^1S_0$  partial wave, the Padé orders are remarkably robust and close to each other, indeed fortifying the reasoning that the dineutron threshold could break the applicability of the method, as presented in section 9.3.1.

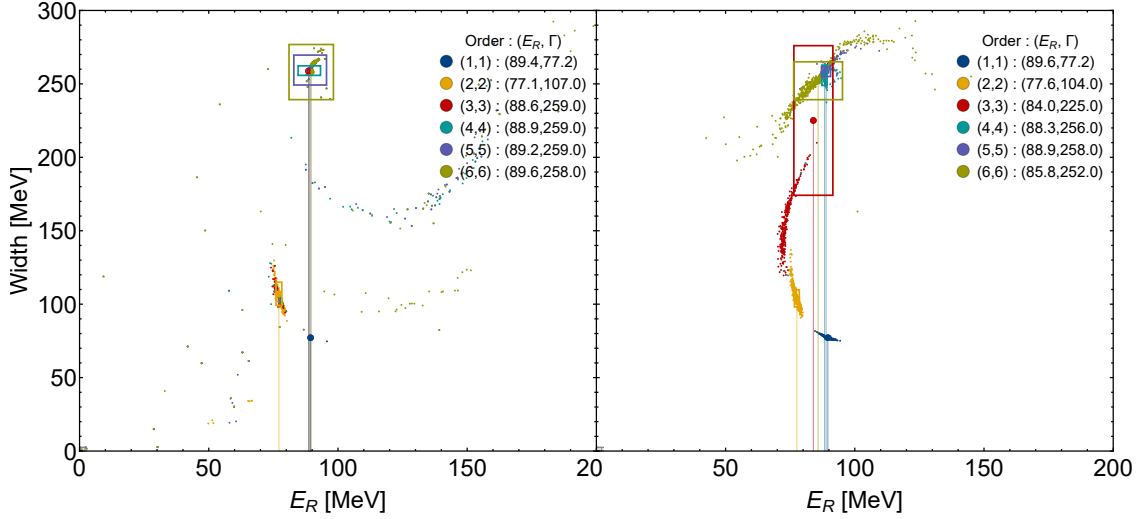


Figure 9.27.: Statistical ACCC of the four-neutron system, with increased matrix element strength, excluding the  $^1S_0$  partial wave, which remains unmodified.  $N_{\text{max}}=28$ , 1000 sets, 30 data points per set. BFGS with weighted mean and standard deviation on the left, unweighted Levenberg-Marquardt on the right.

Omitting the main attractive component of the interaction, in an attempt to bind the four-neutron system, results in a very different trajectory in the  $S$ -matrix pole that we are actually tracking with the ACCC. Obtaining a bound system in this case requires very strong modifications in the interaction, and could lead to any number of unforeseen effects. In light of these findings, the modification of only three-body matrix elements should fare no better to obtain an artificially bound tetra-neutron which gives clear, indicative results from the performed fit.

## 9.4. Tetraneutron Conclusion

The results presented here lead us to the following conclusions: Firstly, the use of the analytic continuation in the coupling constant is achieved with data obtained from a configuration-interaction type many-body method. The relative coordinate implementation of the No-Core Shell Model, the Jacobi-NCSM, reaches large enough model spaces to guarantee sufficient  $N_{\max}$  convergence, at least when using pseudo-external potentials. This is clearly not the case for the direct matrix element modification, where strongly bound states exhibited markedly different convergence than the weaker bound states.

Secondly, our main findings, presented in figure 9.22 and compared with other works in table 9.13, support the existence of a tetraneutron resonance. The eigenvector binding, as additional potential, was successfully applied to bind a system to perform the ACCC. Due to the construction, it acts only in four-body space, and, therefore, does not bind the di- and trineutron. The approach has the deficiency of not being independent of the additional potential, making the results model dependent. This is apparent by the strong variation in the obtained values of the resonance position and width as the HO length  $a_{\text{HO}}$  increases. However, under the assumption of a diffuse system, which thus requires a minimal  $a_{\text{HO}}$  to be sufficiently contained within the HO, we arrive at approximate values for an upper limit. Given by the stabilization in the Padé orders at  $a_{\text{HO}} = 3.5$  fm, we determine this to be the minimal  $a_{\text{HO}}$ . Further, by the behaviour for  $a_{\text{HO}} \rightarrow \infty$  obtained from the heuristic fits shown in figure 9.18, we observe a resonance in the possible range of  $(0.56 \leq E_R \leq 4.56 \pm 0.09)$  MeV and  $(0.5 \leq \Gamma \leq 6.1 \pm 0.46)$  MeV. Secondly, the direct modification of all interaction matrix elements to achieve binding does not support a resonance, judging by the statistical ACCC calculations we performed, however, this is primarily due to its erratic behaviour in the fits, suggesting an inadequate binding method, considering the extrapolation through the dineutron threshold.

Thirdly, the approach of leaving the  $^1S_0$  partial wave untouched, the main carrier of internuclear attraction, as well as being responsible to bind the dineutron, while increasing the strength of the other partial waves, is not in favour of a tetraneutron resonance. The obtained fits were stable in the Padé orders, but returned values in the order of 90 MeV for the resonance energy and 250 MeV for the width.

The favourable existence of a resonance, potentially a very broad one, is contradicting to previous works employing the ACCC to study the four-neutron system, which came to the conclusion that a resonance does not exist [LC05].



## 10. Summary and Outlook

The inclusion of continuum degrees of freedom into *ab initio* nuclear structure calculations is a crucial, yet challenging task. They are an indispensable ingredient for the accurate treatment of nuclear structure and the connection to experiments performed at the extremes of low energy scattering. The development of truly unified *ab initio* approach for treating bound and scattering states on equal footing is an ongoing effort in the community. One special aspect of scattering physics are resonances. Their existence has important influence on the formation of other systems throughout the nuclear chart, so their determination is of vital importance. One such resonance, whose existence is the focus of current research, is the tetra-neutron. It was the aim of this work to combine the bound-state method of the NCSM and advanced  $\chi$ EFT interactions, together with approaches that give access to continuum physics and resonance parameters, and investigate their application to the tetra-neutron. The methods to achieve this presented in this work were the Harmonic Oscillator Representation of Scattering Equations and the Analytic Continuation in the Coupling Constant.

We have introduced the HORSE method and its variation, the Single-State HORSE. With this method, we calculated phase shifts in the so-called democratic decay approximation, meaning we assumed true four-particle to four-particle scattering, which was done in a hyperspherical framework. This work was a continuation of the already published Single-State HORSE tetra-neutron investigation of Shirokov et al. [SPM<sup>+</sup>16]. We employed an array of advanced  $\chi$ EFT interactions, with different SRG flow parameters, compared them to a bare interaction, as well as to the inverse scattering potentials JISP16 and DAEJEON16. All this was done in large model spaces of  $N_{\max} \geq 26$ . The resulting phase shifts are characteristic for resonances with noticeable background contribution, if one applies the two-body scattering interpretation of phase shifts. They clearly passed the  $90^\circ$  with increasing energy, and went up to almost  $110^\circ$ . We demonstrated a remarkably robust behaviour in the phase shifts with respect to different interaction families and SRG parameters. This was not guaranteed, as the calculations are performed in the NCSM pseudo-continuum, potentially allowing for larger differences between the different interactions than it would be the case in a bound-state calculation. While the SRG-evolved interaction showed convergence in the phase shifts at higher energies, there was room for improvement at lower energies. We showed that the bare interaction was far from convergence, even at large model spaces of  $N_{\max} = 30$ . We determined an approximate resonance position with the inflection point criterion and the width via the Breit-Wigner formula, and obtained values of  $E_R \approx 0.7$  MeV, and a width of  $\Gamma \approx 1.4$  MeV.

We also introduced the groundwork for obtaining the hyperspherical basis needed for the calculation of the full HORSE Green's function within the framework of the Jacobi-NCSM.

In an alternative approach to obtain resonance parameters, we introduced the Analytic Continuation in the Coupling Constant, which makes resonances on the complex  $k$ -plane accessible. The biggest challenge in combining the ACCC with the NCSM is finding a binding mechanism, which does not bind substructures, to avoid further complications and uncertainties, and at the same time is compatible with the symmetries of the relative-coordinate many-body basis. To that end, we introduced a binding scheme, that constructs an additional binding potential from eigenvectors of a smaller model space. This is done in four-body space, and thus does not bind

## 10. Summary and Outlook

two- and three-body subsystems. As a second approach to achieve binding, motivated by other publications, we modified the interaction matrix elements, increasing the binding via a prefactor. Further, we introduced the statistical ACCC to absorb data selection dependencies and fit effects in a large set of randomly chosen subsets of the initially generated eigenenergies. Applied to the non-resonant system of the dineutron, we made sure not to artificially create resonances with the eigenvector binding, which was indeed not the case, for both binding approaches. We studied the effect of eigenvector binding in the tetra-neutron, performing a parameter study in the HO length parameter  $a_{\text{HO}}$ , model space size  $N_{\text{max}}$ , the binding model space size  $N_{\text{max}}^{\text{bin}}$  and number of eigenvectors  $n_{\text{ev}}$  considered, the minimization algorithm, and start parameter value dependence. All parameters influenced the ACCC extrapolation within varying degrees, with the exception of  $N_{\text{max}}$ , which showed proper convergence and almost independent end results for  $N_{\text{max}} \geq 20$ . The ACCC results support the existence of a resonance. However, the binding potential is  $a_{\text{HO}}$  dependent, so the extrapolations are as well. We obtained different parameters for different  $a_{\text{HO}}$ , giving resonance positions in a wide range.

By the arguments presented in sections 9.2.3 and 9.4, we arrived at a range for the resonance energy and width of  $(0.56 \leq E_R \leq 4.56 \pm 0.09)$  MeV and  $(0.5 \leq \Gamma \leq 6.1 \pm 0.46)$  MeV.

The modification of all interaction matrix elements delivered a different result. No clear relation between the Padé orders emerged, and difficulties in fitting consistently indicated that the ACCC is not applicable. In this binding scheme, weakening the modification still binds the dineutron after the four-neutron system becomes unbound. This was presented as possible origin of the observed inconsistencies. The omission of the  $^1S_0$  partial wave in the modification delivered more stable fits with less data point dependence, relative to the complete matrix element modification and the magnitude of the obtained values. These were extremely large, with resonance energies of the order of 90 MeV and widths of order 250 MeV, incompatible with observable resonances, and indicative that the modification of all matrix elements, and binding the dineutron, is indeed problematic. The large values raise the question about validity of modifying higher partial waves and the possibility to infer physical results from these ACCC extrapolations.

The HORSE method has yet a few interesting applications, where we laid the path for future investigation of the scattering  $S$ -matrix, calculated from the complete HORSE Green's function in the Jacobi-NCSM.

And exciting prospect, and important test to the eigenvector binding, is the use of a many-body potential not directly linked to the initial Hamiltonian, which would correspond to a phenomenological potential of simple and finite shape, expanded in the NCSM basis. Phenomenological four-body potentials, which can be calculated on-the-fly, are currently being implemented, albeit for the  $m$ -scheme NCSM. The inclusion of such a scheme into the Jacobi-NCSM is unfortunately no simple task. However, the presented results at a model space size of  $N_{\text{max}} = 20$  were already promising in the convergence of the extrapolations, meaning that also the  $m$ -scheme NCSM might be viable for the ACCC, and maybe even  $A = 5$  systems could be investigated, if the model space size can be reached. Limiting factor is the computational feasibility and cost. Using the Importance-Truncated NCSM for the ACCC might be possible and raises an interesting question regarding the interplay of an importance-truncated basis and the behaviour of the  $S$ -matrix poles. Future development in the NCGSM and its application to the tetra-neutron will hopefully be able to shed further light onto the existence of a tetra-neutron resonance.

# Appendix



# A. Properties of Padé approximants

The following properties of Padé approximants are taken from the references [BGM96, Bak12, KKH89]. We present a very restricted selection of the most important features. For proofs, further properties and generally much more information, we refer to the above references.

Let  $f(z)$  be a function representable as power series

$$f(z) = \sum_{j_0}^{\infty} f_j x^j. \quad (\text{A.1})$$

The Padé approximant of the function  $f(z)$  is given as a rational fractional of two polynomials

$$f^{[N,M]}(z) = \frac{P_N(z)}{Q_M(z)} = f(z) + O(z^{N+M+1}). \quad (\text{A.2})$$

One can differentiate between three types of Padé approximants:

- I. The coefficient coincide with the coefficients of the Taylor series in equation (A.1) of order  $N + M + 1$
- II. The values at  $N + M + 1$  points of  $f(z_i)$  coincide
- III. The function values are given at  $K > N + M + 1$  points with errors  $\{\epsilon_i\}$ . This is also referred to as statistical Padé.

The are consequently referred to as type I, type II and type III Padé approximants.

## Invariance under conformal transformation of the argument

A transformation of the argument of the function  $f(z)$

$$z = \frac{az'}{1 + bz'} \quad (\text{A.3})$$

does not change the diagonal Padé approximants

$$f^{[N,N]}(z) = f^{[N,N]} \left( \frac{az'}{1 + bz'} \right) = g^{[N,N]}(z') \quad (\text{A.4})$$

## Unitarity:

The diagonal Padé approximant fulfils the unitarity relation of the partial wave scattering matrix  $S_\ell(z)S_\ell^*(z^*) = 1$

$$(f^*(z^*))^{[N,M]} = (f^{[N,M]}(z^*))^* \quad (\text{A.5})$$

## Convergence:

The convergence of the Padé approximants in the region of  $z \in D$

$$f(z) = \lim_{N \rightarrow \infty} \lim_{M \rightarrow \infty} f^{[N,N]}(z) \quad (\text{A.6})$$

is conjectured for the general case. Some proofs exist for meromorphic functions.

## B. Special Functions

A comprehensive list special functions is collected in the Digital Library of Mathematical Functions (DLMF) [DLM14], the official successor to the handbook by Abramowitz and Stegun [AS64]. We list special functions used in this work in the following.

### B.1. Hypergeometric Function

For  $|z| < 1$ , the hypergeometric function is defined as

$${}_2F_1(a; b; z) = \sum_{n=0}^{\infty} \frac{a^{(n)} b^{(n)} z^n}{c^{(n)} n!}, \quad (\text{B.1})$$

with the rising factorial ( $\equiv$  Pochhammer symbol)<sup>1</sup>

$$q^{(n)} = \begin{cases} 1 & \text{for } n = 0 \\ \prod_{k=1}^n (q + k - 1) = q(q+1)\dots(q+n-1) & \text{for } n > 0 \end{cases}. \quad (\text{B.2})$$

### B.2. Confluent Hypergeometric Function

$$M(a, c, z) = \sum_{n=0}^{\infty} \frac{a^{(n)} z^n}{c^{(n)} n!} = {}_1F_1(a; c; z) \quad (\text{B.3})$$

$$= \lim_{b \rightarrow \infty} {}_2F_1(a; b; c; z/b). \quad (\text{B.4})$$

$a^{(n)}$  as in eq. (B.2).

### B.3. Laguerre Polynomials

$$L_n(x) = \sum_{k=0}^n \frac{(-1)^k}{(k!)(n-k)!} x^k. \quad (\text{B.5})$$

Rodriguez representation

$$L_n(x) = \frac{e^x}{n!} \frac{d^n}{dx^n} (e^{-x} x^n) = \frac{1}{n!} \left( \frac{d}{dx} - 1 \right)^n x^n. \quad (\text{B.6})$$

$$L_n^k(x) = \frac{e^x x^{-k}}{n!} \frac{d^n}{dx^n} (e^{-x} x^{n+k}) \quad (\text{B.7})$$

$$= \sum_{m=0}^n (-1)^m \frac{(n+k)!}{(n-m)!(k+m)!m!} x^m. \quad (\text{B.8})$$

---

<sup>1</sup>the falling factorial will be denoted here as  $(q)_n$

## B.4. Hermite Polynomials

Connection with Laguerre polynomials

$$H_{2n}(x) = (-4)^n n! L_n^{(-\frac{1}{2})}(x^2) = 4^n n! \sum_{i=0}^n (-1)^{n-i} \binom{n-\frac{1}{2}}{n-i} \frac{x^{2i}}{i!}. \quad (\text{B.9})$$

## B.5. Coulomb Function

### B.5.1. Coulomb Wave Functions With Complex Arguments

The dimensionless Coulomb-Schrödinger equation reads

$$w''(z) - \left( \frac{l(l+1)}{z^2} - \frac{2\eta}{z} + 1 \right) w(z) = 0. \quad (\text{B.10})$$

Regular solution, the regular Coulomb Wave Functions (CWF)

$$F_{l,\eta}(z) = C_l(\eta) z^{l+1} e^{\pm iz} {}_1F_1(1+l \pm i\eta; 2l+2; \mp 2iz) \quad (\text{B.11})$$

$$C_l(\eta) = 2^l \exp \left[ \frac{1}{2} \left\{ -\pi\eta + (\ln \Gamma(1+l+i\eta)) + \ln(\Gamma(1+l-i\eta)) \right\} - \ln(\Gamma(2l+2)) \right]. \quad (\text{B.12})$$

Here,  ${}_1F_1$  is the Kummer confluent hyper-geometric function,  $C_l$  the normalizing Gamow factor.

- For real parameters, Coulomb functions (CWF) vary over wide range with moderately varying  $|\eta|$
- CWF are multivalued for complex  $z$ . This means branch cuts must be imposed on the negative real  $z$ -axis  $\Rightarrow$  no straightforward implementation of complex variables.
- In the past, some cases were impossible to calculate numerically. Among these were
  - Whittaker functions with  $\eta$  purely imaginary.
  - CWF close to imaginary axis for large modulus of  $\eta$  or  $\text{Im}(l)$ .
  - Direct calculation of  $H_{l,\eta}^{\pm}(z)$  for  $\text{Re}(z) < 0$  and  $\pm \text{Im}(z) < 0$  impossible.

## C. Phase Shift $N_{\max}$ Sequences of Interactions Used in the Single-State HORSE Analysis

Here we show the  $N_{\max}$  sequences of the phase shifts of the various interactions only shown in the summarising plot figure 7.1, at  $N_{\max} = 26$ .

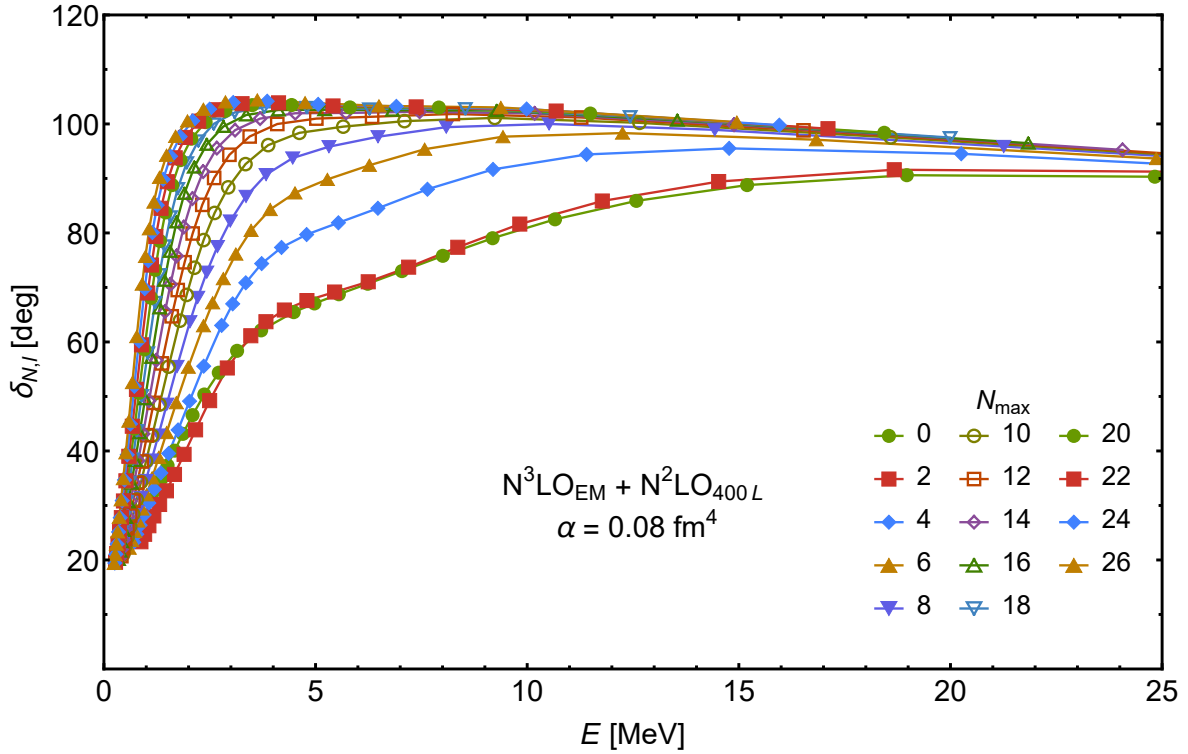


Figure C.1.: Tetra-neutron phase shift as function of the energy. Interaction  $N^3LO_{EM} + N^2LO_{400,L}$  SRG evolved with  $\alpha = 0.08 \text{ fm}^4$ .

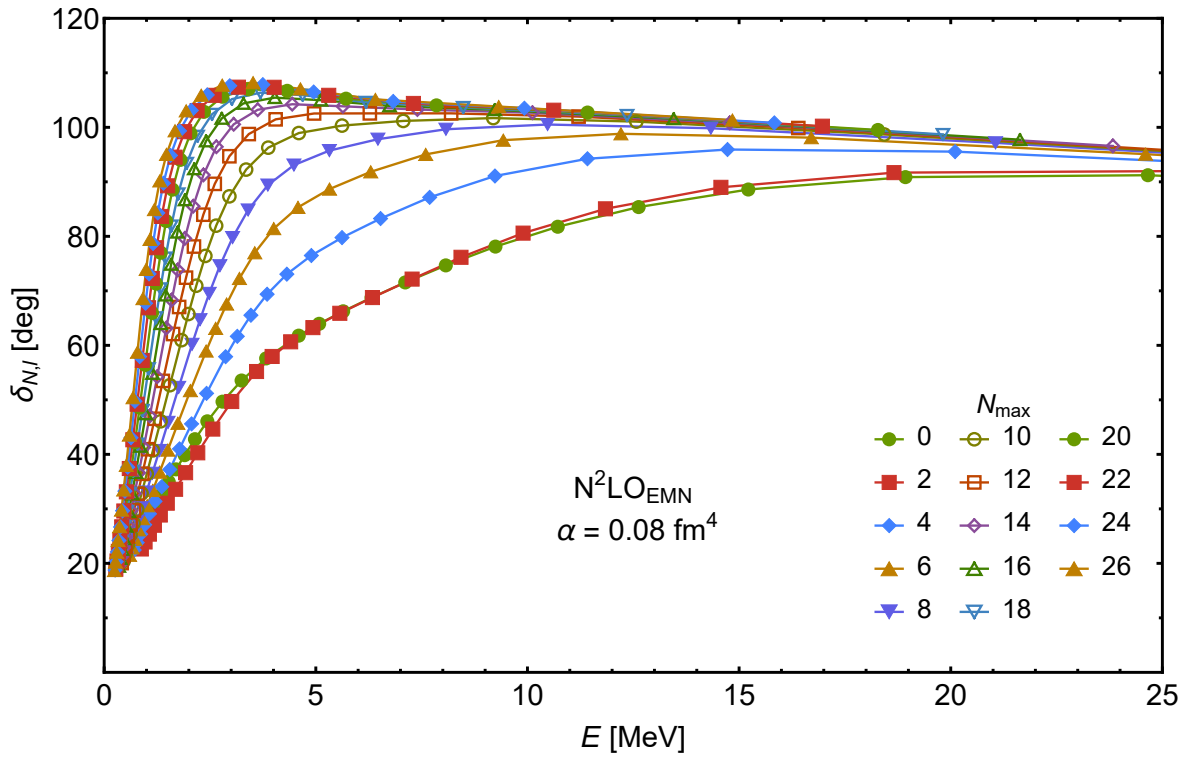


Figure C.2.: Tetraneutron phase shift. Interaction  $N^2\text{LO}_{\text{EMN}}$  SRG evolved with  $\alpha = 0.08 \text{ fm}^4$ .

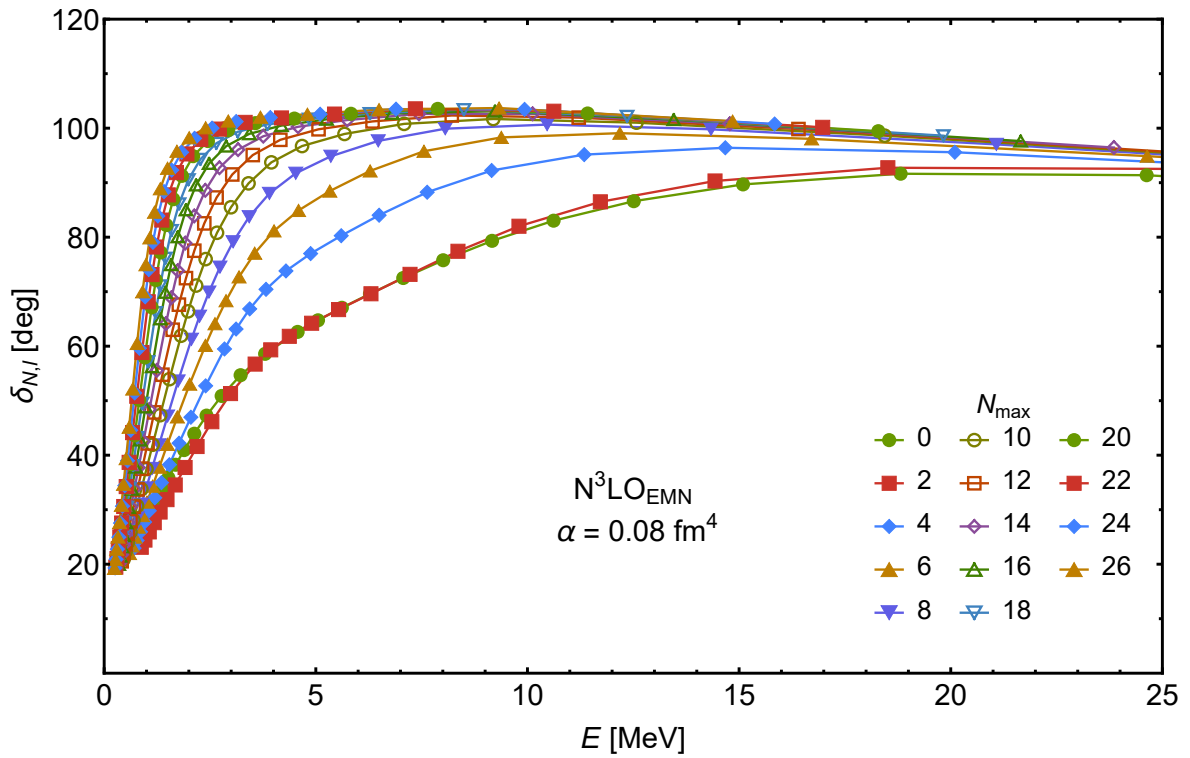


Figure C.3.: Tetraneutron phase shift. Interaction  $N^3\text{LO}_{\text{EMN}}$  SRG evolved with  $\alpha = 0.08 \text{ fm}^4$ .

C. Phase Shift  $N_{\max}$  Sequences of Interactions Used in the Single-State HORSE Analysis

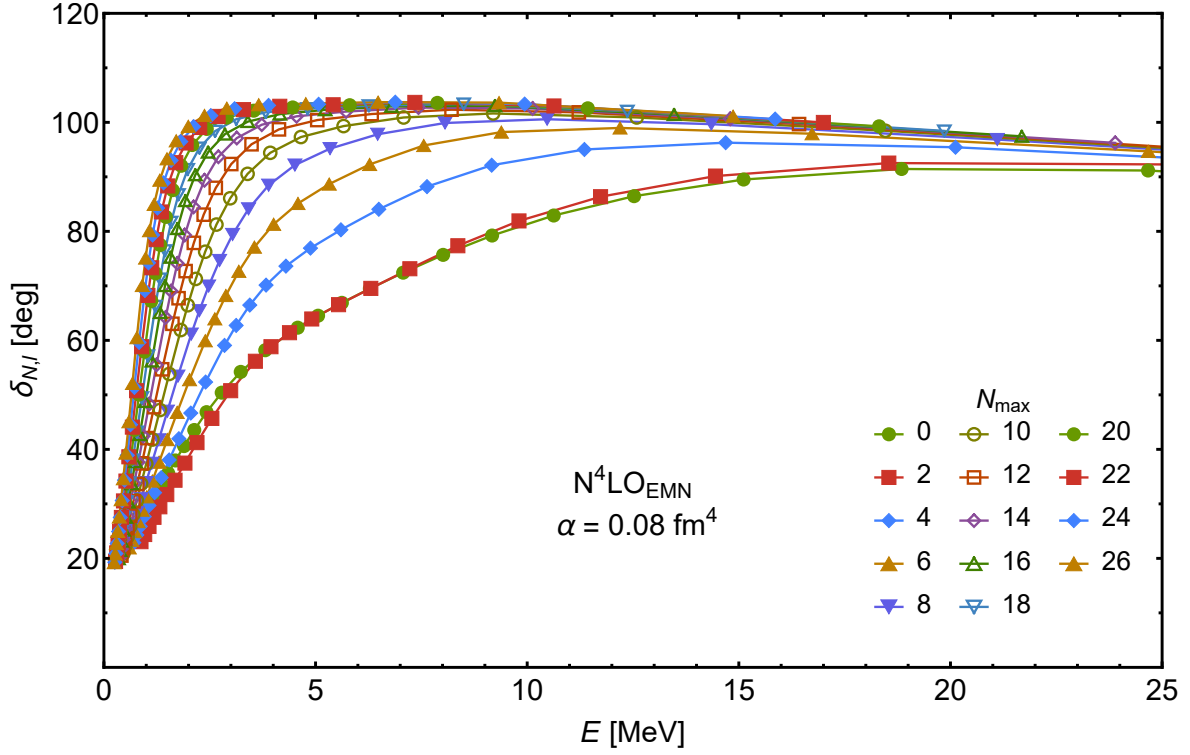


Figure C.4.: Tetra-neutron phase shift. Interaction  $N^4\text{LO}_{\text{EMN}}$  SRG evolved with  $\alpha = 0.08 \text{ fm}^4$ .

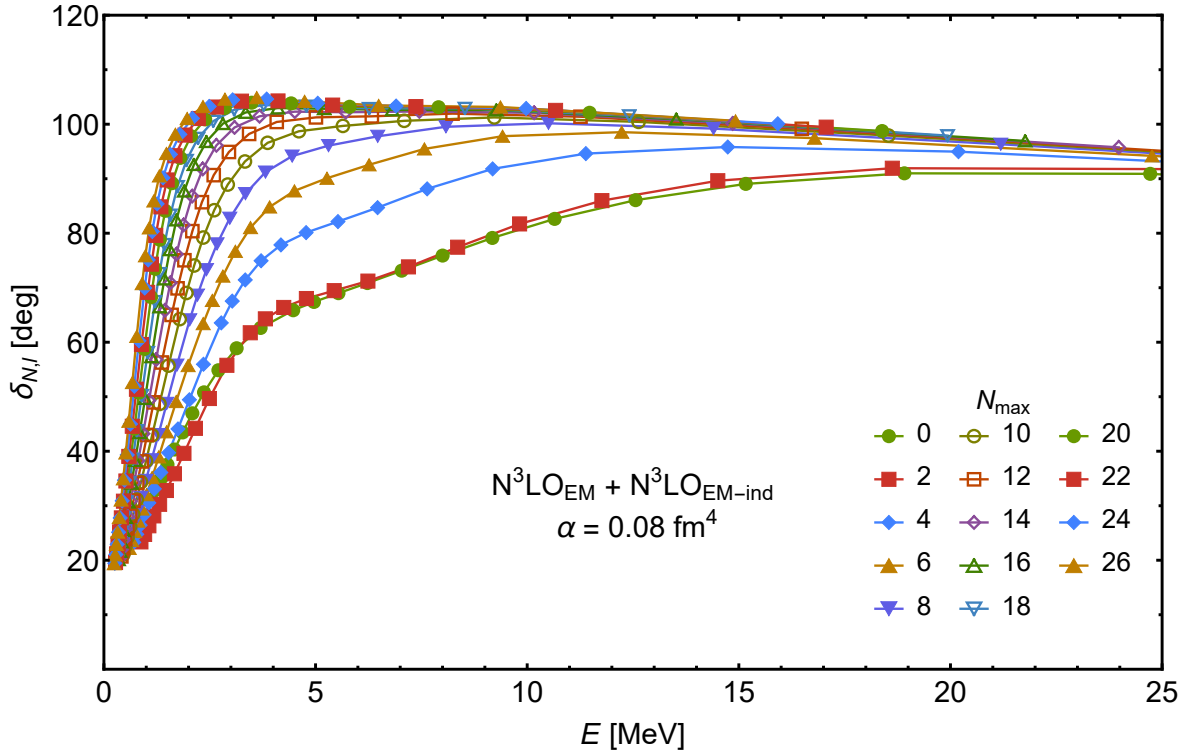


Figure C.5.: Tetra-neutron phase shift. Interaction  $N^3\text{LO}_{\text{EM}} + \text{induced } 3\text{N}$  SRG evolved with  $\alpha = 0.08 \text{ fm}^4$ .

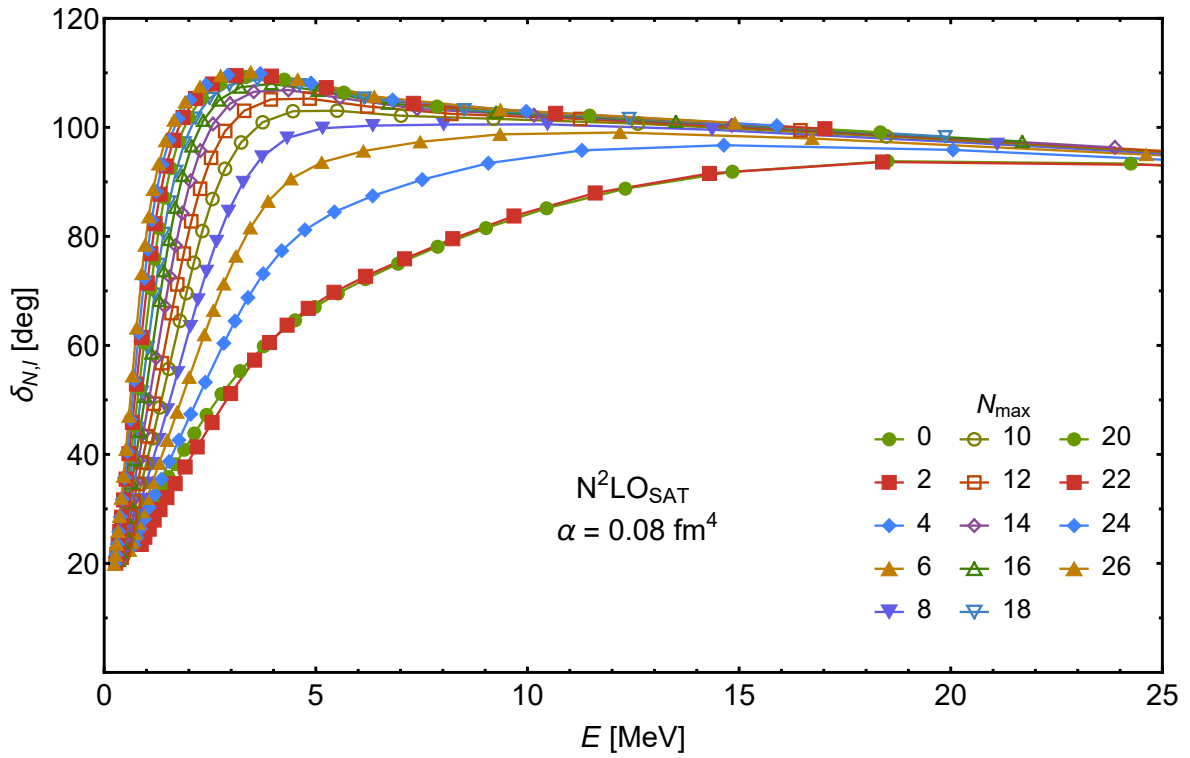


Figure C.6.: Tetraneutron phase shift. Interaction  $N^2LO_{SAT}$  SRG evolved with  $\alpha = 0.08 \text{ fm}^4$ .

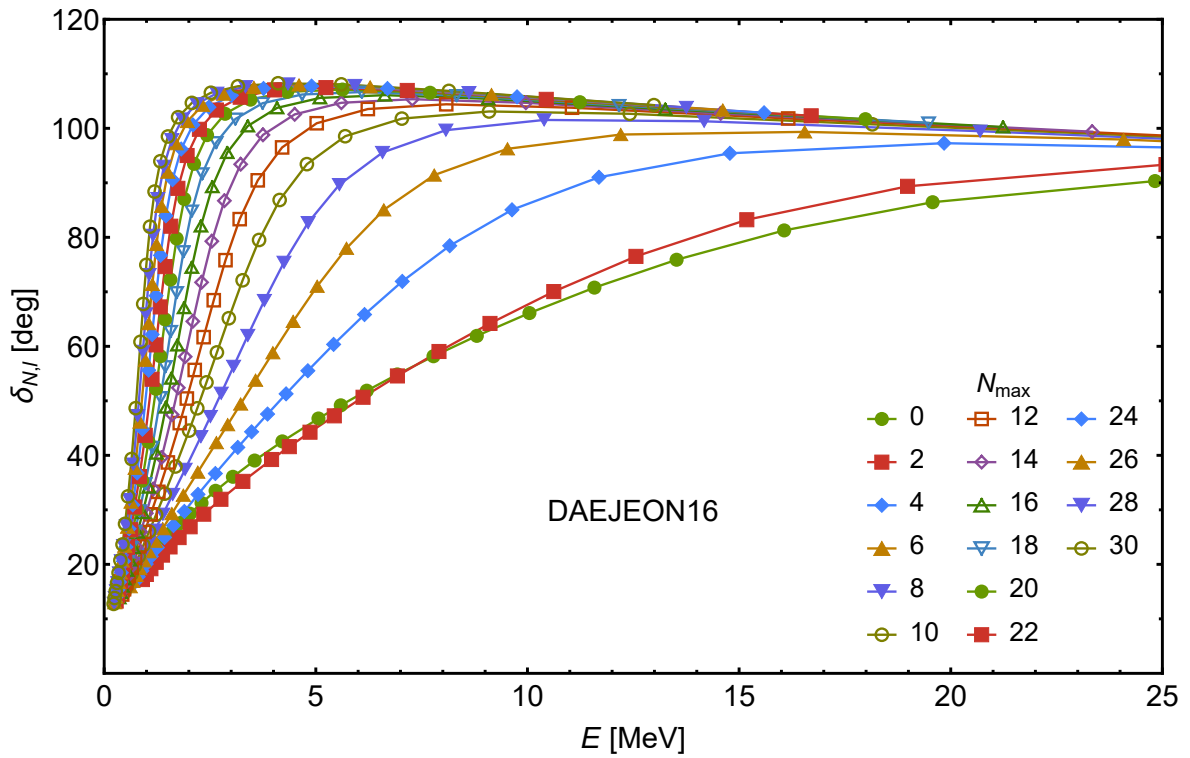


Figure C.7.: Tetraneutron phase shift. Interaction DAEJEON16.

## D. Alternative Derivation of Low-Energy Behaviour of $k(\lambda)$

The derivation given in [KKH89] uses the Hellmann-Feynman Theorem. Starting with the Schrödinger equation

$$\left( -\frac{d^2}{dr^2} + \frac{\ell(\ell+1)}{r^2} + \lambda \frac{2\mu}{\hbar^2} V(r) - k^2 \right) \psi_{\lambda,\ell}(k, r) = 0, \quad (\text{D.1})$$

where  $\psi_{\lambda}(k, r)$  is the bound-state eigenfunction at some  $\lambda$ . We use the Hellmann-Feynman theorem

$$\frac{\partial E_{\ell}}{\partial \lambda} = \frac{\hbar^2 k_{\ell}(\lambda)}{\mu} \frac{\partial k_{\ell}(\lambda)}{\partial \lambda} = \frac{\langle \psi_{\lambda} | V | \psi_{\lambda} \rangle}{\langle \psi_{\lambda} | \psi_{\lambda} \rangle}. \quad (\text{D.2})$$

Assuming the potential to be of finite range, being negligible after point  $R$ , we get

$$\frac{\hbar^2 k_{\ell}(\lambda)}{\mu} \frac{\partial k_{\ell}(\lambda)}{\partial \lambda} = \frac{\int_0^R dr |\psi_{\lambda}(k, r)|^2 V(r)}{\int_0^R dr |\psi_{\lambda}(k, r)|^2 + \int_R^{\infty} dr |\psi_{\lambda}(k, r)|^2}, \quad (\text{D.3})$$

The configuration space separation allows us to consider two distinct analytic functions with known properties. In the region  $[r, R]$  we find

$$\psi_{\lambda,\ell}(k, r) = c_1 (kr)^{\ell+1} \sum_{i=0}^{\infty} a_i (kr)^{2i}. \quad (\text{D.4})$$

The region  $[R, \infty[$  gives

$$\psi_{\lambda,\ell}(k, r) = c_2 k^{\ell+2} K_{\ell}(ikr), \quad (\text{D.5})$$

where  $K_{\ell}(ikr)$  is the modified Bessel function of the second kind [DLM14]. We distinguish between the  $\ell = 0$  and the  $\ell \neq 0$  case. For  $\ell = 0$  we find

$$\frac{\hbar^2 k_0(\lambda)}{\mu} \frac{\partial k_0(\lambda)}{\partial \lambda} = k_0 \frac{\sum_{j=0}^{\infty} d_j k_0^{2j}}{\sum_{j=0}^{\infty} f_j k_0^j}, \quad (\text{D.6})$$

the coefficients are radial integrals. For  $\ell \neq 0$ , the result reads

$$\frac{\hbar^2 k_{\ell}(\lambda)}{\mu} \frac{\partial k_{\ell}(\lambda)}{\partial \lambda} = \frac{\sum_{j=0}^{\infty} g_j k_{\ell}^{2j}}{\sum_{j=0}^{\ell-1} h_j k_{\ell}^{2j} + \sum_{j=2k}^{\infty} q_j k_{\ell}^{j-1}} \quad (\text{D.7})$$

Only taking the leading terms, one arrives at the same conclusion for  $k(\lambda)$  as given in section 8.1,

$$k_0(\lambda) \sim (\lambda - \bar{\lambda}_0) \tag{D.8}$$

with  $k_0(\bar{\lambda}_0) = 0$ . For  $\ell \neq 0$ , we have

$$k_\ell(\lambda) = \pm c \sqrt{\lambda - \lambda_0} \tag{D.9}$$

with some constant  $c$ .

## E. ACCC Fits to Fixed Data Sets

To gauge the impact of the different threshold values, different data sets as well as the effect the algorithm has on the fit, we perform for each  $\lambda_0$  from the IACCC the corresponding ACCC with the same algorithm as is used in the IACCC, with one exception for the data set C and the Levenberg-Marquardt algorithm, where we used the  $\lambda_0$  values obtain from the BFGS method. These plots show the  $S$ -matrix pole trajectories in the complex  $k$ -plane. How to read this plot is shown in figure 8.4. On the positive imaginary axis lie the bound states which are fitted. The fit is then extrapolated into the fourth quadrant, with  $\lambda = 0$  corresponding to the end of the line. Shown in each figure are the ACCC fits with the  $\lambda_0$  from the IACCC with the corresponding order given in the lower left corner of each window.

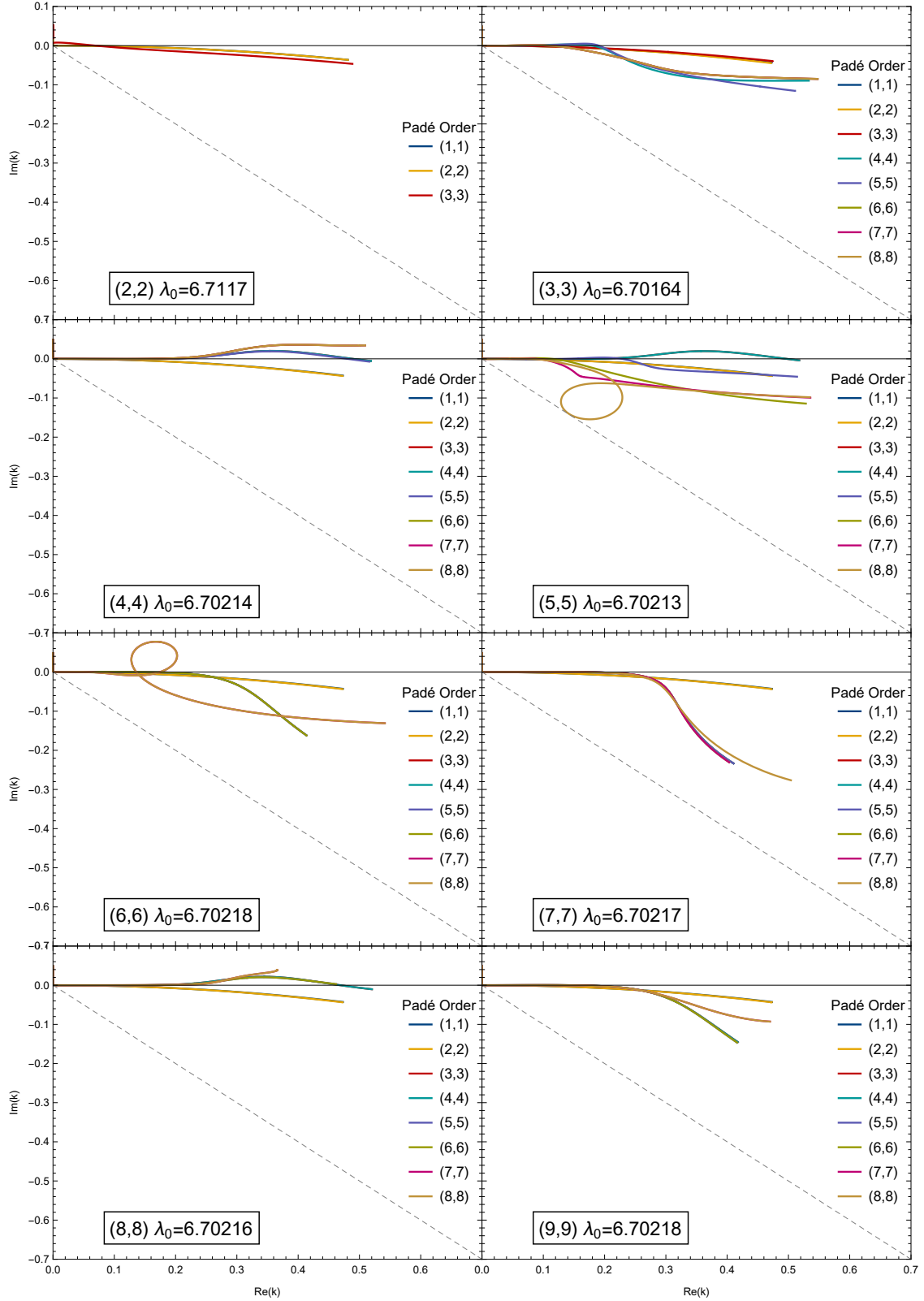


Figure E.1.: Tetra-neutron  $S$ -matrix pole trajectories. Data set A,  $\lambda_0$  determination and fit performed with Quasi-Newton BFGS.  $N_{\text{max}} = 28$ ,  $a_{\text{HO}} = 2.5$  fm. The grey dashed line is the angle bisector.

E. ACCC Fits to Fixed Data Sets

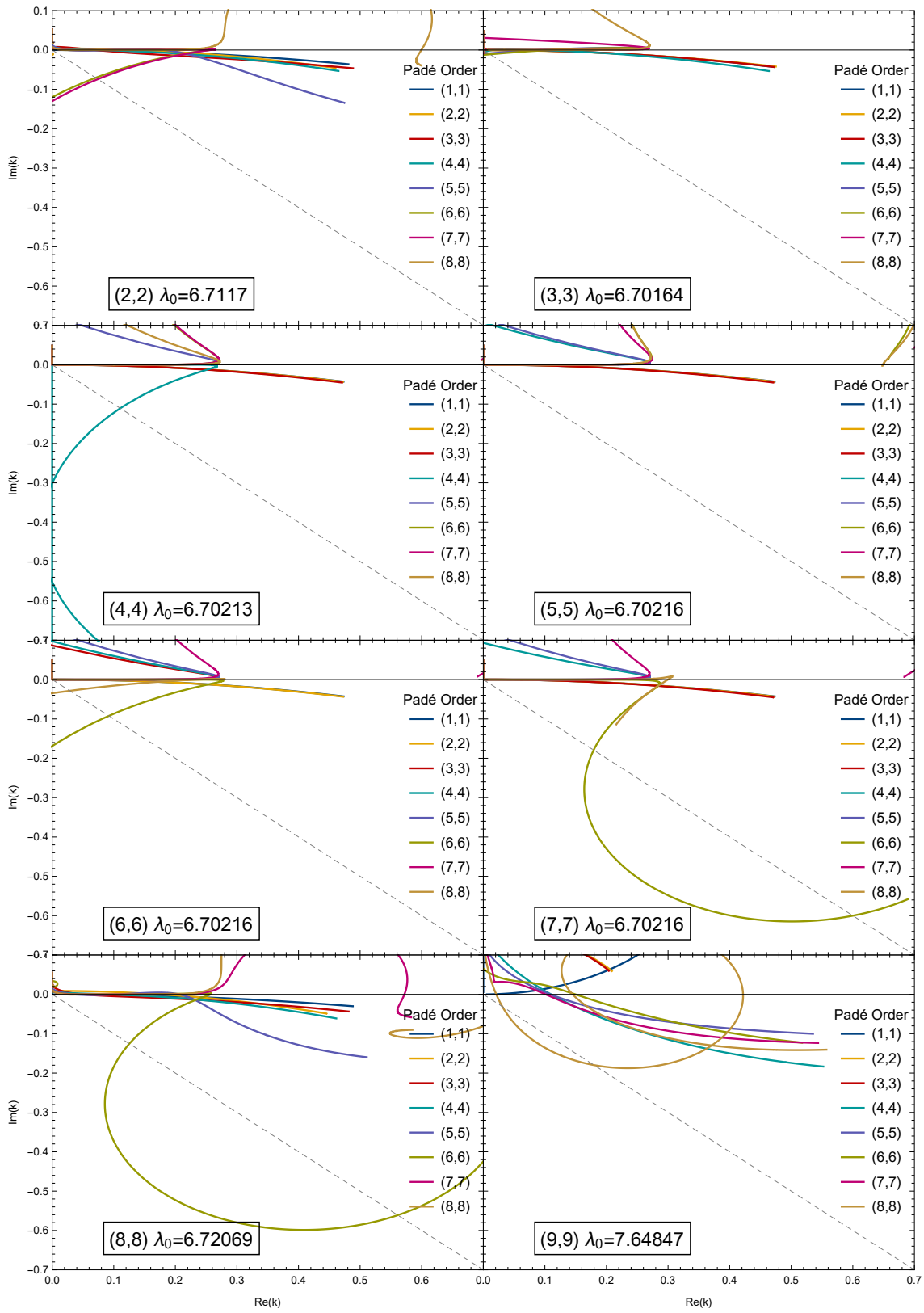


Figure E.2.: Tetraneutron  $S$ -matrix pole trajectories. Data set A,  $\lambda_0$  determination and fit performed with Levenberg-Marquardt.  $N_{\max} = 28$ ,  $a_{\text{HO}} = 2.5$  fm.

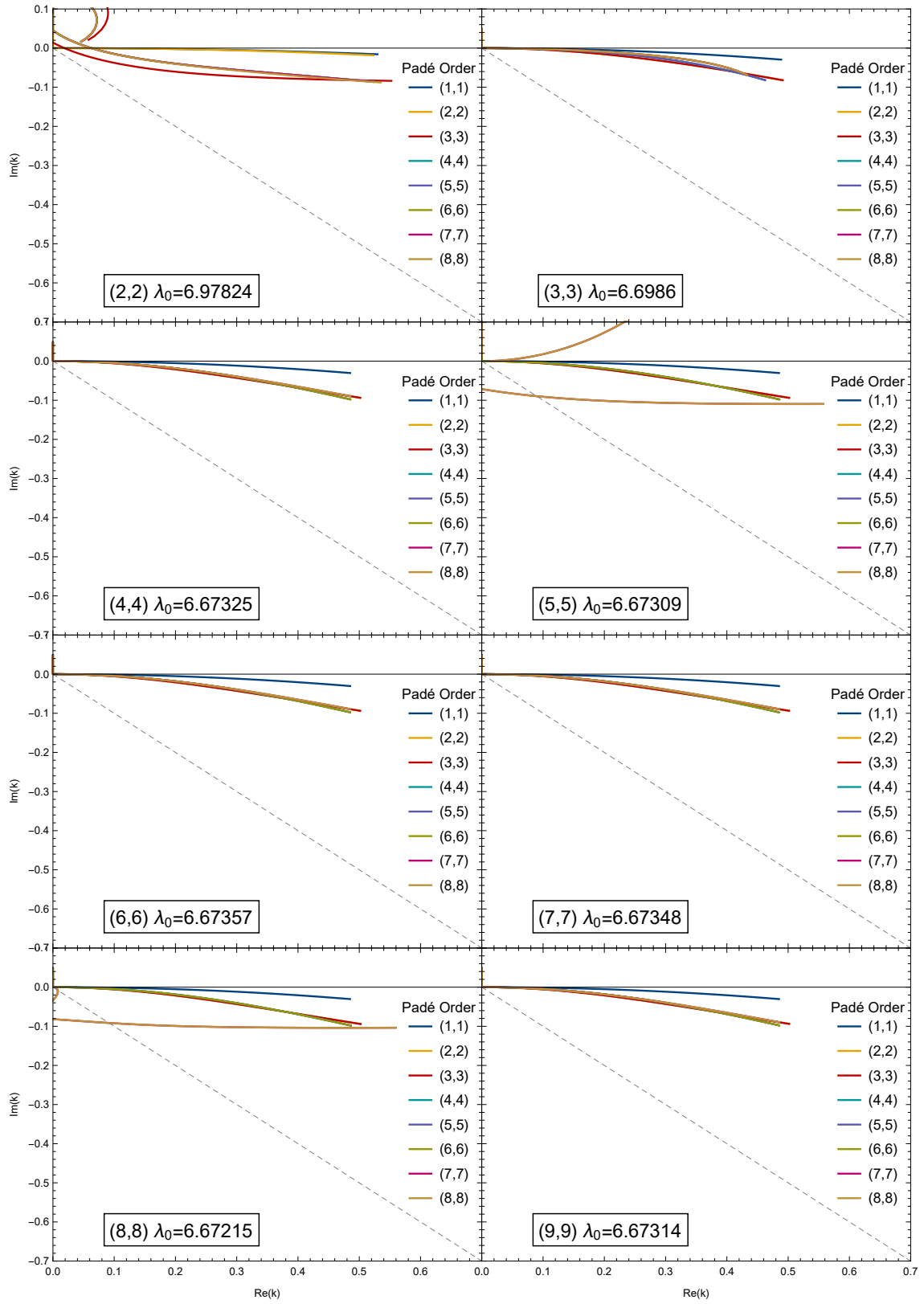


Figure E.3.: Tetraneutron  $S$ -matrix pole trajectories. Data set C,  $\lambda_0$  determination and fit performed with Quasi-Newton BFGS.  $N_{\max} = 28$ ,  $a_{\text{HO}} = 2.5$  fm.

E. ACCC Fits to Fixed Data Sets

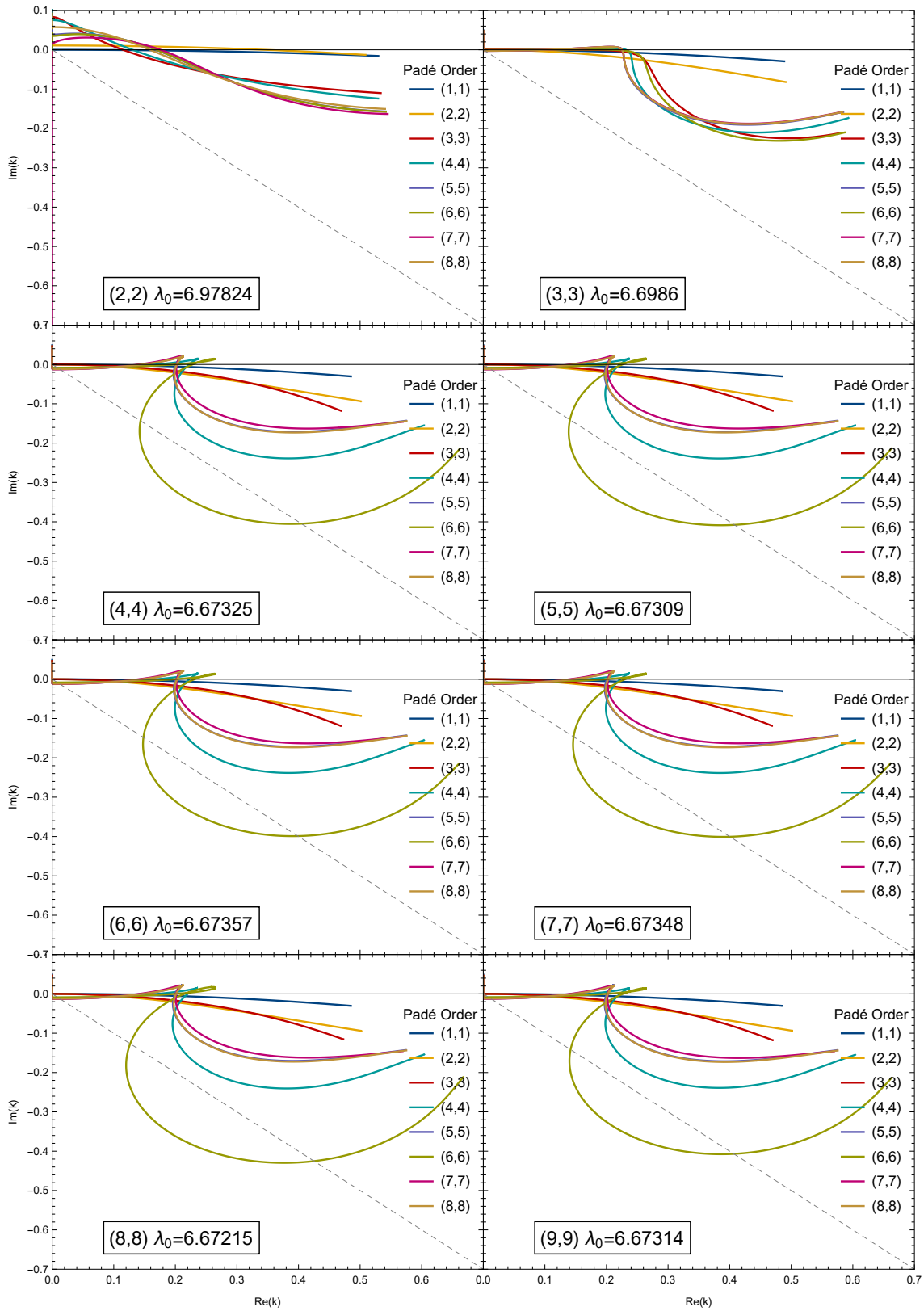


Figure E.4.: Tetra-neutron  $S$ -matrix pole trajectories. Data set C,  $\lambda_0$  from result with Quasi-Newton BFGS and fit performed with Levenberg-Marquardt.  $N_{\max} = 28$ ,  $a_{\text{HO}} = 2.5$  fm.

# Bibliography

- [AGS67] E.O. Alt, P. Grassberger, and W. Sandhas. Reduction of the three-particle collision problem to multi-channel two-particle lippmann-schwinger equations. *Nuclear Physics B*, 2(2):167–180, 1967, doi: 10.1016/0550-3213(67)90016-8.
- [Aoy03] Shigeyoshi Aoyama. New method of analytic continuation in the coupling constant with the complex scaling method. *Physical Review C*, 68(3), 2003, doi: 10.1103/physrevc.68.034313.
- [AS64] Milton Abramowitz and Irene A. Stegun, editors. *Handbook of Mathematical Functions with Formulas, Graphs, and Mathematical Tables*. Number 55 in National Bureau of Standards Applied Mathematics Series. U.S. Government Printing Office, Washington, D.C., 1964.
- [AW13] George Arfken and Hans Weber. *Mathematical Methods for Physicists*. Elsevier, 2013, doi: 10.1016/c2009-0-30629-7.
- [AYHA08] Abdulaziz D. Alhaidari, Hashim A. Yamani, Eric J. Heller, and Mohamed S. Abdelmonem, editors. *The J-Matrix Method*. Springer Netherlands, 2008, doi: 10.1007/978-1-4020-6073-1.
- [Bak12] George Jr Baker. Padé approximant. *Scholarpedia*, 7(6):9756, 2012, doi: 10.4249/scholarpedia.9756.
- [Ber68] Tore Berggren. On the use of resonant states in eigenfunction expansions of scattering and reaction amplitudes. *Nuclear Physics A*, 109(2):265–287, 1968, doi: 10.1016/0375-9474(68)90593-9.
- [BFP07] S. K. Bogner, R. J. Furnstahl, and R. J. Perry. Similarity renormalization group for nucleon-nucleon interactions. *Physical Review C*, 75(6), 2007, doi: 10.1103/physrevc.75.061001.
- [BFW77] B. Buck, H. Friedrich, and C. Wheatley. Local potential models for the scattering of complex nuclei. *Nuclear Physics A*, 275(1):246–268, 1977, doi: 10.1016/0375-9474(77)90287-1.
- [BGM96] George A. Baker and Peter Graves-Morris. *Padé Approximants Second Edition*. Cambridge University Press, 1996, doi: 10.1017/cbo9780511530074.
- [Bin10] Sven Binder. Angular Momentum Projection and Three-Body Forces in the No-Core Shell Model. Master’s thesis, Technische Universität Darmstadt, 2010.
- [BKS03] S.K. Bogner, T.T.S. Kuo, and A. Schwenk. Model-independent low momentum nucleon interaction from phase shift equivalence. *Physics Reports*, 386(1):1–27, 2003, doi: 10.1016/j.physrep.2003.07.001.
- [BLCR14] Sven Binder, Joachim Langhammer, Angelo Calci, and Robert Roth. Ab-initio Path to Heavy Nuclei. *Physics Letters B*, 736:119–123, 2014, doi: 10.1016/j.physletb.2014.07.010.

- [BLO00] Nir Barnea, Winfried Leidemann, and Giuseppina Orlandini. State dependent effective interaction for the hyperspherical formalism. *Physical Review C*, 61(5), 2000, doi: 10.1103/physrevc.61.054001.
- [BMS<sup>+</sup>00] J.M. Bang, A.I. Mazur, A.M. Shirokov, Yu.F. Smirnov, and S.A. Zaytsev. P-Matrix and J-Matrix Approaches: Coulomb Asymptotics in the Harmonic Oscillator Representation of Scattering Theory. *Annals of Physics*, 280(2):299–335, 2000, doi: 10.1006/aphy.1999.5992.
- [BNQ13a] Simone Baroni, Petr Navrátil, and Sofia Quaglioni. Ab Initio Description of the Exotic Unbound  ${}^7\text{He}$  Nucleus. *Physical Review Letters*, 110(2), 2013, doi: 10.1103/PhysRevLett.110.022505.
- [BNQ13b] Simone Baroni, Petr Navrátil, and Sofia Quaglioni. Unified ab initio approach to bound and unbound states: No-core shell model with continuum and its application to  ${}^7\text{He}$ . *Physical Review C*, 87(3), 2013, doi: 10.1103/PhysRevC.87.034326.
- [BNV13] Bruce R. Barrett, Petr Navrátil, and James P. Vary. Ab initio no core shell model. *Progress in Particle and Nuclear Physics*, 69:131–181, 2013, doi: 10.1016/j.ppnp.2012.10.003.
- [BZ03] Carlos A. Bertulani and Vladimir Zelevinsky. Is the tetra-neutron a bound dineutron–dineutron molecule? *Journal of Physics G: Nuclear and Particle Physics*, 29(10):2431–2437, 2003, doi: 10.1088/0954-3899/29/10/309.
- [Car88] J. Carlson. Alpha particle structure. *Physical Review C*, 38(4):1879–1885, 1988, doi: 10.1103/physrevc.38.1879.
- [Cha32] James Chadwick. The existence of a neutron. *Proceedings of the Royal Society A*, 136(830):692–708, 1932, doi: 10.1098/rspa.1932.0112.
- [CLHK17] J. Carbonell, R. Lazauskas, E. Hiyama, and M. Kamimura. On the possible existence of four neutron resonances. *Few-Body Systems*, 58(2), 2017, doi: 10.1007/s00601-017-1219-0.
- [ČPH16] Roman Čurík, Ivana Paidarová, and Jiří Horáček. The  ${}^2\Pi_g$  shape resonance of acetylene anion: an investigation with the RAC method. *European Physical Journal D: Atomic, Molecular and Optical Physics*, 70(7):146, 2016, doi: 10.1140/epjd/e2016-70133-6.
- [DB10] P. Descouvemont and D. Baye. The R-matrix theory. *Reports on Progress in Physics*, 73(3):036301, 2010, doi: 10.1088/0034-4885/73/3/036301.
- [Del18] A. Deltuva. Tetra-neutron: Rigorous continuum calculation. *Physics Letters B*, 782:238–241, 2018, doi: 10.1016/j.physletb.2018.05.041.
- [Der17] Daniel Derr. Di- and Tetra-neutron within the HORSE Formalism, 2017. Bachelor’s Thesis, Technische Universität Darmstadt.
- [DL19a] A. Deltuva and R. Lazauskas. Comment on “Is a Trineutron Resonance Lower in Energy than a Tetra-neutron Resonance?”. *Physical Review Letters*, 123(6), 2019, doi: 10.1103/PhysRevLett.123.069201.
- [DL19b] A. Deltuva and R. Lazauskas. Tetra-neutron resonance in the presence of a dineutron. *Physical Review C*, 2019, doi: 10.1103/PhysRevC.100.044002.

- [DLM14] DLMF. NIST Digital Library of Mathematical Functions. <http://dlmf.nist.gov/>, Release 1.0.26 of 2020-03-15, 2014. Frank W. J. Olver, Daniel W. Lozier, Ronald F. Boisvert, and Charles W. Clark.
- [Dru87] G. F. Drukarev. *Collisions of Electrons with Atoms and Molecules*. Springer US, 1987, doi: 10.1007/978-1-4613-1779-1.
- [EHM09] E. Epelbaum, H.-W. Hammer, and Ulf-G. Meißner. Modern theory of nuclear forces. *Reviews of Modern Physics*, 81(4):1773–1825, 2009, doi: 10.1103/revmodphys.81.1773.
- [EJW<sup>+</sup>15] A. Ekström, G. R. Jansen, K. A. Wendt, et al. Accurate nuclear radii and binding energies from a chiral interaction. *Physical Review C*, 91(5), 2015, doi: 10.1103/physrevc.91.051301.
- [EM02] D.R. Entem and R. Machleidt. Accurate nucleon–nucleon potential based upon chiral perturbation theory. *Physics Letters B*, 524(1-2):93–98, 2002, doi: 10.1016/s0370-2693(01)01363-6.
- [EM03] D. R. Entem and R. Machleidt. Accurate charge-dependent nucleon-nucleon potential at fourth order of chiral perturbation theory. *Physical Review C*, 68(4), 2003, doi: 10.1103/physrevc.68.041001.
- [EMN17] D. R. Entem, R. Machleidt, and Y. Nosyk. High-quality two-nucleon potentials up to fifth order of the chiral expansion. *Physical Review C*, 96(2), 2017, doi: 10.1103/physrevc.96.024004.
- [Epe10] Evgeny Epelbaum. Nuclear forces from chiral effective field theory: a primer. arXiv:1001.3229v1, 2010.
- [Fad61] Ludwig Faddeev. Scattering Theory For A Three-particle System. *Journal of Experimental and Theoretical Physics*, 12, 1961.
- [Fes58] Herman Feshbach. A Unified theory of Nuclear Reactions I. *Annals of Physics*, 5(4):357–390, 1958, doi: 10.1016/0003-4916(58)90007-1.
- [Fes62] Herman Feshbach. A unified theory of nuclear reactions. II. *Annals of Physics*, 19(2):287–313, 1962.
- [FHT06] Y. Funaki, H. Horiuchi, and A. Tohsaki. New Treatment of Resonances with a Bound State Approximation Using a Pseudo-Potential. *Progress of Theoretical Physics*, 115(1):115–127, 2006, doi: 10.1143/ptp.115.115.
- [Fil81] G. F. Filippov. On Taking Account of Correct Asymptotics in Expansions in Terms of Oscillator Basis. *Soviet Journal of Nuclear Physics*, 33:488, 1981.
- [FM93] L. D. Faddeev and S. P. Merkuriev. *Quantum Scattering Theory for Several Particle Systems*. Springer Netherlands, 1993, doi: 10.1007/978-94-017-2832-4.
- [FNRS98] H. Feldmeier, T. Neff, R. Roth, and J. Schnack. A unitary correlation operator method. *Nuclear Physics A*, 632(1):61–95, 1998, doi: 10.1016/s0375-9474(97)00805-1.
- [Fri13] Harald Friedrich. *Scattering Theory*. Springer Berlin Heidelberg, 2013, doi: 10.1007/978-3-642-38282-6.

- [FRMP17] K. Fosse, J. Rotureau, N. Michel, and M. Płoszajczak. Can Tetraneutron be a Narrow Resonance? *Physical Review Letters*, 119(3), 2017, doi: 10.1103/physrevlett.119.032501.
- [Gam28] G. Gamow. Zur quantentheorie des atomkernes. *Zeitschrift für Physik*, 51(3-4):204–212, 1928, doi: 10.1007/BF01343196.
- [GHK<sup>+</sup>17] S. Gandolfi, H.-W. Hammer, P. Klos, J. E. Lynn, and A. Schwenk. Is a trineutron resonance lower in energy than a tetraneutron resonance? *Physical Review Letters*, 118(23), 2017, doi: 10.1103/PhysRevLett.118.232501.
- [GHK<sup>+</sup>19] S. Gandolfi, H.-W. Hammer, P. Klos, J. E. Lynn, and A. Schwenk. Gandolfi et al. Reply:. *Physical Review Letters*, 123(6), 2019, doi: 10.1103/physrevlett.123.069202.
- [GSW62] Jeffrey Goldstone, Abdus Salam, and Steven Weinberg. Broken symmetries. *Physical Review*, 127(3):965–970, 1962, doi: 10.1103/physrev.127.965.
- [GW93] Stanisław D. Głazek and Kenneth G. Wilson. Renormalization of hamiltonians. *Physical Review D*, 48(12):5863–5872, 1993, doi: 10.1103/physrevd.48.5863.
- [HGKV20] Michael D. Higgins, Chris H. Greene, Alejandro Kievsky, and Michele Viviani. Non-resonant density of states enhancement at low energies for three or four neutrons. arXiv:2005.04714v1, 2020.
- [HJS49] Otto Haxel, J. Hans D. Jensen, and Hans E. Suess. On the “magic numbers” in nuclear structure. *Physical Review*, 75(11):1766–1766, 1949, doi: 10.1103/physrev.75.1766.2.
- [HKL74] Y. Hahn, D. J. Kouri, and F. S. Levin. Channel coupling arrays and the reduction method in many-body scattering. *Physical Review C*, 10(5):1615–1619, 1974, doi: 10.1103/physrevc.10.1615.
- [HLCK16] E. Hiyama, R. Lazauskas, J. Carbonell, and M. Kamimura. Possibility of generating a 4-neutron resonance with a  $T=3/2$  isospin 3-neutron force. *Physical Review C*, 93(4), 2016, doi: 10.1103/physrevc.93.044004.
- [HP10] J. Horáček and I. Páidarová. On the calculation of resonances by means of analytic continuation in coupling constant. *Journal of Physics: Conference Series*, 257:012002, 2010, doi: 10.1088/1742-6596/257/1/012002.
- [HPČ14] Jiří Horáček, Ivana Páidarová, and Roman Čurík. Determination of the Resonance Energy and Width of the  ${}^2B_{2g}$  Shape Resonance of Ethylene with the Method of Analytical Continuation in the Coupling Constant. *The Journal of Physical Chemistry A*, 118(33):6536–6541, 2014, doi: 10.1021/jp503075a.
- [HPD<sup>+</sup>07] G. Hagen, T. Papenbrock, D. J. Dean, et al. Coupled-cluster theory for three-body hamiltonians. *Physical Review C*, 76(3), 2007, doi: 10.1103/physrevc.76.034302.
- [HQN15] Guillaume Hupin, Sofia Quaglioni, and Petr Navrátil. Unified Description of  ${}^6\text{Li}$  Structure and Deuterium- ${}^4\text{He}$  Dynamics with Chiral Two- and Three-Nucleon Forces. *Physical Review Letters*, 114(21), 2015, doi: 10.1103/physrevlett.114.212502.

- [HSPT09] Jiří Horáček, Theodore E. Simos, George Psihoyios, and Ch. Tsitouras. Determination of Resonance Parameters by Use of Padé III Approximation. In *AIP Conference Proceedings*. AIP, 2009, doi: 10.1063/1.3241349.
- [HT70] Andrew U. Hazi and Howard S. Taylor. Stabilization method of calculating resonance energies: Model problem. *Physical Review A*, 1(4):1109–1120, 1970, doi: 10.1103/physreva.1.1109.
- [HVH<sup>+</sup>19] Thomas Hüther, Klaus Vobig, Kai Hebel, Ruprecht Machleidt, and Robert Roth. Family of Chiral Two- plus Three-Nucleon Interactions for Accurate Nuclear Structure Studies. arXiv:1911.04955v1, 2019.
- [HY73] Eric J. Heller and Hashim A. Yamani. New  $L^2$  approach to quantum scattering: Theory. *Physical Review A*, 9(9):1201, 1973, doi: 10.1103/PhysRevA.9.1201.
- [Jac42] Carl Gustav Jacob Jacobi. Sur l'élimination des noeuds dans le problème des trois corps. *Comptes Rendus de l' Academie des Sciences*, 1842(15):236, 1842.
- [JLA<sup>+</sup>19] Calvin W. Johnson, Kristina D. Launey, Naftali Auerbach, et al. From bound states to the continuum. arXiv:1912.00451, 2019.
- [Joa76] Charles J. Joachain. *Quantum Collision Theory: 2v.in 1v*. North-Holland, 1976.
- [JRZ85] M Sotona J Revai and J Zofka. Note on the use of harmonic-oscillator wavefunctions in scattering calculations. *Journal of Physics G: Nuclear Physics*, 11(6), 1985, doi: 10.1088/0305-4616/11/6/011.
- [KK77] V I Kukulín and V M Krasnopol'sky. Description of few-body systems via analytical continuation in coupling constant. *Journal of Physics A: Mathematical and General*, 10(2):L33–L37, 1977, doi: 10.1088/0305-4470/10/2/002.
- [KK78] V.M. Krasnopol'sky and V.I. Kukulín. Theory of resonance states based on analytical continuation in the coupling constant. *Physics Letters A*, 69(4):251–254, 1978, doi: 10.1016/0375-9601(78)90177-9.
- [KKH89] V. I. Kukulín, V. M. Krasnopol'sky, and J. Horáček. *Theory of Resonances*. Springer Netherlands, 1989, doi: 10.1007/978-94-015-7817-2.
- [KSM<sup>+</sup>16] K. Kisamori, S. Shimoura, H. Miya, et al. Candidate Resonant Tetraneutron State Populated by the  $^4\text{He}(^8\text{He}, ^8\text{Be})$  Reaction. *Physical Review Letters*, 116(5), 2016, doi: 10.1103/physrevlett.116.052501.
- [Lan50] C. Lanczos. An iteration method for the solution of the eigenvalue problem of linear differential and integral operators. *Journal of Research of the National Bureau of Standards*, 45(4):255, 1950, doi: 10.6028/jres.045.026.
- [Laz18a] Rimantas Lazauskas. Description of five-nucleon systems using Faddeev-Yakubovsky equations. *Few-Body Systems*, 59(2), 2018, doi: 10.1007/s00601-018-1333-7.
- [Laz18b] Rimantas Lazauskas. Solution of the  $n\text{-}^4\text{He}$  elastic scattering problem using the Faddeev-Yakubovsky equations. *Physical Review C*, 97(4), 2018, doi: 10.1103/physrevc.97.044002.

- [LC05] Rimantas Lazauskas and Jaume Carbonell. Is a physically observable tetra-neutron resonance compatible with realistic nuclear interactions? *Physical Review C*, 72(3), 2005, doi: 10.1103/physrevc.72.034003.
- [LCH17] R. Lazauskas, J. Carbonell, and E. Hiyama. Modeling the double charge exchange response function for a tetra-neutron system. *Progress of Theoretical and Experimental Physics*, 2017(7), 2017, doi: 10.1093/ptep/ptx078.
- [Lev49] Norman Levinson. On the uniqueness of the potential in a schrodinger equation for a given asymptotic phase. *Kgl. Danske Videnskab. Selskab. Mat. Fys. Medd.*, 25(9), 1949.
- [LHC19] R. Lazauskas, E. Hiyama, and J. Carbonell. Ab initio calculations of  ${}^5\text{H}$  resonant states. *Physics Letters B*, 791:335–341, 2019, doi: 10.1016/j.physletb.2019.02.047.
- [LMH<sup>+</sup>19] Jian Guo Li, Nicolas Michel, Bai Shan Hu, Wei Zuo, and Fu Rong Xu. Ab-initio No-core Gamow Shell Model Calculations of Multi-neutron Systems. *Physical Review C*, 100(054313), 2019, doi: 10.1103/PhysRevC.100.054313.
- [LMOP47] C. M. G. Lattes, H. Muirhead, G. P. S. Occhialini, and C. F. Powell. Processes Involving Charged Mesons. *Nature*, 159(4047):694–697, 1947, doi: 10.1038/159694a0.
- [LP12] Traian Lalescu and Émile Picard. *Introduction à la théorie des équations intégrales*. Paris : Hermann & Fils, 1912.
- [LS50] B. A. Lippmann and Julian Schwinger. Variational principles for scattering processes. i. *Physical Review*, 79(3):469–480, 1950, doi: 10.1103/PhysRev.79.469.
- [LS80] S.Y. Lee and K. Suzuki. The effective interaction of two nucleons in the s-d shell. *Physics Letters B*, 91(2):173–176, 1980, doi: 10.1016/0370-2693(80)90423-2.
- [LS04] Yu. A. Lurie and A. M. Shirokov. Loosely bound three-body nuclear systems in the J-matrix approach. *Annals of Physics*, 312(2):284–318, 2004, doi: 10.1016/j.aop.2004.02.002.
- [LTGL19] J.E. Lynn, I. Tews, S. Gandolfi, and A. Lovato. Quantum monte carlo methods in nuclear physics: Recent advances. *Annual Review of Nuclear and Particle Science*, 69(1):279–305, 2019, doi: 10.1146/annurev-nucl-101918-023600.
- [Mac01] R. Machleidt. High-precision, charge-dependent bonn nucleon-nucleon potential. *Physical Review C*, 63(2), 2001, doi: 10.1103/physrevc.63.024001.
- [Mat20] Mathematica. Unconstrained Optimization: Methods for Local Minimization, 2020. <https://reference.wolfram.com/language/tutorial/UnconstrainedOptimizationMethodsForLocalMinimization.html#492573133>.
- [May49] Maria Goeppert Mayer. On closed shells in nuclei. II. *Physical Review*, 75(12):1969–1970, 1949, doi: 10.1103/physrev.75.1969.
- [MLO<sup>+</sup>02] F. M. Marqués, M. Labiche, N. A. Orr, et al. Detection of neutron clusters. *Physical Review C*, 65(4), 2002, doi: 10.1103/physrevc.65.044006.

- [MLP14] Nan Meng, Bo-Lin Li, and Jia-Lun Ping. Tetra-neutron in the chiral quark model. *Chinese Physics Letters*, 31(1):011201, 2014, doi: 10.1088/0256-307x/31/1/011201.
- [MOF<sup>+</sup>05] F. M. Marqués, N. A. Orr, H. Al Falou, G. Normand, and N. M. Clarke. On the possible detection of  $^4\text{n}$  events in the breakup of  $^{14}\text{Be}$ . arXiv:nucl-ex/0504009v1, 2005.
- [Moo08] M. Moore. Introduction to Scattering Theory. <http://www.pa.msu.edu/~mmoore/852scattering.pdf>, 2008.
- [Mos59] Marcos Moshinsky. Transformation brackets for harmonic oscillator functions. *Nuclear Physics*, 13(1):104–116, 1959, doi: 10.1016/0029-5582(59)90143-9.
- [MSS<sup>+</sup>18] T. D. Morris, J. Simonis, S. R. Stroberg, et al. Structure of the lightest tin isotopes. *Physical Review Letters*, 120(15), 2018, doi: 10.1103/physrevlett.120.152503.
- [Nav07] P. Navrátil. Local three-nucleon interaction from chiral effective field theory. *Few-Body Systems*, 41(3-4):117–140, 2007, doi: 10.1007/s00601-007-0193-3.
- [New60] Roger G. Newton. Analytic Properties of Radial Wave Functions. *Journal of Mathematical Physics*, 1(4):319, 1960, doi: 10.1063/1.1703665.
- [New82] Roger G. Newton. *Scattering Theory of Waves and Particles*. Springer Berlin Heidelberg, second edition, 1982, doi: 10.1007/978-3-642-88128-2.
- [NKB00] P. Navrátil, G. P. Kamuntavičius, and B. R. Barrett. Few-nucleon systems in a translationally invariant harmonic oscillator basis. *Physical Review C*, 61(4), 2000, doi: 10.1103/physrevc.61.044001.
- [NRQ11] Petr Navrátil, Robert Roth, and Sofia Quaglioni. Ab initio many-body calculation of the  $^7\text{be}(p, \gamma)^8\text{b}$  radiative capture. *Physics Letters B*, 704(5):379–383, 2011, doi: 10.1016/j.physletb.2011.09.079.
- [Ôku54] Susumu Ôkubo. Diagonalization of hamiltonian and tamm-dancoff equation. *Progress of Theoretical Physics*, 12(5):603–622, 1954, doi: 10.1143/ptp.12.603.
- [OS72] V. N. Ostrovskii and E. A. Solov'ev. Perturbation Theory for Weakly Bound States. *Journal of Experimental and Theoretical Physics*, 1972.
- [Pie03] Steven C. Pieper. Can modern nuclear hamiltonians tolerate a bound tetra-neutron? *Physical Review Letters*, 90(25), 2003, doi: 10.1103/physrevlett.90.252501.
- [PNB09] I. Stetcu P. Navrátil, S. Quaglioni and B. R. Barrett. Recent developments in no-core shell-model calculations. *Journal of Physics G: Nuclear and Particle Physics*, 36(8):083101, 2009, doi: 10.1088/0954-3899/36/8/083101.
- [PRM<sup>+</sup>13] G. Papadimitriou, J. Rotureau, N. Michel, M. Płoszajczak, and B. R. Barrett. Ab initio no-core gamow shell model calculations with realistic interactions. *Physical Review C*, 88(4), 2013, doi: 10.1103/physrevc.88.044318.
- [PvMM<sup>+</sup>13] P Papp, Š Matejčí, P Mach, et al. Analytical continuation in coupling constant method; application to the calculation of resonance energies and widths for organic molecules: Glycine, alanine and valine and dimer of formic acid. *Chemical Physics*, 418:8–13, 2013, doi: 10.1016/j.chemphys.2013.03.023.

- [PY19] I. V. Panov and A. V. Yudin. Light neutral clusters in supernova matter. *Physics of Atomic Nuclei*, 82(5):483–490, 2019, doi: 10.1134/s1063778819040161.
- [QN08] Sofia Quaglioni and Petr Navrátil. Ab Initio Many-Body Calculations of n-<sup>3</sup>H, n-<sup>4</sup>He, p-<sup>3,4</sup>He, and n-<sup>10</sup>Be Scattering. *Physical Review Letters*, 101(9), 2008, doi: 10.1103/PhysRevLett.101.092501.
- [QN09] Sofia Quaglioni and Petr Navrátil. Ab Initio Many-body Calculations of Nucleon-nucleus Scattering. *Physical Review C*, 79(4), 2009, doi: 10.1103/PhysRevC.79.044606.
- [RN07] R. Roth and P. Navrátil. Ab Initio Study of <sup>40</sup>Ca with an Importance-Truncated No-Core Shell Model. *Physical Review Letters*, 99(9), 2007, doi: 10.1103/physrevlett.99.092501.
- [RNF10] Robert Roth, Thomas Neff, and Hans Feldmeier. Nuclear structure in the framework of the unitary correlation operator method. *Progress in Particle and Nuclear Physics*, 65(1):50–93, 2010, doi: 10.1016/j.ppnp.2010.02.003.
- [RR70] J. Raynal and J. Revai. Transformation coefficients in the hyperspherical approach to the three-body problem. *Il Nuovo Cimento A Series 10*, 68(4):612–622, 1970, doi: 10.1007/bf02756127.
- [Rut11] Ernest Rutherford. The scattering of alpha and beta particles by matter and the structure of the atom. *Philosophical Magazine*, Volume 21:669–688, 1911, doi: 10.1080/14786440508637080.
- [Rut19] E. Rutherford. Collision of  $\alpha$  particles with light atoms. IV. An anomalous effect in nitrogen. *The London, Edinburgh, and Dublin Philosophical Magazine and Journal of Science*, 37(222):581–587, 1919, doi: 10.1080/14786440608635919.
- [Sch13] Stefan Schulz. SRG-Induced Four-Body Forces in Ab Initio Nuclear Structure. Master’s thesis, Technische Universität Darmstadt, 2013.
- [Sch18] Stefan Schulz. *Four-Nucleon Forces in Ab Initio Nuclear Structure*. PhD thesis, Technische Universität Darmstadt, Darmstadt, 2018.
- [Sie39] A. J. F. Siegert. On the derivation of the dispersion formula for nuclear reactions. *Physical Review*, 56(8):750–752, 1939, doi: 10.1103/PhysRev.56.750.
- [SMHE17] Thomas Sommerfeld, Joshua B. Melugin, Prakash Hamal, and Masahiro Ehara. Resonance energies and lifetimes from the analytic continuation of the coupling constant method: Robust algorithms and a critical analysis. *Journal of Chemical Theory and Computation*, 13(6):2550–2560, 2017, doi: 10.1021/acs.jctc.6b01228.
- [Smi61] Yu.F. Smirnov. Talmi transformations for particles with different masses. *Nuclear Physics*, 27(2):177–187, 1961, doi: 10.1016/0029-5582(61)90343-1.
- [SMMV16] A. M. Shirokov, A. I. Mazur, I. A. Mazur, and J. P. Vary. Shell model states in the continuum. *Physical Review C*, 94(6), 2016, doi: 10.1103/PhysRevC.94.064320.
- [SMVM12] A. M. Shirokov, A. I. Mazur, J. P. Vary, and I. A. Mazur. Oscillator basis, scattering and nuclear structure. *Journal of Physics: Conference Series*, 403:012021, 2012, doi: 10.1088/1742-6596/403/1/012021.

- [SMZ<sup>+</sup>04] A.M. Shirokov, A. I. Mazur, S. A. Zaytsev, J. P. Vary, and T. A. Weber. Nucleon-nucleon Interaction in the J-matrix Inverse Scattering Approach and Few-nucleon Systems. *Physical Review C*, 70(044005), 2004, doi: 10.1103/PhysRevC.70.044005.
- [SN82] Yu. F. Smirnov and Yu. I. Nechaev. The elements of scattering theory in the harmonic oscillator representation. *Kinam Rev. Fís.*, 4(4):445, 1982.
- [SN17] J. J. Sakurai and Jim Napolitano. *Modern Quantum Mechanics*. Cambridge University Press, second edition, 2017, doi: 10.1017/9781108499996.
- [SPM<sup>+</sup>16] A. M. Shirokov, G. Papadimitriou, A. I. Mazur, et al. Prediction for a four-neutron resonance. *Physical Review Letters*, 117(18), 2016, doi: 10.1103/physrevlett.117.182502.
- [SSK<sup>+</sup>16] A.M. Shirokov, I.J. Shin, Y. Kim, et al. N<sup>3</sup>LO NN interaction adjusted to light nuclei in ab exitu approach. *Physics Letters B*, 761:87–91, 2016, doi: 10.1016/j.physletb.2016.08.006.
- [SV63] J.P. Schiffer and R. Vandenbosch. Search for a particle-stable tetra neutron. *Physics Letters*, 5(4):292–293, 1963, doi: 10.1016/s0375-9601(63)96134-6.
- [SVMW07] A. M. Shirokov, J.P. Vary, A.I. Mazur, and T.A. Weber. Realistic nuclear hamiltonian: Ab exitu approach. *Physics Letters B*, 644(1):33–37, 2007, doi: 10.1016/j.physletb.2006.10.066.
- [TBS11] K. Tsukiyama, S. K. Bogner, and A. Schwenk. In-medium similarity renormalization group for nuclei. *Physical Review Letters*, 106(22), 2011, doi: 10.1103/physrevlett.106.222502.
- [THH<sup>+</sup>18] M. Tanabashi, K. Hagiwara, K. Hikasa, et al. Review of particle physics. *Physical Review D*, 98(3), 2018, doi: 10.1103/physrevd.98.030001.
- [TKG<sup>+</sup>04] D.R. Tilley, J.H. Kelley, J.L. Godwin, et al. Energy levels of light nuclei. *Nuclear Physics A*, 745(3-4):155–362, 2004, doi: 10.1016/j.nuclphysa.2004.09.059.
- [TLT78] Y. C. Tang, M. LeMere, and D. R. Thompson. Resonating-group method for nuclear many-body problems. *Physics Reports*, 47(3):167–223, 1978, doi: 10.1016/0370-1573(78)90175-8.
- [TSV97] N. Tanaka, Y. Suzuki, and K. Varga. Exploration of resonances by analytic continuation in the coupling constant. *Physical Review C*, 56(1):562–565, 1997, doi: 10.1103/physrevc.56.562.
- [TSVL99] N. Tanaka, Y. Suzuki, K. Varga, and R. G. Lovas. Unbound states by analytic continuation in the coupling constant. *Physical Review C*, 59(3):1391–1399, 1999, doi: 10.1103/physrevc.59.1391.
- [VNAB01] V. Vasilevsky, A. V. Nesterov, F. Arickx, and J. Broeckhove. Algebraic model for scattering in three-s-cluster systems. i. theoretical background. *Physical Review C*, 63(3), 2001, doi: 10.1103/physrevc.63.034606.
- [Weg94] Franz Wegner. Flow-equations for hamiltonians. *Annalen der Physik*, 506(2):77–91, 1994, doi: 10.1002/andp.19945060203.
- [Wei64] Steven Weinberg. Systematic solution of multiparticle scattering problems. *Physical Review*, 133(1B):B232–B256, 1964, doi: 10.1103/physrev.133.b232.

- [Wei79] Steven Weinberg. Phenomenological lagrangians. *Physica A: Statistical Mechanics and its Applications*, 96(1-2):327–340, 1979, doi: 10.1016/0378-4371(79)90223-1.
- [Wei90] Steven Weinberg. Nuclear forces from chiral lagrangians. *Physics Letters B*, 251(2):288–292, 1990, doi: 10.1016/0370-2693(90)90938-3.
- [Wei91] Steven Weinberg. Effective chiral lagrangians for nucleon-pion interactions and nuclear forces. *Nuclear Physics B*, 363(1):3–18, 1991, doi: 10.1016/0550-3213(91)90231-1.
- [WHGM17] Alec F. White, Martin Head-Gordon, and C. William McCurdy. Stabilizing potentials in bound state analytic continuation methods for electronic resonances in polyatomic molecules. *The Journal of Chemical Physics*, 146(4):044112, 2017, doi: 10.1063/1.4974761.
- [Whi02] Steven R. White. Numerical canonical transformation approach to quantum many-body problems. *The Journal of Chemical Physics*, 117(16):7472–7482, 2002, doi: 10.1063/1.1508370.
- [Wie89] U.-J. Wiese. Identification of resonance parameters from the finite volume energy spectrum. *Nuclear Physics B - Proceedings Supplements*, 9:609–613, 1989, doi: 10.1016/0920-5632(89)90171-0.
- [WSS95] R. B. Wiringa, V. G. J. Stoks, and R. Schiavilla. Accurate nucleon-nucleon potential with charge-independence breaking. *Physical Review C*, 51(1):38–51, 1995, doi: 10.1103/physrevc.51.38.
- [YA93] H. A. Yamani and M. S. Abdelmonem. A simple method to extract resonance information from the Harris energy eigenvalues and eigenvectors. *Journal of Physics A: Mathematical and General*, 26:L1183–L1187, 1993, doi: 10.1088/0305-4470/26/22/009.
- [Yak67] O. A. Yakubovsky. On the Integral equations in the theory of N particle scattering. *Soviet Journal of Nuclear Physics*, 5:937, 1967. *Yad. Fiz.*5,1312 (1967).
- [Yam82] Hashim A. Yamani. The equivalence of the Feshbach and J-matrix methods. *Journal of Mathematical Physics*, 23(1):83–86, 1982, doi: 10.1063/1.525210.
- [YF75] Hashim A. Yamani and Louis Fishman. J-matrix method: Extensions to arbitrary angular momentum and to Coulomb scattering. *Journal of Mathematical Physics*, 16:410, 1975, doi: 10.1063/1.522516.
- [Yuk35] Hideki Yukawa. On the Interaction of Elementary Particles. I. *Proceedings of the Physico-Mathematical Society of Japan. 3rd Series*, 1935, doi: 10.11429/ppmsj1919.17.048.
- [ZBJ+93] D. C. Zheng, B. R. Barrett, L. Jaqua, J. P. Vary, and R. J. McCarthy. Microscopic calculations of the spectra of light nuclei. *Physical Review C*, 48(3):1083–1091, 1993, doi: 10.1103/physrevc.48.1083.
- [ZMZH04] S. S. Zhang, J. Meng, S. G. Zhou, and G. C. Hillhouse. Analytic continuation of single-particle resonance energy and wave function in relativistic mean field theory. *Physical Review C*, 70(3), 2004, doi: 10.1103/physrevc.70.034308.

- [ZSS98] S. A. Zaitsev, Yu. F. Smirnov, and A. M. Shirokov. True many-particle scattering in the oscillator representation. *Theoretical and Mathematical Physics*, 117(2):1291–1307, 1998, doi: 10.1007/bf02557169.



# Danksagung

Ich möchte mich bei Robert Roth bedanken, überhaupt erst die Möglichkeit geschaffen zu haben diese Arbeit zu verfassen. Danke für Korrekturen und Rückmeldungen selbst an Tagen und Zeiten, wo niemand mehr sonst noch arbeiten würde.

Danke an Jens Braun, die Rolle des Korreferent zu übernehmen.

Danke an alle aktuellen und ehemaligen Mitglieder der TNP++ Gruppe / AG Roth, die ich kennenlernen durfte. Für Schabernack, Spiele, Prager Bier und vegetarische Kaninchen, TRI-UMFale Konferenzen und dass für jeden von euch auch andere Dinge im Leben als Physik existieren. Danke and Klaus, Christina, Stefan, Roland, Richard, Eskendr, Alexender, Thomas, Laura, Tobias, Tobias, Marco, Julius und viele weitere, die vielleicht nur etwas kürzer in der Gruppe waren.

Danke Thomas, für technische Unterstützung, Coden, Diskussion, stilles Gegenübersitzen, Schnee- und Bergwanderungen (“You gonna be a doctor!”) und Korrekturen für diese Arbeit.

Danke Roland, dafür, ein Zauberer zu sein.

Danke Charel, für Besuche im entfernten Darmstadt, generellen Blödsinn, Bouldern, zu viel Zocken, speziellen Blödsinn und eine lange Vergangenheit .

Danke Detlef, für Selbstverständlichkeiten, die nicht selbstverständlich sind.

Danke Doris, für sehr viel Herzblut.

Danke Jan und Dirk, dafür, mir lesen beigebracht zu haben. Halbwegs...

Danke Katrin, Fabian, Viola und Andi für Escape Rooms, Mini-Golfen im Dunkeln und Hellen, Bowlen und wer weiß was noch.

Danke Kai “Quai-Rona” Rilcy, der gigantische Gewinn, aka Spiel, Spaß und Schokolade, für gigantische Gewinne, Spiel, Spaß und Schokolade.

Danke Anna, Bastian, Pia und Toni, dass ihr Kai Rilcy seid und nicht andere.

Danke Hannah, dafür, dass Du der Mensch bist, der Du bist. Für uns. Für die besten Zeiten, für selbstlose Unterstützung, für Antrieb, Terminplanung, Organisation, Information. Für's Mitleiden. Für Korrekturen über Korrekturen. Für Lacher, wenn ich sie am dringsten gebrauchte habe. Ohne dich wäre diese Arbeit auch jetzt noch nicht fertig (zu egal welchem “jetzt”).

# Akademischer Werdegang

## Stefan Vasco Alexa

Geboren am 14. Mai 1989 in Luxemburg, Luxemburg

- 18.06.2009 Abitur, Hinterzarten, Baden-Württemberg, Deutschland
- 2009 - 2010 Bachelor Studium, Universität Luxemburg, Luxemburg
- 2010 - 2014 Bachelor Studium, TU Darmstadt, Deutschland
- 20.02.2014 Bachelorabschluss, Thesis: "Phase transitions in spin- and mass-imbalanced ultra-cold Fermi gases"
- 2014 - 2016 Master Studium, TU Darmstadt, Deutschland
- 30.05.2016 Masterabschluss, Thesis: "R-Matrix Theory for the Resonating Group Method, Master Thesis"
- 2016 - 2020 Promotionsstudium, TU Darmstadt, Deutschland



# Erklärung gemäß §9 Promotionsordnung

Hiermit versichere ich, dass ich die vorliegende Dissertation selbstständig angefertigt und keine anderen als die angegebenen Quellen und Hilfsmittel verwendet habe. Alle wörtlichen und paraphrasierten Zitate wurden angemessen kenntlich gemacht. Die Arbeit hat bisher noch nicht zu Prüfungszwecken gedient.

Darmstadt, den 16.06.2020

---

Stefan Vasco Alexa